CONSTRAINED DYNAMICS OF HOLOGRAPHIC DARK ENERGY IN MODIFIED $f(R)$ GRAVITY

A.Y. Shaikh[a#], A.P. Jenekar[b†], S.M. Shingne[c*]

aDepartment of Mathematics, Indira Gandhi Kala Mahavidyalaya, Ralegaon-445402, (M.S.) India
bDepartment of Mathematics, Arts, Commerce and Science College, Maregaon-445303, (M.S.) India
cDepartment of Mathematics, G. S. Science, Arts and Commerce College, Khamgaon-444312, (M.S.) India
*Corresponding Author E-mail: smshingne131@gmail.com; #E-mail: shaikh_2324ay@yahoo.com; †E-mail: apjenekar@gmail.com

In the present work, we examine the dynamical behaviour of holographic dark energy (HDE) within the framework of modified $f(R)$ gravity in a hypersurface-homogeneous space-time. To explore the universe's evolutionary behaviour under the influence of dark energy, we consider both exponential and power-law expansions. The cosmic evolution is analysed using standard cosmological diagnostics, including the density parameter and equation of state (EoS) parameter along with the deceleration parameter. Furthermore, the statefinder diagnostic pair is tested to detect precisely different phases of the universe. The squared speed of sound parameter was used to incorporate the stability analysis for our models. This investigation links the principles of quantum gravity to cosmology, producing testable predictions for forthcoming research and illustrating that HDE functions as a credible alternative to ΛCDM.
Keywords: *Hypersurface-homogeneous space time; f(R) gravity; Holographic dark energy*
PACS: 98.80.−k, 04.50.Kd, 95.36.+x

1. INTRODUCTION

The revelation of cosmic acceleration was a game-changing discovery in the history of cosmology. The initial detection occurred through the observation of Type Ia supernovae by Riess et al. [1-3], also analysed through Cosmic Microwave Background Radiation (CMBR) [4]. This discovery totally changed how we see the universe. It showed that the rate of expansion is getting faster, which goes against what we thought matter-dominated Friedmann model predictions were. These groundbreaking findings showed that the cosmos is actually expanding at a faster rate than it previously was thought, which totally changes what we know about how the cosmos works. The recently discovered measurements carried out by means of Type Ia supernovae match the precision of standard candles, demonstrating that distant supernovae appeared fainter than expected in a decelerating universe, strongly suggesting the presence of a mysterious repulsive force counteracting gravitational attraction on cosmological scales. We now have a lot of evidence which shows that our universe is expanding faster and faster, where dark energy is the main source causing it. We have got different probes that include precision observations of CMB anisotropies by WMAP and Planck [5], which measure the detailed mapping of baryon acoustic oscillations (BAO) [6] and comprehensive large-scale structure surveys [7], which have established beyond reasonable doubt that we live in an accelerating universe dominated by what we now call dark energy. All of the available evidence shows that dark energy – an enigmatic component constituting approximately a whopping 68% of the universe's energy –exhibits negative pressure characteristics.

The simplest theoretical framework that explains these observations is the ΛCDM model. This model adds Einstein's cosmological constant, represented with Λ into the field equations of general relativity (GR) to represent a constant vacuum energy density that fills all of space. This standard model has been successful in the fitting of observational data; however, it is confronted by two significant challenges. Firstly, the significant difference between the predicted values from quantum field theory and the observed value of the cosmological constant leads to the fine-tuning concern [8-11]; and second, the coincidence problem asks why dark energy became dynamically important only recently in cosmic history, at the special epoch when human observers happen to exist [12]. These basic issues have led cosmologists to check out dynamical dark energy models where the energy density evolves with time and remains constant. Out of these most interesting options, that holographic dark energy (HDE) is emerging as one of the most compelling alternatives that relies on quantum gravity's holographic principle [13-16].

The HDE framework is based on some interesting ideas from black hole thermodynamics and string theory. It proposes that the amount of dark energy density in a given volume is fundamentally limited by the amount of information allowed to boundthe volume's boundary, leading to the characteristic relation $\rho_{de} = 3c^2 M_p^2 L^{-2}$ [17], where represents an infrared cutoff scale that is identified with the future event horizon. This elegant formulation naturally sidesteps the fine-tuning problem because of its inherent scale dependence and provides a dynamical equation of state that may resolve the coincidence problem while maintaining a deep connection to fundamental quantum gravitational principles. Pawar et al. [18] recent work has shown the advantages of this in anisotropic cosmological settings and how the holographic approach works even in generalised spacetime geometries. However, when the HDE model is implemented within general relativity, these models

also encounter difficulties in simultaneously describing both the early inflationary epoch and late-time acceleration [19-20], limitations that have prompted investigation and study of generalised versions of the Einstein-Hilbert interaction for modified gravity to include additional curvature-dependent terms. Buchdahl [21] introduced $f(R)$ gravity as a generalisation of Einstein's relativity, whereas Starobinsky gravity $f(R) = R + \alpha R^l$ [22] is the most motivated modification, which is an exhilaratingly innovative theory of gravity that introduces a quadratic curvature correction to the Einstein-Hilbert action. It was among the first and most successful models of cosmic inflation, providing a purely geometric explanation for the exponential expansion of the early universe without requiring additional scalar fields. This theory was originally proposed to explain inflation through the dominant effects of the term at high curvatures and subsequently shown to produce inflationary predictions in excellent agreement with precision CMB measurements from Planck [23], while it might play a role in contributing to late-time acceleration through its curvature effects.

To fully explore what happens when the cosmological implications combine holographic dark energy with modified gravity, it is essential to move beyond the restrictive assumption of perfect isotropy inherent in the standard Friedmann-Lemaître-Robertson-Walker metric. Instead, we should explore a more general geometrical structure that maintains spatial homogeneity while allowing for anisotropic expansion effects, meaning allowing for different rates of expansion along different spatial directions. Hypersurface-homogeneous spacetimes [24-30] provide such a framework, offering a richer dynamical context for investigating dark energy that is particularly relevant for understanding the early universe before inflation erased primordial anisotropies [31,32], as well as for probing potential connections between the presence of dark energy followed by the formation of immense structures [33]. In this study, we examine holographic dark energy within the $f(R)$ gravity framework using a hypersurface-homogeneous spacetime background. We come up to deriving exact solutions for both exponential $\left(a(t) \sim e^{nt}\right)$ and power-law $\left(a(t) \sim t^m\right)$ expansion scenarios. These represent idealized cases of inflationary and late-time acceleration respectively. Through detailed analysis of key cosmological parameters including the evolution of density components $\Omega_i(z)$ [34-36], the dynamical equation of state $\omega(z)$ [37-39], the deceleration parameter $q(z)$ with statefinder diagnostics $\{r, s\}$ [40], while carefully tracking the development of anisotropy through the shear scalar σ^2, we have demonstrate several significant results: the model naturally produces accelerated expansion without fine-tuning. It also shown an asymptotic approach to a cosmological constant-like equation of state $(\omega = -1)$ at late times, and shows anisotropy evolution patterns consistent with current observational constraints from the CMB. These findings suggest that the synthesis of HDE with $f(R)$ gravity in an anisotropic cosmological framework may provide a more comprehensive and theoretically satisfying description of cosmic acceleration that addresses fundamental limitations of the standard ΛCDM model [41] while maintaining consistency with current observational evidence. Furthermore, this approach offers new insights into the deep connection between quantum gravity, modified gravity, and dark energy [42, 43], while making specific predictions that can be tested with next-generation cosmological surveys.

This motivates us to consider volumetric expansion of the exponential, and power-law kinds to examine the $f(R)$ gravity-based HDE within hypersurface-homogeneous space-time. The paper is structured as follows. Section 2 examines cosmology in considered space-time by integrating the HDE model with pressureless dark matter. The quadrature solutions for scale factors in field equations are contained in section 3. The physical and kinematical characteristics of our volumetric expansion models are explored in sections 4 and 5, whereas section 6 offers statefinder diagnostics along with the model's stability analysis. Section 7 concludes with a discussion of the results.

2. METRIC AND FIELD EQUATIONS

The action for $f(R)$ gravity is expressed as

$$S = \int \sqrt{-g} \left(f(R) + L_m \right) d^4x, \tag{1}$$

where $f(R)$ serves as a general function of the Ricci scalar R and L_m stands for the usual matter Lagrangian.

The field equations can be derived by varying the action pertaining to the metric $g_{\mu\nu}$ as

$$F(R) R_{\mu\nu} - \frac{1}{2} f(R) g_{\mu\nu} - \nabla_\mu \nabla_\nu F(R) + g_{\mu\nu} \nabla^\mu \nabla_\mu F(R) = -(T_{\mu\nu} + \bar{T}_{\mu\nu}), \tag{2}$$

with $F(R) \equiv \dfrac{df(R)}{dR}$, ∇_μ represents covariant differentiation, $T_{\mu\nu}$ serves as the standard matter energy momentum tensor whereas $\bar{T}_{\mu\nu}$ serves as energy momentum tensor associated with HDE.

Contraction of the field Equations (2) leads to

$$F(R) R - 2f(R) + 3\nabla^\mu \nabla_\mu F(R) = -(T + \bar{T}), \tag{3}$$

with $T = g_{\mu\nu}T^{\mu\nu}$ and $\overline{T} = g_{\mu\nu}\overline{T}^{\mu\nu}$. In a vacuum, the right-hand side of equation (3) vanishes, which gives us the relation between $f(R)$ and $F(R)$ as follows:

$$f(R) = \frac{1}{2}\left[3\nabla^{\mu}\nabla_{\mu}F(R) + F(R)R\right]. \tag{4}$$

Hypersurface-homogeneous models have been the subject of a significant amount of research, which can be described as

$$ds^2 = -dt^2 + A^2(t)dx^2 + B^2(t)\left[dy^2 + \Sigma^2(y,K)dz^2\right], \tag{5}$$

where A and B denotes the scale factors that depends on t only while $\Sigma(y,K) = \sin y, y, \sinh y$ with $K = 1, 0, -1$ respectively.

The corresponding scalar curvature R is

$$R = 2\left[\frac{\ddot{A}}{A} + 2\frac{\dot{A}\dot{B}}{AB} + 2\frac{\ddot{B}}{B} + \frac{\dot{B}^2}{B^2} + \frac{K}{B^2}\right], \tag{6}$$

where ' $\cdot$ ' denotes differentiation with respect to cosmic time t.

The energy momentum tensors are defined for both pressureless matter and HDE as

$$T_{\mu\nu} = \rho_m u_\mu u_\nu; \quad \overline{T}_{\mu\nu} = (\rho_{de} + p_{de})u_\mu u_\nu + g_{\mu\nu}p_{de}, \tag{7}$$

where ρ_m serves as the energy density of matter, p_{de} and ρ_{de} are pressure and energy density of the HDE respectively while u_μ are component of the four-velocity vector of fluid satisfying $g_{\mu\nu}u^\mu u^\nu = -1$.

Using definition of EoS parameter (ω_{de}), the energy momentum tensors (7) can be written as

$$T_{\mu\nu} = \text{diag}\left[0,0,0,-1\right]\rho_m; \quad \overline{T}_{\mu\nu} = \text{diag}\left[\omega_{de},\omega_{de},\omega_{de},-1\right]\rho_{de}. \tag{8}$$

And after parametrization, it reduces to

$$T_{\mu\nu} = \text{diag}\left[0,0,0,-1\right]\rho_m; \quad \overline{T}_{\mu\nu} = \text{diag}\left[\omega_{de}+\gamma,\omega_{de},\omega_{de},-1\right]\rho_{de}. \tag{9}$$

within which the skewness parameter γ represents an offset from EoS parameter (ω_{de}) on x-direction.

Using equations (7)-(9), the field equations turn out to be

$$F\left[\frac{\ddot{A}}{A} + 2\frac{\ddot{B}}{B}\right] - \frac{1}{2}f(R) - \left(\frac{\dot{A}}{A} + 2\frac{\dot{B}}{B}\right)\dot{F} = \rho_m + \rho_{de}, \tag{10}$$

$$F\left[\frac{\ddot{A}}{A} + 2\frac{\dot{A}\dot{B}}{AB}\right] - \frac{1}{2}f(R) - 2\frac{\dot{B}}{B}\dot{F} - \ddot{F} = -(\omega_{de}+\gamma)\rho_{de}, \tag{11}$$

$$F\left[\frac{\ddot{B}}{B} + \frac{\dot{A}\dot{B}}{AB} + \frac{\dot{B}^2}{B^2} + \frac{K}{B^2}\right] - \frac{1}{2}f(R) - \left(\frac{\dot{A}}{A} + \frac{\dot{B}}{B}\right)\dot{F} - \ddot{F} = -\omega_{de}\rho_{de}. \tag{12}$$

Here, we have the HDE density in the form

$$\rho_{de} = 3\left(\alpha H^2 + \beta\dot{H}\right), \tag{13}$$

where H stands for the Hubble parameter while α, β serve as constants.

The above requisite was stated by Granda and Oliveros and requires compliance with constraints established according to the existing observational data. The directional Hubble parameters, indicating the rates of cosmic expansion alongside designated axes, are defined underneath as

$$H_x = \frac{\dot{A}}{A}, \quad H_y = \frac{\dot{B}}{B} = H_z. \tag{14}$$

The mean Hubble parameter is defined by

$$H = \frac{1}{3}\frac{\dot{V}}{V} = \frac{1}{3}\left(\frac{\dot{A}}{A} + 2\frac{\dot{B}}{B}\right), \tag{15}$$

with $V = AB^2$ expressing the volume of the cosmos.

Using equations (14) and (15), the average anisotropy parameter turns out to be

$$\Delta = \frac{1}{3}\left(\frac{\Delta H_x + \Delta H_y + \Delta H_z}{H}\right)^2 = \frac{2}{9H^2}\left(\frac{\dot{A}}{A} - \frac{\dot{B}}{B}\right)^2. \tag{16}$$

Using equations (11) and (12), we obtain

$$\frac{\dot{A}}{A} - \frac{\dot{B}}{B} = \frac{\lambda}{FV} + \frac{1}{FV}\int\left(\frac{KF}{B^2} - \gamma\rho_{de}\right)Vdt, \tag{17}$$

with λ denoting a constant of integration.

Consequently, the anisotropy parameter becomes

$$\Delta = \frac{2}{9H^2}\left[\frac{\lambda}{FV} + \frac{1}{FV}\int\left(\frac{KF}{B^2} - \gamma\rho_{de}\right)Vdt\right]^2. \tag{18}$$

By choosing $\gamma = 0$ in equation (18), we get isotropic case as

$$\Delta = \frac{2}{9H^2}\left[\frac{\lambda}{FV} + \frac{K}{FV}\int\frac{FV}{B^2}dt\right]^2. \tag{19}$$

The integral component in equation (18) is omitted with

$$\gamma = \frac{KF}{B^2\rho_{de}}. \tag{20}$$

Hence, the energy-momentum tensor (9) turns out to be

$$\overline{T}_{\mu\nu} = \text{diag}\left[\omega_{de} + \frac{KF}{B^2\rho_{de}}, \omega_{de}, \omega_{de}, -1\right]\rho_{de}, \tag{21}$$

whereas the anisotropy parameter (18) reduces to

$$\Delta = \frac{2\lambda^2}{9H^2F^2}V^{-2}. \tag{22}$$

3. SOLUTION TO FIELD EQUATIONS

Using equations (17) and (20), we obtain

$$\frac{A}{B} = c_1\exp\left(\lambda\int\frac{dt}{FV}\right), \tag{23}$$

where c_1 is integration constant.

Solving equation (23), we obtained the quadrature solutions associated with scale factors A and B described as

$$A = d_1 a\exp\left[q_1\int\frac{dt}{Fa^3}\right], \tag{24}$$

and

$$B = d_2 a\exp\left[q_2\int\frac{dt}{Fa^3}\right]. \tag{25}$$

Here $a = \left(AB^2\right)^{\frac{1}{3}} = V^{\frac{1}{3}}$ is average scale factor and $d_1 = c_1^{\frac{2}{3}}$, $d_2 = c_1^{-\frac{1}{3}}$, $q_1 = \frac{2\lambda}{3}$, $q_2 = -\frac{\lambda}{3}$, satisfying $d_1 d_2^2 = 1$ and

$q_1 + 2q_2 = 0$.

In order to solve the integral (24)-(25), we use the connection among the differential and scalar components of $f(R)$ as considered by Sharif and Shamir [36,37] given by

$$F = c_2 a^{-2},$$ (26)

where c_2 is constant.

Using equations (24)-(26), we get

$$A = d_1 a \exp\left[\frac{q_1}{c_2} \int \frac{dt}{a}\right],$$ (27)

and

$$B = d_2 a \exp\left[\frac{q_2}{c_2} \int \frac{dt}{a}\right].$$ (28)

We currently have three distinct equations involving seven unknown variables $A, B, \rho_m, \rho_{de}, \omega_{de}, \gamma$ and $f(R)$. Consequently, additional conditions are required to fully resolve the system. Additional conditions can be introduced through assumptions related to specific physical scenarios or arbitrary mathematical suppositions. Therefore, we assume three volumetric expansion laws expressed as

$$V = c_3 e^{3nt},$$ (29)

$$V = c_4 t^{3m}$$ (30)

where c_3, c_4, n and m are positive constants.

4. EXPONENTIAL EXPANSION MODEL

The mean scale factor results in

$$a = k_1 e^{nt},$$ (31)

where $k_1 = c_3^{1/3}$.

Using the established relation between scale factor $a(t)$ and redshift (z) as $a(t) = \frac{1}{1+z}$, we get the expression for cosmic time in relation to redshift for model (31) as follows

$$t(z) = -\frac{1}{n} \log\left[k_1(z+1)\right].$$ (32)

Using equations (27), (28) and (31), the metric potentials are obtained as

$$A(z) = \frac{d_1}{1+z} \exp\left[\frac{2q_1}{nc_2}(1+z)\right].$$ (33)

and

$$B(z) = \frac{d_2}{1+z} \exp\left[\frac{2q_2}{nc_2}(1+z)\right].$$ (34)

Physical and Kinematical Properties

The directional Hubble Parameter are found to be

$$H_x = n + \frac{q_1}{c_2}(1+z); \; H_y = n + \frac{q_2}{c_2}(1+z) = H_z.$$ (35)

while the Mean Hubble Parameter turns out to be

$$H = n.$$ (36)

From equations (35)-(36), we noted that the H remains invariant, while the directional Hubble parameters fluctuate with time. The directional Hubble parameters approach to mean Hubble parameter as $t \to \infty$. The mean Hubble

parameter's derivative with regard to cosmic time being zero reveals the cosmos expanding at a rapid pace. Thus, it is possible to use the model that emerges to describe the dynamism of the late-time progression.

The deceleration parameter turns out to be

$$q = -1. \tag{37}$$

In accordance with recent studies of supernovae Ia , the negative value of q implies that universe appears to be expanding faster. Additionally, our findings align with the studies of Katore and Gore [19] and that of Rao and Neelima [44].

Scalar expansion and shear scalar are described respectively by

$$\theta = 3n , \tag{38}$$

and

$$\sigma^2 = \frac{q_1^2 + 2q_2^2}{2c_2^2}(1+z)^2 . \tag{39}$$

The consistency of the exponential growth is indicated by the steady value of the expansion scalar θ. At the very beginning epoch, the shear scalar σ^2 reaches a constant value, while both parameters approach zero over extended periods of time. The ratio σ^2/θ^2 vanishes at sufficient large time indicating the universe's isotropic expansion which resemble with the work of Katore and Gore [19].

From equation (22), the mean anisotropic parameter turns out to be

$$\Delta = \frac{2\lambda^2}{9n^2 c_2^2}(1+z)^2 . \tag{40}$$

Using equations (13) and (36), the HDE density exhibits constant physical behaviour as it turns out to be

$$\rho_{de} = 3n^2\alpha. \tag{41}$$

Using equations (20), (26), (33) and (41), the Skewness parameter is obtained as

$$\gamma = \frac{Kc_2}{3\alpha n^2 d_2^2}(1+z)^4 \exp\left[\frac{2q_2}{nc_2}(1+z)\right]. \tag{42}$$

From equations (6) and (33), the Ricci scalar is obtained as

$$R = 2\left\{6n^2 + \frac{K}{d_2^2}(1+z)^2 \exp\left[\frac{2q_2}{nc_2}(1+z)\right] + \frac{3q_2^2}{c_2^2}(1+z)^2\right\}. \tag{43}$$

and the scalar function $f(R)$ is given by equation (4)

$$f(R) = \left\{\frac{9n^2}{(1+z)^2} + \frac{K}{d_2^2}\exp\left[\frac{2q_2}{nc_2}(1+z)\right]\right\}c_2(1+z)^4 + 3c_2^{-1}q_2^2(1+z)^4 . \tag{44}$$

The matter energy density is

$$\rho_m = \frac{c_2}{2}(1+z)^2\left\{9n^2 - \frac{K}{d_2^2}(1+z)^2 \exp\left[\frac{2q_2}{nc_2}(1+z)\right]\right\} + \frac{(q_1-q_2)^2}{2c_2}(1+z)^4 - 3n^2\alpha. \tag{45}$$

The EoS parameter is given by

$$\omega_{de} = \frac{(1+z)^4}{6n^2\alpha c_2 d_2^2}\left\{d_2^2\left(\frac{3n^2 c_2^2}{(1+z)^2} + q_1^2 - q_2^2\right) - Kc_2^2 \exp\left[\frac{2q_2}{nc_2}(1+z)\right]\right\} \tag{46}$$

Dark energy pressure is found to be

$$p_{de} = \frac{c_2(1+z)^4}{2}\left\{\frac{3n^2}{(1+z)^2} - \frac{K}{d_2^2}\exp\left[\frac{2q_2}{nc_2}(1+z)\right]\right\} + \frac{(q_1^2-q_2^2)}{2c_2}(1+z)^4 . \tag{47}$$

Overall density is given by

$$\Omega = \frac{c_2\left(1+z\right)^4}{6n^2}\left\{\frac{9n^2}{\left(1+z\right)^2} - \frac{K}{d_2^2}\exp\left[\frac{2q_2}{nc_2}\left(1+z\right)\right] + c_2^{-2}\left(q_1 - q_2\right)^2\right\}. \tag{48}$$

Now we obtain the graphical representation of these parameters against redshift for three cases of $K = 1, 0, -1$ by taking appropriate choices of various constants involved in it. We take $d_2 = 0.1$, $\alpha = 5$, $c_2 = 1$, $k_1 = 1$, $q_1 = 2/3$, and $q_2 = -1/3$, with $\lambda = 1$, and from equation (36), we take $n = 67$ with reference to the current Hubble parameter value $H_0 = 67.4 \pm 0.5$ $kms^{-1}Mpc^{-1}$ by the Planck 2018 results [45], assuming the standard ΛCDM cosmology.
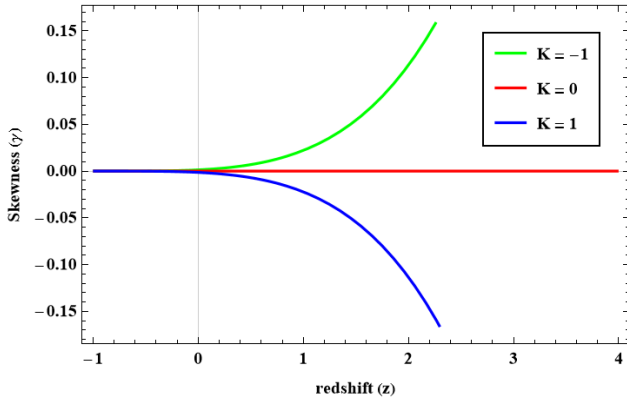
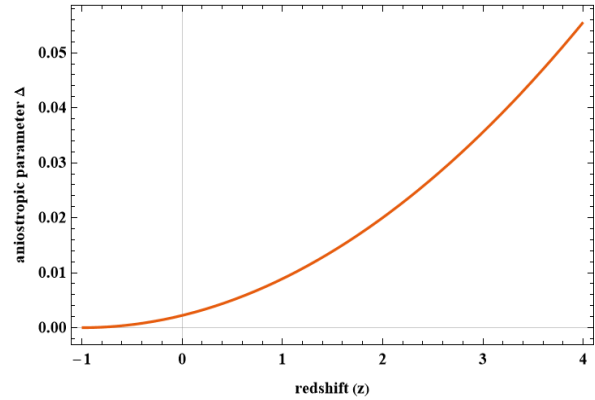**Figure 1.** Plot of skewness parameter (γ) versus redshift (z).

Figure 2. Plot of anisotropic parameter (Δ) versus redshift (z).
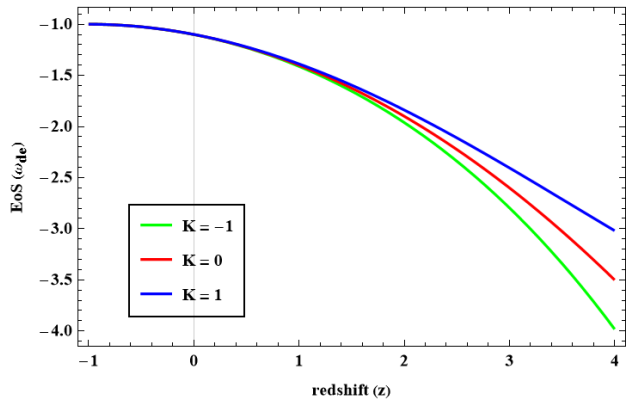
Figure 3. Plot of EoS parameter (ω_{de}) versus redshift (z)
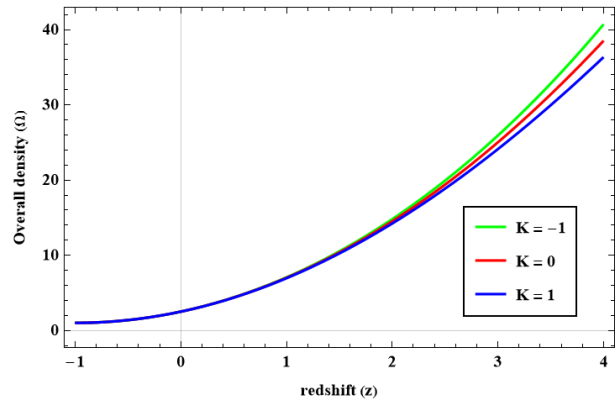

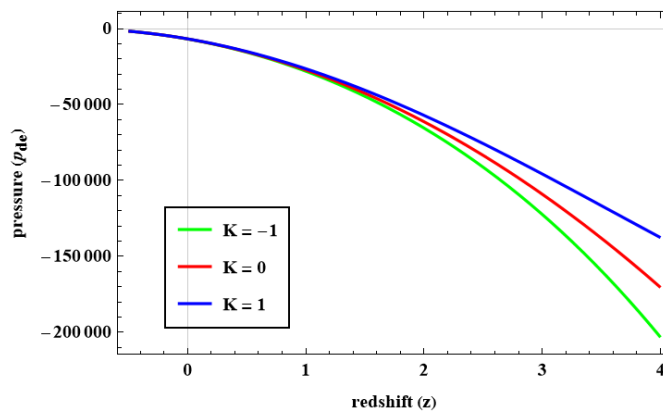**Figure 4.** Plot of overall density (Ω) versus redshift (z)

Figure 5. Plot of pressure (p) versus redshift (z)

From Figs. 1 and 2, the skewness parameter and anisotropic parameter indicate isotropisation of the universe as similar to the case of the hybrid model. The graphical representation in Fig. 3 depicts the variation of the EoS parameter during the progression of redshift. In the past, the behaviour of $\omega_{de} < -1$ shows the dominance by phantom energy. However, in the near future, $\omega_{de} \to -1$ predicts the ΛCDM model. The progression of the overall density parameter

against redshift is illustrated in Fig. 4. As cosmic development progresses, the overall density parameter diminishes, and for a proper choice of the constants, it approaches 1, indicating the flat universe that agrees with evidence from observations of the cosmos, whereas matter energy density follows the increasing behaviour as $z \to \infty$. Fig. 5 displays the approach of pressure against redshift, which shows that the resulting model is accelerating due to an ongoing presence of negative pressure, which is in accordance with the findings underlined in [46].

5. POWER EXPANSION MODEL

The mean scale factor results in

$$a = k_3 t^m, \tag{49}$$

where $k_3 = c_5^{1/3}$.

The relation for cosmic time and redshift for model (49) is found to be

$$t(z) = \left[k_2 (z+1) \right]^{-1/m}. \tag{50}$$

Using equations (27)-(28) and (49)-(50), the prospective metrics potentials in redshift are obtained as

$$A(z) = \frac{d_1}{1+z} \exp\left[-\frac{(1+z)q_1}{(m-1)c_2} \left((1+z)k_2 \right)^{-1/m} \right], \tag{51}$$

and

$$B(z) = \frac{d_1}{1+z} \exp\left[-\frac{(1+z)q_2}{(m-1)c_2} \left((1+z)k_2 \right)^{-1/m} \right]. \tag{52}$$

The Ricci scalar is

$$R = 6m(2m-1)\left(k_2(1+z) \right)^{2/m} + 2(1+z)^2 \left\{ \frac{K}{d_2^2} \exp\left[\frac{2q_2(1+z)}{(m-1)c_2} \left((1+z)k_2 \right)^{-1/m} \right] + \frac{3q_2^2}{c_2^2} \right\} \tag{53}$$

PHYSICAL AND KINEMATICAL PROPERTIES

The directional Hubble parameters can be expressed as

$$H_x = m\left[k_2(z+1) \right]^{1/m} + \frac{q_1}{c_2}(1+z); \ H_y = m\left[k_2(z+1) \right]^{1/m} + \frac{q_2}{c_2}(1+z) = H_z. \tag{54}$$

and mean Hubble parameter turns out to be

$$H = m\left[k_2(z+1) \right]^{1/m}. \tag{55}$$

The deceleration parameter turns out to be

$$q = \frac{1}{m} - 1. \tag{56}$$

For $m < 1$, it indicates a decelerating cosmos as $q > 0$, whereas for $m > 1$, it describes rapid expansion of the cosmos as $q < 0$, that is in line with the studies of Sarkar and Mahanta [47].

The scalar expansion, shear scalar and mean anisotropic parameter are expressed respectively by

$$\theta = 3H = 3m\left[k_2(z+1) \right]^{1/m} \tag{57}$$

$$\sigma^2 = \frac{q_1^2 + 2q_2^2}{2c_2^2}(1+z)^2. \tag{58}$$

and

$$\Delta = \frac{2\lambda^2}{9m^2 c_2^2}(1+z)^2 \left[k_2(1+z) \right]^{-2/m} \tag{59}$$

The HDE density is

$$\rho_{de} = 3m(m\alpha - \beta)\left[k_2(1+z) \right]^{2/m} \tag{60}$$

Skewness parameter is found to be

$$\gamma = \frac{Kc_2(1+z)^4\left((1+z)k_2\right)^{-2/m}}{3m(m\alpha-\beta)d_2^2}\exp\left[-\frac{(1+z)q_2}{(m-1)c_2}\left((1+z)k_2\right)^{-1/m}\right]. \tag{61}$$

From equation (6), the Ricci scalar is obtained as

$$R = 6m(2m-1)\left(k_2(1+z)\right)^{2/m} + 2(1+z)^2\left\{\frac{K}{d_2^2}\exp\left[\frac{2q_2(1+z)}{(m-1)c_2}\left(k_2(1+z)\right)^{-1/m}\right] + \frac{3q_2^2}{c_2^2}\right\}. \tag{62}$$

and the scalar function $f(R)$ is given by equation (4)

$$f(R) = \frac{(1+z)^4}{c_2}\left\{\frac{3m(3m-2)}{(1+z)^2}\left((1+z)k_2\right)^{2/m} + c_2^2\left(\frac{K}{d_2^2}\exp\left[\frac{2q_2(1+z)}{(m-1)c_2}\left(k_2(1+z)\right)^{-1/m}\right]\right) + 3q_2^2\right\}. \tag{63}$$

The matter density is

$$\rho_m = \frac{c_2(1+z)^4}{2}\left\{\frac{9m^2\left((1+z)k_2\right)^{2/m}}{(1+z)^2} - \frac{K}{d_2^2}\exp\left[\frac{2(1+z)q_2}{(m-1)c_2}\left(k_2(1+z)\right)^{-1/m}\right]\right\}$$
$$+ 3m(\beta-m\alpha)\left(k_2(1+z)\right)^{2/m} + \frac{(q_1-q_2)^2}{2c_2}(1+z)^4. \tag{64}$$

The EoS parameter is given by

$$\omega_{de} = \frac{(1+z)^4}{6m(m\alpha-\beta)c_2}\left\{\frac{3m^2c_2^2}{(1+z)^2} + \frac{\left((1+z)k_2\right)^{-2/m}}{d_2^2}\left(-Kc_2^2\exp\left[\frac{2q(1+z)_2}{(m-1)c_2}\left(k_2(1+z)\right)^{-1/m}\right] + d_2^2\left(q_1^2-q_2^2\right)\right)\right\}. \tag{65}$$

Dark energy pressure is obtained as

$$p_{de} = \frac{(1+z)^4}{2c_2d_2^2}\left\{-c_2^2K\exp\left[\frac{2q(1+z)_2}{(m-1)c_2}\left(k_2(1+z)\right)^{-1/m}\right] + \frac{3m^2d_2^2c_2^2}{(1+z)^2}\left((1+z)k_2\right)^{2/m} + d_2^2\left(q_1^2-q_2^2\right)\right\}. \tag{66}$$

Overall density is found to be

$$\Omega = \frac{(1+z)^4}{6m^2c_2d_2^2}\left((1+z)k_2\right)^{-2/m}\left\{\frac{9m^2d_2^2c_2^2}{(1+z)^2}\left(k_2(1+z)\right)^{2/m} - c_2^2K\exp\left[\frac{2q(1+z)_2}{(m-1)c_2}\left(k_2(1+z)\right)^{-1/m}\right] + d_2^2\left(q_1-q_2\right)^2\right\}. \tag{67}$$

Now, the graphical representation of these parameters against redshift for three cases of $K = 1, 0, -1$ are obtained by taking appropriate choices of various constants involved in it. We consider $d_2 = 0.1$, $\alpha = 5, \beta = 1$ $c_2 = 1$, $k_2 = 1$, $q_1 = 2/3$, $q_2 = -1/3$, with $\lambda = 1$, and from equation (55), we take $m = 67$ with reference to the $H_0 = 67.4 \pm 0.5$ $kms^{-1}Mpc^{-1}$ estimated in the Planck 2018 results [45].

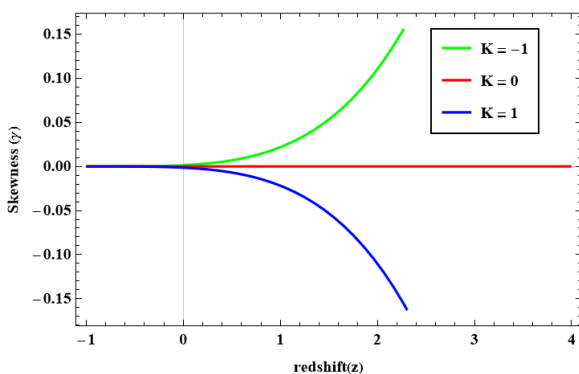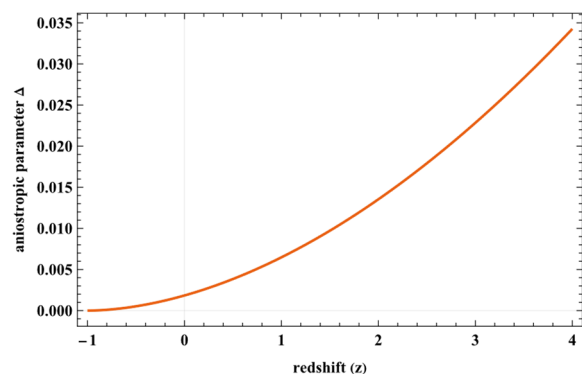**Figure 6.** Plot of skewness parameter (γ) versus redshift (z)
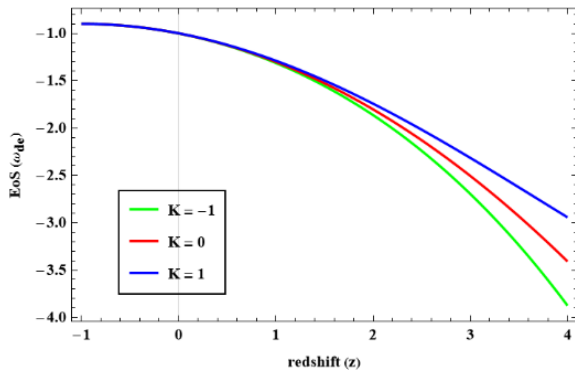

Figure 7. Plot of anisotropic parameter (Δ) versus redshift (z)

Figure 8. Plot of EoS (ω_{de}) versus redshift (z)
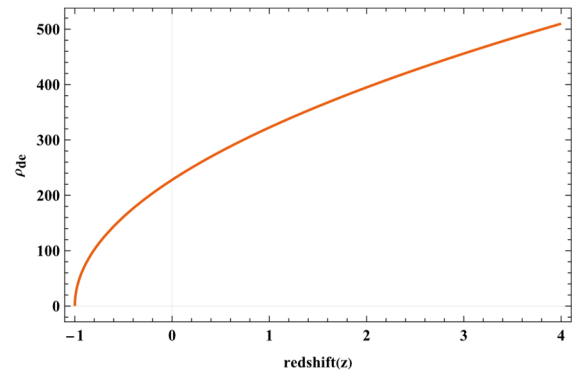

Figure 9. Plot of HDE density (ρ_{de}) versus redshift (z)
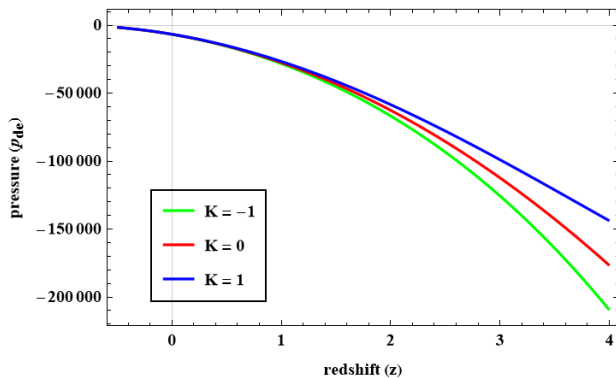

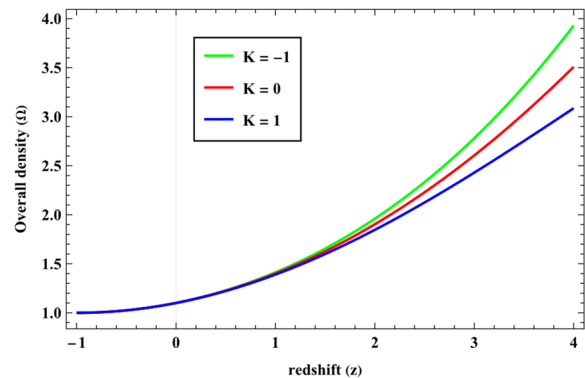**Figure 10.** Approach of pressure (p_{de}) against redshift (z)

Figure 11. Plot of overall density (Ω) versus redshift (z)

Late-time isotropisation of the cosmos is reflected through the demonstration in Fig. 6 and Fig. 7 as the skewness parameter and anisotropic parameter become zero at $z \to -1$. From Fig. 8, the EoS parameter initially starts with a positive value and reaches to $\omega_{de} = -1$ at $z \to -1$ indicating the model in the future. The evolution of HDE density is displayed in Fig. 9, which indicates its declining nature while avoiding fine-tuning. The negative value of pressure with the evolution of redshift is illustrated in Fig. 10, indicating that the expansion of the cosmos is accelerating, while Fig. 11 displays the progression of the overall density parameter against redshift with $\Omega \to 1$ at $z \to -1$ specifying a flat cosmos.

6. STATEFINDER DIAGNOSTIC AND STABILITY ANALYSIS OF MODELS
6.1 Statefinder Diagnostics of Models

The statefinder diagnostic as proposed by Sahni et al. [54], serves as a proficient tool for differentiating among various cosmological models. Its definition is

$$r \equiv \frac{\dddot{a}}{aH^3} \text{ and } s \equiv \frac{r-1}{3\left(q - \frac{1}{2}\right)}. \tag{68}$$

6.1.1 **For exponential expansion model**

From equations (31), (36)-(37), statefinder parameters pair (68) for exponential expansion model reduces to $\{r, s\} \to \{1, 0\}$ representing the ΛCDM model and resembles with the investigations of Katore and Gore [19] and Samanta [46].

6.1.2 **For power expansion model**

The statefinder parameters (68) for power expansion model turn out to be

$$r = \frac{(m-1)(m-2)}{m^2} \text{ and } s = \frac{2}{3m}. \tag{69}$$

And their association is found to be

$$r = 1 + \frac{9}{2}s(s-1). \tag{70}$$

The visualization of r against s is displayed in Fig. 12. Its route goes through the DE region of Chaplygin Gas (CG) and quintessence [56] in the $r-s$ plane and tends to approach the ΛCDM model in the near future, which resemble with the findings discussed in [57].
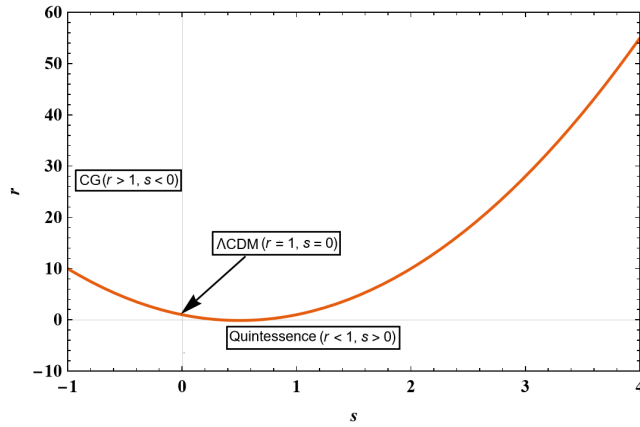

Figure 12. Plot of r versus s (Power expansion model)

6.2 STABILITY ANALYSIS OF MODEL

The model's stability is evaluated through the examination of the parameter identified as the squared speed of sound v_s^2 as proposed by Sadeghi et al. [58]. If the value of v_s^2 is positive, model exhibits stability whereas for a negative value of v_s^2, the model is unstable. It is specified by

$$v_s^2 = \frac{dp_{de}}{d\rho_{de}}. \tag{71}$$

Using equations (66) and (66), the stability parameter (71) for power expansion model is found to be

$$v_s^2 = \frac{(1+z)^5}{6m(m\alpha - \beta)c_2 d_2^2} \times \left\{ \begin{array}{l} \frac{3m^2 c_2^2 d_2^2}{(1+z)^3}(m+1) - Kc_2 q_2 \left[k_2(1+z)\right]^{-3/m} \exp\left[\frac{2q_2(1+z)}{(m-1)c_2}\left((1+z)k_2\right)^{-1/m}\right] \\ -\frac{2m\left[k_2(1+z)\right]^{-2/m}}{1+z}\left[Kc_2^2 \exp\left[\frac{2q_2(1+z)}{(m-1)c_2}\left((1+z)k_2\right)^{-1/m}\right] + d_2^2\left(q_2^2 - q_1^2\right)\right] \end{array} \right\}. \tag{72}$$
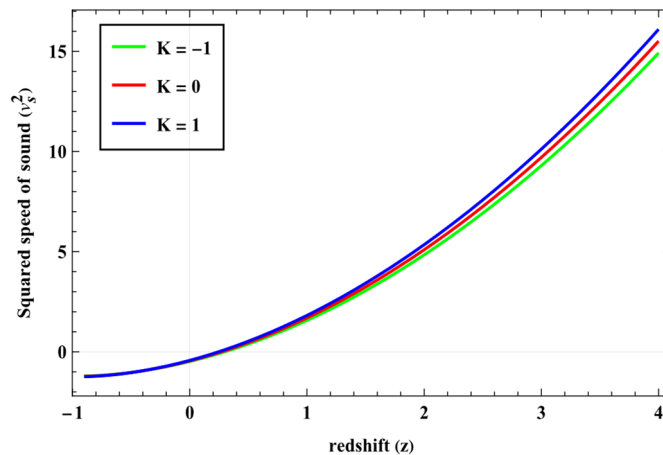

Figure 13. Inspection of squared speed of sound (v_s^2) against redshift (z)

Fig. 13 illustrates the variations in the squared speed of sound (v_s^2) against redshift (z). We noticed that $v_s^2 > 0$ for all the positive values of redshift (z), indicating its stability up to the present time, but $v_s^2 < 0$ for the negative domain indicating the model's instability in the future.

7. CONCLUSIONS

This paper examined the behaviour of HDE in $f(R)$ gravity across a hypersurface-homogeneous spacetime, focusing on exponential and power-law expansions. Here is a brief overview of our study's findings:

- The exponential expansion model yields a constant Hubble parameter while $q = -1$ indicating sustained accelerated expansion and an EoS transitioning from phantom-like ($\omega_{de} < -1$) to ΛCDM ($\omega_{de} \to -1$), aligning with late-time acceleration.

- The power-law model shows deceleration-to-acceleration behaviour ($q > 0$ and $q < 0$) depending on $m < 1$ and $m > 1$ respectively, with the EoS parameter evolving from quintessence to ΛCDM.

- Both models exhibit complete late-time isotropisation (Δ, $\gamma \to 0$), consistent with CMB observations that suggest large-scale homogeneity.

- The statefinder diagnostic distinguishes the evolutionary paths of the two models: the exponential model closely tracks the ΛCDM trajectory, while the power-law model passes through the quintessence and phantom regimes before covering ΛCDM.

- We have done some stability tests, and it looks like the exponential solution is the most stable throughout cosmic evolution, whereas the power-law model shows late-time instabilities.

- The HDE density shows a declining nature while avoiding fine-tuning, and the overall density parameter is maintaining $\Omega \to 1$ for a flat cosmos.

- The present framework successfully unifies inflation and contemporary cosmic acceleration, with residual anisotropic effects providing a potential window into early-universe dynamics.

This work links quantum gravity principles with cosmology, making testable predictions for future research and showing that HDE is a viable alternative to ΛCDM.

ORCID

A.Y. Shaikh, https://orcid.org/0000-0001-5315-559X; **A.P. Jenekar**, https://orcid.org/0009-0005-8928-3725

REFERENCES

[1] A.G. Riess, *et al.*, Astron. J. **116**, 1009 1998). https://doi.org/10.1086/300499
[2] A.G. Riess, *et al.*, Astron. J. **117**, 707 (1999). https://doi.org/10.1086/300738
[3] S. Perlmutter, *et al.*, Astrophys. J. **517**, 565 (1999). https://doi.org/10.1086/307221
[4] P. De Bernardis, *et al*., Nature, **404**, (2000). https://doi.org/10.1038/35010035
[5] E. Komatsu, *et al.*, Astrophys. J. Suppl. Ser. **192**, 18 (2011). http://dx.doi.org/10.1088/0067-0049/180/2/330
[6] M. Tegmark, *et al.*, Phys. Rev. D, **69**, 103501 (2004). https://doi.org/10.1103/PhysRevD.69.103501
[7] U. Seljak, *et al.*, Phys. Rev. D, **71**, 103515 (2005). https://doi.org/10.1103/PhysRevD.71.103515
[8] K. Bamba, *et al.*, Astrophys. Space Sci. **342**, 155 (2012). https://doi.org/10.1007/s10509-012-1181-8
[9] M. Sharif and M. Zubair, Astrophys. Space Sci. **330**, 399 (2010). https://doi.org/10.1007/s10509-010-0414-y
[10] S.M. Carroll, W.H. Press, and E.L. Turner, Annu. Rev. Astron. Astrophys. **30**, 499 (1992). https://doi.org/10.1146/annurev.aa.30.090192.002435
[11] M.S. Turner, and M. White, Phys. Rev. D, **56**, R4439 (1997). https://doi.org/10.1103/PhysRevD.56.R4439
[12] V. Sahni, and L. Wang, Phys. Rev. D, **62**, 103517 (2000). https://doi.org/10.1103/PhysRevD.62.103517
[13] A.G. Cohen, D.B. Kaplan, and A.E. Nelson, Phys. Rev. Lett. **82**, 4971 (1999). https://doi.org/10.1103/PhysRevLett.82.4971
[14] M. Li, Physics Letters B, **603**, 1-2 (2004). https://doi.org/10.1016/j.physletb.2004.10.014
[15] V.C. Dubey, and U.K. Sharma, New Astron. **86**, 101586 (2021). https://doi.org/10.1016/j.newast.2021.101586
[16] S. Capozziello, P. Martin-Moruno, and C. Rubano, Phys. Lett. B, **664**, 12 (2008). https://doi.org/10.1016/j.physletb.2008.04.061
[17] S. Nojiri, and S. D. Odintsov, Phys. Lett. B, **659**, 821 (2008). https://doi.org/10.1016/j.physletb.2007.12.001
[18] D.D. Pawar, R.V. Mapari, and P.K. Agrawal, J. Astrophys. Astron. **40**, 13 (2019). https://doi.org/10.1007/s12036-019-9582-5
[19] S.D. Katore, and S.V. Gore, J. Astrophys. Astron. **41**, 12 (2020). https://doi.org/10.1007/s12036-020-09632-z
[20] C.P. Singh, and A. Beesham, Gravit. Cosmol. **17**, 284 (2011). https://doi.org/10.1134/S020228931103008X
[21] H.A. Buchdahl, Mon. Not. R. Astron. Soc. **150**, 1 (1970). https://doi.org/10.1093/mnras/150.1.1
[22] A.A. Starobinsky, JETP Lett. **86**, 157 (2007). https://doi.org/10.1134/S0021364007150027
[23] P.A.R. Ade, *et al.*, A&A, **571**, A22 (2014). https://doi.org/10.1051/0004-6361/201321569
[24] S.D. Katore, and A.Y. Shaikh, Astrophys. Space Sci. **357**, 27 (2015). https://doi.org/10.1007/s10509-015-2297-4
[25] S.H. Shekh, and K. Ghaderi, Phys. Dark Universe **31**, 100785 (2021). https://doi.org/10.1016/j.dark.2021.100785
[26] T. Vinutha, K.V. Vasavi, and K.S. Kavya, Int. J. Geom. Methods Mod. Phys. **20**, 2350119 (2023). https://doi.org/10.1142/S0219887823501190
[27] L.N. Granda, and A. Oliveros, Phys. Lett. B, **669**, 275 (2008). https://doi.org/10.1016/j.physletb.2008.10.017
[28] S. Kumar, and C.P. Singh, Astrophys. Space Sci. **312**, 57 (2007). https://doi.org/10.1007/s10509-007-9623-4
[29] C.P. Singh, S. Ram, and M. Zeyauddin, Astrophys. Space Sci. **315**, 181 (2008). https://doi.org/10.1007/s10509-008-9811-x
[30] J.P. Singh, and P.S. Baghel, Int. J. Theor. Phys. **48**, 449 (2009). https://doi.org/10.1007/s10773-008-9820-0

[31] Ö. Akarsu, and C.B. Kılınç, Gen. Relativ. Gravit. **42**, 119 (2009). https://doi.org/10.1007/s10714-009-0821-y
[32] Ö. Akarsu, and C.B. Kılınç, Gen. Relativ. Gravit. **42**, 763 (2010). https://doi.org/10.1007/s10714-009-0878-7
[33] K.S. Adhav, *et al.*, Astrophys. Space Sci. **332**, 497 (2011). https://doi.org/10.1007/s10509-010-0519-3
[34] V.B. Johri, and K. Desikan, Gen. Relativ. Gravit. **26**, 1217 (1994). https://doi.org/10.1007/BF02106714
[35] K. Uddin, J.E. Lidsey, and R. Tavakol, Class. Quantum Gravity, **24**, 3951 (2007). https://doi.org/10.1088/0264-9381/24/15/012
[36] M. Sharif and M.F. Shamir, Class. Quantum Gravity, **26**, 235020 (2009). https://doi.org//10.1088/0264-9381/26/23/235020
[37] M. Sharif and M.F. Shamir, Mod. Phys. Lett. A, **25**, 1281 (2010). https://doi.org/10.1142/S0217732310032536
[38] S.D. Katore, *et al.*, Commun. Theor. Phys. **62**, 768 (2014). https://doi.org/10.1088/0253-6102/62/5/21
[39] Y. Younesizadeh, and A. Rezaie, Int. J. Mod. Phys. A, **37**, 2250040 (2022). https://doi.org/10.1142/S0217751X22500403
[40] V. Sahni, *et al.*, J. Phys. Lett. 77, 201-206 (2003). https://doi.org/10.1134/1.1574831
[41] L. Perivolaropoulos and F. Skara, New Astron. Rev. **95**, 101659 (2022). https://doi.org/10.1016/j.newar.2022.101659
[42] P.A.R. Ade, *et al.*, Astron. Astrophys. **571**, A16 (2014). https://doi.org/10.1051/0004-6361/201525830
[43] R.A. Knop, *et al.*, Astrophys. J. **598**, 102 (2003). https://doi.org/10.1086/378560
[44] V.U.M. Rao, and D. Neelima, Eur. Phys. J. Plus, **128**, 35 (2013). https://doi.org/10.1140/epjp/i2013-13035-y
[45] Planck Collaboration, *et al.*, Astron. Astrophys. **641**, A6 (2020). https://doi.org/10.1051/0004-6361/201833910
[46] G.C. Samanta, Int. J. Theor. Phys. **52**, 4389 (2013). https://doi.org/10.1007/s10773-013-1757-2
[47] S. Sarkar, and C.R. Mahanta, Int. J. Theor. Phys. **52**, 1482 (2013). https://doi.org/10.1007/s10773-012-1468-0
[48] C. Zhang, *et al.*, Res. Astron. Astrophys. **14**, 1221 (2014). https://doi.org/10.1088/1674-4527/14/10/002
[49] J. Simon, L. Verde, and R. Jimenez, Phys. Rev. D, **71**, 123001 (2005). https://doi.org/10.1103/PhysRevD.71.123001
[50] M. Moresco, *et al.*, J. Cosmol. Astropart. Phys. 006 (2012). https://doi.org/10.1088/1475-7516/2012/08/006
[51] M. Moresco, *et al.*, J. Cosmol. Astropart. Phys. 014 (2016). https://dx.doi.org/10.1088/1475-7516/2016/05/014
[52] A.L. Ratsimbazafy, *et al.*, Mon. Not. R. Astron. Soc. **467**, 3239 (2017). https://doi.org/10.1093/mnras/stx301
[53] S. Capozziello, S. Nojiri, and S. D. Odintsov, Phys. Lett. B, **781**, 99 (2018). https://doi.org/10.1016/j.physletb.2018.03.064
[54] V. Sahni, *et al.*, J. Exp. Theor. Phys. Lett. **77**, 201 (2003). https://doi.org/10.1134/1.1574831
[55] U. Alam, *et al.*, Mon. Not. R. Astron. Soc. **344**, 1057 (2003). https://doi.org/10.1103/PhysRevD.68.127501
[56] Y.B. Wu, *et al.*, Gen. Relativ. Gravit. **39**, 653 (2007). https://doi.org/10.1007/s10714-007-0412-8
[57] A.Y. Shaikh, Eur. Phys. J. Plus, **138**, 301 (2023). https://doi.org/10.1140/epjp/s13360-023-03931-4
[58] J. Sadeghi, A.R. Amani, and N. Tahmasbi, Astrophys. Space Sci. **348**, 559 (2013). https://doi.org/10.1007/s10509-013-1579-y

ОБМЕЖЕНА ДИНАМІКА ГОЛОГРАФІЧНОЇ ТЕМНОЇ ЕНЕРГІЇ В МОДИФІКОВАНІЙ f(R) ГРАВІТАЦІЇ

А.Й. Шейх[a], А.П. Дженекар[b], С.М. Шінгне[c]
[a]Кафедра математики, Індіра Ганді Кала Махавідьялая, Ралегаон-445402, M.S., Індія
[b]Кафедра математики, мистецтв, комерції та науки Коледж, Марегаон-445303, M.S., Індія
[c]Кафедра математики, Коледж наук, мистецтв та комерції ім. Г.С., Кхамгаон-444312, M.S., Індія

У цій роботі ми досліджуємо динамічну поведінку голографічної темної енергії (ГТЕ) в рамках модифікованої *f*(*R*) гравітації в однорідному гіперповерхневому просторі-часі. Щоб дослідити еволюційну поведінку Всесвіту під впливом темної енергії, ми розглядаємо як експоненціальні, так і степеневі розклади. Космічну еволюцію проаналізовано за допомогою стандартної космологічної діагностики, включаючи параметр густини та параметр рівняння стану (EoS) разом із параметром уповільнення. Крім того, діагностична пара statefinder тестується для точного виявлення різних фаз Всесвіту. Параметр квадрата швидкості звуку був використаний для включення аналізу стабільності до наших моделей. Це дослідження пов'язує принципи квантової гравітації з космологією, створюючи перевірені прогнози для майбутніх досліджень та ілюструючи, що HDE функціонує як надійна альтернатива ΛCDM.
Ключові слова: *гіперповерхнево-однорідний простір-час; f(R) гравітація; голографічна темна енергія*

FLRW MODEL COUPLED WITH MASSLESS SCALAR FIELD IN $f(T)$ GRAVITY – TWO FLUID SCENARIO

Vilas B. Raut[a#], Sanjay A. Salve[b]*

aDepartment of Mathematics, Mungsaji Maharaj Mahavidyalaya, Darwha, Dist. Yavatmal – 445 202, Maharashtra, India
bDepartment of Mathematics, Jijamata Mahavidyalaya, Buldana – 443 001, Maharashtra, India
Corresponding Author's E-mail: salvesanjaya@gmail.com; #E-mail: drvilasraut@gmail.com

In this work, we investigate a cosmological model within the framework of modified teleparallel gravity, known as $f(T)$ gravity, by considering a spatially flat Friedmann-Lemaître-Robertson-Walker (FLRW) Universe filled with two fluids-barotropic matter and a dark fluid-alongside a massless scalar field. We study an interacting case of the fluids, deriving exact solutions of the field equations under a time-dependent deceleration parameter scenario. The model demonstrates a viable cosmological sequence: early decelerating expansion followed by late-time acceleration. The torsion scalar T, its function $f(T)$, and the scalar field ϕ all evolve dynamically, transitioning from dominant roles in the early Universe to diminished effects at late times. The dark fluid energy density remains nearly constant, supporting accelerated expansion, while the matter density decreases with cosmic time. The effective equation of state (EoS) parameter evolves from a matter-like behavior to negative values, suggesting a natural transition from matter domination to a dark energy-dominated phase. These results affirm that $f(T)$ gravity coupled with a scalar field can explain cosmic acceleration and provide an alternative to the standard ΛCDM model without invoking exotic energy components.
Keywords: *Two fluids; f(T) gravity; Linear deceleration parameter; Cosmology*
PACS: 95.36.+x; 04.20.Cv; 98.80-k.

1. INTRODUCTION

Observations have consistently demonstrated the Universe's accelerating expansion in its later stages [1, 2], with supernova type Ia (SN Ia) data providing strong confirmation [3, 4]. Analyses of the cosmic microwave background (CMB) and large-scale structure (LSS) point towards this accelerated expansion being driven by a component with negative pressure, termed dark energy (DE), within a spatially flat Universe. The behavior of DE is typically described using the equation of state (EoS) parameter, defined as the ratio of pressure (p) to energy density (ρ). Current cosmological data, particularly from SN Ia, suggest that the EoS parameter (w) is close to -1. Values precisely at -1, slightly above, or slightly below correspond to standard cosmology, quintessence, or phantom regions, respectively, while values significantly greater than -1 are disfavoured. Numerous researchers have explored DE models in diverse contexts [5-9]. The exploration of two-fluid cosmological models has gained significant traction in contemporary cosmology, offering a framework to understand the complex interplay of cosmic constituents. These models typically consider the Universe as a composition of distinct fluids, such as baryonic matter, dark matter, dark energy, or radiation, and examine their interactions and evolution. Recent research has delved into the dynamics of these models within modified gravity theories, to account for the observed accelerated expansion of the Universe. For example, studies have investigated scenarios where one fluid represents ordinary matter and the other models dark energy, or where radiation is considered alongside matter, allowing for a more nuanced understanding of cosmic evolution. Investigations into interacting and non-interacting scenarios between DE and barotropic fluids have also been conducted, with examples including Chen and Wang's study [10] on interacting viscous DE in Einstein cosmology using the Friedmann-Robertson-Walker (FRW) Universe, Avellino's work [11] on DE interactions with bulk viscosity in a flat FRW Universe, and Saha's exploration [12] of two-fluid DE models within FRW cosmology. Further research by Amirhashchi *et al.* [13, 14] has examined interacting two-fluid viscous DE in non-flat and anisotropic Universes. These investigations aim to reconcile theoretical predictions with observational data from sources like the Cosmic Microwave Background and supernovae, providing the fundamental nature of the Universe.

Researchers have investigated various $f(T)$ functions to better fit observational data, with particular attention to the late-time accelerated expansion of the Universe. Some studies have probed the interaction between dark energy and dark matter within the $f(T)$ framework, seeking to resolve tensions in the standard cosmological model. Additionally, there's been increased interest in analyzing the stability and viability of $f(T)$ models through phase-space analysis and perturbation studies. These investigations aim to constrain the free parameters of $f(T)$ theories and to distinguish them from other modified gravity approaches. For instance, studies have explored the viability of specific $f(T)$ models using data from the Pantheon+ Supernovae dataset and CMB observations, while others have focused on the theoretical implications of $f(T)$ gravity for early-Universe cosmology and the resolution of cosmological singularities.

However, the late-time accelerated expansion, supported by substantial observational evidence, presents a challenge to the framework of General Relativity (GR). An alternative approach to explain this phenomenon involves

modifications to GR, tracing back to Einstein's 1928 attempt to unify gravity and electromagnetism via the introduction of a tetrad (vierbein) field and the concept of absolute parallelism, also known as Teleparallel Gravity (TG) or $f(T)$ gravity [15]. In $f(T)$ gravity, the gravitational field equations are formulated using torsion rather than curvature [16], offering the advantage of second-order field equations. Various aspects of $f(T)$ theory have been studied [17-20]. For instance, Jamil *et al.* [21, 22] investigated the dark matter (DM) problem within $f(T)$ gravity, successfully modelling flat rotation curves of galaxies and deriving DM density profiles. Additionally, they explored interacting DE models within this framework for a specific choice of $f(T)$. Setare and Darabi [23] examined power-law solutions in the phantom phase, identifying exit solutions for certain $f(T)$ scenarios. Setare and Houndjo [24] investigated particle creation in a flat FRW Universe within $f(T)$ gravity, and Chirde and Shekh [25] studied barotropic bulk viscous cosmological models in $f(T)$ gravity.

The investigation of interacting fields, particularly those involving zero-mass scalar fields, is pivotal for addressing the unification of gravitational and quantum theories. Recent decades have seen a resurgence of interest in gravitational theories incorporating zero-mass scalar fields. Maniharsingh [26], Singh and Bhamra [27], and Singh [28, 29] have explored various one-fluid models coupled with scalar fields. Singh and Deo [30] examined zero-mass scalar field interactions in the presence of a gravitational field for FRW spacetime within GR, demonstrating that the 'Big-Bang' singularity might be avoided through the introduction of such fields. Further research by authors [31, 32] has investigated cosmological models involving zero-mass scalar fields. Building upon the preceding analysis, this paper explores a two-fluid cosmological model within $f(T)$ gravity, incorporating a scalar field to uncover the underlying dynamics of this Universe, with a particular focus on the interacting scenario.

2. A BRIEF REVIEW OF $f(T)$ COSMOLOGY

The line element of the Riemannian manifold is given by

$$dS^2 = g_{\mu\nu}dx^\mu dx^\nu. \tag{1}$$

This line element can be converted to the Minkowskian description of the transformation called tetrad, as follows

$$dS^2 = g_{\mu\nu}dx^\mu dx^\nu = \eta_{ij}\theta^i\theta^j, \tag{2}$$

$$dx^\mu = e_i^\mu \theta^i, \quad \theta^i = e_\mu^i dx^\mu, \tag{3}$$

where $\eta_{ij} = diag[\,-1,\ 1,\ 1,\ 1\,]$ and $e_i^\mu e_\mu^i = \delta_\nu^\mu$ or $e_i^\mu e_\mu^j = \delta_i^j$.

The root of metric determinant is given by $\sqrt{-g} = det[\,e_\mu^i\,] = e$. For a manifold in which the Riemann tensor part without the torsion terms is null (contribution of the Levi-Civita connection) and only the non-zero torsion terms exist, the Weitzenbocks connection components are defined as

$$\Gamma_{\mu\nu}^\alpha = e_i^\alpha \partial_\nu e_\mu^i = -e_\mu^i \partial_\nu e_i^\alpha. \tag{4}$$

Through the connection, we can define the components of the torsion and contorsion tensors as

$$T_{\mu\nu}^\alpha = \Gamma_{\mu\nu}^\alpha - \Gamma_{\mu\nu}^\alpha = e_i^\alpha (\partial_\mu e_\nu^i - \partial_\mu e_\mu^i), \tag{5}$$

$$K_{\alpha}^{\mu\nu} = \left(-\frac{1}{2}\right)(T_{\alpha}^{\mu\nu} - T_{\alpha}^{\nu\mu} - T_\alpha^{\mu\nu}). \tag{6}$$

For facilitating the description of the Lagrangian and the equations of motion, we can define another tensor $S_\alpha^{\mu\nu}$ from the components of the torsion and contorsion tensors, as

$$S_\alpha^{\mu\nu} = \left(\frac{1}{2}\right)\left(K_{\alpha}^{\mu\nu} + \delta_\alpha^\mu T_{\beta}^{\beta\nu} - \delta_\alpha^\nu T_{\beta}^{\beta\mu}\right). \tag{7}$$

The torsion scalar T is

$$T = T_{\mu\nu}^\alpha S_\alpha^{\mu\nu}. \tag{8}$$

Now, we define the action by generalizing the Teleparallel Theory i.e. f(T) theory as [18]

$$S = \int [T + f(T) + L_{matter}]\, e\, d^4x. \tag{9}$$

Here, f(T) denotes an algebraic function of the torsion scalar T. Making the functional variation of the action (9) with respect to the tetrads, we get the following equations of motion

$$S_\mu^{\nu\rho}\partial_\rho T f_{TT} + [e^{-1}e_\mu^i \partial_\rho(ee_i^\alpha S_\alpha^{\nu\rho}) + T_{\lambda\mu}^\alpha S_\alpha^{\nu\lambda}](1 + f_T) + \frac{1}{4}\delta_\mu^\nu(T + f) = 16\pi T_\mu^\nu, \tag{10}$$

where T_μ^ν is the energy momentum tensor, $f_T = df(T)/dT$ and, by setting $f(T) = a_0 =$ constant this is dynamically equivalent to the General Relativity.

3. METRIC AND FIELD EQUATIONS

We consider the spatially homogeneous and isotropic flat Friedman- Robertson-Walker (FRW) line element in the form

$$ds^2 = -dt^2 + a^2(t)[dr^2 + r^2 d\Omega^2], \tag{11}$$

where a be the metric potential or average scale factor and $d\Omega^2 = d\theta^2 + sin^2 \theta \, d\varphi^2$.

The energy momentum tensor T_μ^ν for the fluid distribution with zero-mass scalar fields is taken as

$$T_\mu^\nu = (p + \rho) \, u^\nu u_\mu + p g_\mu^\nu + \phi_{,\mu} \phi^{,\nu} - \frac{1}{2} g_\mu^\nu \phi_{,\lambda} \phi^{,\lambda}, \tag{12}$$

together with co-moving co-ordinates

$$u^\nu = (0, 0, 0, 1) \text{ and } u^\nu u_\nu = -1 \tag{13}$$

where u^ν is the four-velocity vector of the cosmic fluid, p and ρ are the isotropic pressure and energy density of the matter respectively and ϕ be the zero-mass scalar field.

The Friedman equation for two fluid scenarios with zero mass scalar fields can be written as

$$\frac{\dot{a}}{a} \dot{T} f_{TT} + \left\{ \frac{\ddot{a}}{a} + 2 \frac{\dot{a}^2}{a^2} \right\} (1 + f_T) + \frac{1}{4}(T + f) = (16\pi)p + 2\dot{\phi}^2, \tag{14}$$

$$3(1 + f_T)\frac{\dot{a}^2}{a^2} + \frac{1}{4}(T + f) = (16\pi)(-\rho) - 2\dot{\phi}^2, \tag{15}$$

$$\ddot{\phi} + 3\frac{\dot{a}}{a}\dot{\phi} = 0. \tag{16}$$

The overhead dot represents the differentiation with respect to time t.

Here we consider $p = (p_m + p_D)$, $\rho = (\rho_m + \rho_D)$,

where p_m and ρ_m are pressure and energy density of barotropic fluid, p_D and ρ_D are pressure and energy density of dark fluid respectively also $p_m = w_m \rho_m$ and $p_D = w_D \rho_D$.

We assume that EoS parameter of the perfect fluid to be a constant, which is already considered by Akarsu [33] and Kumar [34] i.e.

$$w_m = \frac{p_m}{\rho_m} = \text{constant}, \tag{17}$$

while w_D has been admitted to be a function of time.

Next, we extend the discussion for interacting case to study the changing aspects of physical behavior of the Universe, we first assume that the perfect fluid and DE components interact minimally. Therefore, the energy momentum tensors of the two sources may be conserved separately. In this case, the densities of DE and matter no longer satisfy independent conservation laws, they obey instead

$$(\dot{\rho}_m) + 3\frac{\dot{a}}{a}(\rho_m + p_m) = Q, \tag{18}$$

$$(\dot{\rho}_D) + 3\frac{\dot{a}}{a}(\rho_D + p_D) = -Q. \tag{19}$$

The quantity Q ($Q > 0$) expressed the interaction term between the DE barotropic matter components. Since we are interested to investigate the interaction between DE and matter, it should be noted that an ideal interaction term must be motivated from the theory of quantum gravity. In the absence of such a theory, we rely on pure dimensional basis for choosing an interaction Q. In our work we consider the interaction term in the form $Q \, \alpha \, H \rho_m$ which is already considered in [12, 13]

$$Q = 3Hk\rho_m \tag{20}$$

where k is a coupling coefficient which can be considered as a constant or variable parameter of redshift.

4. SOLUTION OF THE FIELD EQUATIONS

In constructing a physically meaningful cosmological model, the Hubble parameter and the deceleration parameter are crucial measurable quantities. The current value of the Hubble parameter reveals the present rate at which the Universe is expanding, while the current value of the deceleration parameter indicates that the observable Universe's expansion is accelerating, rather than slowing down. This suggests that a viable model should incorporate a phase of decelerating expansion during the early matter-dominated era, allowing for the formation of large-scale structures, followed by the observed late-time acceleration. Solutions to Einstein's field equations, derived using a law governing the Hubble parameter's variation that results in a constant deceleration parameter, have been extensively investigated. However, other researchers have proposed forms of the Hubble parameter as a function of the scale factor. Observations of Type Ia supernovae and anisotropies in the cosmic microwave background have indicated a transition from a

decelerating expansion in the past to the current accelerated expansion. Consequently, for a Universe exhibiting this transition, the deceleration parameter must undergo a sign change, which is a key reason for considering a time-varying deceleration parameter. Hence, in the present study, we consider the deceleration parameter to be a suitable linear function of Hubble's parameter as

$$q = -1 + \beta H, \tag{21}$$

which yields a scale factor of the form $a = Exp\left[\left(\frac{\sqrt{2\beta t + k}}{\beta}\right)\right]$, where β and k are the constants. From the above equations the Hubble's parameter H is observed as $H = \frac{1}{\sqrt{1 + 2t\beta}}$.

5. PHYSICAL PARAMETERS

Here in this section, we find some other parameter of dark fluid/energy in interacting two fluid models such as: The Torsion scalar of the model is observed as

$$T = 6H^2. \tag{22}$$

The Figure 1, illustrates the behavior of the Torsion scalar in $f(T)$ gravity with $\beta = 0.5$, showing an decreasing trend over time towards a constant value.
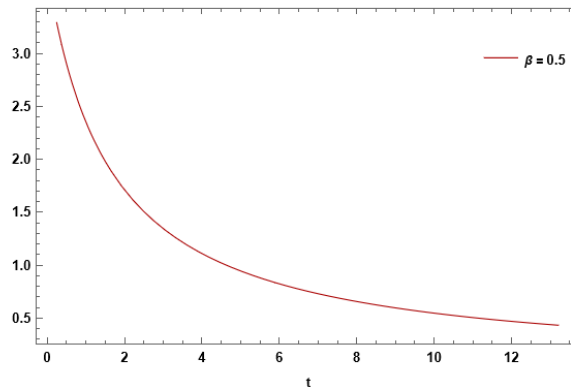

Figure 1. The behavior of Torsion scalar (T) versus time (t)

This suggests an evolution from a torsion-dominated early Universe to a later phase where torsion's influence diminishes, potentially leading to a de Sitter-like expansion. The asymptotic behavior indicates that the Torsion scalar may settle into a constant, possibly related to the late-time acceleration of the Universe, offering an alternative cosmological scenario to standard General Relativity.

The function of torsion scalar is observed as
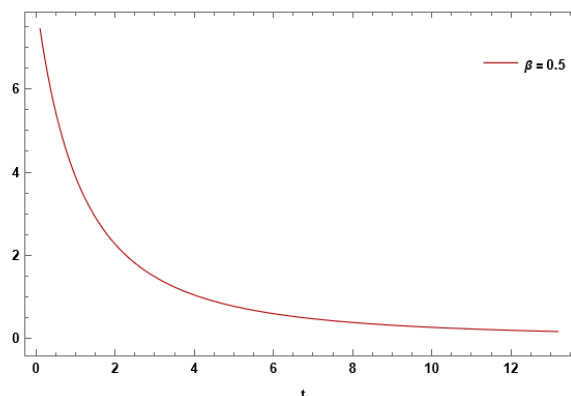
$$f(T) = (6H^2)^n. \tag{23}$$

Figure 2. The behavior of function of torsion scalar (f(T)) versus time (t)

Figure 2 shows the evolution of the function $f(T)$, which modifies the teleparallel equivalent of general relativity. Unlike standard teleparallel gravity, which uses the linear form $f(T) = T^n$, modified gravity theories consider nonlinear functions to explain cosmic acceleration without a cosmological constant. From the plot, $f(T)$ shows a decreasing trend over time, echoing the behaviour of T. This indicates that the deviation from standard teleparallel gravity is most pronounced in the early Universe. As time progresses, $f(T)$ tends to a less dominant or nearly linear

regime, suggesting that the Universe approaches a state similar to standard GR or TEGR (teleparallel equivalent of general relativity). This behaviour has significant implications. It supports the notion that modified gravity effects are necessary to explain early cosmic acceleration or inflation but may not be required or may even diminish in the late Universe. The evolution of $f(T)$ thus mirrors the transition from an early Universe dominated by torsion-induced acceleration to a dark energy-dominated cosmos at late times.

The scalar field ϕ is obtained as

$$\dot{\phi} = \phi_0 a^{-3}, \tag{24}$$

where ϕ_0 be the constant of integration.

The Figure 3, depicts the behavior of a zero-mass scalar field in $f(T)$ gravity with $\beta = 0.5$, showing a rapid decay from a significant initial value towards zero as time progresses. This indicates a transient influence of the scalar field, prominent in the early Universe but becoming negligible in the late-time evolution. The field's diminishing effect suggests it plays a crucial role in the initial cosmological dynamics, potentially representing additional degrees of freedom or dynamical fields that quickly lose relevance as the Universe expands, ultimately leaving the late-time evolution dominated by other factors within the $f(T)$ framework.
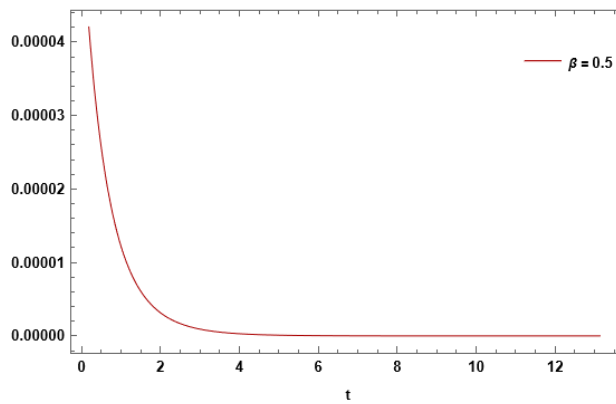

Figure 3. The behavior of scalar function (ϕ) versus time (t)

We obtain an energy density of barotropic fluid for interacting case as

$$\rho_m = \rho_0 (a)^{-3(1+w_m-k)}, \tag{25}$$

where ρ_0 be the constant of integration.

Matter density (ρ_m) represents the contribution of ordinary and dark matter to the total energy content of the Universe. As expected from the standard cosmological principle and shown in Figure 4, ρ_m decreases over time.
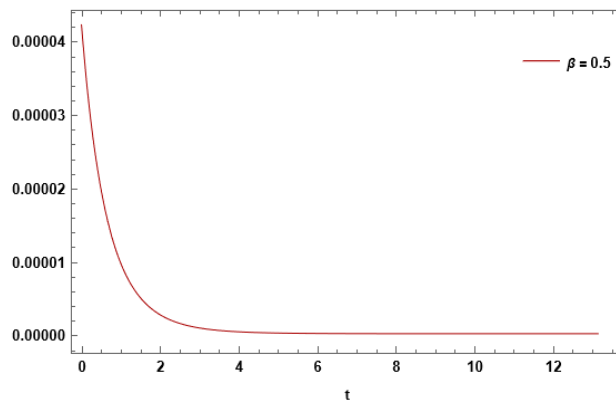

Figure 4. The behavior of matter density (ρ_m) versus time (t)

This decrease is due to the expansion of the Universe: as the volume increases, the matter density dilutes as (ρ_m varies with a^{-3}), where a is the scale factor. This trend is consistent with observations and reflects the diminishing dominance of matter as the Universe evolves from a matter-dominated era to a dark energy-dominated era. In a two-fluid scenario, this behavior is contrasted with that of the dark fluid. The declining ρ_m supports the transition required for cosmic acceleration, wherein the dark fluid's energy density must evolve differently either remaining constant (as with a cosmological constant) or decaying more slowly. This contrast underpins the need for modified gravity or dark energy components in cosmological models.

The Energy density is observed as,

$$\rho_D = \frac{18H^2 + 6^n(H^2)^n(1+2n) + 4(4\pi\rho_m + \dot{\phi}^2)}{64\pi} \tag{26}$$

The dark fluid energy density ρ_D, shown in Figure 5, is crucial in explaining late-time acceleration. Unlike ρ_m, ρ_D exhibits a nearly constant or slowly varying behavior over time, which is a hallmark of dark energy.
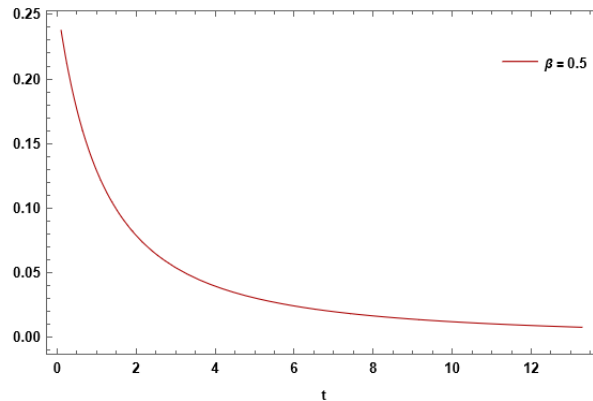

Figure 5. The behavior of energy density (ρ_D) versus time (t)

This behavior mimics that of a cosmological constant, which has a constant energy density and negative pressure, driving accelerated expansion. In modified gravity models like $f(T)$, the dark fluid can arise from geometric corrections rather than invoking a separate energy component. Thus, ρ_D relative constancy suggests that the model effectively produces an acceleration-driving component that matches observations, such as those from supernovae, the CMB, and large-scale structure surveys.

Such a dark fluid may correspond to an effective field emerging from the scalar sector or from the torsional modifications. Its energy density becomes increasingly dominant as ρ_m fades, leading to the observed late-time acceleration.

Isotropic pressure,

$$p_D = -\frac{30H^4 + 6^n(H^2)^n(2\dot{H}(-1+2n)n) + H^2(3+2n)) + 12H^2(\dot{H} - 16\pi p_m - 2\dot{\phi}^2)}{192H^2\pi}. \tag{27}$$

The isotropic pressure p_D of the dark fluid plays a vital role in dictating the dynamics of cosmic acceleration in modified gravity models like $f(T)$ gravity. As observed in Figure 6, p_D exhibits an interesting behavior: it starts off as negative and then gradually transitions into positive values as the Universe evolves. This transition holds significant physical implications.
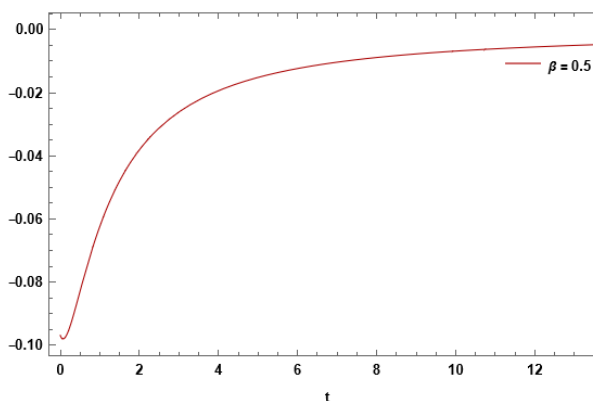

Figure 6. The behavior of isotropic pressure (p) versus time (t)

Initially, the negative and then positive pressure corresponds to initially dark energy and then a phase dominated by ordinary (baryonic) matter, where gravitational attraction governs the dynamics. During this epoch, the Universe experiences decelerated expansion, which aligns with our understanding of the matter-dominated era following radiation domination. As the Universe expands further, the torsional corrections and the influence of the scalar field become more prominent. This is reflected in the transition of p_D from negative to positive values. The emergence of negative pressure marks a critical shift; this is the regime where dark fluid effects take over, generating a repulsive gravitational component that drives accelerated expansion. Negative pressure is essential for this behavior, as it counters

the gravitational pull of matter, a phenomenon supported by Type Ia supernovae observations and large-scale structure data initially.

In the framework of $f(T)$ gravity, the isotropic nature of this pressure is also consistent with the Cosmological Principle, ensuring uniformity in all directions of space, a foundational requirement for the FLRW metric. Overall, the behavior of p_D depicted in Figure 6 effectively demonstrates the Universe's transition from a dark energy-dominated phase to a matter-dominated phase, underlining the success of the $f(T)$ model in capturing both acceleration and deceleration within a unified framework.

EoS Parameter,

$$w_D = -\frac{(30H^4+6^nH^{2n}(2\dot{H}n(-1+2n)+H^2(3+2n))+12H^2(\dot{H}-16\pi pm-\dot{\phi}^2))}{3H^2(18H^2+6^nH^{2n}(1+2n)+64\pi\rho_m+4\dot{\phi}^2)} \qquad (28)$$

The equation of state (EoS) parameter is a fundamental cosmological quantity defined by the ratio of pressure to energy density of a fluid component in the Universe. This parameter critically determines the dynamical behavior of the Universe, including whether it is accelerating, decelerating, or undergoing exotic evolution.
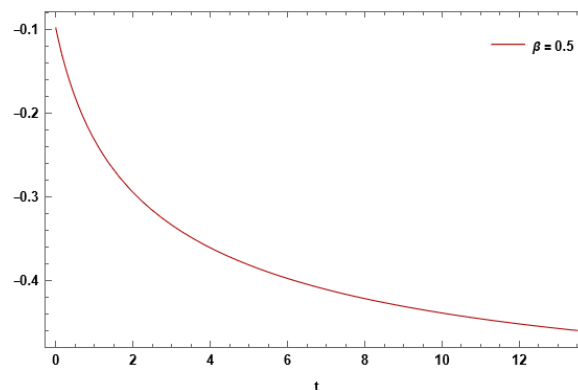

Figure 7. The behavior of equation of state parameter (w) versus time (t)

In Figure 7, w exhibits a clear evolution with time, indicating a transition in the nature of the dominant cosmic component. Initially, w starts in the negative regime, suggesting a dark energy like behaviour. Over time, it drops and present into the negative region, reflecting a shift towards dark energy dominance. Such behavior is highly relevant and consistent with modern cosmological observations. As, the range of w is:

$w = 0$ – Dust-like matter (pressureless). This regime corresponds to non-relativistic matter such as baryons and cold dark matter, where pressure is negligible. It signifies the matter-dominated era of the Universe.

$w = 1/3$ – Radiation. This applies to ultra-relativistic particles (photons, neutrinos). It dominates the early Universe before matter becomes significant.

$w > -1/3$ – No accelerated expansion. The deceleration parameter q is positive in this regime, meaning gravitational attraction dominates and expansion slows down.

$-1 < w < -1/3$ – **Quintessence**-like behavior. This is the sweet spot for dark energy driving **accelerated expansion**. It arises from scalar field models with canonical kinetic terms. The Universe transitions to accelerated expansion in this range.

$w = -1$ – **Cosmological Constant (Λ)**. This case corresponds to a constant vacuum energy density with negative pressure, the simplest form of dark energy in the ΛCDM model. It leads to a de Sitter-like exponential expansion.

$w < -1$ – **Phantom Energy**. This regime predicts **super-acceleration**, where the expansion rate increases without bound. Such behavior can lead to a future cosmic singularity known as the "Big Rip", where all bound structures are torn apart.

$w > 1$ – **Stiff fluid**, less common but possible in early Universe models.

In your model, as seen in Figure 7, w starts near zero and gradually becomes negative. This evolution shows the model effectively **mimics the cosmological sequence** from matter domination to dark energy domination.

• The **early phase**, where w is close to zero or slightly positive, supports a **matter-dominated decelerating expansion**, essential for structure formation (galaxies, clusters, etc.).

• The **later evolution**, where w drops below $-1/3$, indicates the onset of **accelerated expansion**.

• If w continues to evolve past -1, entering the **phantom regime**, the model can describe **exotic cosmic fates**, such as the Big Rip scenario.

Such dynamical behavior is advantageous over constant $-w$ models like ΛCDM, which assume a static $w = -1$. Dynamical dark energy allows for better fits to datasets and can explain tensions like the Hubble tension.

6. CONCLUSION

In this study, we explored a two-fluid cosmological model within the framework of $f(T)$ gravity, considering a massless scalar field and the flat FLRW metric. We analyzed an interacting between barotropic and dark fluids, aiming to understand the dynamic evolution of the Universe and its current acceleration. The model assumes a time-varying deceleration parameter, which leads to a scale factor consistent with observational data showing a transition from decelerated to accelerated expansion. Our solution confirms that the torsion scalar T starts with a large negative value and gradually approaches a constant value over time, implying a transition from a torsion-dominated early Universe to a more stable late-time phase resembling de Sitter expansion.

The scalar field ϕ demonstrates a rapid decay with time, indicating its significant role in early Universe dynamics but a negligible contribution at late times. This aligns well with the concept that scalar fields may drive early inflationary or transitional epochs before dark energy effects dominate.

The behavior of the function $f(T)$ indicates significant deviations from standard teleparallel gravity in the early Universe, with these deviations diminishing over time. This evolution is crucial in explaining early acceleration and smoothly transitioning into a standard-like regime consistent with late-time observations.

From the matter sector, the barotropic fluid's energy density consistently decreases with time, in line with cosmic expansion, and the energy density of the dark fluid remains nearly constant. This nearly constant behavior of energy density of the dark fluid effectively plays the role of a dark energy component driving the accelerated expansion of the Universe.

The isotropic pressure of the dark fluid exhibits a critical transition: it starts negative as dark energy dominates and turns positively in the matter-dominated phase, mirroring the dynamics required for cosmic acceleration. This pressure evolution provides clear evidence of a shift from gravitational attraction to repulsion as expansion accelerates.

A particularly notable result is the dynamic evolution of the equation of state parameter w. Initially near zero, indicating dark energy-like behaviour, w progressively drops into negative values. This transition supports the idea that the Universe has governed by dark energy-like behavior. Should w evolve further into the phantom region ($w < -1$), it could even allow the model to describe exotic scenarios such as the "Big Rip".

Overall, this model successfully captures the essential features of cosmic history from matter domination and structure formation to present-day accelerated expansion within the unified framework of $f(T)$ gravity and scalar field dynamics. It confirms the viability of modified torsional gravity as a compelling alternative to the ΛCDM model, capable of addressing cosmic acceleration without resorting to a cosmological constant or exotic matter fields.

ORCID

Vilas B. Raut, https://orcid.org/0009-0003-3639-9578; **Sanjay A. Salve,** https://orcid.org/0009-0009-3293-6915

REFERENCES

[1] A. Riess, *et al.*, "Observational Evidence from Supernovae for an Accelerating Universe and a Cosmological Constant," Astron. J. **116**, 1009 (1998). https://doi.org/10.1086/300499

[2] S. Perlmutter, *et al.*, "Measurements of Ω and Λ from 42 High-Redshift Supernovae," Astrohpys. J. **517**, 565 (1999). https://doi.org/10.1086/307221

[3] J. Tonry, *et al.*, "Cosmological Results from High-z Supernovae", Astrophys. J. **594**, 1 (2003). https://doi.org/10.1086/376865

[4] A. Riess, *et al.*, "Type Ia Supernova Discoveries at z > 1 from the Hubble Space Telescope: Evidence for Past Deceleration and Constraints on Dark Energy Evolution," Astrophys. J. **607**, 665 (2004). https://doi.org/10.1086/383612

[5] X. Meng, and X. Dou, "Friedmann cosmology with bulk viscosity: a concrete model for dark energy," Commun. Theor. Phys. **52**, 377 (2009). https://doi.org/10.1088/0253-6102/52/2/36

[6] A. Mohammadi, and M. Malekjani, "Interacting Entropy-Corrected Holographic Scalar Field Models in Non-Flat Universe," Commun. Theor. Phys. **55**, 942 (2011). https://doi.org/10.1088/0253-6102/55/5/37

[7] M. Xin-He, and D. Xu, "Singularities and Entropy in Bulk Viscosity Dark Energy Model," Commun. Theor. Phys. **56**, 957 (2011). https://doi.org/10.1088/0253-6102/56/5/27

[8] M. Setare, "Interacting holographic dark energy model in non-flat universe," Phys. Lett. B, **642**, 1-4 (2006). https://doi.org/10.1016/j.physletb.2006.09.027

[9] M. Setare, "Interacting holographic generalized Chaplygin gas model," Phys. Lett. B, **654**, 1-6 (2007). https://doi.org/10.1016/j.physletb.2007.08.038

[10] J. Chen, and Y. Wang, "Evolution of the interacting viscous dark energy model in Einstein cosmology," arXiv:0904.2808v4 [gr-qc] (2009). https://doi.org/10.48550/arXiv.0904.2808

[11] A. Avelino, "Interacting viscous matter with a dark energy fluid," arXiv:1205.0613v2 [astro-ph.CO] (2012). https://doi.org/10.48550/arXiv.1205.0613

[12] B. Saha, H. Amirhashchi, and A. Pradhan, "Two-Fluid Scenario for Dark Energy Models in an FRW Universe," Astrophys. Space Sci. **342**, 257-267 (2012). https://doi.org/10.1007/s10509-012-1155-x

[13] H. Amirhashchi, *et al.*, "Interacting Two-Fluid Viscous Dark Energy Models In Non-Flat Universe," Res. in Astron. Astrophys **13**(2), 129-138 (2013). https://doi.org/10.1088/1674-4527/13/2/001

[14] A. Amirhashchi, *et al.*, "Two-Fluid Dark Energy Models in Bianchi Type-III Universe with Variable Deceleration Parameter," Int. J. Theor Phys. **52**, 2735-2752 (2013). https://doi.org/10.1007/s10773-013-1566-7

[15] A. Einstein, "Sitzungsber. Preuss. Akad. Wiss. Berlin," Phys. Math. Kl. **17**, 217 (1928).

[16] Aио Einstein, "Auf die Riemann-Metrik und den Fern-Parallelismus gegründete einheitliche Feldtheorie", Math. Ann. 102, 685 (1930).

[17] G. Bengochea, "Observational information for f (T) theories and Dark Torsion," Phys. Lett. B. **695**, 405-411 (2011). https://doi.org/10.1016/j.physletb.2010.11.064

[18] B. Li, T. Sotiriou, and J. Barrow, "Large –scale structure in f (T) gravity," Phys. Rev. D, **83**, 104017 (2011). https://doi.org/10.1103/PhysRevD.83.104017

[19] S. Chen, J. Dent, S. Dutta, and E. Saridakis, "Cosmological perturbations in gravity," Phys. Rev. D, **83**, 023508 (2011). https://doi.org/10.1103/PhysRevD.83.023508

[20] K. Karami, and A. Abdolmaleki, "Polytropic and Chaplygin f (T)-gravity models," J. Phys. Conf. Ser. **375**, 032009 (2012). https://iopscience.iop.org/article/10.1088/1742-6596/375/1/032009/pdf

[21] M. Jamil, D. Momeni, and R. Myrzakulov, "Resolution of dark matter problem in f (T) gravity," Eur. Phys. J. C, **72**, 2122 (2012). https://doi.org/10.1140/epjc/s10052-012-2122-y

[22] M. Jamil, K. Yesmakhanova, D. Momeni, and R. Myrzakulov, "Phase space analysis of interacting dark energy in f (T) cosmology," Cen. Eur. J. Phys. **10**, 1065-1071 (2012). https://doi.org/10.2478/s11534-012-0103-2

[23] M. Setare, and F. Darabi, "Power-law solutions in f (T) gravity," Gen. Rel. Grav. **44**, 2521-2527 (2012). https://doi.org/10.1007/s10714-012-1408-6

[24] M. Setare, and M. Houndjo, "Finite-time future singularity models in f (T) gravity and the effects of viscosity," Can. J. Phys. **91**, 260–267 (2013). https://doi.org/10.1139/cjp-2012-0533

[25] V. Chirde, and S. Sheikh, "Barotropic Bulk Viscous FRW Cosmological Model in Teleparallel Gravity," Bulg. J. Phys. **41**, 258 (2014). https://www.bjp-bg.com/papers/bjp2014_4_258-273.pdf

[26] K. Maniharsingh, "Slowly rotating universes with radiating perfect fluid distribution coupled with a scalar field in general relativity," Gen. Rel. Grav. **27**, 1145-1165 (1995). https://doi.org/10.1007/BF02108230

[27] K. Singh, and K. Bhamra, "Radiating viscous universes coupled with zero-mass scalar field: Exact solutions," Int. J. Theor. Phys. **29**, 10151029 (1990). https://doi.org/10.1007/BF00673688

[28] K. Singh, "Some rotating perfect fluid universes coupled with electromagnetic field interacting with gravitation," Astrophys. Space Sci. **325**, 127-135 (2010). https://doi.org/10.1007/s10509-009-0153-0

[29] K. Singh, "Rotational perturbations of radiating Universes coupled with zero-mass scalar field," Astrophys. Space Sci. **325**, 293-302 (2010). https://doi.org/10.1007/s10509-009-0188-2

[30] R. Singh, and S. Deo, "Zero-mass scalar field interactions in the Robertson-Walker universe," Acta Physica Hungarica, **59**, 321-325 (1986). https://doi.org/10.1007/BF03053778

[31] S. Katore, A. Shaikh, M. Sancheti, and J. Pawade, "Einstein Rosen Bulk Viscous Cosmological Solutions with Zero Mass Scalar Field in Lyra Geometry," Prespacetime Jour. **3**, 83 (2012). https://prespacetime.com/index.php/pst/article/view/319/327

[32] V. Chirde, and P. Rahate, "FRW Cosmological Solution in Self Creation Theory," Int. J. Theor. Phys. **51**, 2262-2271 (2012). https://doi.org/10.1007/s10773-012-1106-x

[33] O. Akarsu, and C. Kilinc, "LRS Bianchi type I models with Anisotropic Dark Energy and Constant Deceleration Parameter," General Relativity and Gravitation," Gen. Relativ. Gravit. **42**, 119 (2010). https://doi.org/10.1007/s10714-009-0821-y

[34] S. Kumar, and A. Yadav, "Some Bianchi Type-V Models of Accelerating Universe with Dark Energy," Mod. Phys. Lett. A, **26**, 647-659 (2011). https://doi.org/10.1142/S0217732311035018

МОДЕЛЬ FLRW, ПОВ'ЯЗАНА З БЕЗМАСОВИМ СКАЛЯРНИМ ПОЛЕМ В ГРАВІТАЦІЇ *f*(*T*) – СЦЕНАРІЙ ДВОХ РІДИН

Вілас Б. Раут[a], Санджай А. Сальве[b]

[a]*Кафедра математики, Мунгсаджі Махарадж Махавідьялая, Дарва, округ Яватмал – 445 202, Махараштра, Індія*
[b]*Кафедра математики, Джіджамата Махавідьялая, Булдана – 443 001, Махараштра, Індія*

У цій роботі ми досліджуємо космологічну модель в рамках модифікованої телепаралельної гравітації, відомої як гравітація *f*(*T*), розглядаючи просторово плоский Всесвіт Фрідмана-Леметра-Робертсона-Вокера (FLRW), заповнений двома рідинами - баротропною матерією та темною рідиною - поряд з безмасовим скалярним полем. Ми вивчаємо взаємодіючий випадок рідин, отримуючи точні розв'язки рівнянь поля за сценарієм параметра уповільнення, що залежить від часу. Модель демонструє життєздатну космологічну послідовність: раннє уповільнення розширення, за яким слідує прискорення наприкінці часу. Торсійний скаляр Т, його функція f(T) та скалярне поле ф динамічно еволюціонують, переходячи від домінантних ролей у ранньому Всесвіті до зменшених ефектів наприкінці часу. Густина енергії темної рідини залишається майже постійною, підтримуючи прискорене розширення, тоді як густина матерії зменшується з космічним часом. Параметр ефективного рівняння стану (EoS) еволюціонує від поведінки, подібної до матерії, до від'ємних значень, що свідчить про природний перехід від домінування матерії до фази, де домінує темна енергія. Ці результати підтверджують, що гравітація *f*(*T*) у поєднанні зі скалярним полем може пояснити космічне прискорення та запропонувати альтернативу стандартній моделі ΛCDM без використання екзотичних компонентів енергії.

Ключові слова: *дві рідини; гравітація f(T); параметр лінійного уповільнення; космологія*

CONSTRAINING THE HYBRID MODEL FOR INVESTIGATING HOLOGRAPHIC DARK ENERGY IN MODIFIED GRAVITY

A.Y. Shaikh[a†], A.P. Jenekar[b*]

aDepartment of Mathematics, Indira Gandhi Kala Mahavidyalaya, Ralegaon-445402 (M.S.), India
bDepartment of Mathematics, Arts, Commerce and Science College, Maregaon-445303 (M.S.), India
Corresponding Author E-mail: apjenekar@gmail.com; †E-mail: shaikh_2324ay@yahoo.com

This study examines the dynamism of holographic dark energy (HDE) in the background of $f(R)$ gravity through a hypersurface-homogeneous space-time setting. Looking at how HDE affects the advancement of the Universe, we used a simplified hybrid expansion law (HEL) to derive a precise solution to the associated field equations. The study begins with the analysis of certain kinematical and physical characteristics related to the model. We applied constraints to the outlined hybrid model using observational Hubble data (OHD), which consists of 32-point data sets, in order to evaluate the model's physical certainty and feasibility. In connection with the values of parameter K that show up in our metric, three dynamically potential cosmological scenarios are outlined. Additionally, we examined various energy conditions (ECs) and discerned distinctive cosmic phases through the inspection of statefinder diagnostics and jerk parameter. The squared speed of sound parameter (v_s^2) is used to ensure the model's stability. The study corroborates the Universe's cosmic acceleration, as our findings conform to prevailing observational data, offering viable projections for future research in substantiating HDE.

Keywords: *Holographic dark energy; f(R) gravity; Homogeneous-Hypersurface space-time; Hybrid expansion law*
PACS: 04.50.Kd, 98.80.-k, 95.36.+x

1. INTRODUCTION

Contemporary cosmological observational data reflect the accelerating expansion of the cosmos explicated using type Ia supernovae by Riess [1,2] and Perlmutter [3], cosmic microwave background radiation (CMBR) by Komatsu et al. [4], weak lensing (WL), large-scale structure (LSS), and baryon acoustic oscillations (BAO) investigated by Tegmark [5] and Seljak [6]. The dark energy (DE) might explain the justification for the Universe's accelerating expansion, as it counteracts matter's natural attraction and speeds up the Universe's expansion, as outlined in [7]. Furthermore, it is estimated that this bewildering substance makes up 68.3% of the Universe, with an additional 26.8% being dark matter (DM). The equation of state (EoS), $p_{de} = \omega_{de}\rho_{de}$, with ω_{de} representing the cosmic time function known as the EoS parameter, determines DE having negative pressure along with a positive energy density [8]. Addressing the DE problem involves considering various candidates, namely, the cosmological constant [9], the X-matter [10,11] and quintessence [12,13]. The cosmological constant (Λ) has been proposed by cosmologists as a prominent candidate appropriate to DE gleaned from the several observational findings [14]. However, it encounters setbacks associated with cosmic coincidence along with fine-tuning challenges. The DE issue associated with theoretical physics remains challenging to resolve, irrespective of the substantial evidence available. A precise appraisal of the Universe's expansion rate proves vital for gaining details on the progression of this rate over eternity. The holographic dark energy (HDE) has emerged as a preferable candidate for explaining DE, which is appropriate to the holographic principle initially outlined by Hooft [15] from the perspective of black hole physics. In conformity with Susskind [16] and Bousso [17], the holographic principle proclaims that the system's entropy is contingent upon its surface area away from its volume. In further detail, Fischer and Susskind [18], in conjunction with Cohen et al. [19], presented a pioneering cosmological integration based on the holographic principle, thereby broadening its relevance far beyond the boundaries of black hole physics. Inquiry procedures in [20] reveal a holographic approach for connecting the early Universe with the Universe's late-time acceleration era, whilst extensive research in [21–24] effectively clarifies the substantial link among these HDE models and recent observational evidence.

Einstein's General Relativity (GR) is an insightful theory for interpreting gravitational circumstances; however, it fails to adequately describe DE and DM, prompting researchers to focus on its modification, which leads to various alternative theories. Modified Gravity (MG) is one such approach, focusing on deviating the space-time geometry within Einstein's equations. Several kinds of MG theories, starting with $f(R)$ gravity, $f(T)$ gravity, $f(G)$ gravity, and $f(Q)$ gravity, are being put forward in this setting. Researchers are increasingly exploring MG as a means to elucidate the Universe's cosmic acceleration and essence of DE. Buchdahl [25] commenced $f(R)$ gravity seeking to clarify the Universe's rapid expansion in addition to the progression of its formations. Starobinsky [26] presented isotropic cosmological models within $f(R)$ gravity that lacked singularities. Capozziello et al. [27] explored exact solutions for

cosmological models, while Nojiri and Odintsov [28] proposed a unified model aiming to reconcile early-time expansion combined with late-time acceleration in $f(R)$ gravity. Katore and Gore [29] delved into Bianchi type-I models, examining the interplay of HDE in the view of $f(R)$ gravity. For an in-depth probe across multiple intriguing $f(R)$ models, see ref. [30–32]. For cosmologically valuable models, $f(R)$ gravity is considered immensely appropriate out of the several MG theories. Its action is expressed as

$$S = \int \sqrt{-g}\left(f(R) + L_m\right)d^4x, \tag{1}$$

wherein $f(R)$ is the generalized function involving the Ricci scalar R, while L_m is the usual matter Lagrangian.

Variating the action appertaining to metric $g_{\mu\nu}$ comprises the relevant field equations

$$F(R)R_{\mu\nu} - \frac{1}{2}f(R)g_{\mu\nu} - \nabla_\mu\nabla_\nu F(R) + g_{\mu\nu}\nabla^\rho\nabla_\rho F(R) = -(T_{\mu\nu} + \overline{T}_{\mu\nu}), \tag{2}$$

Here $F(R) \equiv \dfrac{df(R)}{dR}$, ∇_μ represents covariant differentiation, $T_{\mu\nu}$ reflects the standard matter energy-momentum tensor deriving out of Lagrangian L_m whereas $\overline{T}_{\mu\nu}$ signifies the energy-momentum tensor associated with HDE.

The present work focuses on the inspection of hypersurface-homogeneous space-time concerning HDE in the setting of $f(R)$ gravity, taking into view a hybrid expansion law (HEL). We organize this article as follows. Sec. 2 addresses cosmology within the walls of hypersurface-homogeneous space–time, integrating pressureless dark matter along with the HDE framework. Sec. 3 describes the derivation of the quadrature solutions aimed at hybrid expansion in consideration of the field equations. Sec. 4 focuses on physical and kinematical properties of our model, while sec. 5 addresses the observational constraints based on Hubble data and sec. 6 explores the cosmic diagnostics. Sec. 7 comprises the ECs, whereas sec. 8 contains the statefinder diagnostics, jerk parameter, and stability analysis of the discussed model. Finally, sec. 9 presents the discussion and conclusions.

2. COSMOLOGY WITH HYPERSURFACE-HOMOGENEOUS SPACE–TIME

Some cosmological models exhibit a simple transitive homogeneity group in three dimensions, making them anisotropic, homogeneous, and particularly relevant for the purpose of explaining the isotropization and the early evolution of the cosmos, known as Bianchi type models. These models, characterized by their simplicity and effectiveness, are commonly employed in explaining the cosmic evolution. Specifically, owing to their homogeneity and anisotropy, these models are exploited to elucidate the Universe's evolution during the past phase along with its isotropic transformation. Some models fall under the category of multiply transitive, such as Kantowski–Sachs models, which lack a simple transitive subgroup. Moreover, to fully address the interaction of HDE integrated with MG, it is essential to transcend the premise of perfect isotropy. The term hypersurface model is used for a model exhibiting both multiple transitive groups as well as simple ones, combining characteristics of cosmological models that are static, spherically symmetric as well as spatially homogenous. For this reason, several authors have shown considerable interest in the inspection of hypersurface-homogeneous models, which is expressed as

$$ds^2 = -dt^2 + A^2(t)dx^2 + B^2(t)\left[dy^2 + \Sigma^2(y,K)dz^2\right], \tag{3}$$

where A and B serve as the scale factors that are functions solely of t, and $\Sigma(y,K) = \sin y, y, \sinh y$ for $K = 1, 0, -1$, respectively.

Stewart and Ellis [33] have determined considerable assistance to Einstein's field equations within the scenario when these hypersurface-homogeneous cosmological models have a perfect fluid distribution that satisfies a barotropic equation of state, whereas Singh and Beesham [34] have examined it in the existence of an adaptive anisotropic EoS parameter. Katore et al. [35] looked into hypersurface-homogeneous space-time that includes the anisotropic DE model within the boundaries of the Brans-Dicke gravity, whereas Verma et al. [36] and Katore and Shaikh [37], have observed this space-time in the setting of the Saez-Ballester gravity. Shekh and Ghaderi [38] examined this space-time, integrating an interfering HDE model by applying Hubble's and then Granda-Oliveros [39] infrared (IR) cut-off, whereas Vinutha et al. [40] observed it with the Renyi HDE by taking the Hubble horizon as a possible IR cut-off.

The scalar curvature derived from metric (3) results in

$$R = 2\left[\frac{\ddot{A}}{A} + 2\frac{\dot{A}\dot{B}}{AB} + 2\frac{\ddot{B}}{B} + \frac{\dot{B}^2}{B^2} + \frac{K}{B^2}\right], \tag{4}$$

where '$\cdot$' signifies differentiation with respect to cosmic time t.

The energy momentum tensors for HDE and pressureless matter are expressed as

$$T_{\mu\nu} = \rho_m u_\mu u_\nu; \; \overline{T}_{\mu\nu} = (\rho_{de} + p_{de}) u_\mu u_\nu + g_{\mu\nu} p_{de}, \tag{5}$$

where ρ_m is the energy density of matter, p_{de} and ρ_{de} are pressure and energy density of the HDE respectively, u_μ are component of the four-velocity vector of fluid adhering to $g_{\mu\nu} u^\mu u^\nu = -1$.

Using definition of EoS parameter (ω_{de}), the energy momentum tensors (5) is articulated in the form

$$T_{\mu\nu} = \text{diag}[0,0,0,-1]\rho_m; \; \overline{T}_{\mu\nu} = \text{diag}[\omega_{de},\omega_{de},\omega_{de},-1]\rho_{de}. \tag{6}$$

Furthermore, parametric modelling turns it to

$$T_{\mu\nu} = \text{diag}[0,0,0,-1]\rho_m; \; \overline{T}_{\mu\nu} = \text{diag}[\omega_{de}+\gamma,\omega_{de},\omega_{de},-1]\rho_{de}, \tag{7}$$

with the skewness parameter γ representing the variation from the EoS parameter (ω_{de}) on *x*-axis.

Using equations (2) and (7), the associated field equations are described as

$$F\left[\frac{\ddot{A}}{A} + 2\frac{\ddot{B}}{B}\right] - \frac{1}{2}f(R) - \left(\frac{\dot{A}}{A} + 2\frac{\dot{B}}{B}\right)\dot{F} = \rho_m + \rho_{de}, \tag{8}$$

$$F\left[\frac{\ddot{A}}{A} + 2\frac{\dot{A}\dot{B}}{AB}\right] - \frac{1}{2}f(R) - 2\frac{\dot{B}}{B}\dot{F} - \ddot{F} = -(\omega_{de}+\gamma)\rho_{de}, \tag{9}$$

and

$$F\left[\frac{\ddot{B}}{B} + \frac{\dot{A}\dot{B}}{AB} + \frac{\dot{B}^2}{B^2} + \frac{K}{B^2}\right] - \frac{1}{2}f(R) - \left(\frac{\dot{A}}{A} + \frac{\dot{B}}{B}\right)\dot{F} - \ddot{F} = -\omega_{de}\rho_{de}. \tag{10}$$

The HDE density is taken into consideration in the form

$$\rho_{de} = 3\left(\alpha H^2 + \beta \dot{H}\right), \tag{11}$$

with H representing the Hubble parameter whereas α and β are constants.

Granda and Oliveros [39] presented this condition, which must meet the constraints given by the recent observational data. The aberration in isotropic expansion is measured by the anisotropy parameter (Δ), and it plays a critical role in determining whether or not the models are appropriate for addressing isotropy. Once the directional and mean Hubble parameters of the expansion have been established, we can be parameterized the anisotropy of the expansion. The directional Hubble parameters, determining expansion rates along x, y and z axes, are respectively defined as

$$H_x = \frac{\dot{A}}{A}, \; H_y = \frac{\dot{B}}{B} = H_z. \tag{12}$$

The mean Hubble parameter is specified by

$$H = \frac{1}{3}\frac{\dot{V}}{V} = \frac{1}{3}\left(\frac{\dot{A}}{A} + 2\frac{\dot{B}}{B}\right), \tag{13}$$

with $V = AB^2$ describing the Universe's volume.

Using equations (12) and (13), the anisotropy parameter develops into

$$\Delta = \frac{2}{9H^2}\left(\frac{\dot{A}}{A} - \frac{\dot{B}}{B}\right)^2. \tag{14}$$

Using equations (9) and (10), we obtain

$$\frac{\dot{A}}{A} - \frac{\dot{B}}{B} = \frac{\lambda}{FV} + \frac{1}{FV}\int\left(\frac{KF}{B^2} - \gamma\rho_{de}\right)Vdt, \tag{15}$$

where λ is a real integration constant.

Using equation (15), the anisotropy parameter (14) reduces to

$$\Delta = \frac{2}{9H^2}\left[\frac{\lambda}{FV} + \frac{1}{FV}\int\left(\frac{KF}{B^2} - \gamma p_{de}\right)Vdt\right]^2. \tag{16}$$

By opting for $\gamma = 0$ in the above equation, it can be reduced to the model that characterized by a perfect fluid distribution, making it isotropic i.e.

$$\Delta = \frac{2}{9H^2}\left[\frac{\lambda}{FV} + \frac{K}{FV}\int\frac{FV}{B^2}dt\right]^2. \tag{17}$$

The integral term in equation (16) disappears when

$$\gamma = \frac{KF}{B^2\rho_{de}}. \tag{18}$$

Consequently, the energy-momentum tensor (7) becomes

$$\overline{T}_{\mu\nu} = \text{diag}\left[\omega_{de} + \frac{KF}{B^2\rho_{de}}, \omega_{de}, \omega_{de}, -1\right]\rho_{de}. \tag{19}$$

The anisotropy parameter (16) further simplifies to

$$\Delta = \frac{2\lambda^2}{9H^2F^2}V^{-2}. \tag{20}$$

We observed that the anisotropy parameter's value provided by the equation (20) resembles those obtained by several researchers pertaining to various cosmological models involving Bianchi-I [41,42], Bianchi-III [43], Bianchi-V [44,45], Bianchi-VI$_0$ [46], and hypersurface-homogenous frameworks [34-37].

3. SOLUTION TO FIELD EQUATIONS VIA HYBRID EXPANSION

Using equations (15) and (18), we obtain

$$\frac{A}{B} = c_1 \exp\left(\lambda\int\frac{dt}{FV}\right), \tag{21}$$

where c_1 is integration constant.

Solving equation (21), the quadrature solutions for scale factors A and B found to be

$$A = d_1 a \exp\left[q_1\int\frac{dt}{Fa^3}\right] \text{ and } B = d_2 a \exp\left[q_2\int\frac{dt}{Fa^3}\right]. \tag{22}$$

Here $a = \left(AB^2\right)^{\frac{1}{3}} = V^{\frac{1}{3}}$ is average scale factor and $d_1 = c_1^{\frac{2}{3}}$, $d_2 = c_1^{-\frac{1}{3}}$, $q_1 = \frac{2\lambda}{3}$, $q_2 = -\frac{\lambda}{3}$, satisfying the expressions $d_1d_2^2 = 1$ along with $q_1 + 2q_2 = 0$.

To solve the integrals in equation (22), we employ the power law relation connecting F with the average scale factor $a(t)$ as discussed by Johri and Desikan [47] in Brans-Dicke gravity. Moreover, this relation in $f(R)$ gravity is found to be $F \propto a^i$, with i being an arbitrary integer according to Kotub Uddin et al. [48] and the relation used by Sharif and Shamir [49,50], allowing us to consider $i = -2$, i.e. $F = c_2 a^{-2}$, with c_2 as a constant.

With this, the equation (22) simplifies to

$$A = d_1 a \exp\left[q_1\int\frac{dt}{a}\right] \text{ and } B = d_2 a \exp\left[q_2\int\frac{dt}{a}\right]. \tag{23}$$

We now possess a collection making up three independent equations that involve seven unknowns $A, B, \rho_m, \rho_{de}, \omega_{de}, \gamma$ and $f(R)$. To comprehensively address the system, it is necessary to incorporate further conditions, which can be established through suppositions associated with particular physical contexts or arbitrary mathematical presumptions. However, these methods are not without their constraints. Although mathematical preconceptions can create scenarios with no practical implications, physical events can sometimes emerge from complex differential

equations that are challenging to integrate. Accordingly, drawing inspiration from the work of Akarsu et al. [51], we consider a simplified HEL described by

$$V = c_3 e^{3nt} t^{3m}, \tag{24}$$

where c_3, n and m are positive constants.

From HEL model (24), it is clear that, we get exponential expansion for $m = 0$ whereas power law expansion for $n = 0$. This model exhibit accelerated volumetric expansion for $n > 1$ and $m > 1$. Consequently, the average scale factor is expressed as

$$a = k_1 e^{nt} t^m, \tag{25}$$

where $k_1 = c_3^{1/3}$.

With eqs. (23) and (25), the metric potentials are determined to be

$$A = d_1 k_1 e^{nt} t^m \exp\left(\frac{q_1}{c_2 k_1}\int\frac{dt}{e^{nt} t^m}\right) \text{ and } B = d_2 k_1 e^{nt} t^m \exp\left(\frac{q_2}{c_2 k_1}\int\frac{dt}{e^{nt} t^m}\right). \tag{26}$$

Then the metric (3) becomes

$$ds^2 = -dt^2 + d_1^2 k_1^2 e^{2nt} t^{2m} \exp\left(\frac{2q_1}{c_2 k_1}\int\frac{dt}{e^{nt} t^m}\right) dx^2 + d_2^2 k_1^2 e^{2nt} t^{2m} \exp\left(\frac{2q_2}{c_2 k_1}\int\frac{dt}{e^{nt} t^m}\right)\left[dy^2 + \Sigma^2(y, K) dz^2\right]. \tag{27}$$

From equation (26), it is noted that the metric potentials vanishes at starting epoch i.e. at $t = 0$ whereas becomes infinite as $t \to \infty$ indicating a big-bang type of initial singularity for the derived model.

4. PHYSICAL AND KINEMATICAL PROPERTIES

Using equations (12), (13) and (26), we obtained the directional Hubble parameters as

$$H_x = n + \frac{m}{t} + \frac{q_1}{c_2 k_1} e^{-nt} t^{-m}; \ H_y = n + \frac{m}{t} + \frac{q_2}{c_2 k_1} e^{-nt} t^{-m} = H_z. \tag{28}$$

The mean Hubble parameter is determined to be

$$H = n + \frac{m}{t}. \tag{29}$$

The deceleration parameter is described by

$$q = -1 - \frac{\dot{H}}{H^2} = -1 + \frac{m}{(m + nt)^2}. \tag{30}$$

The scalar expansion θ and the shear scalar σ^2 are expressed as

$$\theta = 3H = 3\left(n + \frac{m}{t}\right), \tag{31}$$

and

$$\sigma^2 = \frac{1}{2}\left[\left(\frac{\dot{A}}{A}\right)^2 + 2\left(\frac{\dot{B}}{B}\right)^2 - \frac{1}{3}\theta^2\right] = \left(\frac{q_1^2 + 2q_2^2}{2c_2^2 k_1^2}\right) e^{-2nt} t^{-2m}. \tag{32}$$

For sufficiently large time, the expansion scalar θ shows the constant nature indicating the uniform expansion, whereas the shear scalar σ^2 vanishes; hence, there is no change in the shape of the cosmos during the evolution. Moreover, we observed that $\frac{\sigma^2}{\theta^2} \to 0$ as $t \to \infty$ indicating the Universe's isotropic expansion in later eras, it is consistent with the analysis done by Sharif and Kausar [52].

The mean anisotropic parameter (20) turns out to be

$$\Delta = \frac{2e^{-2nt} t^{2-2m} \lambda^2}{9c_2^2 k_1^2 (m + nt)^2}. \tag{33}$$

Using equations (11) and (29), the HDE parameter is found to be

$$\rho_{de} = \frac{3}{t^2}\left[(m+nt)^2\alpha - m\beta\right].\tag{34}$$

Subsequently, the skewness parameter (18) turns out to be

$$\gamma = \frac{Kc_2\,e^{-4nt}t^{2(1-2m)}}{3d_2^2k_1^4\left((m+nt)^2\alpha - m\beta\right)}\exp\left(-\frac{2q_2}{c_2k_1}\int\frac{dt}{e^{nt}t^m}\right).\tag{35}$$

From equation (4), the Ricci scalar is obtained as

$$R = \frac{2Ke^{-2nt}t^{-2m}}{c_2^2k_1^2d_2^2}\left(Kc_2^2\exp\left(-\frac{2q_2}{c_2k_1}\int\frac{dt}{e^{nt}t^m}\right)+3q_2^2d_2^2\right)+\frac{6}{t^2}\left(2m^2+m(4nt-1)+2n^2t^2\right).\tag{36}$$

The scalar function $f(R)$ is obtained via the Starobinsky model [53] expressed as $f(R)=R+bR^l$, with $l=2$. This model can be considered as a simple inflationary model, where b is an arbitrary constant representing the energy scale as discussed in [54]. A crucial aspect of considering this Starobinsky model is the existence of curvature-squared components that result in an effective cosmological constant that drives the inflationary era, resolving cosmological problems with observational evidence [55,56].

From equation (10), the matter energy density emerges as

$$\rho_m = \frac{3q_2^2e^{-2nt}t^{-2(m+1)}}{c_2^2k_1^2}\left\{t^2+24bm^2-4bt\left(Ke^{-\frac{2q_2}{c_2k_1}\int\frac{dt}{e^{nt}t^m}}-6n^2\right)^2+12bm(4nt-1)\right\}-18bt^4q_2^4\frac{e^{-4nt}t^{-4(1+m)}}{c_2^4k_1^4}$$

$$-\frac{Ke^{-2nt}t^{-2(m+1)}}{d_2^2k_1^2}\left(t^2+12b\left(m(2m-1)+4mnt+2n^2t^2\right)\right)e^{-\frac{2q_2}{c_2k_1}\int\frac{dt}{e^{nt}t^m}}-2bK^2t^4\frac{e^{-4nt}t^{-4(1+m)}}{d_2^4k_1^4}e^{-\frac{4q_2}{c_2k_1}\int\frac{dt}{e^{nt}t^m}}$$

$$+3c_2k_1^{-2}e^{-2nt}t^{-2(m+1)}\left(3m^2-m(1+6nt)+3n^2t^2\right)-18bt^{-4}m^2\left(2m+2nt(ntm^{-2}+2)-1\right)^2\tag{37}$$

$$+\frac{e^{-4nt}t^{(4m+1)}}{c_2^2k_1^4}\left(c_2^3+q_1^2+2q_2^2\right)-3t^{-2}(\alpha+2)\left(m^2-m(1+\beta-2nt)+n^2t^2\right).$$

Using equation (9), the expression for EoS parameter is

$$\omega_{de} = \frac{1}{3\left[(m+nt)^2\alpha-m\beta\right]}\times\left\{\begin{array}{l}\dfrac{e^{-2nt}t^{-2m}}{d_2^2k_1^2}\left[t^2+12b\left(m(2m-1)+4mnt+2n^2t^2\right)\right]\left(Ke^{-\frac{2q_2}{c_2k_1}\int\frac{dt}{e^{nt}t^m}}+3q_2^2d_2^2c_2^{-2}\right)\\[2ex]+3c_2^{-4}t^{-2}\left[m(2m-1)+4mnt+2n^2t^2\right]\left[t^2+6b\left(m(2m-1)+4mnt+2n^2t^2\right)\right]\\[2ex]+K\dfrac{e^{-4nt}t^{-2(2m-1)}}{c_2^2d_2^2k_1^4}\left[\left(12bq_2^2-c_2^3\right)e^{-\frac{2q_2}{c_2k_1}\int\frac{dt}{e^{nt}t^m}}+\dfrac{2Kb}{c_2^{-2}d_2^2}e^{-\frac{4q_2}{c_2k_1}\int\frac{dt}{e^{nt}t^m}}\right]\\[2ex]-3\dfrac{e^{-2nt}t^{-2m}}{c_2^{-1}k_1^2}\left(m^2-m+2mnt+n^2t^2\right)+\dfrac{18bq_2^4}{c_2^4k_1^4}e^{-4nt}t^{-2(2m-1)}\end{array}\right\}.\tag{38}$$

The expression for the pressure is obtained using $p_{de}=\omega_{de}\rho_{de}$, and it turns out to be

$$p_{de} = -\frac{e^{-4nt}t^{-4m}}{d_2^2c_2^2k_1^4}\left[\left(12bq_2^2-c_2^3\right)Ke^{-\frac{2q_2}{c_2k_1}\int\frac{dt}{e^{nt}t^m}}+2K^2bc_2^2e^{-\frac{4q_2}{c_2k_1}\int\frac{dt}{e^{nt}t^m}}\right]-3c_2k_1^{-2}e^{-2nt}t^{-2(1+m)}\left(m^2-m+2mnt+n^2t^2\right)$$

$$+\frac{e^{-2nt}t^{-2(1+m)}}{d_2^2k_1^2}\left[\left(K+3q_2^2\right)\left(t^2+12b\left(2m^2-m+4mnt+2n^2t^2\right)\right)e^{-\frac{2q_2}{c_2k_1}\int\frac{dt}{e^{nt}t^m}}\right]-\frac{18bq_2^4}{d_2^4c_2^4k_1^4}e^{-4nt}t^{-4m}\tag{39}$$

$$+3t^{-4}\left(2m^2-m+4mnt+2n^2t^2\right)\left(t^2+6b\left(2m^2-m+4mnt+2n^2t^2\right)\right).$$

Using the matter energy density parameter $\Omega_m = \dfrac{\rho_m}{3H^2}$ along with HDE density parameter $\Omega_{de} = \dfrac{\rho_{de}}{3H^2}$, the overall density parameter $\Omega = \Omega_m + \Omega_{de}$ is found to be

$$\Omega = \frac{1}{3(m+nt)^2} \times \left\{ \begin{array}{l} -\dfrac{3q_2^2 e^{-2nt} t^{-2m}}{c_2^2 k_1^2}\left[t^2 + 12b\left(m(2m-1)+4mnt+2n^2t^2\right)+\left(m-3m^2-6mnt-3n^2t^2\right)c_2^3\right] \\[2ex] -Ke^{-\frac{2q_2}{c_2 k_1}\int \frac{dt}{e^{nt}t^m}}\left[\dfrac{e^{-2nt}t^{-2m}}{d_2^2 k_1^2}\left(t^2+12b\left(m(2m-1)+4mnt+2n^2t^2\right)\right)+\dfrac{12bq_2^2}{c_2^2 d_2^2 k_1^4}e^{-4nt}t^{-2m}\right] \\[2ex] +\dfrac{e^{-4nt}t^{-2(2m-1)}}{c_2^4 k_1^4}\left[c_2^3\left(q_1^2+2q_2^2\right)-18bq_2^4\right]-2bK^2 \dfrac{e^{-4nt}t^{-2(2m-1)}}{d_2^4 k_1^4}e^{-\frac{4q_2}{c_2 k_1}\int \frac{dt}{e^{nt}t^m}} \\[2ex] -3t^{-2}\left[m(2m-1)+4mnt+2n^2t^2\right]\left[t^2+6b\left(m(2m-1)+4mnt+2n^2t^2\right)\right] \end{array}\right\}. \qquad (40)$$

Now, to visualize various components of our model in relation to redshift z, we employ the established relation $a(t) = \dfrac{a_0}{1+z}$ with $a_0 = 1$ to derive the expression for cosmic time concerning redshift as follows

$$t(z) = \left(\frac{m}{n}\right) W\left(\frac{n}{m}\left[k_1(1+z)\right]^{-\frac{1}{m}}\right), \qquad (41)$$

where $W(x)$ is the Lambert W function [57].

Consequently, the Hubble parameter (29) in relation to redshift (z) is articulated in the form

$$H(z) = n\left\{1 + \left[W\left(\frac{n}{m}\left[k_1(1+z)\right]^{-\frac{1}{m}}\right)\right]^{-1}\right\}. \qquad (42)$$

5. OBSERVATIONAL CONSTRAINTS

We use Hubble datasets to apply constraints to our model's parameters, improving predictions and refining estimates for a more robust understanding of cosmological parameters. The Hubble constant has been computed by a number of studies [58–65] at various redshifts employing the differential age technique together with the galaxy clustering method. Table 1. lists the 32 $H(z)$ measurements, together with their associated errors $\sigma(z)$, within the redshift bounds of $0.07 \le z \le 1.965$.

Table 1. Hubble parameter $H(z)$ along with their associated errors $\sigma(z)$ over redshift (z).

z	$H(z)$ [a]	$\sigma(z_i)$	References	z	$H(z)$ [a]	$\sigma(z_i)$	References
0.07	69.0	19.6	[58]	0.4783	80.9	9.0	[61]
0.09	69.0	12.0	[59]	0.48	97.0	62.0	[63]
0.12	68.6	26.2	[58]	0.593	104.0	13.0	[60]
0.17	83.0	8.0	[59]	0.68	92.0	8.0	[60]
0.179	75.0	4.0	[60]	0.75	98.8	33.6	[64]
0.199	75.0	5.0	[60]	0.781	105.0	12.0	[60]
0.2	72.9	29.6	[58]	0.875	125.0	17.0	[60]
0.27	77.0	14.0	[59]	0.88	90.0	40.0	[63]
0.28	88.8	36.6	[58]	0.9	117.0	23.0	[59]
0.352	83.0	14.0	[60]	1.037	154.0	20.0	[60]
0.3802	83.0	13.5	[61]	1.3	168.0	17.0	[59]
0.4	95.0	17.0	[59]	1.363	160.0	33.6	[65]
0.4004	77.0	10.2	[61]	1.43	177.0	18.0	[59]
0.4247	87.1	11.2	[61]	1.53	140.0	14.0	[59]
0.4497	92.8	12.9	[61]	1.75	202.0	40.0	[59]
0.47	89.0	50.0	[62]	1.965	186.5	50.4	[65]

[a] *km s^{-1} Mpc^{-1}*

Using the eq. (42), we have determined the theoretical values of $H(z)$ in accordance with our hybrid model and applied it to constrain the model's parameters n, m and k_1. To find mean values of these parameters, the corresponding chi-square function is

$$\chi^2(n,m,k) = \sum_{i=1}^{32} \frac{\left(H_{th}(z_i;n,m,k_1) - H_{ob}(z_i)\right)^2}{\sigma^2(z_i)}, \qquad (43)$$

with $H_{th}(z_i)$ and $H_{ob}(z_i)$ specify the $H(z)$'s theoretical and observed values respectively while $\sigma(z_i)$'s stands for corresponding errors in $H_{ob}(z_i)$.

Table 2. A description of best fit values derived via the minimized χ^2-test.

Dataset	Parameters	Hybrid model
$H(z)$	n	$n = 1.45 \pm 0.34$
	m	$m = 1.15 \pm 0.01$
	k_1	$k_1 = 100 \pm 0.68$
	χ^2_{min}	$\chi^2_{min} = 0.691$

Table 2. displays the best fit values of the model's parameters n, m and k_1 estimated via the minimized χ^2-test. The observed Hubble data with error bars and theoretical values of Hubble parameter H according to our model is depicted in Fig. 1 which shows that the Hubble parameter H emerges as an increasing function of redshift. There is close agreement between the observed and theoretical values in the redshift range $0 < z < 1$, which validates our model in the recent past, elaborating the late matter-dominated era transitioning to DE domination, while struggling to show close agreement in the range $1 < z < 2$ in the early epoch. These deviations possibly occurred at higher redshifts $(z > 1)$, as HDE models are designed to address late-time acceleration and might not be applicable when extrapolated backwards to higher redshifts.
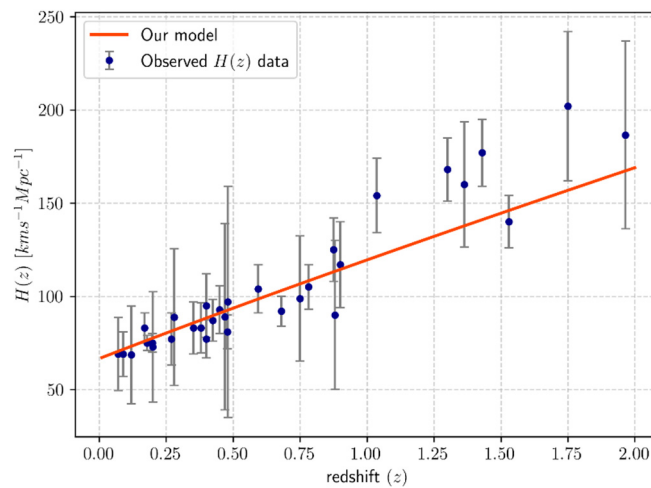

Figure 1. The inspection of Hubble Parameter H against redshift (z).

6. COSMOLOGICAL DIAGNOSTICS

The study of cosmological diagnostics is crucial for understanding how the Universe has evolved. We constructed visual illustrations of the various cosmological components, showing how they vary with redshift (z) by making use of relation (42), thereby facilitating more precise predictions and a deeper insight into cosmic dynamics. We specified a trio of situations based on $K = -1, 0, 1$ by appropriately selecting values for the various associated constants, taking reference from recent studies. We take $b = -0.1$ [66] as the negative value of b is essential for the Starobinsky model to be viable as a model of inflation, $\alpha = 10, \beta = 1$, [67] and $c_2 = 1$ while taking $n = 1.45, m = 1.15$ and $k_1 = 100$ based on estimated best-fit values as specified in Table 2. The variation of the skewness parameter and the anisotropic parameter against redshift is depicted in Fig. 2. The skewness parameter for $K = 1$ and anisotropic parameter both have positive values in the past, whereas in the case of $K = -1$, the skewness parameter has a negative value and is zero for $K = 0$. Consequently,

both these parameters vanish at $z \to -1$ which indicates that there is a phase transformation of the Universe in our model from anisotropy to isotropy, which leads to the attainment of the Universe's isotropization.
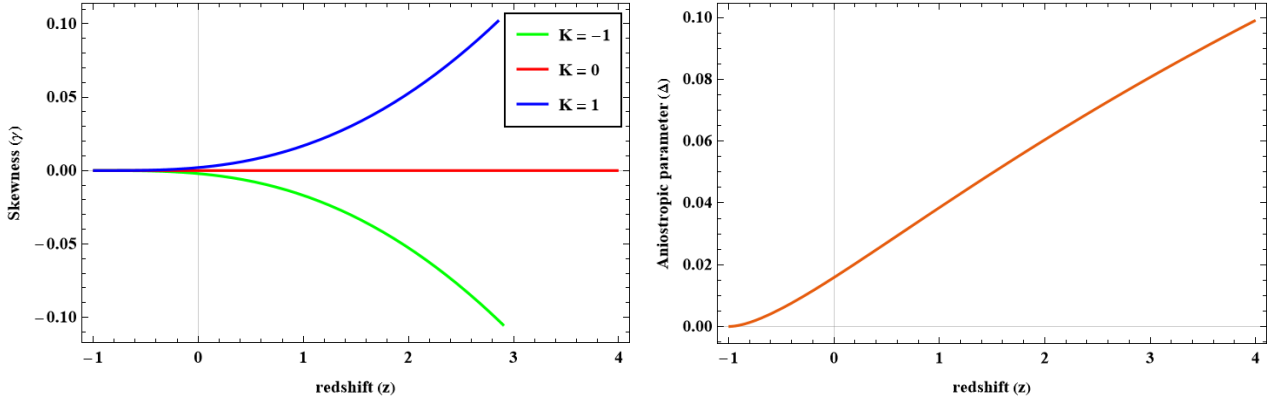

Figure 2. The variation of the skewness parameter (left panel) and the anisotropic parameter (right panel) against redshift.
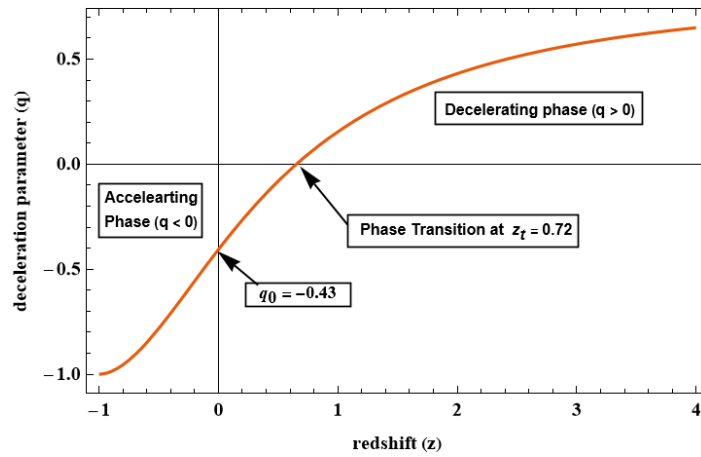

Figure 3. The approach of the deceleration parameter (q) up against redshift (z).

The sign of q serves as an indicator of detecting the accelerating or decelerating nature of the cosmos. A positive q signifies the conventional decelerating model, while a negative q indicates an accelerating Universe. Recent cosmological observations from Ade et al. [68] demonstrate that the current value of the deceleration parameter abides within the bounds of $-1 < q < 0$ as confirmed from observational data, and hence the Universe is presently undergoing acceleration, whereas it decelerated in the past. As depicted in Fig. 3, the deceleration parameter presently abides in this range, indicating the Universe's accelerated expansion, and its track reveals the progression in cosmic history, transitioning from a stage of deceleration to an instance of acceleration, with this transition happening at a point $z_t = 0.62$ that resembles with recent observational estimates of $z_{tr} = 0.60^{+0.21}_{-0.12}$ from Lu et al. [69] and $z_{tr} = 0.597^{+0.214}_{-0.214}$ from Myrzakulov et al. [70], while the present value of deceleration parameter being $q_0 = -0.43$ lies close to the widely accepted value $q_0 \approx 0.55$ as per the recent observations [71,72].

Inspecting the EoS parameter for DE is an essential component in the field of observational cosmology. The quintessence dark era occurs when $\omega_{de} > -1$, whereas phantom-dominated Universe is observed if $\omega_{de} < -1$ and the ΛCDM model for $\omega_{de} = -1$. Fig. 4 represents the cosmic progression of the EoS parameter in regard to redshift. Initially, it begins in the phantom-dominated region, and at present, it gets slightly close to -1 indicating the ΛCDM model and reaches the quintessence model in the future for all three situations. The data from SN Ia, as discussed in [73], indicates a range of $-1.67 < \omega_{de} < -0.62$, whereas considering SN Ia data combined with CMB anisotropy and galactic clumping statistics, the constrained limit becomes $-1.33 < \omega_{de} < -0.79$ as investigated by Tegmark et al. [5]. The Planck collaborations [74] provide the range $-1.26 \le \omega_{de} \le -0.92$ (Planck+WP+Union2.1) and $-1.38 \le \omega_{de} \le -0.89$ (Planck+WP+BAO). At the present epoch, the EoS parameter's value is found to be $\omega_0 = -0.931, -1.004, -1.102$ for $K = -1, 0, 1$ respectively, which thereby corresponds closely to the recent observational estimates [75].
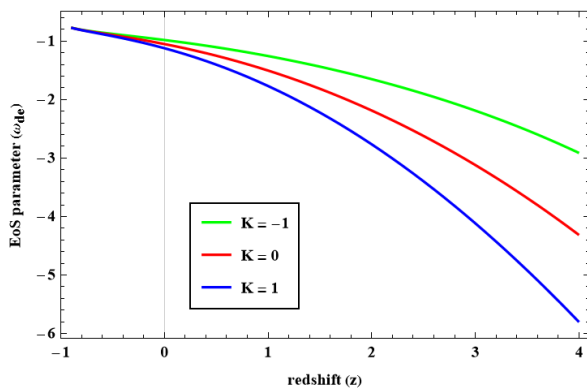
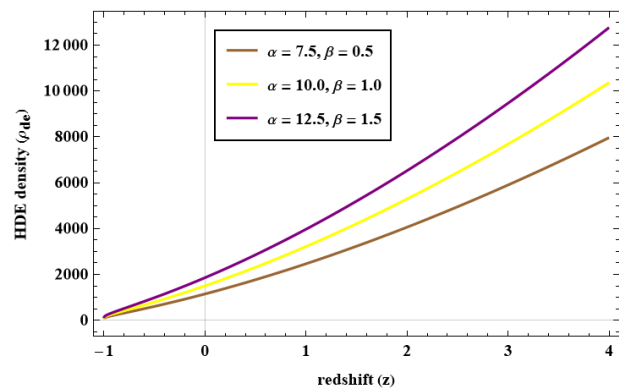**Figure 4.** Progression of EoS parameter (ω_{de}) against redshift

Figure 5. Plot of HDE density for various values of α and β.

The plot of HDE density with the evolution of redshift concerning different values of α and β is depicted in Fig. 5, which shows that the nature of the HDE density is positive and decreasing. It declines from a high starting value to a low ending value. Consequently, energy density drops from the past to the future, or from high to low redshift. This indicates that DE will unquestionably take control of the Universe in the future. The hypothesis that the density of matter declines whereas space grows as the Universe expands is supported by this study. As depicted in Fig. 6, the pressure stays negative throughout. This showcases more backing that the Universe expanding rapidly. The open, flat, and closed Universes are represented by the overall density parameters with $\Omega > 1$, $\Omega = 1$ and $\Omega < 1$ respectively. Fig. 7 is a graphical presentation of the overall density parameter, revealing its approach to a constant value close to 1 at late times, which suggests that the Universe tends to become flat, aligning with observational findings in accordance with the derived model [76].
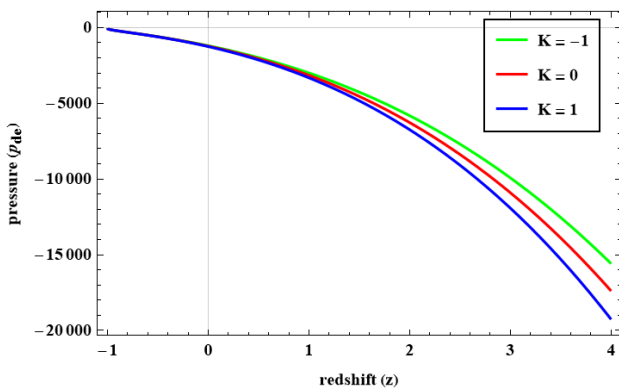
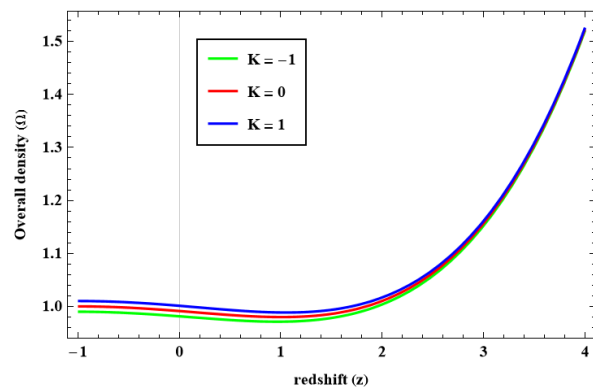

Figure 6. Plot of pressure (p_{de}) versus redshift (z).

Figure 7. Plot of overall density (Ω) versus redshift (z).

7. ENERGY CONDITIONS

In $f(R)$ gravity, the Energy Conditions (ECs) have a crucial aspect in exploring the cosmological progression. It includes the null, weak, strong, and dominant ECs stated by

    i.   Null energy condition (NEC) $\Leftrightarrow \rho_{de} + p_{de} \geq 0$.

    ii.   Weak energy condition (WEC) $\Leftrightarrow \rho_{de} + p_{de} \geq 0$; $\rho_{de} \geq 0$.

    iii.   Strong energy condition (SEC) $\Leftrightarrow \rho_{de} + p_{de} \geq 0$; $\rho_{de} + 3p_{de} \geq 0$.

    iv.   Dominant energy condition (DEC) $\Leftrightarrow \rho_{de} - |p_{de}| \geq 0$; $\rho_{de} \geq 0$.

For $f(R)$ gravity, J. Santos et al. [77] obtained the NEC and SEC by applying Raychaudhuri's equation, ensuring gravity to be attractive, while the WEC and DEC were derived by comparing them with conditions derived straightway from the proficient energy-momentum tensor. Moreover, S. Capozziello et al. [78] investigate how the energy conditions can affect the cosmological evolution and the emergence of singularities in $f(R)$ gravity. The NEC asserts that as the Universe expands, its energy density will recede, and any breach of this premise could potentially lead to the Big Rip possibility for the cosmos, whereas the accelerated pace of the Universe's expansion is attributed to SEC violation.

The graphical presentations of ECs versus redshift are depicted in Fig. 8 with WEC reflected in Fig. 5. These graphical presentations of ECs specified that WEC, NEC, and DEC are considerably validated, whereas the violation of

SEC culminates in the accelerating expansion of the Universe, which is in concurrence with the current scenario of the cosmos [79,80].
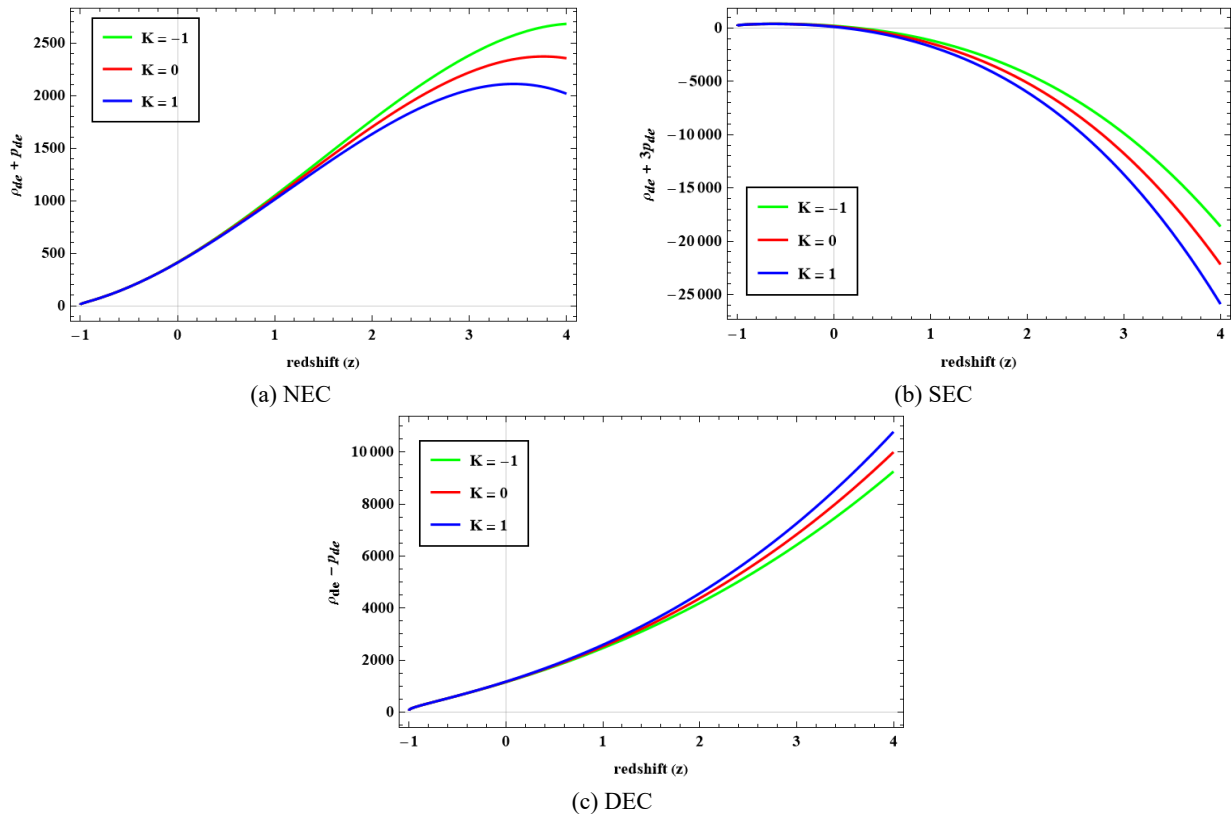

(a) NEC

(b) SEC

(c) DEC

Figure 8. Profile of ECs against redshift

8.   PHASE DIAGNOSTICS AND STABILITY ANALYSIS

The examination of statefinder and jerk parameters indicates variations across conventional expansion, thereby improving perception of the implications of DE models, while the stability assessment ensures our model's stability.

8.1 Statefinder Diagnostics

An investigation into the variability of the expansion of cosmos via higher-order derivatives of the expansion factor is introduced by Sahni et al. [81] as a diagnostic perspective for DE using the pairing of parameters $\{r, s\}$, with r representing jerk parameter, whereas s specifying the substance of the DE. This so-called "statefinder" is outlined below.

$$r \equiv \frac{\ddot{a}}{aH^3} \text{ and } s \equiv \frac{r-1}{3\left(q - \frac{1}{2}\right)}. \tag{44}$$

Since the statefinder is dependent on the expansion factor $\ddot{a}$ as well as the metric representing space-time, it can be considered a "geometrical" diagnostic. It effectively distinguishes between different types of cosmological models such as interacting DE models, brane models, quintessence, Chaplygin gas (CG), and cosmological constant as discussed in [82,83]. In a case of $(r, s) = (1,1)$, it signals cold dark matter (CDM), whereas $(r, s) = (1,0)$ represents the ΛCDM model. The DE regions can be specified as quintessence for $r < 1$ and phantom for $s > 0$, while the trajectory for the CG model belongs to the region $r > 1$ with $s < 0$. The statefinder settings for our HEL model are found to be $r = 1 - \frac{3m(m+nt) - 2m}{(m+nt)^3}$ and $s = \frac{2}{3(m+nt)} - \frac{2nt}{3m^2 + 2m(3nt-1) + 3n^2t^2}$ with their association, described by

$$r = \frac{9ms^2(1+s)\left(m(1+s)^3 - 4s\right)}{4\left[2\sqrt{m^2s^9\left(9s - 2m(1+s)^3\right)} + ms^3\left(6s^2 - 6ms(1+s)^3 + m^2(1+s)^6\right)\right]^{1/3}} + \frac{9}{4}(m-2)s + \frac{9}{2}ms^2$$

$$+ \frac{9}{4}\left[2\sqrt{m^2s^9\left(9s - 2m(1+s)^3\right)} + ms^3\left(6s^2 - 6ms(1+s)^3 + m^2(1+s)^6\right)\right]^{1/3} + \frac{9}{4}ms^3 + 1. \tag{45}$$
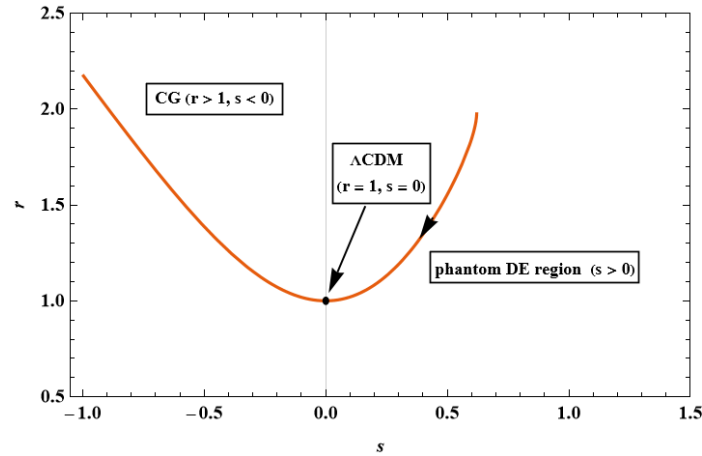
Figure 9. Plot of r vs s.

Fig. 9 illustrates the variation of r across s, suggesting that the state finder measurements will precisely correspond along the lines of the ΛCDM model in the near future. The resulting alignment progresses seamlessly toward the ΛCDM point while incorporating the CG and even Phantom DE portions.

8.2 Jerk Parameter

This parameter serves the purpose of recognizing models that conform to the ΛCDM model. A negative deceleration parameter accompanied by a positive jerk value reflects transitions between acceleration and deceleration phases. The jerk parameter of our model appears to be

$$j(t) = \frac{1}{H^3}\frac{\ddot{a}}{a} = 1 - \frac{m(3nt + 3m - 2)}{(m + nt)^3}. \tag{46}$$
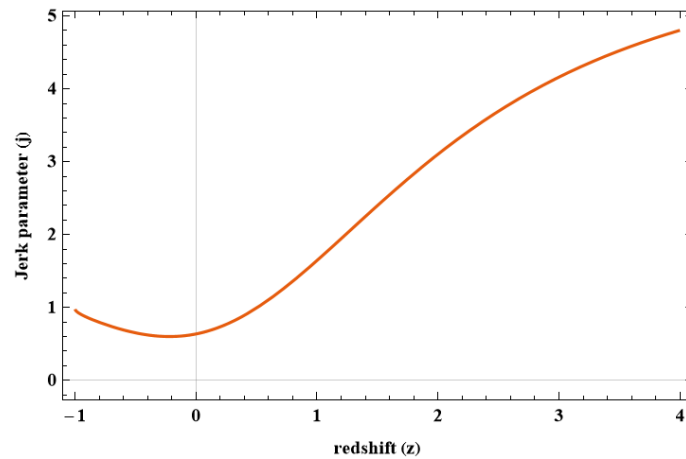
Figure 10. The plot of jerk parameter against redshift

For $j = 1$, it is identified to be the ΛCDM model. Fig. 10 presents the variations of the jerk parameter against redshift, which reflects a declining trend of the jerk parameter until it attains one as $z \to -1$, thus sustaining the model's conformity with the ΛCDM model based on the observational evidence [84].

8.3 Stability Analysis

To verify the stability of our model, we utilized the squared speed of sound parameter v_s^2, defined by $v_s^2 = dp_{de}/d\rho_{de}$, as proposed by Sadeghi et al. [85]. If the value of v_s^2 is positive, this implies that the model is stable, whereas it is unstable for a negative value of v_s^2. Using equations (34) and (39), the stability parameter v_s^2 for our model is obtained, and its graphical visualization over the redshift is presented in Fig. 11, which shows a positive nature for all three situations thoroughly over the course of progression, indicating our model's stability.
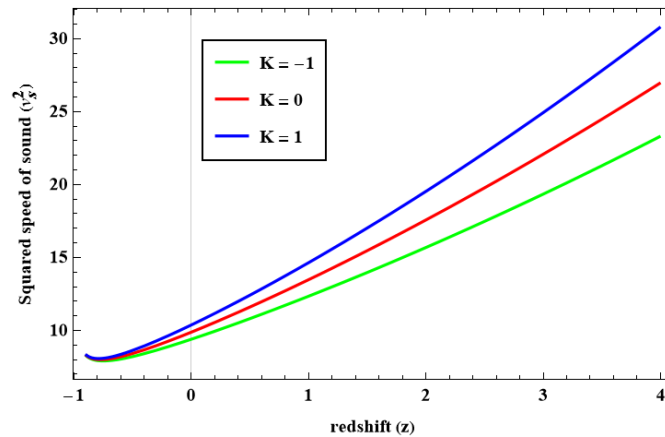
Figure 11. The variation of plot of squared speed of sound (v_s^2) against redshift.

9. CONCLUSIONS

This article is engrossed to delve into hypersurface-homogeneous metric from the perspective of $f(R)$ gravity. Having an account of two fluids viz pressureless matter together with HDE, the field equations are assimilated, and their solutions are estimated by taking simplified HEL accompanied by the Starobinsky model [53]. By using OHD with 32-point datasets, observational constraints are applied to examine the physical dependability and feasibility of the model. We observed that Hubble parameter H emerges as increasing function of redshift z as illustrated in Fig. 1 which shows that there is a close agreement between the observed and theoretical values of H in the redshift range $0 < z < 1$, elaborating the late matter-dominated era transitioning to dark energy domination, which eventually validates our model. From the graphical presentations of various parameters pertaining to redshift involving three cases of $K = 0, 1, -1$, we observed the following implications:

- Both the skewness (γ) and anisotropic parameter (Δ) tend to zero at $z \to -1$ as reflected in Fig. 2, thereby satisfying the isotropization of the Universe which is additionally supported by the fact that the ratio of expansion scalar θ and shear scalar σ^2 tends to zero at later times.

- The model effectively allows for the transition from decelerated to rapid expansion. The deceleration parameter progresses from positive to negative, transitioning from a stage of deceleration to an instance of acceleration as shown in Fig. 3, with the transition point $z_t = 0.62$ resembling the observational estimates in [69,70].

- Fig. 4 outlined the cosmic progression of the EoS parameter (ω_{de}) in regard to redshift, which shows that it begins from a phantom-dominated region initially, and at present, it gets slightly close to -1 indicating the ΛCDM model, whereas it reaches to the quintessence model in the future. Moreover, the EoS parameter's current values, $\omega_0 = -0.931, -1.004, -1.102$ for $K = 0, 1, -1$, respectively, are consistent with the values observed in recent cosmological data [75].

- The hypothesis that the density of matter declines and space grows as the Universe expands is supported by the positive and decreasing nature of HDE density (ρ_{de}) with the evolution of redshift as shown in Fig. 5. The pressure (p_{de}) stays negative over the course of the evolution of our model, as reflected in Fig. 6. This lends reassurance to the conceptualization that the cosmos is expanding at a faster pace. The approach of the overall density (Ω) parameter revealed that it tends to a constant value slightly close to 1 at late times, as displayed in Fig. 7, thereby implying that the Universe tends to become flat in the future, aligning with observational findings of [76] in accordance with the derived model.

- From the variability of ECs as reflected in Figs. 5 and 8, we found that WEC, NEC, and DEC are considerably validated, whereas the violation of SEC culminates in the accelerating expansion of the cosmos, which is in concurrence with the current scenario of the cosmos.

- It is observed from statefinder diagnostics as shown in Fig. 9 that our model tends to approach the ΛCDM model in the near future. Fig. 10 reflects a declining trend of the jerk parameter until it attains one as $z \to -1$, thus, sustaining the model's conformity with the ΛCDM model based on the observational evidence [84].

- Our model's stability is established via the squared speed of sound (v_s^2) parameter as illustrated in Fig. 11, which shows a positive nature thoroughly over the course of progression of redshift, thereby indicating the stable nature of our model.

Based on the preceding discussion, it is evident that our study's findings concur with existing observational data, which supports our interpretation of the Universe's cosmic acceleration and enables us to make specific predictions that can be tested with forthcoming cosmological probes.

ORCID

A.Y. Shaikh, https://orcid.org/0000-0001-5315-559X; **A.P. Jenekar**, https://orcid.org/0009-0005-8928-3725

REFERENCES

[1] A.G. Riess, *et al.*, Astron. J. **116**, 1009 (1998). https://doi.org/10.1086/300499
[2] A. G. Riess, *et al.*, Astron. J. **117**, 707 (1999). https://doi.org/10.1086/300738
[3] S. Perlmutter, *et al.*, Astrophys. J. **517**, 565 (1999). https://doi.org/10.1086/307221
[4] E. Komatsu, *et al.*, Astrophys. J. Suppl. Ser. **192**, 18 (2011). https://doi.org/10.1088/0067-0049/192/2/18
[5] M. Tegmark, *et al.*, Phys. Rev. D **69**, 103501 (2004). https://doi.org/10.1103/PhysRevD.69.103501
[6] U. Seljak, *et al.*, Phys. Rev. D **71**, 103515 (2005). https://doi.org/10.1103/PhysRevD.71.103515
[7] K. Bamba, *et al.*, Astrophys. Space Sci. **342**, 155 (2012). https://doi.org/10.1007/s10509-012-1181-8
[8] M. Sharif, and M. Zubair, Astrophys. Space Sci. **330**, 399 (2010). https://doi.org/10.1007/s10509-010-0414-y
[9] S. M. Carroll, *et al.*, Annu. Rev. Astron. Astrophys. **30**, 499 (1992). https://doi.org/10.1146/annurev.aa.30.090192.002435
[10] M. S. Turner, and M. White, Phys. Rev. D **56**, R4439 (1997). https://doi.org/10.1103/PhysRevD.56.R4439
[11] Z.-H. Zhu, M.-K. Fujimoto, and D. Tatsumi, Astron. Astrophys. **372**, 377 (2001). https://doi.org/10.1051/0004-6361:20010458
[12] B. Ratra, and P. J. E. Peebles, Phys. Rev. D **37**, 3406 (1988). https://doi.org/10.1103/PhysRevD.37.3406
[13] V. Sahni, and L. Wang, Phys. Rev. D **62**, 103517 (2000). https://doi.org/10.1103/PhysRevD.62.103517
[14] S. Weinberg, Rev. Mod. Phys. **61**, 1 (1989). https://doi.org/10.1103/RevModPhys.61.1
[15] G.'t Hooft, (Conf. Proc. C, **284**, 930308 (1993). https://doi.org/10.48550/arXiv.gr-qc/9310026
[16] L. Susskind, and J. Uglum, Phys. Rev. D **50**, 2700 (1994). https://doi.org/10.1103/PhysRevD.50.2700
[17] R. Bousso, J. High Energy Phys. **1999**, 004 (1999). https://doi.org/10.1088/1126-6708/1999/07/004
[18] W. Fischler, and L. Susskind, arXiv:hep-th/9806039 (1998). https://doi.org/10.48550/arXiv.hep-th/9806039
[19] A. G. Cohen, D. B. Kaplan, and A. E. Nelson, Phys. Rev. Lett. **82**, 4971 (1999). https://doi.org/10.1103/PhysRevLett.82.4971
[20] S. Nojiri, *et al.*, Phys. Rev. D **102**, (2020). https://doi.org/10.1103/physrevd.102.023540
[21] X. Zhang, Phys. Rev. D **79**, 103509 (2009). https://doi.org/10.1103/PhysRevD.79.103509
[22] L. Xu, and Y. Wang, J. Cosmol. Astropart. Phys. **2010**, 002 (2010). https://doi.org/10.1088/1475-7516/2010/06/002
[23] Y. Wang, and L. Xu, Phys. Rev. D **81**, 083523 (2010). https://doi.org/10.1103/PhysRevD.81.083523
[24] I. Durán, and D. Pavón, Phys. Rev. D **83**, 023504 (2011). https://doi.org/10.1103/PhysRevD.83.023504
[25] H. A. Buchdahl, Mon. Not. R. Astron. Soc. **150**, 1 (1970). https://doi.org/10.1093/mnras/150.1.1
[26] A. A. Starobinsky, Phys. Lett. B **91**, 99 (1980). https://doi.org/10.1016/0370-2693(80)90670-X
[27] S. Capozziello, P. Martin-Moruno, and C. Rubano, Phys. Lett. B **664**, 12 (2008). https://doi.org/10.1016/j.physletb.2008.04.061
[28] S. Nojiri, and S. D. Odintsov, arXiv:0807.0685 [hep-th] (2008). https://doi.org/10.48550/arXiv.0807.0685
[29] S. D. Katore, and S. V. Gore, J. Astrophys. Astron. **41**, 12 (2020). https://doi.org/10.1007/s12036-020-09632-z
[30] A. De Felice, and S. Tsujikawa, Living Rev. Relativ. **13**, 3 (2010). https://doi.org/10.12942/lrr-2010-3
[31] T. P. Sotiriou, and V. Faraoni, Rev. Mod. Phys. **82**, 451 (2010). https://doi.org/10.1103/RevModPhys.82.451
[32] S. Nojiri, and S. D. Odintsov, Phys. Rep. **505**, 59 (2011). https://doi.org/10.1016/j.physrep.2011.04.001
[33] J. M. Stewart, and G. F. R. Ellis, J. Math. Phys. **9**, 1072 (1968). https://doi.org/10.1063/1.1664679
[34] C. P. Singh, and A. Beesham, Gravit. Cosmol. **17**, 284 (2011). https://doi.org/10.1134/S020228931103008X
[35] S. D. Katore, *et al.*, Commun. Theor. Phys. **62**, 768 (2014). https://doi.org/10.1088/0253-6102/62/5/21
[36] M. K. Verma, S. Chandel, and S. Ram, Pramana **88**, 8 (2017). https://doi.org/10.1007/s12043-016-1317-4
[37] S. D. Katore, and A. Y. Shaikh, Astrophys. Space Sci. **357**, 27 (2015). https://doi.org/10.1007/s10509-015-2297-4
[38] S. H. Shekh, and K. Ghaderi, Phys. Dark Universe **31**, 100785 (2021). https://doi.org/10.1016/j.dark.2021.100785
[39] L. N. Granda, and A. Oliveros, Phys. Lett. B **669**, 275 (2008). https://doi.org/10.1016/j.physletb.2008.10.017
[40] T. Vinutha, *et al.*, Int. J. Geom. Methods Mod. Phys. **20**, 2350119 (2023). https://doi.org/10.1142/S0219887823501190
[41] S. Kumar, and C. P. Singh, Astrophys. Space Sci. **312**, 57 (2007). https://doi.org/10.1007/s10509-007-9623-4
[42] Ö. Akarsu, and C. B. Kılınç, Gen. Relativ. Gravit. **42**, 119 (2009). https://doi.org/10.1007/s10714-009-0821-y
[43] Ö. Akarsu, and C. B. Kılınç, Gen. Relativ. Gravit. **42**, 763 (2010). https://doi.org/10.1007/s10714-009-0878-7
[44] C. P. Singh, *et al.*, Astrophys. Space Sci. **315**, 181 (2008). https://doi.org/10.1007/s10509-008-9811-x
[45] J. P. Singh, and P. S. Baghel, Int. J. Theor. Phys. **48**, 449 (2009). https://doi.org/10.1007/s10773-008-9820-0
[46] K. S. Adhav, *et al.*, Astrophys. Space Sci. **332**, 497 (2011). https://doi.org/10.1007/s10509-010-0519-3
[47] V. B. Johri, and K. Desikan, Gen. Relativ. Gravit. **26**, 1217 (1994). https://doi.org/10.1007/BF02106714
[48] K. Uddin, J. E. Lidsey, and R. Tavakol, Class. Quantum Gravity **24**, 3951 (2007). https://doi.org/10.1088/0264-9381/24/15/012
[49] M. Sharif, and M. F. Shamir, Class. Quantum Gravity **26**, 235020 (2009). https://doi.org/10.1088/0264-9381/26/23/235020
[50] M. Sharif, and M. F. Shamir, Mod. Phys. Lett. A **25**, 1281 (2010). https://doi.org/10.1142/S0217732310032536
[51] Ö. Akarsu, *et al.*, J. Cosmol. Astropart. Phys. **2014**, 022 (2014). https://doi.org/10.1088/1475-7516/2014/01/022
[52] M. Sharif, and H. R. Kausar, Phys. Lett. B **697**, 1 (2011). https://doi.org/10.1016/j.physletb.2011.01.027
[53] A. A. Starobinsky, JETP Lett. **86**, 157 (2007). https://doi.org/10.1134/S0021364007150027
[54] Y. Younesizadeh, and A. Rezaie, Int. J. Mod. Phys. A **37**, 2250040 (2022). https://doi.org/10.1142/S0217751X22500403
[55] A. S. Koshelev, *et al.*, J. High Energy Phys. **2018**, (2018). https://doi.org/10.1007/jhep03(2018)071
[56] G. Germán, J. C. Hidalgo, and L. E. Padilla, Eur. Phys. J. Plus **139**, (2024). https://doi.org/10.1140/epjp/s13360-024-05065-7

[57] R. M. Corless, *et al.*, Adv. Comput. Math. **5**, 329 (1996). https://doi.org/10.1007/BF02124750
[58] C. Zhang, *et al.*, Res. Astron. Astrophys. **14**, 1221 (2014). https://doi.org/10.1088/1674-4527/14/10/002
[59] J. Simon, L. Verde, and R. Jimenez, Phys. Rev. D **71**, 123001 (2005). https://doi.org/10.1103/PhysRevD.71.123001
[60] M. Moresco, *et al.*, J. Cosmol. Astropart. Phys. **2012**, 006 (2012). https://doi.org/10.1088/1475-7516/2012/08/006
[61] M. Moresco, *et al.*, J. Cosmol. Astropart. Phys. **2016**, 014 (2016). https://doi.org/10.1088/1475-7516/2016/05/014
[62] A. L. Ratsimbazafy, *et al.*, Mon. Not. R. Astron. Soc. **467**, 3239 (2017). https://doi.org/10.1093/mnras/stx301
[63] D. Stern, *et al.*, J. Cosmol. Astropart. Phys. **2010**, 008 (2010). https://doi.org/10.1088/1475-7516/2010/02/008
[64] N. Borghi, M. Moresco, and A. Cimatti, Astrophys. J. Lett. **928**, L4 (2022). https://doi.org/10.3847/2041-8213/ac3fb2
[65] M. Moresco, Mon. Not. R. Astron. Soc. Lett. **450**, L16 (2015). https://doi.org/10.1093/mnrasl/slv037
[66] P. H. R. S. Moraes, *et al.*, Adv. Astron. **2019**, 1 (2019). https://doi.org/10.1155/2019/8574798
[67] M. T. Manoharan, Eur. Phys. J. C **84**, (2024). https://doi.org/10.1140/epjc/s10052-024-12926-z
[68] P. A. R. Ade, *et al.*, Astron. Astrophys. **571**, A16 (2014). https://doi.org/10.1051/0004-6361/201321591
[69] J. Lu, L. Xu, and M. Liu, Phys. Lett. B **699**, 246 (2011). https://doi.org/10.1016/j.physletb.2011.04.022
[70] Y. Myrzakulov, *et al.*, Nucl. Phys. B **1016**, 116916 (2025). https://doi.org/10.1016/j.nuclphysb.2025.116916
[71] A. Kolhatkar, S. S. Mishra, and P. K. Sahoo, Eur. Phys. J. C **84**, (2024). https://doi.org/10.1140/epjc/s10052-024-13237-z
[72] D. M. Naik, *et al.*, Phys. Lett. B **844**, 138117 (2023). https://doi.org/10.1016/j.physletb.2023.138117
[73] R. A. Knop, *et al.*, Astrophys. J. **598**, 102 (2003). https://doi.org/10.1086/378560
[74] Planck Collaboration, *et al.*, Astron. Astrophys. **641**, A6 (2020). https://doi.org/10.1051/0004-6361/201833910
[75] M. Jaber, and A. de la Macorra, Astropart. Phys. **97**, 130 (2018). https://doi.org/10.1016/j.astropartphys.2017.11.007
[76] S. Kumar, Astrophys. Space Sci. **332**, 449 (2011). https://doi.org/10.1007/s10509-010-0540-6
[77] J. Santos, *et al.*, Phys. Rev. D **76**, 083513 (2007). https://doi.org/10.1103/PhysRevD.76.083513
[78] S. Capozziello, S. Nojiri, and S. D. Odintsov, Phys. Lett. B **781**, 99 (2018). https://doi.org/10.1016/j.physletb.2018.03.064
[79] A. Y. Shaikh, Eur. Phys. J. Plus **138**, 301 (2023). https://doi.org/10.1140/epjp/s13360-023-03931-4
[80] A. Y. Shaikh, Indian J. Phys. (2024). https://doi.org/10.1007/s12648-024-03151-1
[81] V. Sahni, *et al.*, J. Exp. Theor. Phys. Lett. **77**, 201 (2003). https://doi.org/10.1134/1.1574831
[82] U. Alam, *et al.*, Mon. Not. R. Astron. Soc. **344**, 1057 (2003). https://doi.org/10.1046/j.1365-8711.2003.06871.x
[83] W. Zimdahl, and D. Pavón, Gen. Relativ. Gravit. **36**, 1483 (2004). https://doi.org/10.1023/B:GERG.0000022584.54115.9e
[84] A. Al Mamon, and K. Bamba, Eur. Phys. J. C **78**, 862 (2018). https://doi.org/10.1140/epjc/s10052-018-6355-2
[85] J. Sadeghi, A. R. Amani, and N. Tahmasbi, Astrophys. Space Sci. **348**, 559 (2013). https://doi.org/10.1007/s10509-013-1579-y

ОБМЕЖЕННЯ ГІБРИДНОЇ МОДЕЛІ ДЛЯ ДОСЛІДЖЕННЯ ГОЛОГРАФІЧНОЇ ТЕМНОЇ ЕНЕРГІЇ В МОДИФІКОВАНІЙ ГРАВІТАЦІЇ

А.Й. Шейх[a], А.П. Дженекар[b]
[a]Кафедра математики, Індіра Ганді Кала Махавідьялая, Ралегаон-445402 (магістр наук), Індія
[b]Кафедра математики, коледжа мистецтв, комерції та науки, Марегаон-445303 (M.S.), Індія

У цьому дослідженні розглядається динамізм голографічної темної енергії (ГТЕ) на тлі гравітації через гіперповерхнево-однорідний просторово-часовий контекст. Розглядаючи, як ГТЕ впливає на розвиток Всесвіту, ми використали спрощений гібридний закон розширення (ГЗР) для отримання точного розв'язку пов'язаних з ним рівнянь поля. Дослідження починається з аналізу певних кінематичних та фізичних характеристик, пов'язаних з моделлю. Ми застосували обмеження до окресленої гібридної моделі, використовуючи дані спостережень Хаббла (OHD), які складаються з 32-точкових наборів даних, щоб оцінити фізичну достовірність та доцільність моделі. У зв'язку зі значеннями параметрів, що відображаються в нашій метриці, окреслено три динамічно потенційні космологічні сценарії. Крім того, ми дослідили різні енергетичні умови (ЕС) та виділили окремі космічні фази за допомогою перевірки діагностики statefinder та параметра ривка. Квадрат швидкості звуку v_s^2 використовується для забезпечення стабільності моделі. Дослідження підтверджує космічне прискорення Всесвіту, оскільки наші висновки відповідають переважаючим даним спостережень, пропонуючи життєздатні прогнози для майбутніх досліджень з обґрунтування HDE.

Ключові слова: *голографічна темна енергія; гравітація; однорідний гіперповерхневий простір-час; гібридний закон розширення*

SPECTRA OF SOME CHARMED HADRONS IN A NON-RELATIVISTIC MODEL

T. Harsha[a], **Chaitanya Anil Bokade**[a], **Raghavendra Kaushal**[a], **Bhaghyesh**[a]

[a] Department of Physics, Manipal Institute of Technology, Manipal Academy of Higher Education, Manipal, Karnataka, India, 576104
[*]Corresponding Author e-mail: bhaghyesh.mit@manipal.edu

In a non-relativistic framework the mass spectra of $c\bar{c}$, cc, ccc and ccu systems are investigated. The potential consists of the Cornell potential along with a logarithmic correction term as suggested from lattice QCD. We analyze the S, P, and D wave charmonium states and, S and P wave cc diquark states and have compared them with existing results from experiments and other potential models. Using the quark-diquark model, we have evaluated the S-wave spectra of doubly charmed baryon Ξ_{cc}^{++} and the triply charmed baryon Ω_{ccc}. These masses are compared with other theoretical studies.

Keywords: *Non-relativistic potential model; LQCD corrections; Charmed hadrons; Diquark-quark model; Mass spectrum*

PACS: 12.39.Pn, 14.65.Dw, 14.40.Gx, 14.20.−c

1. INTRODUCTION

Since the discovery of J/ψ, the first charmonium ($c\bar{c}$) state, at SLAC [1] and BNL [2] in 1974, charmed hadrons have been continuously investigated both theoretically and experimentally. At present a large number of charmed states have been experimentally discovered [3] and even more states have been theoretically predicted. Other than the mesonic and baryonic states, unanticipated states, classified as X, Y and Z, exotic states such as tetraquarks and pentaquarks, which cannot be classified under the conventional quark model have been detected [4, 5, 6, 7]. In 2017, the LHCb collaboration discovered a resonance in the $\Lambda_c^+ K^- \pi^+ \pi^+$ mass spectrum [8]. This was identified as the doubly charmed baryon Ξ_{cc}^{++} and its mass was measured to be $3621.40 \pm 0.72 \pm 0.27$ MeV. This has led to an extensive study of doubly and also triply heavy baryons theoretically. In literature, there are various studies [9, 10] that discuss the prospects for the disvovery of multi charmed baryons in future experiments at LHC. Hence, it becomes important to study charmed baryons theoretically. Charmed hadrons are important systems for they provide valuable information about the strong and weak interactions in the standard model [11].

In this work, we have investigated the spectra of charmed hadrons including charmonium ($c\bar{c}$), cc diquarks and, doubly charmed (ccu) and triply charmed (ccc) baryons: Ξ_{cc}^{++} and Ω_{ccc}. We make use of diquark-quark model to evaluate the spectra of baryons [12]. A diquark is a bound state of two quarks. Since they exist as colored states, they are not experimentally detected as isolated entities. Nonetheless, diquark models provide qualitative explanations for various puzzles of exotic hadron spectroscopy [13, 14]. In the case of baryons, it is found that the constituent quark model predicts more states than those observed experimentally, which is generally referred as the missing resonance problem [15, 16]. However, the diquark model addresses this issue as the effective degrees of freedom is less compared to constituent quark model [17, 18]. Also, the diquark-quark interaction in baryons can be visualized similar to the quark-antiquark interaction in mesons [18].

This article is structured as follows. In section 2, we have given the theoretical framework where we have explained our potential model formalism. In section 3, we discuss our results and in section 4, we give our summary.

2. THEORETICAL MODEL

In the present work, the mass spectra are estimated by solving the non relativistic Schrodinger equation,

$$\left[\frac{1}{2\mu} \left(-\frac{d^2}{dr^2} + \frac{l(l+1)}{r^2} \right) + V(r) \right] \psi(r) = E\psi(r), \tag{1}$$

where μ is the reduced mass and l is the (relative) orbital angular momentum of the system. Here the potential $V(r)$ we use, is of the form

$$V(r) = \frac{\kappa \alpha_s(Q^2)}{r} + br + k \ln(ar) \tag{2}$$

The first term in the potential is a coulomb-like term that dominates at small distances, second term is the linear confinement term that dominates at large distances. The last term in Eq.(2) corresponds to the relativistic corrections to the static

quarkonium potential at order $1/m$ in the quark mass as suggested from various studies such as lattice [19, 20, 21, 22, 23] and effective string theory [24]. Models incorporating a quark-antiquark potential modified by a $\ln(r)$ term have successfully described quarkonium spectra [21, 22, 25]. In Eq.(2) $\alpha_s(Q^2)$ is the QCD coupling constant, κ is the color factor whose value is $-\frac{4}{3}$ for quark-antiquark (and also quark-diquark) interaction and $-\frac{2}{3}$ for quark-quark interactions [26], b is the QCD string tension, k and a are phenomenological constants. The $\alpha_s(Q^2)$ is evaluated using the formula [27],

$$\alpha_s(Q^2) = \frac{4\pi}{(11 - \frac{2}{3}n_f)\ln(\frac{Q^2}{\Lambda^2})} \tag{3}$$

Here n_f denotes the number of active quark flavors, Q is the renormalization scale, and Λ is the QCD scale parameter, which is taken as $0.168\ GeV$ [28]. The model parameters are fitted by minimizing the chi square for some of the available experimental states for charmonium. The up quark mass is fitted by minimizing the chi square for Ξ_{cc}^{++}. The values of the parameters used in our model are listed in Table 1. The Schrodinger equation 1 is solved numerically using the Runge-Kutta method [29]. The eigenvlaues (E) of Eq.(1) corresponds to the spin-averaged masses. The spin-dependent contributions to the masses are incorporated perturbatively. The spin-dependent potentials: spin-spin ($V_{SS}(r)$), spin-orbit ($V_{LS}(r)$), and tensor ($V_T(r)$) potentials are given by [30, 31],

$$V_{SS}(r) = \frac{8\pi|\kappa|\alpha_s}{3m_1m_2}\left(\frac{\sigma}{\sqrt{\pi}}\right)^3 exp(-\sigma^2r^2)\mathbf{S_1}\cdot\mathbf{S_2} \tag{4}$$

$$V_{LS}(r) = \frac{1}{2m_c^2r}\left(3\frac{dV_V(r)}{dr} - \frac{dV_S(r)}{dr}\right)\mathbf{L}\cdot\mathbf{S}. \tag{5}$$

$$V_T(r) = \frac{1}{12m_c^2}\left(\frac{1}{r}\frac{dV_V(r)}{dr} - \frac{d^2V_V(r)}{dr^2}\right)S_{12}. \tag{6}$$

where,

$$S_{12} = 12\left((\mathbf{S_1}\cdot\hat{r})(\mathbf{S_2}\cdot\hat{r}) - \frac{1}{3}\mathbf{S_1}\cdot\mathbf{S_2}\right). \tag{7}$$

Here, we take the Lorentz vector term $V_V(r) = \frac{\kappa\alpha_s(Q^2)}{r}$ and the Lorentz scalar term $V_S(r) = br$. The masses of charmonium states are given by

$$M_{c\bar{c}} = 2m_c + E_{c\bar{c}} + \langle V_{SS}(r) + V_{LS}(r) + V_T(r)\rangle_{c\bar{c}}, \tag{8}$$

where $E_{c\bar{c}}$ are the eigenvalues (spin-averaged charmonium masses) obtained by solving the Schrodinger equation (Eq.(1)) taking $\mu = m_c/2$ and using the potential given in Eq.(2) with $\kappa = -4/3$. Using the eigenfunctions corresponding to these eigenvalues, we evaluate the expectation values in Eq.(8). For charmonium, $m_1 = m_2 = m_c$ in Eq.(4), where m_c is the charm quark mass.

We use diquark-quark model to evaluate the mass spectra of doubly and triply charmed baryons: Ξ_{cc}^{++} and Ω_{ccc}. For this, we first estimate the diquark spectrum and then once again solve the Schrodinger equation for a two-body system composed of diquark and quark. In both Ξ_{cc}^{++} and Ω_{ccc}, we assume the two c quarks to form the cc diquark. For modelling the quark-quark interaction (V_{qq}) in a diquark, we use the general rule [32, 33, 29],

$$V_{qq}(r) = \frac{V_{q\bar{q}}(r)}{2}, \tag{9}$$

where ($V_{q\bar{q}}$) is the quark-antiquark potential. Hence, the central potential for diquarks becomes,

$$V_{qq}(r) = -\frac{2\alpha_s(Q^2)}{3r} + \frac{br}{2} + k\ln(ar). \tag{10}$$

Here we have not considered the factor of $1/2$ for the $O(1/m)$ correction term present in $V_{q\bar{q}}$. In diquark-quark model, baryons are treated as bound states of diquark and quark. The diquark-quark interaction in baryons is assumed to be similar to the quark-antiquark interaction in mesons [18]. Therefore, the diquark-quark potential within baryons is taken to be,

$$V_{dq}(r) = -\frac{4\alpha_s(Q^2)}{3r} + br + k\ln(ar). \tag{11}$$

Due to the Pauli exclusion principle, for the diquarks in the $l = 0$ (S-wave) state, the total spin $S = 1$ (spin-triplet) and for the diquarks in the $l = 1$ (P-wave) state, the total spin $S = 0$ (spin-singlet). There will be no contribution to the masses

Table 1. Values of parameters

m_c [GeV]	m_u [GeV]	b [GeV²]	a [GeV]	k [GeV]	σ [GeV]
1.298	0.175	0.136	1.105	0.195	2.600

from the spin-orbit and tensor interactions for $l = 0$ and $S = 0$ states. Hence, the masses of (S and P wave) diquark states are given by

$$M_{cc} = 2m_c + E_{cc} + \langle V_{SS}(r) \rangle_{cc}, \tag{12}$$

where E_{cc} are the eigenvalues (spin-averaged diquark masses) obtained by solving the Schrodinger equation (Eq.(1)) taking $\mu = m_c/2$ and using the potential given in Eq.(10). Using the eigenfunctions corresponding to these eigenvalues, we evaluate the expectation value in Eq.(12). For diquarks, $m_1 = m_2 = m_c$ in Eq.(4).

In this work, we only consider the radial excitations of the diquark-quark system with diquark in ground state. Hence, for baryons we will not be considering the spin-orbit and tensor interactions. The masses of baryons in our diquark-quark model are given by the relation

$$M_{dq} = M_{cc} + m_q + E_{dq} + \langle V_{SS}(r) \rangle_{dq}, \tag{13}$$

where E_{dq} are the eigenvalues obtained by sloving the Schrodinger equation (Eq.(1)) taking $\mu = (M_{cc}m_q/M_{cc} + m_q)$ and using the potential given in Eq.(11). $m_q = m_u$ in the case of Ξ_{cc}^{++} and $m_q = m_c$ in the case of Ω_{ccc}. Using the eigenfunctions corresponding to these eigenvalues, we evaluate the expectation value in Eq.(13). Here we take $m_1 = M_{cc}, m_2 = m_q$ in Eq.(4). For the $l = 0$ states, Ω_{ccc} has $J^P = \frac{3}{2}^+$ whereas Ξ_{cc}^{++} have $J^P = \frac{1}{2}^+$ and $\frac{3}{2}^+$.

3. RESULTS AND DISCUSSIONS
3.1. Charmonium and cc diquark

The mass spectra of S, P, and D-wave charmonium states are presented in Tables 2,3, and 4 respectively, where we have compared our results with exisiting results from experiments and other potential models. In Figure 1, we have compared our $c\bar{c}$ spectra with results from experiments. From Figure 1, we can see that the masses of states below the $D\bar{D}$ threshold predicted from our model are in reasonable agreement with the experimental results. In literarture, the $3\,^3S_1$ and $4\,^3S_1$ states are suggested to be the experimentally detetcted $\psi(4040)$ and $\psi(4415)$ states respectively [31]. The masses of $3\,^3S_1$ and $4\,^3S_1$ states from our model are 4165 MeV and 4530 MeV respectively, which are approximately 125 MeV higher than the masses of $\psi(4040)$ and $\psi(4415)$ states. It is to be noted that since $\psi(4040)$ and $\psi(4415)$ lie above the $D\bar{D}$ threshold, there will be large $S - D$ mixing in these states [34]. Hence $\psi(4040)$ and $\psi(4415)$ cannot be considered as pure $^3S_1$ states [34, 35].

Table 2. S-wave charmonium spectrum (in MeV).

State	J^{PC}	PDG [3]	Our Work	[36]	[37]	[38]	[27]
$1\,^1S_0$	0^{-+}	2984.1 ± 0.4	2985	3004	2981	2982	2989
$1\,^3S_1$	1^{--}	3096.900 ± 0.006	3093	3086	3096	3090	3094
$2\,^1S_0$	0^{-+}	3637.7 ± 0.9	3657	3645	3635	3630	3602
$2\,^3S_1$	1^{--}	3686.097 ± 0.010	3722	3708	3685	3672	3681
$3\,^1S_0$	0^{-+}		4101	4124	3989	4043	4058
$3\,^3S_1$	1^{--}	$\psi(4040)$	4165	4147	4039	4072	4129
$4\,^1S_0$	0^{-+}		4478	4534	4401	4384	4448
$4\,^3S_1$	1^{--}	$\psi(4415)$	4530	4579	4427	4406	4514
$5\,^1S_0$	0^{-+}		4807	4901	4811	4685	4799
$5\,^3S_1$	1^{--}		4853	4942	4837	4703	4863

For $1P$ charmonium states ($h_c(1P)$, $\chi_{c0}(1P)$, $\chi_{c1}(1P)$, and $\chi_{c2}(1P)$) the masses predicted from our model are in agreement with the expreimental results and shows only small deviations (< 15 MeV). In some theoretical models [39, 40], $2\,^3P_0$, $3\,^3P_0$, $2\,^3P_2$ and $3\,^3P_1$ are suggested to be the experimentally detected $\chi_{c0}(3860)$, $X(4160)$, $\chi_{c2}(3930)$ and $X(4274)$ states respectively, with measured masses of 3862^{+26+40}_{-32-13} MeV, 4153^{+23}_{-21} MeV, 3922.5 ± 1 MeV and 4286^{+8}_{-9} MeV [3]. Our obtained masses for $2\,^3P_0$, $3\,^3P_0$, $2\,^3P_2$ and $3\,^3P_1$ states deviates from the measured masses of $\chi_{c0}(3860)$, $X(4160)$, $\chi_{c2}(3930)$ and $X(4274)$. This may be due to the fact that, for states close or above the open-charm thresholds, the coupled-channel effects are significant [35]. The mass of $1\,^3D_1$ state obtained from our analysis is close to the mass of $\psi(3770)$ state, which is assigned as $1\,^3D_1$ in some potential models [31]. But the inconsistency in the predicted leptonic decay width of this state in potential models, compels to interpret $\psi(3770)$ as an $S - D$ mixture [35]. In literature, the states

Table 3. *P*-wave charmonium spectrum (in MeV).

State	J^{PC}	PDG [3]	Our Work	[36]	[37]	[38]	[27]
$1\,^3P_0$	0^{++}	3414.71 ± 0.30	3420	3440	3413	3424	3428
$1\,^3P_1$	1^{++}	3510.67 ± 0.05	3496	3492	3511	3505	3468
$1\,^1P_1$	1^{+-}	3525.37 ± 0.14	3526	3496	3525	3516	3470
$1\,^3P_2$	2^{++}	3556.17 ± 0.07	3565	3511	3555	3549	3480
$2\,^3P_0$	0^{++}		3924	3932	3870	3852	3897
$2\,^3P_1$	1^{++}		3994	3984	3906	3925	3938
$2\,^1P_1$	1^{+-}		4061	3991	3926	3934	3943
$2\,^3P_2$	2^{++}		4023	4007	3949	3965	3955
$3\,^3P_0$	0^{++}		4284	4394	4301	4201	4296
$3\,^3P_1$	1^{++}		4351	4401	4319	4271	4338
$3\,^1P_1$	1^{+-}		4417	4410	4337	4279	4344
$3\,^3P_2$	2^{++}		4380	4427	4354	4309	4358
$4\,^3P_0$	0^{++}		4621	4722	4698	4509	4653
$4\,^3P_1$	1^{++}		4686	4771	4728	4576	4696
$4\,^1P_1$	1^{+-}		4752	4784	4744	4585	4704
$4\,^3P_2$	2^{++}		4715	4802	4763	4614	4718

Table 4. *D*-wave charmonium spectrum (in MeV).

State	J^{PC}	PDG [3]	Our Work	[36]	[37]	[38]	[27]
$1\,^3D_3$	3^{--}		3830	3798	3813	3805	3755
$1\,^3D_2$	2^{--}		3839	3814	3795	3800	3772
$1\,^3D_1$	1^{--}	3773.7 ± 0.7	3836	3815	3783	3785	3775
$1\,^1D_2$	2^{-+}		3834	3806	3807	3799	3765
$2\,^3D_3$	3^{--}		4236	4273	4220	4165	4176
$2\,^3D_2$	2^{--}		4237	4248	4190	4158	4188
$2\,^3D_1$	1^{--}		4230	4245	4150	4141	4188
$2\,^1D_2$	2^{-+}		4235	4242	4196	4158	4182
$3\,^3D_3$	3^{--}		4585	4626	4574	4481	4549
$3\,^3D_2$	2^{--}		4583	4632	4544	4472	4557
$3\,^3D_1$	1^{--}		4573	4627	4507	4455	4555
$3\,^1D_2$	2^{-+}		4582	4629	4549	4472	4553

$\psi_2(3823)$, $X(3842)$, $\psi(4160)$ and $\psi(4360)$ are assigned as $1\,^3D_2$, $1\,^3D_3$, $2\,^3D_1$ and $3\,^3D_2$ respectively [31, 41, 42, 43, 44]. But other interpretations for some of these states to be either mixed states, hybrids, tetraquarks etc., cannot be completely ruled out.
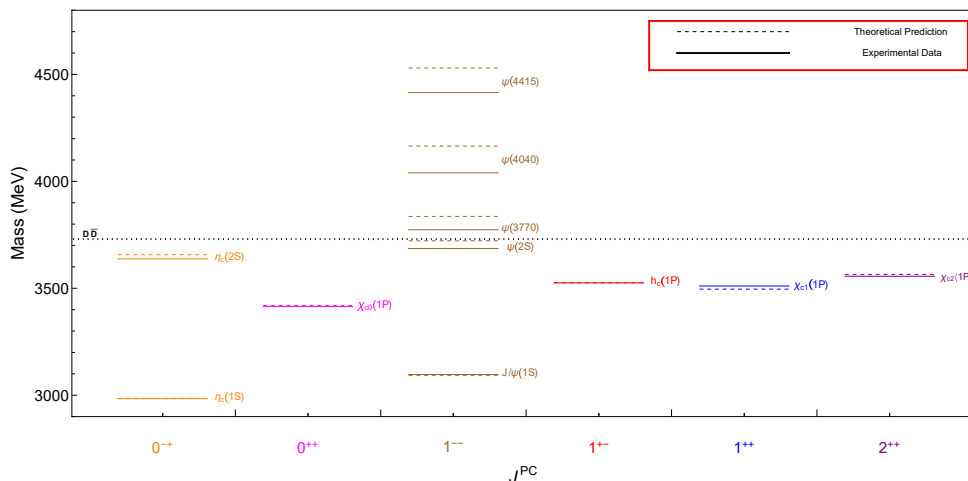

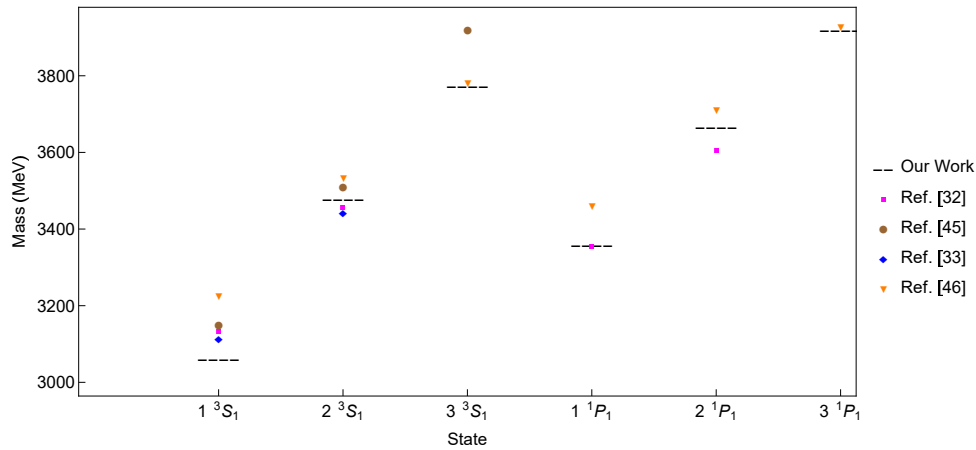**Figure 1.** Comparison of predicted $c\bar{c}$ spectra with experiment.

Figure 2. Comparison of cc-diquark spectrum with other models.

In Table 5 and Figure 2, we have compared the mass spectra of cc-diquarks obtained from our model with other theoretical models. We can observe from Figure 2 that the cc-diquark masses varries from model to model. The ground

Table 5. cc diquark spectrum (in MeV).

State	Our Work	[32]	[45]	[33]	[46]
$1\,^3S_1$	3063	3133	3150	3114	3226
$1\,^1P_1$	3358	3353			3460
$2\,^3S_1$	3478	3456	3510	3443	3535
$2\,^1P_1$	3666	3606			3712
$3\,^3S_1$	3774		3920		3782
$3\,^1P_1$	3921				3928

state mass of cc diquark obtained from our model is 3063 MeV. The ground state diquark mass obtained from our model is used further to determine the S-wave mass spectra of Ξ_{cc}^{++} and Ω_{ccc} baryons.

3.2. Ξ_{cc}^{++} and Ω_{ccc} baryons

The S-wave mass spectra of Ξ_{cc}^{++} and Ω_{ccc} baryons are evaluated using diquark-quark model. The Ξ_{cc}^{++} baryon is considered as a bound state of cc-diquark and u quark, and Ω_{ccc} baryon is considered as a bound state of cc-diquark and c quark. The S-wave mass spectrum of Ξ_{cc}^{++} baryons are presented in Tables 6, 7 for $J^P = \frac{1}{2}^+$ and $\frac{3}{2}^+$ respectively. In Figures 3 and 4, we show the comparison of S-wave mass spectra of Ξ_{cc}^{++} baryons obtained from our model with other theoretical models. The ground state mass of Ξ_{cc}^{++} obtained from our model is 3621 MeV which is very close to the experimental

Table 6. S-wave Ξ_{cc}^{++} spectrum corresponding to $J^P = \frac{1}{2}^+$ (in MeV).

State	Our Work	PDG [3]	[18] $\{cc\}u$	[18] $\{uc\}c$	[47]
$1S$	3621	3621.55 ± 0.23	3621	3687	3511
$2S$	4705		4478	4274	3920
$3S$	5412		5026	4666	4159
$4S$	5991		5482	4992	4501
$5S$	6501		5888	5281	4748

value of 3621.6 ± 0.4 MeV. The authors in Ref [18] suggest that uc-diquark clustering is more favourable than that of cc-diquark clustering. In the present work we have considered the cc-diquark clustering which is reasonable within the heavy quark symmetry suggesting that quarks with equal masses form a compact configuration [48]. The ground state mass of Ω_{ccc} obtained from our model is 4779 MeV. We have compared the ground state mass of Ω_{ccc} obtained from our model with other theoretical models in Table 8. We see that our predicted Ω_{ccc} ground state mass is in agreement with the LQCD predictions. The S-wave mass spectrum of Ω_{ccc} are presented in Table 9.

Table 7. *S*-wave Ξ_{cc}^{++} spectrum corresponding to $J^P = \frac{3}{2}^+$ (in MeV).

State	Our Work	[18] $\{cc\}u$	[18] $\{uc\}c$	[47]
1*S*	4057	4019	3773	3687
2*S*	4970	4670	4339	3983
3*S*	5631	5170	4725	4261
4*S*	6187	5602	5048	4519
5*S*	6681	5993	5334	4759
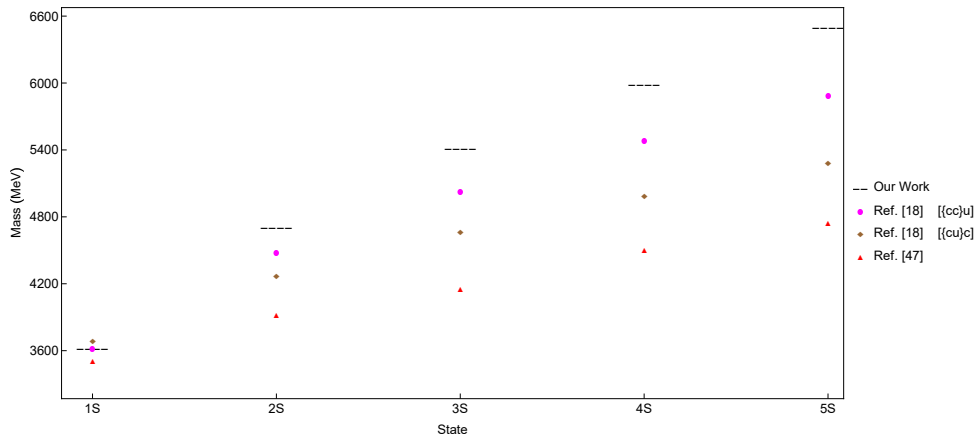
Figure 3. Comparison of *S*-wave mass spectra of *ccu* baryon corresponding to $J^P = \frac{1}{2}^+$ with other models.

Table 8. Comparison of ground state mass of Ω_{ccc} (in MeV).

Approach	Mass
Our Work	4779
LQCD [49]	4796
LQCD [50]	4769
LQCD [51]	4789
LQCD [52]	4761
LQCD [53]	4733
Hypercentral CQM [54]	4806
Constituent QM [55]	4965
Bag model [56]	4777
Variational Cornell [57]	4799
QCD sum rules[58]	4670
Relativistic Quark model [59]	4803
Quark diquark model [60]	4760

Table 9. *S*-wave Ω_{ccc} spectrum corresponding to $J^P = \frac{3}{2}^+$ (in MeV).

State	Our Work	[54]
1*S*	4779	4806
2*S*	5362	5300
3*S*	5764	5865
4*S*	6097	6488
5*S*	6390	7037

4. SUMMARY

We have evaluated the mass spectra of $c\bar{c}$, cc, Ξ_{cc}^{++}, and Ω_{ccc} systems using a phenomenological potential model incorporating a logarithmic correction term. The evaluated mass spectra of charmonium are consistent with the experimental results. The ground state mass of Ξ_{cc}^{++} obtained from our model is close to the experimental value, which validates the diquark-quark model and also supports our assumption that the Ξ_{cc}^{++} baryon can be treated as a bound state of *cc*-diquark and *u* quark. The *S*-wave mass spectrum of Ω_{ccc} baryon have been evaluated. The Ω_{ccc} ground state mass is comparable
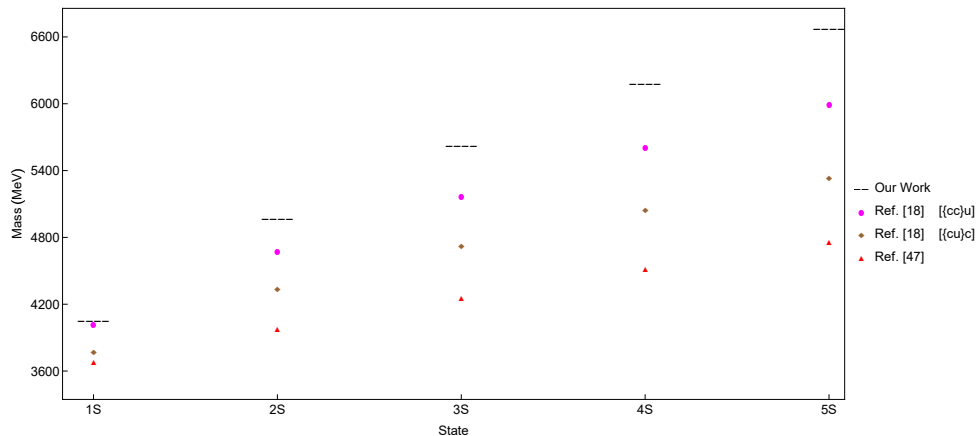
Figure 4. Comparison of S-wave mass spectra of ccu baryon corresponding to $J^P = \frac{3}{2}^+$ with other models.

with the LQCD predictions. Since we have no experimental data for Ω_{ccc} baryon, we need to rely on theoretical models to investigate its properties.

ORCID

T. Harsha, https://orcid.org/0009-0006-4872-3947; **Chaitanya Anil Bokade**, https://orcid.org/0009-0007-5463-6812;
Raghavendra Kaushal, https://orcid.org/0009-0000-9014-534X; **Bhaghyesh**, https://orcid.org/0000-0003-3994-9945

REFERENCES

[1] J.-E. Augustin, *et al.*, "Discovery of a Narrow Resonance in e^+e^- Annihilation," Phys. Rev. Lett. **33**, 1406 (1974). https://doi.org/10.1103/PhysRevLett.33.1406

[2] J.J. Aubert, *et al.*, "Experimental Observation of a Heavy Particle J," Phys. Rev. Lett. **33**, 1404 (1974). https://doi.org/10.1103/PhysRevLett.33.1404

[3] S. Navas, et al. (Particle Data Group Collaboration), "Review of Particle Physics," Phys. Rev. D **110**, 030001 (2024). https://doi.org/10.1103/PhysRevD.110.030001

[4] E. Braaten, and R. Bruschini, "Exotic hidden-heavy hadrons and where to find them," Phys. Lett. B, **863**, 139386 (2025). https://doi.org/10.1016/j.physletb.2025.139386

[5] N. Brambilla, S. Eidelman, C. Hanhart, A. Nefediev, C.-P. Shen, C. E. Thomas, A. Vairo, and C.-Z. Yuan, "The XYZ states: experimental and theoretical status and perspectives," Phys. Rep. **873**, 1 (2020). https://doi.org/10.1016/j.physrep.2020.05.001

[6] C.-Z. Yuan, "Exotic states in the quarkonium sector - status and perspectives," EPJ Web Conf. **274**, 01001 (2022). https://doi.org/10.1051/epjconf/202227401001; arXiv:2211.07217 [hep-ph]. https://arxiv.org/abs/2211.07217v1

[7] L. Maiani, "Charm and hadrons," Nucl. Phys. B, 1012, 116831 (2025). https://doi.org/10.1016/j.nuclphysb.2025.116831

[8] R. Aaij, *et al.*, (LHCb Collaboration), "Observation of the Doubly Charmed Baryon Ξ_{cc}^{++}"," Phys. Rev. Lett. **119**, 112001 (2017). https://doi.org/10.1103/PhysRevLett.119.112001

[9] Y.-Q. Chen, and S.-Z. Wu, "Production of triply heavy baryons at LHC," J. High Energ. Phys. **2011**, 144 (2011). https://doi.org/10.1007/JHEP08(2011)144

[10] ALICE Collaboration, "Letter of intent for ALICE 3: A next-generation heavy-ion experiment at the LHC," arXiv: 2211.02491 physics.ins-det, CERN (2022). https://doi.org/10.48550/arXiv.2211.02491

[11] M. Gersabeck, "Introduction to Charm Physics," PoS FWNP, 001 (2015). https://doi.org/10.22323/1.220.0001; arXiv:1503.00032 [hep-ex], https://doi.org/10.48550/arXiv.1503.00032

[12] D.B. Lichtenberg, "Baryon Supermultiplets of SU(6) × $O(3)$ in a Quark-Diquark Model," Phys. Rev. **178**, 2197 (1969). https://doi.org/10.1103/PhysRev.178.2197

[13] R.L. Jaffe, "Exotica," Phys. Rep. **409**, 1 (2005). https://doi.org/http://dx.doi.org/10.1016/j.physrep.2004.11.005

[14] F. Wilczek, "Diquarks as inspiration and as objects," in: *Deserfest: A Celebration of the Life and Works of Stanley Deser*, edited by S. Deser, and J.T. Liu, (World Scientific, 2006) pp. 322–338, https://doi.org/10.1142/9789812775344_0007; arXiv:hep-ph/0409168. https://doi.org/10.48550/arXiv.hep-ph/0409168

[15] E. Klempt, and J.-M. Richard, "Baryon spectroscopy," Rev. Mod. Phys. **82**, 1095 (2010). https://doi.org/10.1103/RevModPhys.82.1095

[16] S. Capstick, and W. Roberts, "Quark models of baryon masses and decays," Prog. Part. Nucl. Phys. **45**, S241-S331 (2000). https://doi.org/10.1016/S0146-6410(00)00109-5; arXiv:nucl-th/0008028. https://doi.org/10.48550/arXiv.nucl-th/0008028

[17] E. Santopinto, "Interacting quark-diquark model of baryons," Phys. Rev. C, **72**, 022201 (2005). https://doi.org/10.1103/PhysRevC.72.022201; arXiv:hep-ph/0412319. https://doi.org/https://doi.org/10.48550/arXiv.hep-ph/0412319

[18] H. Mutuk, "The status of Ξ_{cc}^{++} baryon: investigating quark–diquark model," Eur. Phys. J. Plus, **137**, 10 (2022). https://doi.org/10.1140/epjp/s13360-021-02256-4; arXiv:2112.06205 [hep-ph]. https://doi.org/10.48550/arXiv.2112.06205

[19] Y. Koma, and M. Koma, "Scaling study of the relativistic corrections to the static potential," in: *PoS LAT2009*, **122** (2009). https://doi.org/10.22323/1.091.0122; arXiv:0911.3204 [hep-lat]. https://doi.org/10.48550/arXiv.0911.3204

[20] Y. Koma, M. Koma, and H. Wittig, "Relativistic corrections to the static potential at O($1/m$) and O($1/m^2$)," in: *PoS LAT2007*, 111 (2007). https://doi.org/https://doi.org/10.22323/1.042.0111; arXiv:0711.2322 [hep-lat]. https://arxiv.org/abs/0711.2322

[21] T. Kawanai, and S. Sasaki, "Potential description of the charmonium from lattice QCD," AIP Conf. Proc. **1701**, 050022 (2016). https://doi.org/10.1063/1.4938662; arXiv:1503.05752 [hep-lat]. https://doi.org/10.48550/arXiv.1503.05752

[22] A. Laschka, N. Kaiser, and W. Weise, "Quark-antiquark potential to order $1/m$ and heavy quark masses," Phys. Rev. D, **83**, 094002 (2011). https://doi.org/10.1103/PhysRevD.83.094002

[23] A. Laschka, N. Kaiser, and W. Weise, "Charmonium potentials: Matching perturbative and lattice QCD," Phys. Lett. B, **715**, 190-193 (2012). https://doi.org/10.1016/j.physletb.2012.07.049

[24] G. Perez-Nadal, and J. Soto, "Effective-string-theory constraints on the long-distance behavior of the subleading potentials," Phys. Rev. D, **79**, 114002 (2009). https://doi.org/10.1103/PhysRevD.79.114002

[25] T.S. Nayana, and A. Bhaghyesh, "Spectra and decay properties of higher lying B_C meson states," Int. J. Mod. Phys. A, **39**, 2450101 (2024). https://doi.org/10.1142/S0217751X2450101X; arXiv:2405.12691 [hep-ph]. https://arxiv.org/abs/2405.12691

[26] P. Lundhammar, and T. Ohlsson, "Nonrelativistic model of tetraquarks and predictions for their masses from fits to charmed and bottom meson data," Phys. Rev. D, **102**, 054018 (2020). https://doi.org/10.1103/PhysRevD.102.054018

[27] N.R. Soni, B.R. Joshi, R.P. Shah, H.R. Chauhan, and J.N. Pandya, "$Q\bar{Q}$ ($Q \in \{b, c\}$) spectroscopy using the Cornell potential," Eur. Phys. J. C, **78**, 592 (2018). https://doi.org/10.1140/epjc/s10052-018-6068-6; arXiv:1707.07144 [hep-ph]. https://arxiv.org/abs/1707.07144

[28] D. Ebert, R.N. Faustov, and V.O. Galkin, "Properties of heavy quarkonia and B_c mesons in the relativistic quark model," Phys. Rev. D, **67**, 014027 (2003). https://doi.org/10.1103/PhysRevD.67.014027

[29] W. Lucha, and F.F. Schoberl, "Solving the Schroedinger equation for bound states with Mathematica 3.0," Int. J. Mod. Phys. C, **10**, 607 (1999). https://doi.org/10.1142/S0129183199000450; arXiv:hep-ph/9811453. https://arxiv.org/abs/hep-ph/9811453

[30] W. Lucha, F.F. Schoberl, and D. Gromes, "Bound states of quarks", Phys. Rept. **200**, 127-240 (1991). https://doi.org/10.1016/0370-1573(91)90001-3

[31] T. Barnes, S. Godfrey, and E.S. Swanson, "Higher charmonia", Phys. Rev. D, **72**, 054026 (2005). https://doi.org/10.1103/PhysRevD.72.054026; arXiv:hep-ph/0505002. https://arxiv.org/abs/hep-ph/0505002

[32] V.R. Debastiani, and F.S. Navarra, "A non-relativistic model for the $[cc][\bar{c}\bar{c}]$ tetraquark," Chin. Phys. C, **43**, 013105 (2019). https://doi.org/10.1088/1674-1137/43/1/013105; arXiv:1706.07553 [hep-ph]. https://arxiv.org/abs/1706.07553

[33] H. Mutuk, "Nonrelativistic treatment of fully-heavy tetraquarks as diquark-antidiquark states," Eur. Phys. J. C, **81**, 367 (2021). https://doi.org/10.1140/epjc/s10052-021-09176-8; arXiv:2104.11823 [hep-ph]. https://arxiv.org/abs/2104.11823

[34] A.M. Badalian, B.L.G. Bakker, and I.V. Danilkin, "The S-D mixing and dielectron widths of higher charmonium 1^{--} states," Phys. Atom. Nucl. **72**, 638-646 (2009). https://doi.org/10.1134/S1063778809040085; arXiv:0805.2291 [hep-ph]. https://arxiv.org/abs/0805.2291

[35] Z.-L. Man, C.-R. Shu, Y.-R. Liu, and H. Chen, "Charmonium states in a coupled-channel model," Eur. Phys. J. C, **84**, 810 (2024). https://doi.org/10.1140/epjc/s10052-024-13132-7; arXiv:2402.02765 [hep-ph]. https://arxiv.org/abs/2402.02765

[36] R. Chaturvedi, and A.K. Rai, "Mass spectra and decay properties of the $c\bar{c}$ meson," Eur. Phys. J. Plus, **133**, 220 (2018). https://doi.org/10.1140/epjp/i2018-12044-8

[37] D. Ebert, R.N. Faustov, and V.O. Galkin, "Spectroscopy and Regge trajectories of heavy quarkonia and B_c mesons," Eur. Phys. J. C, **71**, 1825 (2011). https://doi.org/10.1140/epjc/s10052-011-1825-9; arXiv:1111.0454 [hep-ph]. https://arxiv.org/abs/1111.0454

[38] M.A. Sultan, N. Akbar, B. Masud, and F. Akram, "Higher hybrid charmonia in an extended potential model," Phys. Rev. D, **90**, 054001 (2014). https://doi.org/10.1103/PhysRevD.90.054001

[39] Z.-H. Wang, and G.-L. Wang, "Two-body strong decays of the 2P and 3P charmonium states," Phys. Rev. D, **106**, 054037 (2022). https://doi.org/10.1103/PhysRevD.106.054037; arXiv:2204.08236 [hep-ph]. https://arxiv.org/abs/2204.08236

[40] L.-C. Gui, L.-S. Lu, Q.-F. Lü, X.-H. Zhong, and Q. Zhao, "Strong decays of higher charmonium states into open-charm meson pairs," Phys. Rev. D, **98**, 016010 (2018). https://doi.org/10.1103/PhysRevD.98.016010; arXiv:1801.08791 [hep-ph]. https://arxiv.org/abs/1801.08791

[41] B. Wang, H. Xu, X. Liu, D.-Y. Chen, S. Coito, and E. Eichten, "Using $X(3823) \to J/\psi\pi^+\pi^-$ to identify coupled-channel effects," Front. Phys. (Beijing) **11**, 111402 (2016). https://doi.org/10.1007/s11467-016-0564-7; arXiv:1507.07985 [hep-ph]. https://arxiv.org/abs/1507.07985

[42] G.-J. Ding, J.-J. Zhu, and M.-L. Yan, "Canonical Charmonium Interpretation for Y(4360) and Y(4660)," Phys. Rev. D, **77**, 014033 (2008). https://doi.org/10.1103/PhysRevD.77.014033; arXiv:0708.3712 [hep-ph]. https://arxiv.org/abs/0708.3712

[43] G.L. Yu, and Z.G. Wang, "Analysis of the $X(3842)$ as a D-wave charmonium meson", Int. J. Mod. Phys. A, **34**, 1950151 (2019). https://doi.org/10.1142/S0217751X19501513; arXiv:1907.00341 [hep-ph]. https://arxiv.org/abs/1907.00341

[44] K. Raghavendra, and A. Bhaghyesh, "Mass spectra of charmed hadrons in a screened potential model," Phys. Scr. **100**, 075303 (2025). https://doi.org/10.1088/1402-4896/add663

[45] L. Gutierrez-Guerrero, J. Alfaro, and A. Raya, "Mass spectra of one or two heavy quark mesons and diquarks within a nonrelativistic potential model," Int. J. Mod. Phy. A, **36**, 2150171 (2021). https://doi.org/10.1142/S0217751X21501712

[46] D. Ebert, R. Faustov, V. Galkin, and A. Martynenko, "Mass spectra of doubly heavy baryons in the relativistic quark model," Phys. Rev. D, **66**, 014008 (2002). https://doi.org/10.1103/PhysRevD.66.014008

[47] Z. Shah, and A.K. Rai, "Excited state mass spectra of doubly heavy Ξ baryons," Eur. Phys. J. C, **77**, 129 (2017). https://doi.org/10.1140/epjc/s10052-017-4688-x; arXiv:1702.02726 [hep-ph]. https://arxiv.org/abs/1702.02726

[48] Y. Yamaguchi, S. Ohkoda, A. Hosaka, T. Hyodo, and S. Yasui, "Heavy quark symmetry in multihadron systems," Phys. Rev. D, **91**, 034034 (2015). https://doi.org/10.1103/PhysRevD.91.034034; arXiv:1402.5222 [hep-ph]. https://arxiv.org/abs/1402.5222

[49] Z.S. Brown, W. Detmold, S. Meinel, and K. Orginos, "Charmed bottom baryon spectroscopy from lattice QCD," Phys. Rev. D, **90**, 094507 (2014). https://doi.org/10.1103/PhysRevD.90.094507

[50] K. Can, G. Erkol, M. Oka, and T. Takahashi, "Look inside charmed-strange baryons from lattice QCD," Phys. Rev. D, **92**, 114515 (2015). https://doi.org/10.1103/PhysRevD.92.114515

[51] Y. Namekawa, S. Aoki, K.-I. Ishikawa, N. Ishizuka, K. Kanaya, Y. Kuramashi, M. Okawa, Y. Taniguchi, *et al.*, (PACS-CS Collaboration), "Charmed baryons at the physical point in 2+1 flavor lattice QCD," Phys. Rev. D, **87**, 094512 (2013). https://doi.org/10.1103/PhysRevD.87.094512

[52] R.A. Briceño, H.-W. Lin, and D.R. Bolton, "Charmed-baryon spectroscopy from lattice QCD with N_f=2+1+1 flavors", Phys. Rev. D, **86**, 094504 (2012). https://doi.org/10.1103/PhysRevD.86.094504

[53] C. Alexandrou, V. Drach, K. Jansen, C. Kallidonis, and G. Koutsou, "Baryon spectrum with $N_f = 2+1+1$ twisted mass fermions," Phys. Rev. D, **90**, 074501 (2014). https://doi.org/10.1103/PhysRevD.90.074501

[54] Z. Shah, and A.K. Rai, "Masses and Regge trajectories of triply heavy Ω_{ccc} and Ω_{bbb} baryons," Eur. Phys. J. A, **53**, 195 (2017). https://doi.org/10.1140/epja/i2017-12386-2

[55] W. Roberts, and M. Pervin, "Heavy baryons in a quark model," Int. J. Mod. Phys. A, **23**, 2817 (2008). https://doi.org/10.1142/S0217751X08041219; arXiv:0711.2492 [nucl-th]. https://arxiv.org/abs/0711.2492

[56] A. Bernotas, and V. Simonis, "Heavy hadron spectroscopy and the bag model," Lith. J. Phys. **49**, 19 (2009). https://doi.org/10.3952/lithjphys.49110; arXiv:0808.1220 [hep-ph]. https://arxiv.org/abs/0808.1220

[57] J.M. Flynn, E. Hernández, and J. Nieves, "Triply heavy baryons and heavy quark spin symmetry," Phys. Rev. D, **85**, 014012 (2012). https://doi.org/10.1103/PhysRevD.85.014012

[58] J.-R. Zhang, and M.-Q. Huang, "Deciphering triply heavy baryons in terms of QCD sum rules," Phys. Lett. B, **674**, 28 (2009). https://doi.org/10.1016/j.physletb.2009.02.056; arXiv:0902.3297 [hep-ph]. https://arxiv.org/abs/0902.3297

[59] A. P. Martynenko, "Ground-state triply and doubly heavy baryons in a relativistic three-quark model," Phys. Lett. B, **663**, 317 (2008). https://doi.org/10.1016/j.physletb.2008.04.030; arXiv:0708.2033 [hep-ph]. https://arxiv.org/abs/0708.2033

[60] K. Thakkar, A. Majethiya, and P.C. Vinodkumar, "Magnetic moments of baryons containing all heavy quarks in the quark-diquark model," Eur. Phys. J. Plus, **131**, 339 (2016). https://doi.org/10.1140/epjp/i2016-16339-4; arXiv:1609.05444 [hep-ph]. https://arxiv.org/abs/1609.05444

СПЕКТРИ ДЕЯКИХ ЧАРІВНИХ АДРОНІВ У НЕРЕЛЯТИВІСТСЬКІЙ МОДЕЛІ
Т. Харша[a], Чайтанья Аніл Бокаде[a], Рагхавендра Каушал[a], Бхаг'єш[a]
[a]Кафедра фізики, Маніпальський технологічний інститут, Маніпальська академія вищої освіти,
Маніпал, Карнатака, 576104 Індія

У нерелятивістських рамках досліджуються мас-спектри систем $c\bar{c}$, cc, ccc та cci. Потенціал складається з потенціалу Корнелла разом із логарифмічним коригувальним членом, як це запропоновано з ґраткової КХД. Ми аналізуємо хвильові стани чармонію S, P та D, а також хвильові стани cc дикварка S та P та порівнюємо їх з існуючими результатами експериментів та інших потенційних моделей. Використовуючи кварк-дикваркову модель, ми оцінили S-хвильові спектри подвійно зачарованого баріона Ξ_{cc}^{++} та тричі зачарованого баріона Ω_{ccc}. Ці маси порівнюються з іншими теоретичними дослідженнями.

Ключові слова: *нерелятивістська потенціальна модель; поправки LQCD; зачаровані адрони; модель дикварка-кварка; мас-спектр*

COUPLED-CHANNELS ANALYSIS AND OPTICAL MODEL POTENTIAL EXTRACTION FOR DEUTERON SCATTERING FROM ^{6}Li TO ^{208}Pb

 Waleed Saleh Alrayashi*

Science Department, Faculty of Education, Sana'a University, Sanna'a, Yemen
*Corresponding Author e-mail: walrayashi@su.edu.ye

Deuteron-nucleus elastic and inelastic scattering from ^{6}Li to ^{208}Pb has been studied for incident energies ranging from 9.9 to 270 MeV. The main goal of this work is to study the effect of coupling the nuclear ground state to inelastic excitation channels on the energy dependence of optical model potential (OMP) parameters. Using the FRESCO and SFRESCO codes, we explicitly coupled the elastic channel to low-lying collective states and extracted OMP parameters through χ^2 minimization. The best-fit optical model parameters were obtained for elastic and inelastic angular distribution data. Our elastic and inelastic angular distribution fits show excellent agreement with the experimental data since more than one set of potential parameters can reproduce a given angular distribution data. When the ground state was coupled to the most important inelastic excitation channels the energy dependence of the OMP parameters was reduced. This is most obvious for optical model parameters whose value became almost constant when channel coupling was considered.

Keywords: *Coupled-Channel Reactions; Deuteron; Elastic scattering; Inelastic scattering; Optical model potential parameters; Differential cross section*

PACS: 24.10.Eq, 24.10.Ht, 25.45.De, 24.10.-i

1. INTRODUCTION

The study of nuclear interactions is extremely important, as it provides valuable information about the properties of nuclei. A nuclear interaction occurs when a projectile (particle or nucleus) interacts with a target nucleus. The study of nuclear particle scattering processes, such as deuteron-nucleus scattering, provides important tools for understanding the nature of fundamental nuclear interactions and determining the characteristics of the potential between the projectile and the target nucleus. Nuclei are complex composite particles composed of a large number of constituent particles. This makes constructing microscopic models of deuteron-nucleus interactions a challenging task, further complicated by the fact that we still do not fully understand the nature of interactions between nucleons. The deuteron is an ideal tool for testing the accuracy of theoretical models, and their ability to describe nuclear scattering. It is easily decomposed during the interaction and has a low binding energy (2.2 MeV). This property makes deuteron scattering highly sensitive to inelastic effects such as collective excitations of the target nucleus and channel transitions, making it an ideal probe for testing theoretical nuclear models. Although the scattering process can be complex, one of the fundamental theoretical tools for interpreting deuteron scattering on nuclei is the Optical Model Potential (OMP), which describes the complex interaction between the projectile and the target nucleus through a complex potential. In this approach, the interaction between the deuteron and the target nucleus is represented by a complex potential. This potential divides the reaction flow into a real part representing elastic scattering and an imaginary part representing all competing inelastic channels [12]. It has proven particularly effective in describing experimental data on nuclei.

The main goal of the optical model is to determine potential parameters that reproduce smooth changes in the differential scattering cross section as a function of the incident energy and the nucleon number of the target nucleus. However, the large variation in these potential parameters, such as real and imaginary depth, radius, and slope, with changes in projectile energy or nucleus type [14], represent a persistent challenge in this model and hinders its ability to predict experimental data, suggesting the presence of non-local sources in the nuclear reaction[11, 46].

One of the most important sources of non-locality in the scattering process is the coupling of inelastic excitations to the nuclear ground state during the scattering process [46]. The full effect of collective excitations is included when these channels are explicitly included using the coupled-channel model, which in turn creates a non-local dynamic polarization potential in the elastic channel as an effective component that modifies the actual potential and redistributes the flux. This, in turn, significantly improves the fit to the data and reduces the variation in the potential parameters. However, due to the large number of possible inelastic excitations, this non-locality is usually explained by the coupling of a few significant inelastic channels to the ground state [6], [17]. The dependence of optical model potential parameters on energy is reduced when channel coupling is taken into account [35].

The work of Bäumer *et al.* [2] measured angular distributions for deuteron scattering on ^{12}C, ^{24}Mg, and ^{58}Ni at 170 MeV and analyzed the data using global OM potentials with simple coupled-channels extensions. The work of ref.

Korff *et al.* [25] extended this approach to a broad mass range ($6 \leq A \leq 116$) at intermediate energies (171–183 MeV), employing CC analysis to examine the role of deformation and to adjust optical model parameters accordingly. While these studies demonstrated the relevance of coupling effects, they were limited in energy coverage, coupling schemes, and often relied on potential parameter adjustments to compensate for missing physics. The stability of parameters and the channel inclusion relationship between them have not been systematically studied quantitatively across a wide range of masses and energies. Most available global models for deuteron scattering still rely on parameters that vary with energy and the nucleus without explicitly accounting for inelastic channels.

In this work, we investigate the effectiveness of the coupled-channels analysis of deuteron elastic and inelastic scattering from a representative set of nuclei: ^{6}Li,^{12}C, ^{24}Mg, ^{58}Ni, ^{120}Sn, and ^{208}Pb. The incident deuteron energies span from 9.9 to 270 MeV also this work should give an assessment of the importance of coupling of the inelastic excitations to the ground state and hence might reduce the energy variations of the optical potential parameters with energy, thus improving our understanding of deuteron – nucleus scattering process. Using the FRESCO and SFRESCO codes [36] to solve the Coupled-Channel Schrödinger equation and hence obtain the angular distribution fits to the elastic processes in addition to simultaneous fits to the angular distributions corresponding to the most important inelastic excitations. It is a well-known fact in scattering phenomenology that more than one set of fit potential parameters lead to almost the same fit to the angular distributions data.

This article is structured as follows: Section 2 introduces the theoretical formalism of the coupled-channels method. Section 3 describes the optical model potentials and deformed nuclei. Section 4 presents the main results, including angular distribution comparisons, best-fit potential parameters, and deformation analysis. Section 5 summarizes the conclusions and outlines directions for future work.

2. COUPLED REACTION CHANNELS FORMALISM

Coupled-channel analysis is very important for describing scattering processes. When the projectile interacts with the target, they can scatter elastically, or may lead to excited states exit channels. Alternatively, rearrangement processes may occur. The coupled-channel theory is a method of accounting for inelastic channels, especially those arising from collective excitations. The formalism was first pointed out by Bohr and Mottelson [42], and then was applied by Margolis et. al. and Chase et. al. [7]. In the center-of-mass coordinate system, the total Hamiltonian $\hat{H}$ of the whole system is expressed as:

$$\hat{H} = H_p(\xi_p) + H_t(\xi_t) + \hat{T}(r) + V(r, \xi_p, \xi_t) \tag{1}$$

where r is the radial coordinate from the target to the projectile, $H_p(\xi_p)$ and $H_t(\xi_t)$ are the internal Hamiltonians for projectile and target, respectively, while the ξ_p and ξ_t are the respective internal coordinates of the projectile and target, and $V(r, \xi_p, \xi_t)$ is the interaction potential between the projectile and target, which can be written as [37]:

$$V(r, \xi_p, \xi_t) = V_{\text{diag}}(r) + V_{\text{coupl}}(r, \xi_p, \xi_t), \tag{2}$$

where $V_{\text{diag}}(r)$ is a scaler potential, and $V_{\text{coupl}}(r, \xi_p, \xi_t)$ represents the interaction that couples the initial state to the final state. Further, $\hat{T}(r)$ is the total kinetic energy, which may be written as

$$\hat{T}(r) = -\frac{\hbar^2}{2\mu}\nabla_r^2, \tag{3}$$

where $\mu = \frac{m_p m_t}{m_p + m_t}$ is the reduced mass of the projectile and target, and ∇_r^2 is the Laplacian operator. The time-independent Schrödinger equation for the whole system consisting of a projectile and a target is:

$$\hat{H}\Psi(\vec{r}, \xi_p, \xi_t) = E\Psi(\vec{r}, \xi_p, \xi_t), , \tag{4}$$

where, E is the total energy, and $\Psi(\vec{r}, \xi_p, \xi_t)$ is the wave function of the whole system. We expand $\Psi(\vec{r}, \xi_p, \xi_t)$ in terms of the eigenstates of the total angular momentum $\psi_{J_{\text{tot}}}^{\pi M_{\text{tot}}}(\vec{r}, \xi_p, \xi_t)$ as follows [37]:

$$\Psi(\vec{r}, \xi_p, \xi_t) = \sum_{\pi J_{\text{tot}} M_{\text{tot}}} A_{J_{\text{tot}} M_{\text{tot}}} \psi_{J_{\text{tot}}}^{\pi M_{\text{tot}}}(\vec{r}, \xi_p, \xi_t), \tag{5}$$

For each channel $[(L'S')J', I_{n'}]$, where L' is orbital angular momentum of a given partial wave, S' is projectile's spin for deuteron, $\vec{J}' = \vec{L}' + \vec{S}'$ is the total angular momentum and $I_{n'}$ is the target's spin. We couple J' and $I_{n'}$ to get the total angular momentum $\vec{J}_{tot} = \vec{J}' + \vec{I}_{n'}$ for the whole system. The factors $A_{J_{tot} M_{tot}}$ are amplitudes specifying how much of the total angular momentum state is present. The wave function $\psi_{J_{tot}}^{\pi M_{tot}}(\vec{r}, \xi_p, \xi_t)$ can be expressed as follows:

$$\psi_{J_{tot}}^{\pi M_{tot}}(\vec{r}, \xi_p, \xi_t) = \sum_{n'(L'S')J'I_{n'}} \psi_{n'(L'S')J'I_{n'}}^{\pi J_{tot}}(r) \, \Phi_{(L'S')J'I_{n'}}^{J_{tot}M_{tot}}(\hat{r}, \xi_p, \xi_t),$$

$$= \sum_{n'(L'S')J'I_{n'}} \frac{1}{r} R^{\pi J_{tot}}_{n'(L'S')J'I_{n'}}(r)\, \Phi^{J_{tot}M_{tot}}_{(L'S')J'I_{n'}}(\hat{r},\xi_p,\xi_t). \tag{6}$$

where $\psi^{\pi J_{tot}}_{n'(L'S')J'I_{n'}}(r) = R^{\pi J_{tot}}_{n'(L'S')J'I_{n'}}(r)/r$. The nuclear wave functions are defined as

$$
\begin{aligned}
\Phi^{J_{tot}M_{tot}}_{(L'S')J'I_{n'}}(\hat{r},\xi_p,\xi_t) &= [\mathcal{Y}_{(L'S')J'}(\hat{r},\xi_p) \otimes \phi_{I_{n'}}(\xi_t)]^{M_{tot}}_{J_{tot}} \\
&= \sum_{M_{J'}m_{I_{n'}}} < J'I_{n'}M_{J'}m_{I_{n'}} \mid J_{tot}M_{tot} > \mathcal{Y}_{(L'S')J'M_{J'}}(\hat{r},\xi_p) \\
&\times \phi^{m_{I_{n'}}}_{I_{n'}}(\xi_t),
\end{aligned} \tag{7}
$$

and the spin-angle functions are defined as

$$
\begin{aligned}
\mathcal{Y}_{(L'S')J'M_{J'}}(\hat{r},\xi_p) &= [Y^{M_{L'}}_{L'}(\hat{r}) \otimes \chi^{m_{s'}}_{S'}(\xi_p)]^{M_{J'}}_{J'} \\
&= \sum_{M_{L'}m_{s'}} < L'S'M_{L'}m_{s'} \mid J'M_{J'} > i^{L'} Y^{M_{L'}}_{L'}(\hat{r})\, \chi^{m_{s'}}_{S'}(\xi_p),
\end{aligned} \tag{8}
$$

where, $R^{\pi J_{tot}}_{n'(L'S')I_{n'}}(r)$ are the radial wave functions in the excited state n', and n' corresponds to the n'th state of the target, while $Y^{M_{L'}}_{L'}(\hat{r})$ are the spherical harmonics. The phase factor $i^{L'}$ comes from the spherical Bessel expansion of the incident plane wave. The symbol $\otimes$ denotes vector addition, and $< L'S'M_{L'}m_{s'} \mid J'M_{J'} >$ are Clebsch-Gordon coefficients for coupling $L'M_{L'}$ and $S'm_{s'}$ to intermediate angular momenta $J'M_{J'}$. In addition, $< J'I_{n'}M_{J'}m_{I_{n'}} \mid J_{tot}M_{tot} >$ are the Clebsch-Gordon coefficients for coupling $J'M_{J'}$ and $I_{n'}m_{I_{n'}}$ to a total of angular momentum $J_{tot}M_{tot}$ for the whole system. Further, $\phi^{m_{I_{n'}}}_{I_{n'}}(\xi_t)$ and $\chi^{m_{s'}}_{S'}(\xi_p)$ are the wave functions for target and projectile, respectively, and π is the parity operator of the whole system which can be expressed as:

$$\pi = (-1)^{L'} \pi_{s'} \pi_{I_{n'}}. \tag{9}$$

The nuclear wave function can be written as

$$
\begin{aligned}
\Phi^{J_{tot}M_{tot}}_{(L'S')J'I_{n'}}(\hat{r},\xi_p,\xi_t) &= [Y^{M_{L'}}_{L'}(\hat{r}) \otimes \chi^{m_{s'}}_{S'}(\xi_p) \otimes \phi^{m_{I_{n'}}}_{I_{n'}}(\xi_t)]^{M_{tot}}_{J_{tot}} \\
&= \sum_{M_{J'}m_{I_{n'}}} \sum_{M_{L'}m_{s'}} i^{L'} Y^{M_{L'}}_{L'}(\hat{r})\, \chi^{m_{s'}}_{S'}(\xi_p)\, \phi^{m_{I_{n'}}}_{I_{n'}}(\xi_t) \\
&\times < L'S'M_{L'}m_{s'} \mid J'M_{J'} > < J'I_{n'}M_{J'}m_{I_{n'}} \mid J_{tot}M_{tot} >,,
\end{aligned} \tag{10}
$$

Now, by substituting Eqs. (5), (6), and (10) into Eq. (4) and noting that :

$$
\begin{aligned}
H_p(\xi_p)\, \chi_p(\xi_p) &= E_p\, \chi_p(\xi_p), \\
H_t(\xi_t)\, \phi_t(\xi_t) &= E_t\, \phi_t(\xi_t).
\end{aligned} \tag{11}
$$

Here, E_p and E_t are the eigenenergies for the projectile and the target, respectively. one obtains

$$\sum_{n'J'I_{n'}S'L'} \left[\hat{T}_{n'L'} + V(r,\xi_p,\xi_t) - E_{n'} \right] R^{\pi J_{tot}}_{n'L'S'J'I_{n'}}(r)\, \Phi^{J_{tot}M_{tot}}_{(L'S')J'I_{n'}}(\hat{r},\xi_p,\xi_t) = 0,$$

where

$$\hat{T}_{n'L'} = \frac{\hbar^2}{2\mu_{n'}} \left[-\frac{d^2}{dr^2} + \frac{L'(L'+1)}{r^2} \right], \tag{12}$$

where $E_{n'} = E - E_p - E_t$ is the external energy for a given excited state. Multiplying Eq. (12) by $[\Phi^{J_{tot}M_{tot}}_{(L'S')J'I_{n'}}(\hat{r},\xi_p,\xi_t)]^*$ from the left, and integrating over the internal coordinates except the radial variable r, leads to the following partial wave coupled differential equations: Finally, the coupled partial-wave equations take the form

$$
\begin{aligned}
\left[E_{n_i} - \hat{T}_{n_iL} - V_{(LS)JI_{n_i};(LS)JI_{n_i}}(r) \right] &R^{\pi J_{tot}}_{n_iLSJI_{n_i}}(r) \\
&= \sum_{n'L'S'J'I_{n'}} V_{(LS)JI_{n_i};(L'S')J'I_{n'}}(r) R^{\pi J_{tot}}_{n'L'S'J'I_{n'}}(r).
\end{aligned} \tag{13}
$$

This equation represents a set of n' coupled differential equations for the radial wave functions $R^{\pi J_{tot}}_{n_i LSJI_{n_i}}(r)$ and $R^{\pi J_{tot}}_{n'L'S'J'I_{n'}}(r)$. Furthermore, $V_{(LS)JI_{n_i};(LS)JI_{n_i}}(r)$ is the diagonal optical potential, including both coulomb and nuclear parts, and $V_{(LS)JI_{n_i};(L'S')J'I_{n'}}(r)$ represent the coupling interaction of the initial $(LS)JI_{n_i}$ state to the final $(L'S')J'I_{n'}$ state. Nuclear structure deformations affect the matrix elements on the right-hand side of Eq. (13). For a non-deformed target nucleus, the coupling potential vanishes, and the set of coupled differential equations reduces to that of the Schrödinger equation for a single channel. Deformed nuclei can be described using either the vibrational or rotational models. In this work, we use the optical model and coupled-channel analysis to couple the ground state to collective excited states of the target nucleus. This coupling introduces off-diagonal couplings in the interaction potential matrix, allowing the incident deuteron to induce transitions from the ground state to inelastic states. These coupling potentials, typically derived from nuclear deformation (e.g., using a deformation parameter β_λ), significantly affect observables such as scattering cross sections and resonance structures. As a result, including channel coupling provides a more accurate description of the reaction dynamics.

3. THE OPTICAL POTENTIAL PARAMETERS

The optical model describes the complicated interaction between the projectile and target in terms of a complex potential. This potential divides the reaction flux into a real part, which corresponds to elastic scattering, and an imaginary part, which corresponds to all competing inelastic channels [11]. The aim of the optical model is to find a potential that describes smooth variations of the scattering cross section as a function of incident energy E and target nucleon number A. The general situation of scattering may be quite complicated. However, great simplification may be obtained if one is only interested in the averaged properties, away from resonances and states strongly excited by direct reactions. For deuteron-nucleus scattering, the phenomenological optical potential, $V(r, E)$, can be expressed as [37]

$$
\begin{aligned}
V(r, E) \quad = \quad & -\left(V(E) + iW_v(E)\right)f(r, R_v, a_v) + i4a_s W_s(E)\frac{d}{dr}f(r, R_s, a_s) \\
+ \quad & \left(V_{so} + iW_{so}\right)(\frac{\hbar}{m_\pi c})^2\frac{1}{r}\frac{d}{dr}f(r, R_{so}, a_{so})\vec{L}\cdot\vec{\sigma} + V_{\text{Coul}}(r),
\end{aligned}
\tag{14}
$$

where $V(E)$, V_{so} are the real components of the volume-central and spin-orbit potentials, respectively. In addition, $W_v(E)$, $W_s(E)$, and W_{so} are the imaginary components of volume, surface, and spin orbit potentials, respectively, and $V_v(r)$ is the coulomb potential. E is the energy of the incident particle in the laboratory frame. As for the radial dependence of the potential, the well-known realistic Woods-Saxon form factor is used [24]:

$$
\begin{aligned}
V_v(r) \quad &= \quad V(E)f(r, R_v, a), \\
W_v(r) \quad &= \quad W_v(E)f(r, R_v, a), \\
W_s(r) \quad &= \quad -4a_s W_s(E)\frac{d}{dr}f(r, R_s, a), \\
V_{so}(r) \quad &= \quad V_{so}(\frac{\hbar}{m_\pi c})^2\frac{1}{r}\frac{d}{dr}f(r, R_{so}, a_{so}), \\
W_{so}(r) \quad &= \quad W_{so}(\frac{\hbar}{m_\pi c})^2\frac{1}{r}\frac{d}{dr}f(r, R_{so}, a_{so}),
\end{aligned}
\tag{15}
$$

where m_π is the pion mass. The form factor $f(r, R_i, a_i)$ is the Saxon-Woods shape[41],

$$
f(r, R_i, a_i) = \frac{1}{1 + \exp[(r - R_i)/a_i]}, \qquad i = v, s, so, c
\tag{16}
$$

where, $R_i = r_i A^{\frac{1}{3}}$ is a potential radius, A the mass number of the target, and a_i the diffuseness parameters. For charged projectiles, the Coulomb term $V_{\text{Coul}}(r)$ is usually obtained by approximating the target nucleus as a uniformly charged sphere,

$$
V_{\text{Coul}}(r) = Z_p Z_t e^2 \int \frac{\rho(r_t)}{|\vec{r} - \vec{r}_t|} d\vec{r}_t,
\tag{17}
$$

where $\vec{r}$ is the position of the projectile and $\vec{r}_t$ is that of target nucleus. The quantities Z_p and Z_t are the atomic numbers of the projectile and target, respectively. The term $\rho(r_t)$ gives the charge distribution in the target.

Deformed nuclei, whose surfaces vibrate about an equilibrium shape, are treated using the vibrational model. Here, the dynamic nuclear radius R_i is taken to be a function of the polar angles θ and ϕ according to:

$$
R_i(\theta, \phi) = r_i A^{\frac{1}{3}}\left[1 + \sum_{\lambda \geq 1}^{\infty} \sum_{\mu=-\lambda}^{\mu=\lambda} \alpha_{\lambda\mu} Y_{\lambda\mu}(\theta, \phi)\right],
\tag{18}
$$

where $R_i(\theta, \phi)$ is the distance from the center of the nucleus to a point at its surface subtending polar and azimuthal angles (θ, ϕ). The spherical tensors $\alpha_{\lambda\mu}$ are the spherical harmonics $(Y_{\lambda\mu}(\theta, \phi))$ coefficients. However, some nuclei have permanent deformations about a symmetry axis and are treated using the rotational model. In this case the nuclear radius is expressed in the form:

$$R_i(\theta') = r_i A^{\frac{1}{3}} \left[1 + \sum_{\lambda} \beta_\lambda Y_{\lambda 0}(\theta') \right],$$ (19)

where, θ' is the polar angle in the body - fixed frame and β_λ is the deformation parameter. When the vibrational or rotational models are used, one has to determine which parts of the potential are to be deformed. Since the nuclear force is a short range force the nuclear potential follows the shape of the nucleus. Therefore, it is a common practice to deform the volume term of the potential. Deforming the imaginary surface part, however, is a matter of dispute. This issue has been discussed and arguments were presented in support and also against deforming the imaginary surface part [5]. However, in a later work [16], the authors stated that "to describe the inelastic scattering best, it is found necessary to deform the imaginary (as well as the real) part of the central potential." Furthermore, in Ref. [2] and [25] the authors used an optical model with channel coupling to analyze deuteron induced reactions. All parts of the nuclear potential were deformed except the spin-orbit term. In Ref. [35] we examined the effect of channel coupling on the variation of the potential parameters corresponding to nucleon scattering off light and heavy nuclei. We obtained excellent angular distribution fits for the elastic and inelastic channels by deforming both the real volume and imaginary surface terms. Therefore, in this work, we shall deform the surface imaginary term in addition to the real volume term. We did not deform the spin - orbit term as the effects of its deformation on the calculated differential cross sections were found to be insignificant [21].

4. RESULTS AND DISCUSSION

This section presents a detailed analysis of deuteron elastic and inelastic scattering from ^{6}Li, ^{12}C, ^{24}Mg, ^{58}Ni, ^{120}Sn, and ^{208}Pb nuclei over an incident energy range spanning from 9.9 to 270 MeV. The theoretical framework employed is the coupled-channels (CC) method, implemented using the FRESCO and SFRESCO codes developed by Thompson [36]. These codes allow for systematic inclusion of couplings between the ground and excited states of the target nuclei, facilitating a unified treatment of elastic and inelastic scattering processes within a consistent reaction model. The main goal of this study is to investigate the effect of ground state coupling to inelastic reaction channels on the energy variations of the optical potential parameters. In doing so, we have used the rotational model to analyze the deuteron elastic and inelastic excitation differential cross sections. The optical potential parameters were obtained by fitting the coupled-channels differential cross sections $d\sigma_{n_i n'}(\theta)/d\Omega$, the experimental data for the elastic and inelastic scattering cross sections for light and heavy nuclei were taken from the Experimental Nuclear Reaction Data (EXFOR) and the Computer Index of Nuclear Reaction Data (CINDA) are displayed in Table 1. The coupled channel analysis shows that nuclei become deformed when the potential couples the ground state to the inelastic excited states. In deformed nuclei, the non-diagonal potential couples the ground state to the inelastic excited states. So, the deformation lengths $\delta_\lambda = \beta_\lambda R$ were extracted by fitting the experimental data of the coupled channels differential cross sections for collective excitations. The multipolarity λ of the reaction can be represented as follows: For $\lambda = 2$, we have quadrupole deformations β_2 [30] and [32]. For $\lambda = 3$ we have octupole deformations β_3 [40]. For $\lambda = 5$ we have quintupole deformations β_5. In order to compare the optical potential parameter calculations with the experimental results, we used the automatic search routine of SFRESCO. This program minimizes the chi-squared value χ^2, which is defined as:

$$\chi^2 = \frac{1}{N} \sum_{i=1}^{N} \left(\frac{\left(\frac{d\sigma(\theta_i)}{d\Omega} \right)_{\text{theo}} - \left(\frac{d\sigma(\theta_i)}{d\Omega} \right)_{\text{exp}}}{\Delta \left(\frac{d\sigma(\theta_i)}{d\Omega} \right)} \right)^2,$$ (20)

where N is the number of experimental points, $(\frac{d\sigma(\theta_i)}{d\Omega})_{theo}$ and $(\frac{d\sigma(\theta_i)}{d\Omega})_{exp}$ are the theoretical and experimental differential cross sections at the angle θ_i, and $\Delta(\frac{d\sigma(\theta_i)}{d\Omega})$ is the corresponding experimental error. We now proceed to discuss the results obtained by fitting the experimental elastic and inelastic differential cross sections. For all the nuclei studied in this work, we have considered incident deuteron energies where EXFOR provides the experimental data for the elastic scattering and inelastic excitations. This enables us to study the effect of ground-state coupling to open reaction channels on the energy variation of the optical potential parameters. It is well known that more than one set of optical potential parameters can fit a given experimental dataset.

Table 1. Experimental data for deuteron elastic and inelastic scattering for the nuclei and energies considered in this work were collected from the EXFOR and CINDA databases.

Nucleus	E (MeV)	Ref.
^{6}Li	14.8, 25.0	[10]
	171	[2]
^{12}C	11.8	[51]
	13.7, 15.3, 25.9	[52]
	60.6	[54]
	77.3, 90	[55]
	170	[2]
	200	[56]
	270	[57]
^{24}Mg	9.97, 10.9, 12.1, 15.3, 21	[52]
	60.6	[54]
	77.3, 90	[55]
	170	[2]
^{58}Ni	12, 12.8	[58]
	27.5	[59]
	79.9	[60]
	170	[2]
^{120}Sn	13.6	[10]
	28.6	[52]
	80, 82	[49]
^{208}Pb	86	[57]

Coupling of the Elastic Channel to a Single Excited State in ^{6}Li and ^{12}C

A detailed coupled-channels analysis was performed for deuteron elastic and inelastic scattering from the light ^{6}Li, and ^{12}C nuclei. Light nuclei differ from heavy ones in that their matter distributions are less uniform. They have diffused edges that results in surface effects playing an important role in the scattering processe. In order to test the effect of channel coupling on the energy variation of the optical potential parameters, we begin by coupling the elastic channel to the first excited state. The diagonal and coupling optical potentials given in Eq. (2) were used to fit the elastic and inelastic angular distributions simultaneously. The analysis of the ^{6}Li data was restricted to coupling the 1^+ ground state to the first 3^+ excited state, whose excitation energy is $E_x = 2.186$ MeV. As shown in Fig. 1, the fits for the angular distributions show good agreement with the experimental data for the elastic (1^+) and the first (3^+) excited channels for incident energies of 14.8, 25, and 171 MeV. The corresponding optical potential best fit parameters as a function of incident energy when the elastic and first excited channels are coupled together, are displayed in Table 2. For ^{12}C ,a well-studied nucleus over the energy range 11.8 to 270 MeV, variations in the angular distributions are strongly influenced by coupling to the ground state via collective transitions. We coupled the 0^+ elastic channel to the first 2^+ excited state ($E_x = 4.438$ MeV). The corresponding fits for the elastic 0^+ and inelastic 2^+ differential cross sections show very good agreement with the experimental data as seen in Fig 2. The optical model parameters corresponding to these fits are listed in Tables 3 and 4. In our fitting procedure, we also searched for the best value of the quadrupole deformation parameter β_2 at each incident energy. Assuming all the obtained values to have the same weight, our average value for the quadrupole deformation is $\beta_2 = 1.39$ for ^{6}Li, which is in good agreement with the value β_2=0.89 obtained in Ref. [25]. In addition, our mean value for the quadrupole deformation is β_2=0.73 for ^{12}C, which is in good agreement with the value β_2=0.60 obtained in Ref. [9].

Table 2. The optical potential best fit parameters for ^{6}Li$(d, d)^6$Li* scattering cross sections for the elastic (1^+) and 3^+ excited state. The Coulomb radius was fixed at $r_c = 1.2$ fm.

Parameters	14.8 MeV	25.0 MeV	171.0 MeV
V (MeV)	89.990	70.090	28.600
r (fm)	1.160	0.910	1.400
a (fm)	0.900	0.220	0.900
W_s (MeV)	5.280	2.160	7.690
r_s (fm)	1.400	1.540	1.080
a_s (fm)	0.900	0.890	0.830
V_{so}(MeV)	2.000	4.790	2.288
$r_s o$ (fm)	0.800	1.040	1.420
$a_s o$ (fm)	0.900	0.300	0.900
β_2 (fm)	1.29	2.07	0.786
χ^2	99.200	1.075	189.600
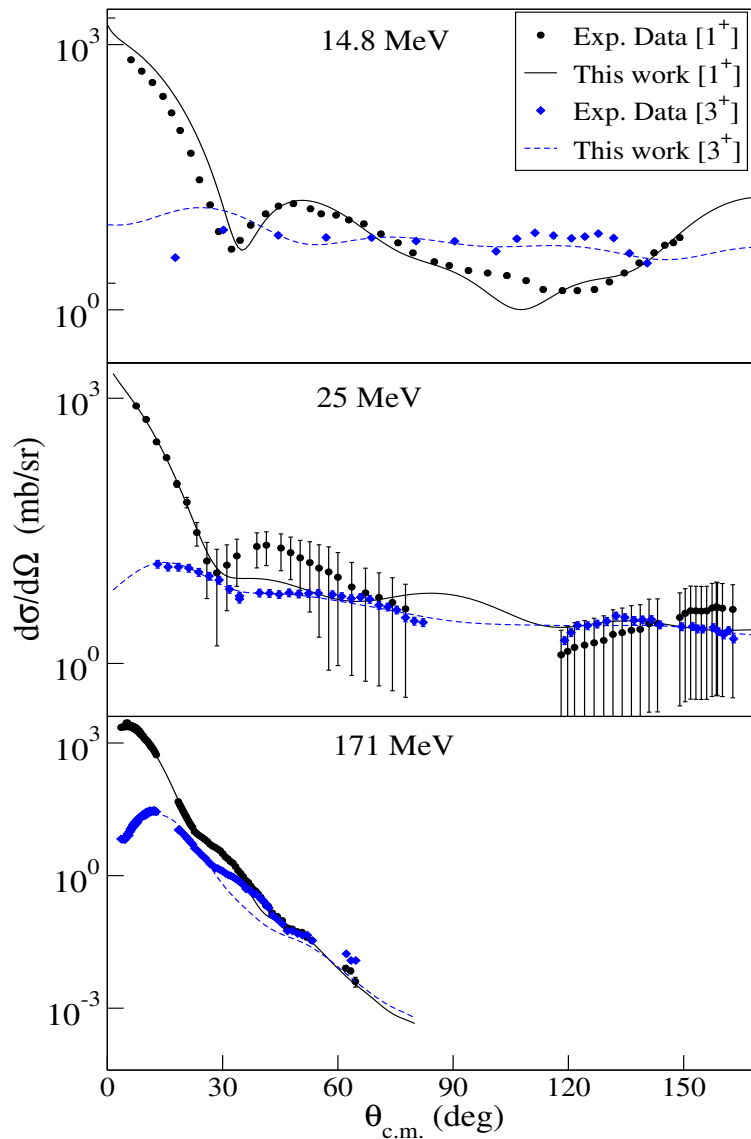
Figure 1. (Color online) Elastic and inelastic best angular distribution fits for deuteron scattering from ^{6}Li.

Table 3. The optical potential best fit parameters for $^{12}C(d,d)^{12}C^*$ scattering cross sections for the elastic (0^+) and (2^+) excited state. The Coulomb radius was fixed at $r_c = 1.2$ fm.

Parameters	11.8 MeV	13.7 MeV	15.3 MeV	25.9 MeV	60.6 MeV
V (MeV)	63.00	62.00	61.9999	54.4645	52.00
r (fm)	0.9956	1.0000	1.0154	1.0562	0.8306
a (fm)	0.8500	0.7958	0.8100	0.7499	0.4137
W_s (MeV)	13.00	12.7351	11.1303	13.00	10.00
r_s (fm)	1.2033	1.2233	1.2343	1.0718	1.0000
a_s (fm)	0.3522	0.3672	0.4029	0.4301	0.5567
V_{so} (MeV)	4.0385	5.1000	3.8314	4.0000	4.5000
r_{so} (fm)	0.9000	0.8152	0.7646	1.0524	0.8855
a_{so} (fm)	0.4512	0.3000	0.3010	0.7000	0.7500
β_2	0.659	0.656	0.606	0.730	0.789
χ^2	10.150	10.049	69.195	69.195	6.194

Table 4. The optical potential best fit parameters for $^{12}C(d,d)^{12}C^*$ scattering cross sections for the elastic (0^+) and (2^+) excited state. The Coulomb radius was fixed at $r_c = 1.2$ fm.

Parameters	77.3 MeV	90.0 MeV	170.0 MeV	200.0 MeV	270.0 MeV
V (MeV)	45.09	40.00	40.00	37.84	31.27
r (fm)	0.800	0.936	0.940	0.900	0.970
a (fm)	0.495	0.850	0.410	0.390	0.440
W_s (MeV)	10.00	18.54	13.00	17.00	16.99
r_s (fm)	0.930	0.904	1.070	1.170	1.109
a_s (fm)	0.714	0.654	0.780	0.710	0.800
V_{so} (MeV)	6.10	4.50	4.03	4.00	4.00
r_{so} (fm)	0.800	0.800	0.840	0.900	0.800
a_{so} (fm)	0.750	0.400	0.800	0.600	0.800
β_2 (fm)	0.966	0.699	0.743	0.776	0.720
χ^2	30.90	49.82	73.45	8.860	6.300

When the elastic channel and the first excited states are coupled together for ^6Li, and ^{12}C, we find that the variations of all OMP parameters are reduced. It is clear from Tables. 2 –4 that the value of V decreased with increasing energy, but its variation is reduced as shown in Fig. (3). In addition, the variations of V for the ^{12}C case are similar to the variations in the ^6Li case as can be seen in Figures (3). The variation in the surface absorption depth W_s is smaller and remains highly stable as a function of incident energy for ^6Li and ^{12}C. Channel coupling has also resulted in the real part of the spin-orbit potential V_{so} being almost constant over the entire energy range around 4.0 MeV for these nuclei. In previous work, Ref. [1]fixed the value of V_{so} at 3.557 MeV, while V_{so} was taken as 3.703 MeV in Ref. [20], 6.0 MeV in Ref. [3]., and 5.5 MeV in Ref. [10]. The variations in the geometric parameters (r, r_s, r_{so}) and (a, a_s, a_{so}) are also highly stable, as shown in Fig. (3). The mean $\bar{\chi^2}$ value for light nuclei is approximately 65 when the elastic channel is coupled with the first excited state.

In what follows, we study the effect of coupled-channel analysis on the energy dependence of the optical potential parameters for heavy nuclei
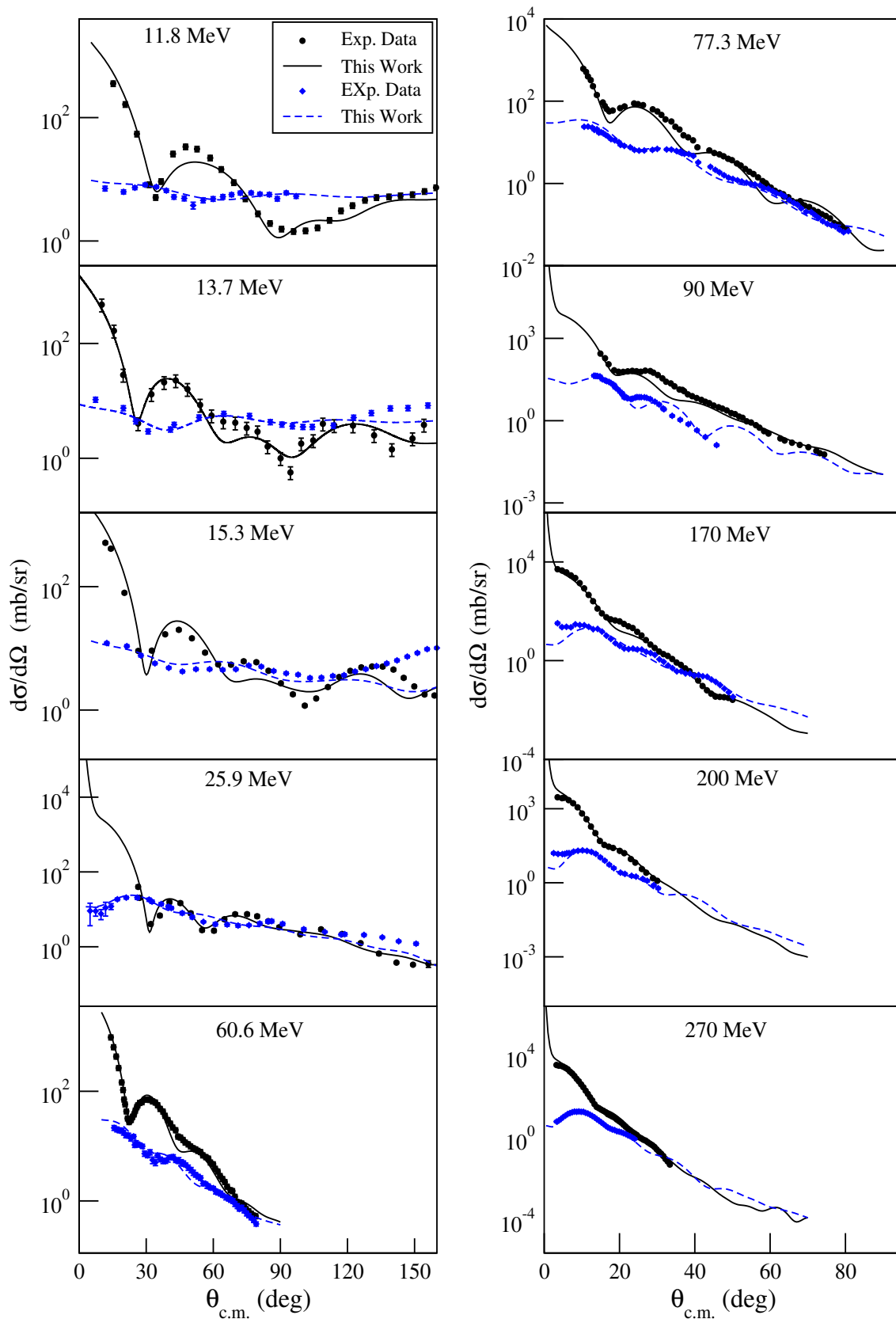
Figure 2. (Color online) Elastic and inelastic best angular distribution fits for deuteron scattering from ^{12}C.
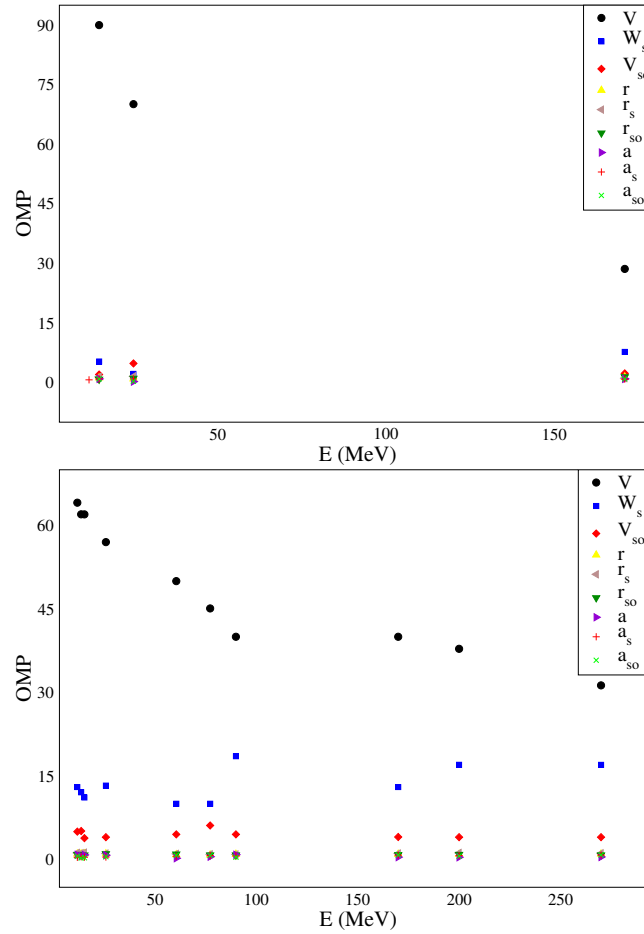
Figure 3. (Color online) The variations of the optical potential depths as a function of incident energy for ^{6}Li (top), ^{12}C (bottom).

Coupling the Ground State of ^{24}Mg, ^{58}Ni, ^{120}Sn, and ^{208}Pb to Collective Excited States

In this section, we investigate the effect of coupled-channels analysis on the optical model parameters for intermediate and heavy nuclei. Heavy nuclei have almost constant matter densities up to large distances away from the nuclear center. Therefore, surface effect, which result in larger energy dependence of the optical potential parameters, are expected to play a reduced role compared to the case of light nuclei. All this is expected to result in more stable optical potential parameters as a function of energy. We present a detailed coupled-channels analysis of deuteron elastic and inelastic scattering on the ^{24}Mg, ^{58}Ni, ^{120}Sn, and ^{208}Pb nuclei over an energy range of 9.9 to 170 MeV. Here, we coupled the 0^+ elastic channel and the first 2^+ excited state corresponding to deuteron scattering from ^{24}Mg, ^{58}Ni, ^{120}Sn, where the respective excitation energies are 1.368 MeV, 1.454 MeV, and 1.171 MeV, respectively. The obtained results for the elastic 0^+ and inelastic 2^+ differential cross sections show excellent agreement with the experimental data as displayed in Figs. (4) to (6). Our fitting procedure also resulted in best-fit for the quadrupole deformation $\beta_2 = 0.64$, $\beta_2 = 0.244$, and $\beta_2 = 0.097$ for coupling the ground state of ^{24}Mg, ^{58}Ni, and ^{120}Sn to the 2^+ excited state, respectively, which are in good agreement with previous work, where the corresponding values of $\beta_2 = 0.605$, $\beta_2 = 0.182$ and $\beta_2 = 0.107$ obtained in Refs. [31].

In the case of ^{208}Pb scattering, we coupled the 0^+ ground state to the 3^- (2.6146 MeV) inelastic excited state at energy 86 MeV for which experimental data are available. The corresponding excellent angular distribution fits are shown in Figure (7). In the coupling between the 0^+ (elastic channel) and first 3^- excited state for the target nucleus ^{208}Pb, an octupole deformation parameter $\beta_3 = 0.11$ was obtained, which is in a good agreement with previous work is $\beta_3 = 0.11$ of [15]. In addition, we shall consider the effect of coupling the ground state to two inelastic channels on the optical potential parameters for ^{208}Pb, when the 0^+ ground state is coupled to the 3^- (2.6146 MeV) and 5^- (3.197 MeV) excited states. In this case, the calculated elastic and inelastic differential cross sections show excellent agreement with experimental data at an incident energies of 86 Mev as shown in Figure (7), and our fitted values are $\beta_3 = 0.11$ for an octupole deformation and $\beta_5 = 0.0563$ for the quintupole deformation. Furthermore, Tables (5) to (9) show the optical potential best fit parameters as a function of incident deuteron energy for the ^{24}Mg to ^{208}Pb target nuclei when the elastic channel and excited states are coupled together. Similar to the case of light nuclei, when the ground state is coupled to the first excited state the energy variations of optical potential parameters are reduced.

Table 5. The optical potential best fit parameters for ^{24}Mg$(d, d)^{24}$Mg* scattering cross sections for the elastic (0^+) and (2^+) excited state. The Coulomb radius was fixed at $r_c = 1.2$ fm.

Parameters	9.97 MeV	10.87 MeV	12.10 MeV	15.30 MeV	21.00 MeV
V (MeV)	73.000	71.545	65.753	66.000	54.216
r (fm)	1.0000	1.0000	1.0281	1.0255	1.0000
a (fm)	0.7712	0.7034	0.5959	0.7163	0.6584
W_s (MeV)	16.000	16.000	16.000	16.000	13.000
r_s (fm)	1.2023	1.1508	1.0765	1.1163	0.9354
a_s (fm)	0.4403	0.4334	0.4721	0.4511	0.6261
V_{so} (MeV)	5.7434	5.0000	5.0000	7.2000	5.0000
r_{so} (fm)	0.9095	0.9000	0.9000	0.9000	0.9870
a_{so} (fm)	0.3000	0.3629	0.3041	0.3624	0.7500
β_2	0.520	0.520	0.506	0.507	0.520
χ^2	4.958	10.127	20.257	150	7.128

Table 6. The optical potential best fit parameters for ^{24}Mg$(d, d)^{24}$Mg* scattering cross sections for the elastic (0^+) and (2^+) excited state. The Coulomb radius was fixed at $r_c = 1.2$ fm.

Parameters	60.6 MeV	77.3 MeV	90.0 MeV	170.0 MeV
V (MeV)	61.999	55.000	53.120	32.384
r (fm)	0.874	0.900	1.000	0.912
a (fm)	0.778	0.494	0.800	0.576
W_s (MeV)	14.632	16.000	15.000	13.836
r_s (fm)	0.928	0.935	0.900	1.027
a_s (fm)	0.614	0.669	0.800	0.763
V_{so} (MeV)	4.000	4.000	4.000	3.092
r_{so} (fm)	0.800	0.800	0.800	0.879
a_{so} (fm)	0.500	0.400	0.800	0.600
β_2 (fm)	0.764	0.805	0.693	0.950
χ^2	12.478	26.833	19.562	128.475

Table 7. The optical potential best fit parameters for ^{58}Ni$(d, d)^{58}$Ni* scattering cross sections for the elastic (0^+) and (2^+) excited state. The Coulomb radius was fixed at $r_c = 1.2$ fm.

Parameters	11.8 MeV	13.6 MeV	27.5 MeV	80.0 MeV	170.0 MeV
V (MeV)	83.000	74.591	78.000	59.999	47.783
r (fm)	1.100	1.196	0.950	1.017	0.916
a (fm)	0.747	0.748	0.780	0.585	0.549
W_s (MeV)	15.000	14.990	15.430	12.000	15.000
r_s (fm)	1.220	1.369	1.060	0.913	1.010
a_s (fm)	0.690	0.666	0.630	0.727	0.749
V_{so} (MeV)	6.000	5.555	4.000	4.913	3.000
r_{so} (fm)	1.100	1.265	1.130	0.906	0.921
a_{so} (fm)	0.700	0.300	0.300	0.205	0.700
β_2 (fm)	0.282	0.222	0.293	0.166	0.257
χ^2	8.448	7.455	4.990	3.865	42.151
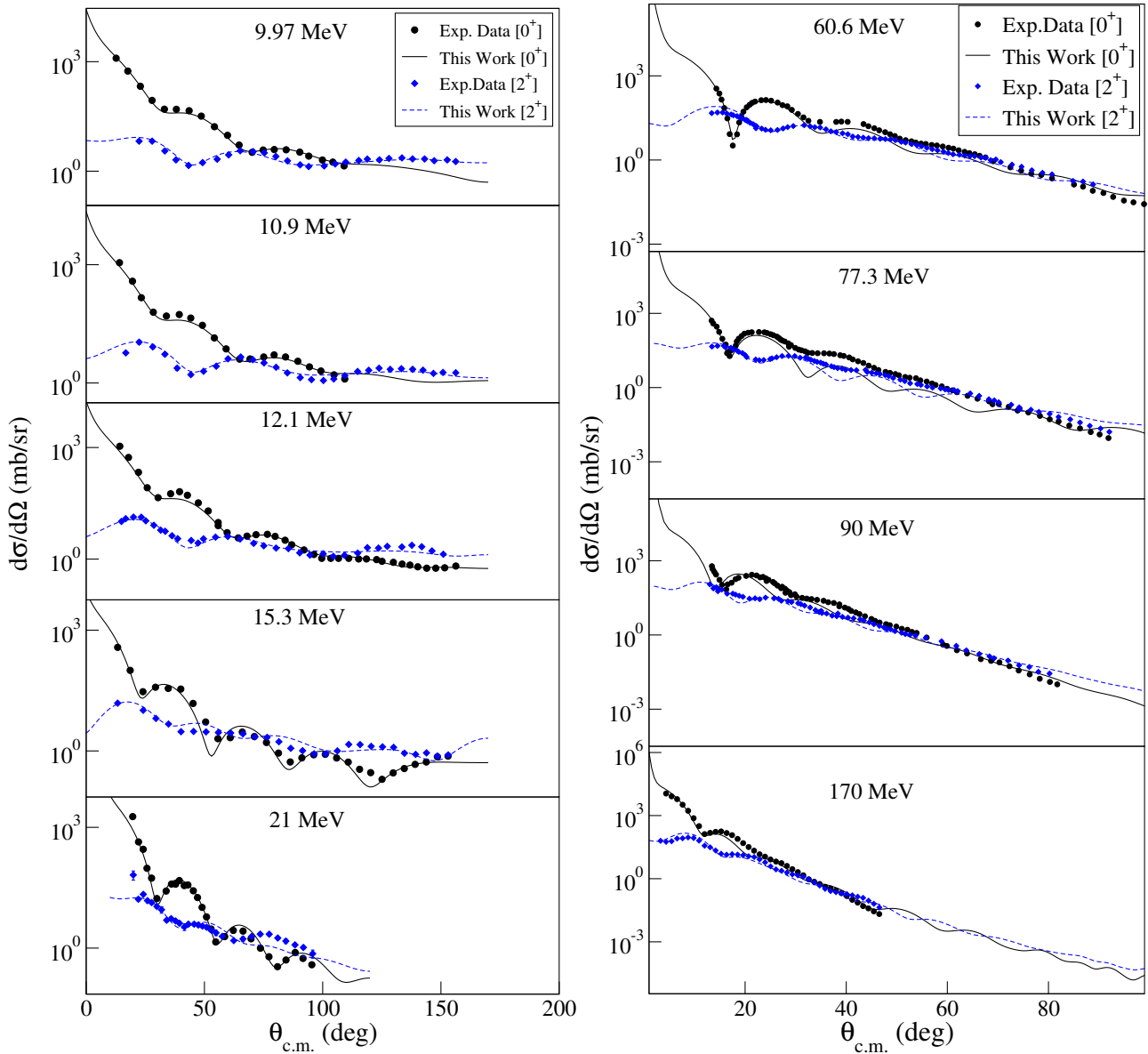
Figure 4. (Color online) Comparison between experimental angular distributions and results of OMP calculations with coupled channles computations for deuteron elastic and inelastic scattering from ^{24}Mg.

Table 8. The optical potential best fit parameters for ^{120}Sn$(d, d)^{120}$Sn* scattering cross sections for the elastic (0^+) and (2^+) excited state. The Coulomb radius was fixed at $r_c = 1.2$ fm.

Parameters	13.6 MeV	28.6 MeV	82.0 MeV
V(MeV)	68.09	69.11	60.00
r(fm)	1.160	1.140	1.460
a(fm)	0.540	0.220	0.440
W_s(MeV)	13.00	7.64	15.21
r_s (fm)	0.900	1.230	1.200
a_s (fm)	0.860	0.810	0.630
V_{so}(MeV)	4.37	6.00	4.27
r_{so} (fm)	1.210	1.240	1.260
a_{so} (fm)	0.300	0.300	0.400
β_2 (fm)	0.161	0.089	0.042
χ^2	3.530	16.90	22.40
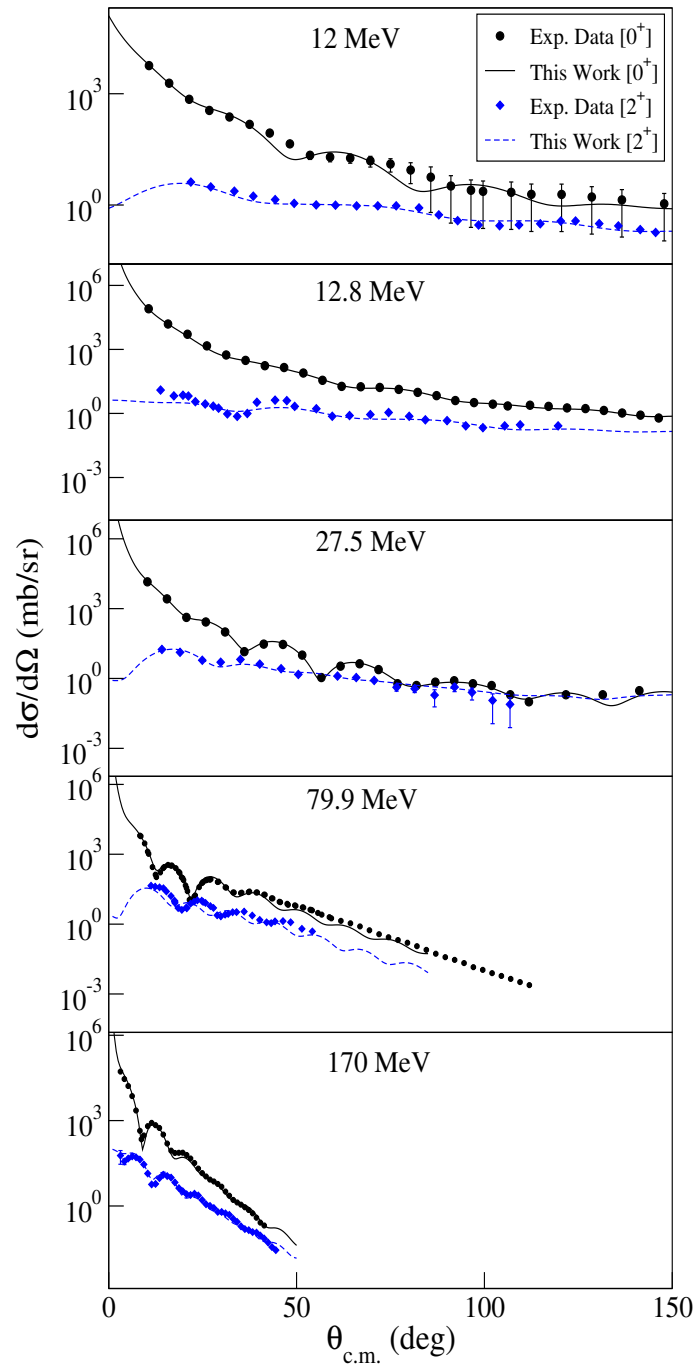
Figure 5. (Color online) Elastic and inelastic best angular distribution fits for deuteron scattering from ^{58}Ni.

Table 10. Theoretical predictions of deformation parameters compared to previous works. Where the values previous works are given in [a [9], b [38], c [31], d [19], e [15], f [39]].

Def.Parameter	Target nucleus					
	^{6}Li	^{12}C	^{24}Mg	^{58}Ni	^{120}Sn	^{208}Pb
β_2		0.582^a	0.600^c	0.182^d	0.107^d	
	1.39	0.73	0.64	0.24	0.097	
β_3						0.110^e
						0.11
β_5						0.056
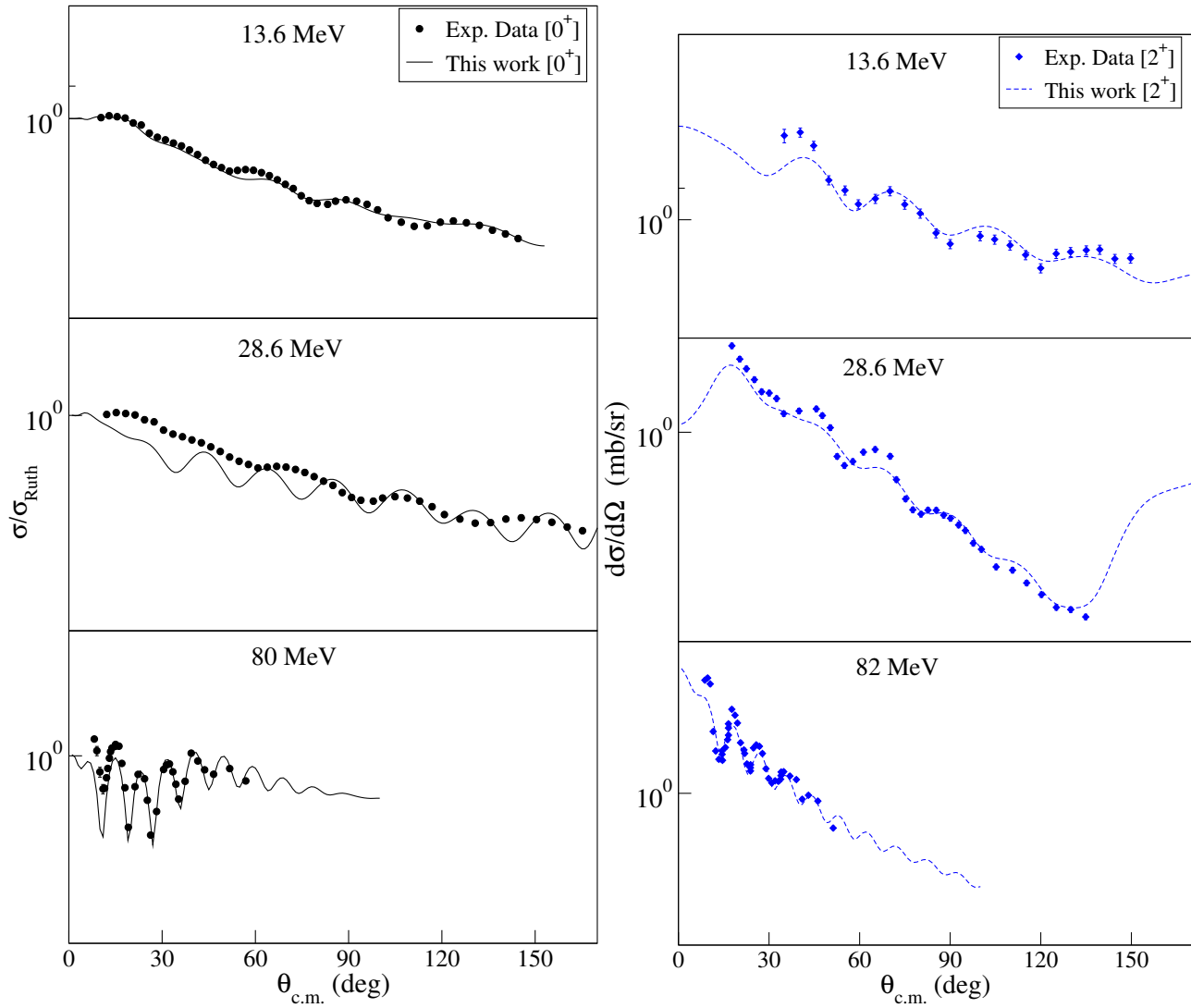
Figure 6. (Color online) Comparison between experimental angular distributions and results of OMP calculations with coupled channles computations for deuteron elastic and inelastic scattering from ^{120}Sn.

Table 9. The optical potential best fit parameters for ^{208}Pb$(d, d)^{208}$Pb* scattering cross sections for the elastic (0^+) and $(3^-, 5^-)$ excited state. The Coulomb radius was fixed at $r_c = 1.2$ fm.

Parameters	Coupling $(0^+, 3^-, 5^-)$ 86.0 MeV	Coupling $(0^+, 3^-)$ 86.0 MeV
V(MeV)	37.34	35.86
r(fm)	1.09	1.12
a(fm)	0.80	0.80
W_s(MeV)	15.99	16.0
r_s (fm)	0.99	1.05
a_s (fm)	0.89	0.77
V_{so}(MeV)	4.0	4.0
r_{so}(fm)	0.98	1.08
a_{so}(fm)	0.64	0.30
β_3(fm)	0.103	0.099
β_5(fm)	0.018	-
χ^2	6.6	4.08
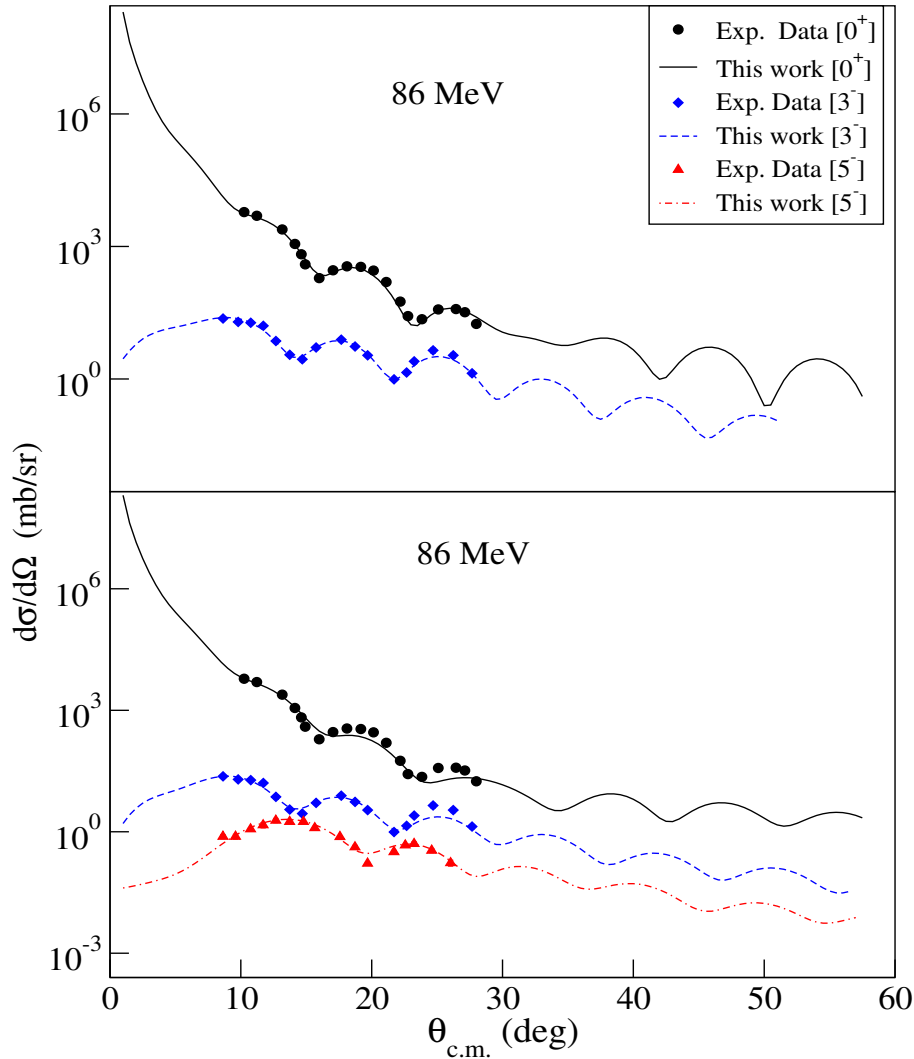
Figure 7. (Color online) Elastic and inelastic best angular distribution fits for deuteron scattering from ^{208}Pb.

Clearly, for all the considered nuclei, we found that the variations in the optical potential parameters with incident energy are reduced. Coupling the 0^+ elastic channel with the first excited state in ^{24}Mg ^{58}Ni, and ^{120}Sn the variations in the real part of the central potential V are smaller, and its value decreased with increased incident energy, as expected. In addition, it can be noted that the behavior of the surface absorption term W_s remains more stable as a function of incident energy for the ^{24}Mg, ^{58}Ni, ^{120}Sn nuclei, as shown in Figs. 8. The real part of the spin-orbit depth (V_{so}) remains highly stable when channel coupling is taken into account. The results of this work yield $V_{so} \approx 4.0$ MeV, as shown in Figs. 8 for heavy nuclei.

Previous works have reported $V_{so} \approx 3.557$ MeV [1], 3.703 MeV [20], and 6.0 MeV [3], and 5.5 MeV in Ref.[10]. The geometric parameters (r, r_s, r_{so}) and (a, a_s, a_{so}) are more stable. For heavy nuclei, our mean value of χ^2 is 18.3. The elastic and inelastic angular distribution fits for the heavy nuclei are better than those for the light nuclei.

Now, to evaluate the improvements achieved in the present coupled-channels (CC) analysis, we perform a detailed comparison with the benchmark study by Bäumer et al. [2], which reported angular distributions for deuteron elastic and inelastic scattering from ^{12}C, ^{24}Mg, and ^{58}Ni at an incident energy of $E_d = 170$ MeV. Their analysis was based on global optical model potentials developed by Daehnick et al. [10] and Bojowald et al. [3]. The superiority of the present approach is reflected in the reduced chi-squared (χ^2) values, which provide a quantitative measure of the fit quality. At $E_d = 170$ MeV, we achieved the following improvements:

- ^{12}C: χ^2 reduced from approximately 600 (using DC/BC fits) to 76,

- ^{24}Mg: χ^2 reduced from around 700 to 128,

- ^{58}Ni: χ^2 decreased from nearly 100 to 42.
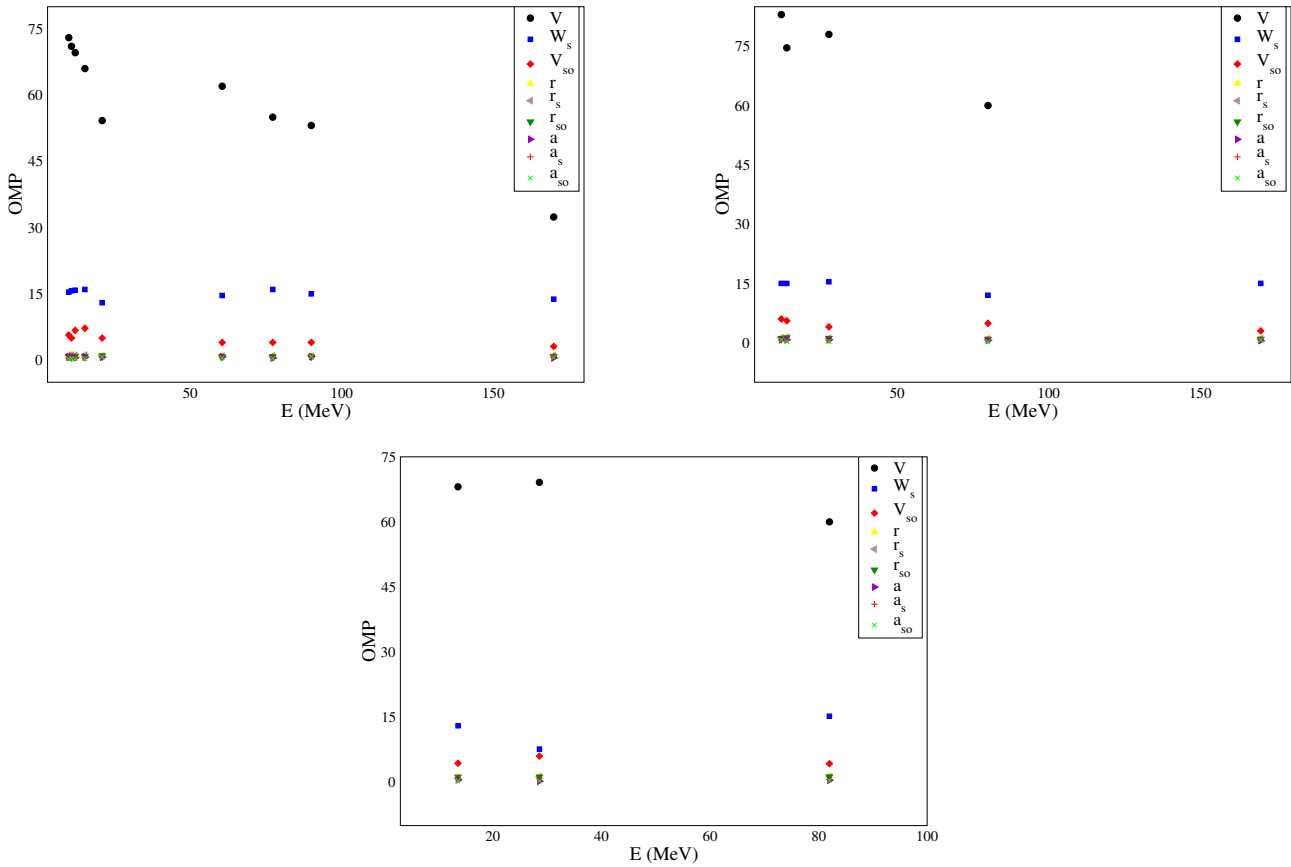
Figure 8. (Color online) The variations of the optical potential depths as a function of incident energy for ^{24}Mg (left), ^{58}Ni (right), and ^{120}Sn (bottom).
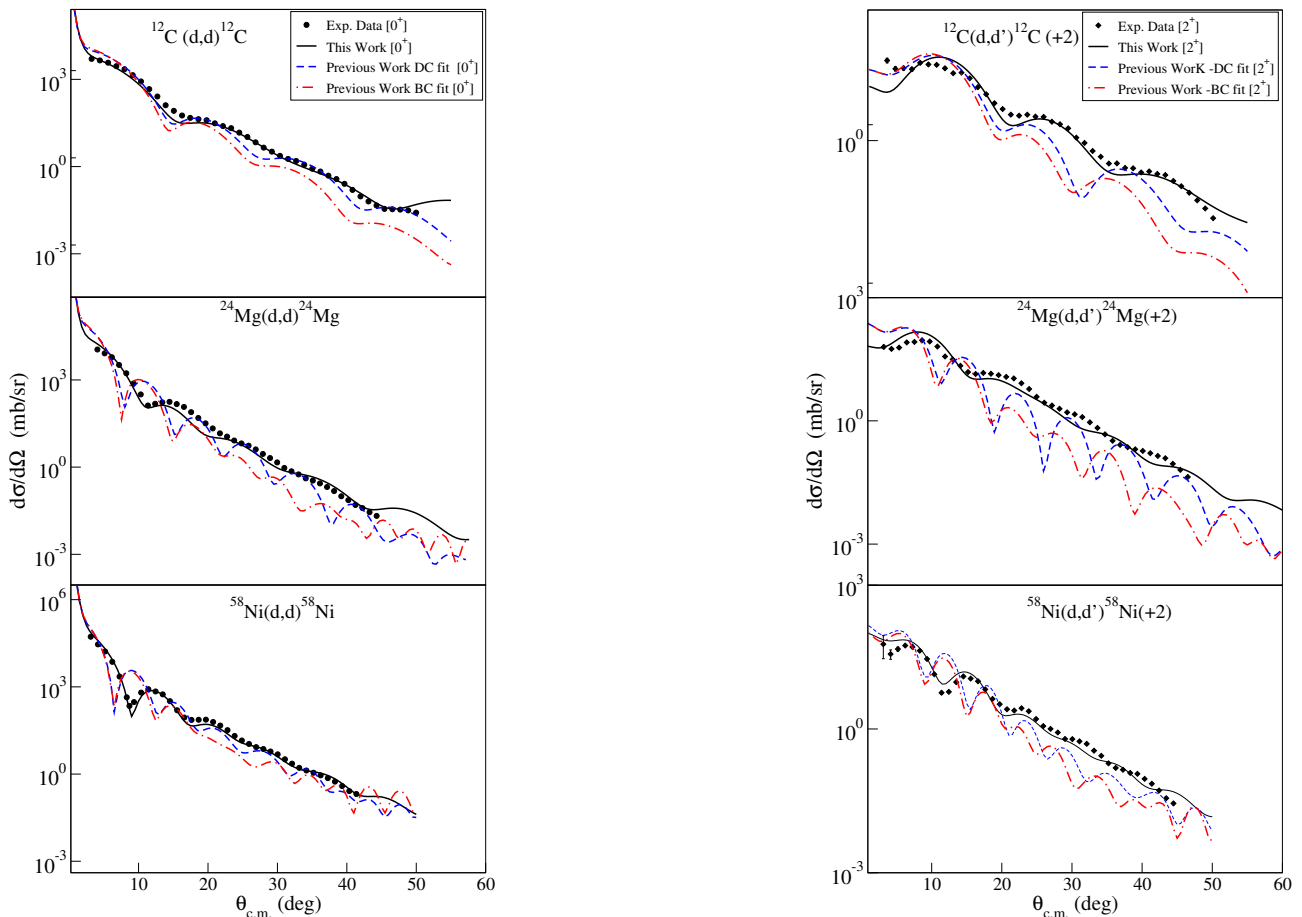
Figure 9. (Color online) Coupled channels analysis of deuteron elastic (0^+) and inelastic (2^+) scattering on ^{12}C, ^{24}Mg, and ^{58}Ni at $E_d = 170$ MeV. Present results (black) are compared with previous DC (blue) and BC (red) fits. The improved agreement with experiment highlights the strength of the current coupled channels approach.

5. CONCLUSIONS

In this work, we employed the coupled-channels analysis to study the deuteron-nucleus elastic and inelastic scattering processes corresponding to light and heavy nuclei in the atomic mass region from ^{6}Li to ^{208}Pb and incident energies ranging from 9.9 to 270 MeV range. The FRESCO code was used to solve the coupled partial-wave equations for a rotational nucleus. Best optical potential fit parameters were obtained for the elastic angular distribution data, in addition to simultaneous fits to the angular distributions corresponding to the most important inelastic excitations.

For light nuclei, when the elastic channel was coupled to inelastic excitations, the angular distribution fits were in excellent agreement with the experimental data as shown in Figs. (1) and (2). The variations in optical potential parameters with energy are reduced, the optical potential fit parameters for ^{6}Li and ^{12}C show lower variations with incident energy in the elastic and inelastic scattering cases.

For heavy nuclei, when coupling the ground state with the most important inelastic excitation channels the differential cross-section fits were in excellent agreement with the experimental data for the ^{24}Mg, ^{58}Ni, ^{120}Sn, and ^{208}Pb nuclei, as shown in Figures (4) to (7). We found that the optical potential fit parameters for heavy nuclei exhibit reduced variations with incident energy as shown in Tables (5) to (9). The potential parameters show smaller energy dependence in the elastic and inelastic scattering.

The main goal of our study has been to test the effect of coupled-channels analysis on the energy variation of the optical potential parameters. We found that the variations of the parameters for light and heavy nuclei are reduced when coupling is taken into account as shown in Figures (3) and (8) for the light and heavy nuclei, respectively. Therefore, we stress the following conclusions:

- The real central potential V decreases with increasing incident energy, when inelastic excitations are taken into account.

- The energy variations of the surface absorption depth W_s are more stable for the channel coupling scheme. This is so, since the imaginary part is responsible for the removal of particles from the elastic channel. Coupled channel analysis takes into account part of the removed flux explicitly. Therefore, the strength W_s of the absorption term naturally decreases.

- The real part of the spin-orbit potential V_{so} is almost constant as a function of incident energy for the light and heavy nuclei. We found that the value of V_{so} is around 4.0 MeV when the elastic channel is coupled to inelastic open excitations.

  In previous studies, the value of V_{so} was fixed at 3.55 MeV [1], V_{so} = 3.703 [20], V_{so} = 6.0 [3], and V_{so}=5.5 [10].

- The variations of the geometric parameters are highly stable when channel coupling is taken into account.

  The results demonstrate that the inclusion of inelastic couplings to collective excited states significantly improves both the physical realism and statistical quality of the fits. For example, at E_d = 170 MeV, the reduced chi-squared values for ^{12}C, ^{24}Mg, and ^{58}Ni were reduced from 600, 700, and 100, respectively, in global optical model fits to 76, 128, and 42 using our fully coupled approach. These improvements were observed not only in the forward-angle region but also in the backward-angle domain, where collective effects and interference patterns are most pronounced.

Finally, compared with previous studies, particularly the widely cited work by Bäumer et al., our approach shows clear improvements. While Bäumer's fits using global optical models and minimal coupling captured general angular trends, they suffered from large χ^2 values and poor agreement at large scattering angles. In contrast, our CC analysis with structure-informed deformation parameters and fully optimized optical potentials, yields significantly better agreement with data and enhanced physical interpretability.

In summary, the channel coupling analysis has been shown to reduce the variations of the optical parameters with energy.

ORCID

 Waleed Saleh Alrayashi, https://orcid.org/0009-0009-6440-8332

REFERENCES

[1] H. An, and C. Cai, Phys. Rev. C, **73**, 054605 (2006). https://doi.org/10.1103/PhysRevC.73.054605

[2] C. Bäumer, *et al.*, Phys. Rev. C, **63**, 037601 (2001). https://doi.org/10.1103/PhysRevC.63.037601

[3] J. Bojowald, *et al.*, Phys. Rev. C, **38**, 1153 (1988). https://doi.org/10.1103/PhysRevC.38.1153

[4] A. Bonaccorso, and R.J. Charity, Phys. Rev. C, **89**, 024619 (2014). https://doi.org/10.1103/PhysRevC.89.024619

Coupled-Channels Analysis and Optical Model Potential Extraction for Deuteron...

67

EEJP. 3 (2025)

[5] B. Buck, Phys. Rev. **130**, 712 (1963). https://doi.org/10.1103/PhysRev.130.712

[6] E. Cereda, *et al.*, Phys. Rev. C, **26**, 1941 (1982). https://doi.org/10.1103/PhysRevC.26.1941

[7] D.M. Chase, L. Wilets, and A.R. Edmonds, Phys. Rev. **110**, 1080 (1958). https://doi.org/10.1103/PhysRev.110.1080

[8] S. Chiba, *et al.*, J. Nucl. Sci. Technol. **44**, 838 (2007). https://doi.org/10.1080/18811248.2007.9711356

[9] S. Cwiok, *et al.*, Comput. Phys. Commun. **46**, 379 (1987). https://doi.org/10.1016/0010-4655(87)90093-2

[10] W.W. Daehnick, J.D. Childs, and Z. Vrcelj, Phys. Rev. C, **21**, 2253 (1980). https://doi.org/10.1103/PhysRevC.21.2253

[11] H. Feshbach, Ann. Phys. **5**, 357 (1958). https://doi.org/10.1016/0003-4916(58)90007-1

[12] H. Feshbach, C.E. Porter, and V.F. Weisskopf, Phys. Rev. **96**, 448 (1954). https://doi.org/10.1103/PhysRev.96.448

[13] R.W. Finlay, *et al.*, Phys. Rev. C, **30**, 796 (1984). https://doi.org/10.1103/PhysRevC.30.796

[14] P. Fraser, *et al.*, Eur. Phys. J. A, **35**, 69 (2008). https://doi.org/10.1140/epja/i2007-10524-1

[15] M.P. Fricke, and G.R. Satchler, Phys. Rev. **139**, B567 (1965). https://doi.org/10.1103/PhysRev.139.B567

[16] M.P. Fricke, *et al.*, Phys. Rev. **156**, 1207 (1967). https://doi.org/10.1103/PhysRev.156.1207

[17] G.H. Rawitscher, Nucl. Phys. A, **475**, 519 (1987). https://doi.org/10.1016/0375-9474(87)90076-5

[18] L.J.B. Goldfarb, Nucl. Phys. **7**, 622 (1958). https://doi.org/10.1016/0029-5582(58)90105-1

[19] L. Grodzins, Phys. Lett. **2**, 88 (1962). https://doi.org/10.1016/0031-9163(62)90138-0

[20] Y. Han, Y. Shi, and Q. Shen, Phys. Rev. C, **74**, 044615 (2006). https://doi.org/10.1103/PhysRevC.74.044615

[21] G. Haouat, *et al.*, Phys. Rev. C, **30**, 1795 (1984). https://doi.org/10.1103/PhysRevC.30.1795

[22] I.N. Ghabar, and M.I. Jaghoub, Phys. Rev. C, **91**, 064308 (2015). https://doi.org/10.1103/PhysRevC.91.064308

[23] M.I. Jaghoub, *et al.*, Can. J. Phys. **100**, 309 (2022). https://doi.org/10.1139/cjp-2021-0380

[24] A.J. Koning, and J.P. Delaroche, Nucl. Phys. A, **713**, 231 (2003). https://doi.org/10.1016/S0375-9474(02)01321-0

[25] A. Korff, *et al.*, Phys. Rev. C, **70**, 067601 (2004). https://doi.org/10.1103/PhysRevC.70.067601

[26] M.I. Jaghoub, A.E. Lovell, and F.M. Nunes, Phys. Rev. C, **98**, 024609 (2018). https://doi.org/10.1103/PhysRevC.98.024609

[27] M.I. Jaghoub, and G.H. Rawitscher, Phys. Rev. C, **84**, 034618 (2011). https://doi.org/10.1103/PhysRevC.84.034618

[28] M.I. Jaghoub, and G.H. Rawitscher, Phys. Rev. C, **85**, 024608 (2012). https://doi.org/10.1103/PhysRevC.85.024608

[29] F. Perey, and B. Buck, Nucl. Phys. **32**, 353 (1962). https://doi.org/10.1016/0029-5582(62)90270-0

[30] S. Raman, C.W. Nestor Jr., and P. Tikkanen, At. Data Nucl. Data Tables **78**, 1 (2001). https://doi.org/10.1006/adnd.2001.0858

[31] S. Raman, *et al.*, Phys. Rev. C, **43**, 556 (1991). https://doi.org/10.1103/PhysRevC.43.556

[32] S. Raman, and C.W. Nestor Jr., Phys. Rev. C, **37**, 805 (1988). https://doi.org/10.1103/PhysRevC.37.805

[33] G.H. Rawitscher, and D. Lukaszek, Phys. Rev. C, **69**, 044608 (2004). https://doi.org/10.1103/PhysRevC.69.044608

[34] S. Alameer, M.I. Jaghoub, and I. Ghabar, J. Phys. G: Nucl. Part. Phys. **49**, 015106 (2022). https://doi.org/10.1088/1361-6471/ac3e3b

[35] W.S. Al-Rayashi, and M.I. Jaghoub, Phys. Rev. C, **93**, 064311 (2016). https://doi.org/10.1103/PhysRevC.93.064311

[36] I.J. Thompson, Comput. Phys. Rep. **7**, 167 (1988). https://doi.org/10.1016/0167-7977(88)90005-2

[37] T. Tamura, Rev. Mod. Phys. **37**, 679 (1965). https://doi.org/10.1103/RevModPhys.37.679

[38] V.M. Strutinsky, Nucl. Phys. A, **95**, 420 (1967). https://doi.org/10.1016/0375-9474(67)90510-6

[39] G.M. Crawley, and G.T. Garvey, Phys. Rev. **160**, 981 (1967). https://doi.org/10.1103/PhysRev.160.981

[40] R.H. Spear, Phys. Rep. **73**, 369 (1981). https://doi.org/10.1016/0370-1573(81)90059-4

[41] D. Woods, and D.S. Saxon, Diffuse Surface Optical Model for Nucleon-Nuclei Scattering, Phys. Rev. **95**, 577 (1954). https://doi.org/10.1103/PhysRev.95.577

[42] A. Bohr, and B.R. Mottelson, *Kgl. Danske Videnskab. Selskab, Mat. Fys. Medd.* **27**, No. 16 (1953).

[43] A. Bohr, and B.R. Mottelson, *Nuclear Structure*, Vol. I (W. A. Benjamin, New York, 1969).

[44] I.J. Thompson, and F.M. Nunes, *Nuclear Reactions for Astrophysics* (Cambridge University Press, Cambridge, 2009).

[45] A.S. Green, *The Nuclear Independent Particle Model: The Shell and Optical Models* (Academic Press, New York, 1968).

[46] H. Feshbach, *Theoretical Nuclear Physics: Nuclear Reactions* (John Wiley and Sons, 1982).

[47] J.M. Eisenberg, and W. Greiner, *Nuclear Models, Vol. I* (North-Holland, Amsterdam, 1970).

[48] A.J. Koning, S. Hilaire, and M. Duijvestijn, in *Proc. Int. Conf. Nucl. Data for Science and Technology*, Nice, France, 2007 (EDP Sciences, 2008), p. 211. https://doi.org/10.1051/ndata:07767

[49] EXFOR — Experimental Nuclear Reaction Data, IAEA. https://www-nds.iaea.org/exfor/

[50] CINDA — Computer Index of Nuclear Reaction Data, IAEA. https://www-nds.iaea.org/exfor/cinda.htm

[51] R.L. Walter, and R.M. Drisko, Phys. Rev. **124**, 832 (1961). https://doi.org/10.1103/PhysRev.124.832

[52] S.M. Smith, and D.A. Goldberg, Phys. Rev. **129**, 2690 (1963). https://doi.org/10.1103/PhysRev.129.2690

[53] D.A. Goldberg, and S.M. Smith, Phys. Rev. **129**, 2683 (1963). https://doi.org/10.1103/PhysRev.129.2683

[54] Y. Sakuragi, M. Yahiro, and M. Kamimura, Phys. Rev. C, **35**, 2161 (1987). https://doi.org/10.1103/PhysRevC.35.2161

[55] O. Aspelund, J.S. Lilley, and J.D. Hemingway, Nucl. Phys. A, **253**, 263 (1975). https://doi.org/10.1016/0375-9474(75)90263-5

[56] Y. Satou, *et al.*, Phys. Rev. C, **65**, 054602 (2002). https://doi.org/10.1103/PhysRevC.65.054602

[57] Y. Satou, *et al.*, Phys. Lett. B, **549**, 307 (2002). https://doi.org/10.1016/S0370-2693(02)02957-X

[58] M. Beiner, *et al.*, Nucl. Phys. A, **238**, 29 (1975). https://doi.org/10.1016/0375-9474(75)90378-7

[59] S. Hinds, *et al.*, Nucl. Phys. A, **113**, 314 (1968). https://doi.org/10.1016/0375-9474(68)90574-0

[60] M.A. Franey, R.L. Boudrie, and B.D. Anderson, Phys. Rev. C, **29**, 1118 (1984). https://doi.org/10.1103/PhysRevC.29.1118

АНАЛІЗ ЗВ'ЯЗАНИХ КАНАЛІВ ТА ВИЛУЧЕННЯ ПОТЕНЦІАЛУ ОПТИЧНОЇ МОДЕЛІ ДЛЯ РОЗСІЮВАННЯ ДЕЙТРОНІВ ВІД ^{6}Li ДО ^{208}Pb

Валід Салех Альраяші
Кафедра науки, факультет освіти, Університет Сани, Сана, Ємен

Пружне та непружне розсіювання дейтрон-ядро від ^{6}Li до ^{208}Pb було досліджено для енергій падіння від 9,9 до 270 МеВ. Головною метою цієї роботи є вивчення впливу зв'язку основного стану ядра з непружними каналами збудження на енергетичну залежність параметрів оптичного модельного потенціалу (ОМП). Використовуючи коди FRESCO та SFRESCO, ми явно пов'язали пружний канал з низько розташованими колективними станами та вилучили параметри ОМП шляхом мінімізації χ^2. Найкращі параметри оптичної моделі були отримані для даних пружного та непружного кутового розподілу. Наші апроксимації кутового розподілу пружності та непружності демонструють чудову відповідність з експериментальними даними, оскільки більше одного набору параметрів потенціалу може відтворити задані дані кутового розподілу. Коли основний стан був пов'язаний з найважливішими непружними каналами збудження, енергетична залежність параметрів ОМП зменшилася. Це найбільш очевидно для параметрів оптичної моделі, значення яких стало майже постійним, коли розглядався зв'язок каналів.

Ключові слова: *реакції зв'язаних каналів; дейтрон; пружне розсіювання; непружне розсіювання; параметри потенціалу оптичної моделі; диференціальний поперечний переріз*

EVENT FRACTIONS AND PROBABILITIES FOR ^{11}Be + ^{209}Bi REACTION IN THE MULTIBODY 3-STAGE CLASSICAL MOLECULAR DYNAMICS APPROACH

Vipul B. Katariya[a*], **Subodh S. Godre**[a], **Pinank H. Jariwala**[b]

^{a}*Veer Narmad South Gujarat University, Surat - 395007, INDIA*
^{b}*Department of Physics, Navyug Science College, Surat - 395009, INDIA*
**Corresponding Author e-mail: vipulkatariya5611@gmail.com*

Unique structures that differ radically from ordinary nuclear matter have been demonstrated by Halo nuclei. Among other halo nuclei, the ^{11}Be nucleus is one of the most studied halo nuclei, and it has a well-established one-neutron halo structure with neutron separation energy $S_n = 0.501$ MeV. We have studied ^{11}Be + ^{209}Bi reaction in the multibody 3-Stage Classical Molecular Dynamics (3S-CMD) model, where ^{11}Be is constructed as a cluster of tightly bound ^{10}Be and one neutron. The separation between ^{10}Be and neutron is adjusted to set the ion-ion potential between them equal to the experimental neutron separation energy. For this reaction, we have calculated fractions of events $F(b)$ for given impact parameter, b and collision energy E_{CM} and event probabilities $P(E_{CM})$ by integrating $F(b)$ over all the values of $b \leq b_{max}$ (b_{max} is impact parameter above which all trajectories results in scattering) for the given E_{CM}. Here in present calculations, it is found that for near barrier energies, neutron transfer is significant for lower impact parameters, but at far above barrier energies, complete fusion dominates for lower impact parameters, while for slightly higher impact parameters, neutron transfer is accountable.

Keywords: *Fusion reactions; Halo nuclei; Heavy-ion collisions; Weakly-bound nuclei; Classical Molecular Dynamics*

PACS: 24.10.-i; 25.70.De; 25.60.Pj

1. INTRODUCTION

There is a remarkable class of nuclei known as Halo Nuclei, which is similar to weakly bound nuclei in many ways, but their structure is strikingly different from normal nuclear matter. These light nuclei are situated near the very boundary of nuclear stability. Several remarkable features were revealed by the groundbreaking experiments [1–4] that were conducted to study characteristics of halo nuclei. Notably, these nuclei exhibit very high interaction cross sections, possess loosely bound outer nucleons with low separation energies (resulting in new surface densities and unique structures), and display exotic modes of collective vibration in the nucleus due to their large dissociation cross sections by high-Z targets. Similar to other weakly bound nuclei, halo nuclei exhibit high breakup probabilities as their outer orbiting protons or neutrons, forming a halo surrounding the core nucleus, have very low separation energy, which can lead to fusion with the target, resulting in incomplete fusion (ICF).

Much interest has been around halo nuclei is due to the development of radioactive beam facilities, which allow studying nuclides at the limits of stability. Among halo nuclei, ^{11}Be is one of the most studied ones and has well well-established one-neutron halo structure having very low neutron separation energy $S_n = 0.501$ MeV [5]. Due to the low separation energy of the valence neutron, this neutron has a relatively high probability of being knocked out. Such breakup effects can be better investigated with a heavier target (i.e., ^{209}Bi) due to the increasing predominance of long-range Coulomb interaction compared to the nuclear potential [6]. Here, the ^{11}Be + ^{209}Bi reaction is studied using the multibody 3-stage Classical Molecular Dynamics (3S-CMD) model, for which ^{11}Be is constructed as a cluster of tightly bound ^{10}Be and one neutron. In the multibody 3S-CMD model, by systematically removing rigidity constraints on the target and projectile, calculations are carried out. As a result, this model can account for a direct reaction like a neutron transfer from the projectile in the present case. Therefore, Event fractions, $F(b)$ and event probabilities, $P(E_{CM})$ as a function of impact parameter, b and center of mass frame energy, E_{CM} are extracted from this calculation.

In this paper, the details of the model are presented in Section – 2 , while the details and the results for event fractions for ^{11}Be + ^{209}Bi are discussed in Section – 3. Finally, conclusions are summarized in Section – 4.

2. MODEL DETAILS

The multibody 3-Stage Classical Molecular Dynamics (3S-CMD) model is used to simulate the ^{11}Be + ^{209}Bi reaction. The projectile ^{11}Be is constructed as a cluster of tightly bound ^{10}Be and one neutron. Tightly bound ^{10}Be and ^{209}Bi are constructed using variational potential energy minimization STATIC [7] code and "cooled" using DYNAMIC [7] code,

for which a purely phenomenological soft-core Gaussian potential is used, which is given by,

$$V_{ij}(r_{ij}) = -V_0 \left(1 - \frac{C}{r_{ij}}\right) \exp\left(-\frac{r_{ij}^2}{r_0^2}\right) \tag{1}$$

where the typical form of the Coulomb potential between protons is,

$$V_C(r_{ij}) = \frac{1.44}{r_{ij}} (MeV) \tag{2}$$

and the potential parameter set $V_0 = 710.0$ MeV, $C = 1.88$ fm and $r_0 = 1.15$ fm is used to produce ground state properties of nuclei. Using a "dynamic cooling" method by carrying out rigid body dynamics [8] like procedure and setting the cluster velocities and their angular moment zero after every time-step and thus obtaining the equilibrium orientation and position of the centre of mass of these constituents (^{10}Be + n). Now, the distance between the center of mass of ^{10}Be and the neutron is adjusted in such a way that the typical ion-ion potential between them is equal to the experimental neutron separation energy of ^{11}Be. Ground-state properties of generated nuclei are mentioned in Table 1 below.

Table 1. Ground-state properties.

Nucleus	Calculated		Experimental	
	B.E. (MeV)	R (fm)	B.E. (MeV) [9]	R (fm)
^{10}**Be**	59.68	2.06	65.97	2.28 [10]
^{11}**Be** (^{10}Be + n)	60.18	2.09	65.55	2.90 [10]
^{209}**Bi**	1606.6	5.55	1640.26	5.52 [11]

In this multibody 3S-CMD model, there are three stages involved in the simulation:
1. Rutherford Trajectories: The target and projectile are initially brought along classical Rutherford trajectories, considering their Coulomb interaction.

2. Classical Rigid Body Dynamics (CRBD): The system evolves dynamically to approach the fusion barrier, incorporating collective motion and interactions [8].

3. Classical Molecular Dynamics (CMD): The entire multibody system undergoes CMD evolution, allowing for interactions and dynamic evolution of the system [7].

In this model, for the first and second stages, the projectile and target are treated as complete rigid bodies, while during the third stage, this rigidity constraint on the target and projectile can be relaxed. In the present calculation, during the third stage of simulation in the multibody 3S-CMD model, for ^{11}Be (^{10}Be + n), the bond between ^{10}Be and the neutron is relaxed and considered non-rigid, while ^{10}Be is treated as a rigid body. Also, the rigidity constraint on ^{209}Bi is relaxed during the third stage.

Previous applications of the multibody 3S-CMD model to the ^{11}Be + ^{209}Bi reaction have yielded fusion cross-sections in good quantitative agreement with experimental data (Figure 1) [12]. Furthermore, these studies emphasized the significant influence of rigidity constraints on the calculated fusion outcomes. In Figure 1, SBPM represents the results of the Static Barrier Penetration Model [13] calculation, where all degrees of freedom are suppressed for the target and projectile. (a) ^{11}Be[^{10}Be(R)-R-n] + ^{209}Bi(NR) represents a case where the ^{11}Be is treated as completely rigid and the target ^{209}Bi is treated as non-rigid. (b) ^{11}Be[^{10}Be(R)-NR-n] + ^{209}Bi(NR) represents a case where the ^{10}Be core of ^{11}Be is treated as rigid, but the bond between the ^{10}Be core and the neutron is treated as non-rigid, and the target ^{209}Bi is treated as non-rigid. So, we used the multibody 3S-CMD approach here to investigate event fractions and probabilities across different event channels. The calculation details of event fractions and probabilities, along with the results for the ^{11}Be + ^{209}Bi reaction, are discussed in Section – 3.

3. EVENT FRACTIONS AND PROBABILITIES

During the collision between weakly bound or halo nuclei and a heavy target, different events like complete fusion, incomplete fusion, and direct reactions like nucleon transfer can take place. Here, for such possible events, the fraction of
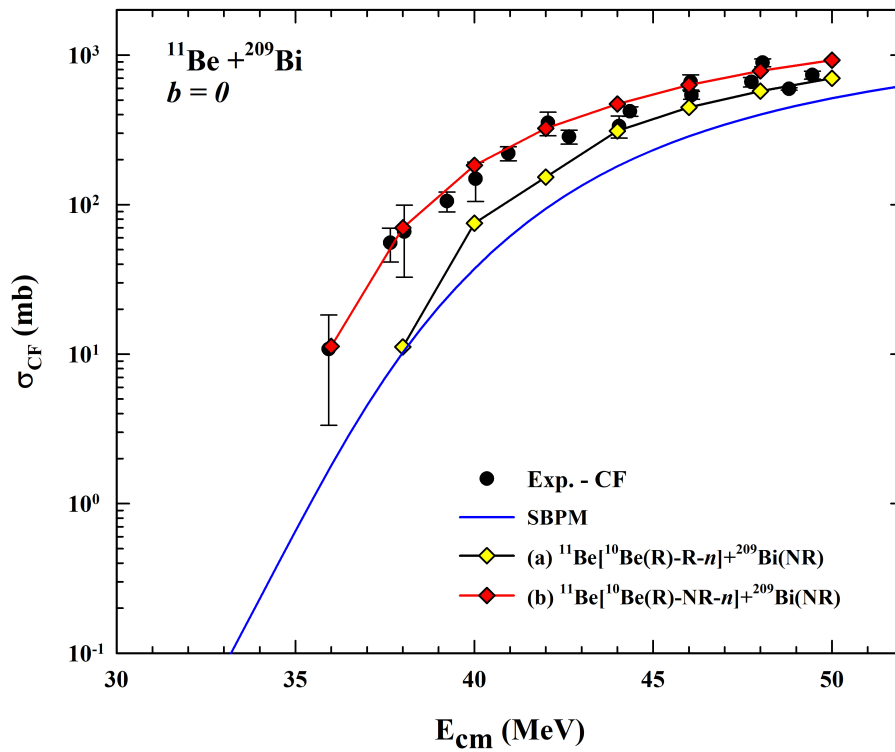
Figure 1. Complete fusion cross sections for the ^{11}Be + ^{209}Bi reaction. Exp. – CF [5].

events, $F(b)$, for the given E_{CM} and b can be defined as,

$$F(b, E_{CM}) = \frac{N_{events}}{N_{total}} \qquad (3)$$

Where, N_{total} = Total number of trajectories for initially random orientations for given E_{CM} and b. N_{events} = total number of events leading to complete fusion, a direct reaction like a neutron transfer, scattering, etc. The event fraction is a function of both b and E_{CM}, but as we have calculated event fractions as a function of b at a given E_{CM}, therefore, for the sake of convenience, we have used the notation $F(b)$ instead of $F(b, E_{CM})$ to denote event fractions.

The event probabilities, $P(E_{CM})$, for all possible events can be found by integrating $F(b)$ over all the values of $b \leq b_{max}$ for given E_{CM},

$$P(E_{CM}) = \left[\frac{1}{(b_{max}/\Delta b) + 1} \right] \int_{b}^{b_{max}} F(b) db \qquad (4)$$

We have calculated fraction of event, $F(b)$ for different three different collision energies, (i) E_{CM} = 38 MeV (Figure 2a) (ii) E_{CM} = 40 MeV (Figure 2b) and (iii) E_{CM} = 50 MeV (Figure 2c) in which 38 MeV and 40 MeV are near barrier energy and 50 MeV is far above barrier energy.

For E_{CM} = 38 MeV (Figure 2a), slightly below the barrier energy, it can be seen that for lower impact parameter neutron transfer from a projectile and direct complete fusion is quite significant while for higher impact parameter most trajectories result in the non-breakup scattering. For E_{CM} = 40 MeV (Figure 2b), slightly above the barrier energy, for lower impact parameters neutron transfer and direct complete reaction are more probable than non-breakup scattering while for higher impact parameters most trajectories result in the non breakup scattering. For E_{CM} = 50 MeV (Figure 2c) for lower impact parameters almost all trajectories result in direct complete fusion but for grazing-like collisions neutron transfer is accountable. For higher impact parameters trajectories results in non-breakup scattering.

For these three energies, Event probabilities, $P(E_{CM})$, are calculated, which are shown in Figure 3. From this, it can be understood that the probability of direct complete fusion increases as the collision energy increases, whereas the probability of no breakup scattering decreases as the collision energy increases. For the neutron transfer, the impact parameter plays a crucial role.
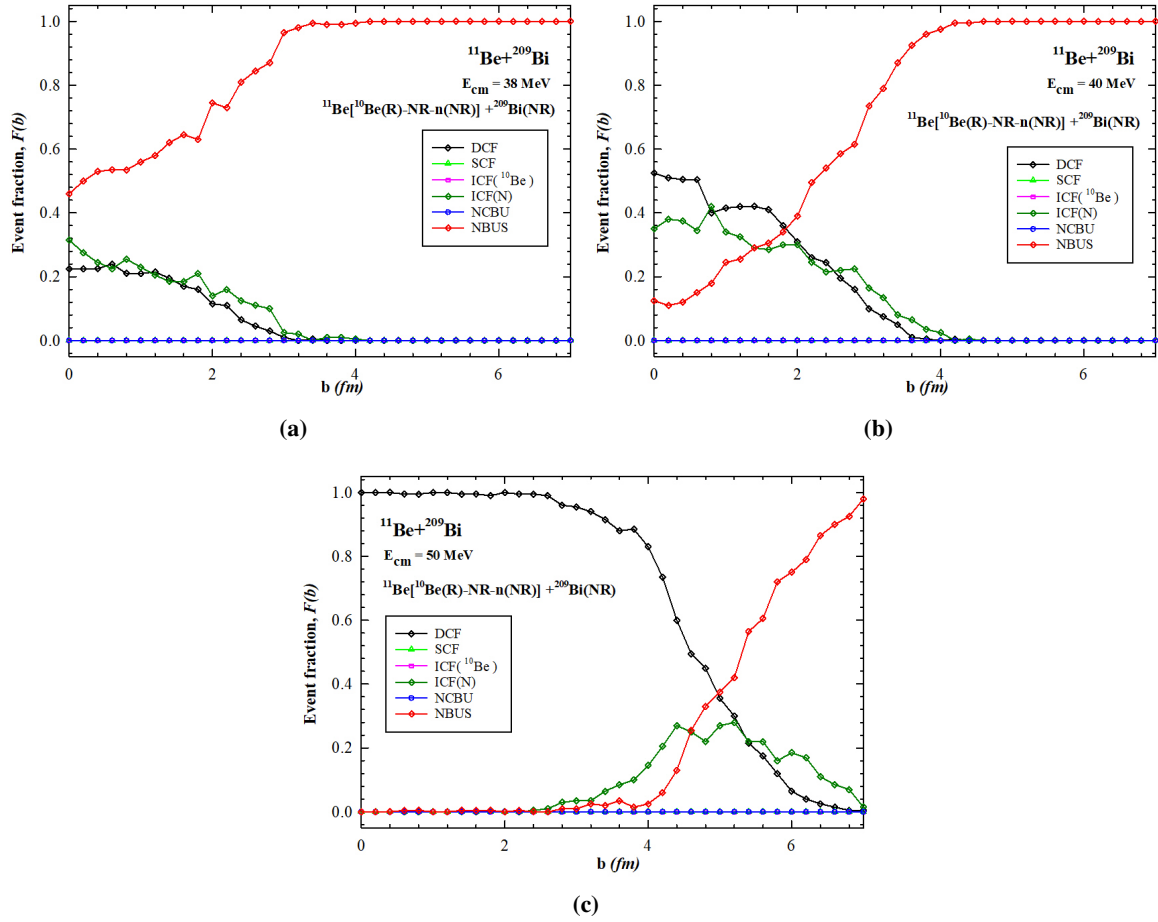
Figure 2. Fraction of event, *F(b)* for different three different collision energies, (a) E_{CM} = 38 MeV (b) E_{CM} = 40 MeV and (c) E_{CM} = 50 MeV.
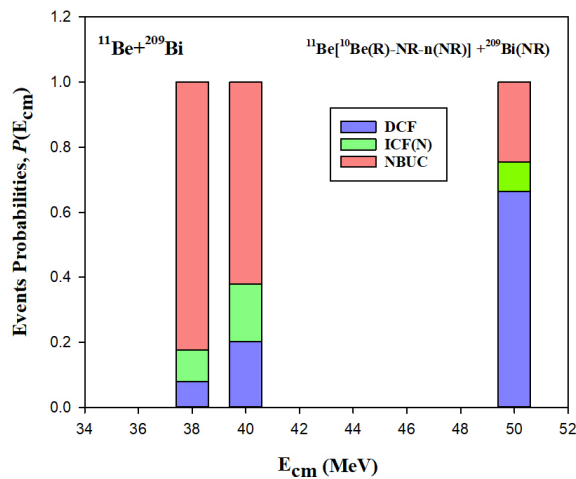
Figure 3. Event probabilities, $P(E_{CM})$ for the system ^{11}Be (^{10}Be + n) + ^{209}Bi for three different collision energy

4. CONCLUSION

The multibody 3S-CMD model calculations are carried out to investigate the ^{11}Be + ^{209}Bi reaction dynamics. The ^{11}Be halo nucleus is explicitly treated as a ^{10}Be core plus a weakly bound neutron, with their interaction potential matched

to the experimental separation energy. In this model, the reactions can be simulated with various rigidity constraints on the projectile fragments, bond between them and the target, which enables the dynamical simulation of various outcomes like complete fusion (CF), neutron transfer, scattering, etc. We calculated event fractions, $F(b)$, versus impact parameter (b) and integrated event probabilities, $P(E_{CM})$, at near-barrier (E_{CM} = 38, 40 MeV) and above-barrier (E_{CM} = 50 MeV) energies. The results highlight a strong dependence of reaction mechanisms on both energy and impact parameter. Near the barrier, neutron transfer significantly competes with complete fusion, particularly in central collisions. At the higher energy (50 MeV), complete fusion dominates at low impact parameters, while neutron transfer becomes the most probable channel for grazing trajectories. The overall probability for CF increases with collision energy, counterbalanced by a decrease in scattering probability. The multibody 3S-CMD model effectively captured the interplay and energy-dependent competition between complete fusion, neutron transfer, and scattering channels in reactions induced by the ^{11}Be halo nucleus. Moreover, understanding the reaction dynamics of Halo nuclei projectiles like ^{11}Be with heavy targets such as ^{209}Bi provides insights into the behaviour of halo nuclei, which can help in improving the accuracy of reaction models used in astrophysical nucleosynthesis simulations, which are used for predicting element formation in stellar environments and understanding energy production in stars. The analysis of neutron transfer, complete fusion processes, and the energy dependence of reaction mechanisms can also facilitate in refining conditions for neutron-rich isotope production.

ORCID
Ⓘ **Vipul B. Katariya**, https://orcid.org/0009-0001-7215-8128; Ⓘ **Subodh S. Godre**, https://orcid.org/0000-0001-5677-648X; Ⓘ **Pinank H. Jariwala**, https://orcid.org/0000-0003-1141-0761

REFERENCES

[1] I. Tanihata, H. Hamagaki, O. Hashimoto, S. Nagamiya, Y. Shida, N. Yoshikawa, O. Yamakawa, *et al.*, Physics Letters B, **160**(6), 380-384 (1985). https://doi.org/10.1016/0370-2693(85)90005-X

[2] I. Tanihata, H. Hamagaki, O. Hashimoto, Y. Shida, N. Yoshikawa, K. Sugimoto, O. Yamakawa, *et al.*, Physical Review Letters, **55**(24), 2676 (1985). https://doi.org/10.1103/PhysRevLett.55.2676

[3] T. Kobayashi, O. Yamakawa, K. Omata, K. Sugimoto, T. Shimoda, N. Takahashi and I. Tanihata, Physical Review Letters, **60**(25), 2599 (1988). https://doi.org/10.1103/PhysRevLett.60.2599

[4] T. Kobayashi, S. Shimoura, I. Tanihata, K. Katori, K. Matsuta, T. Minamisono, K. Sugimoto, *et al.*, Physics Letters B, **232**(1), 51-55 (1989). https://doi.org/10.1016/0370-2693(89)90557-1

[5] C. Signorini, A. Yoshida, Y. Watanabe, D. Pierroutsakou, L. Stroe, T. Fukuda, M. Mazzocco, *et al.*, Nuclear Physics A, **735**(3-4), 329-344 (2004). https://doi.org/10.1016/j.nuclphysa.2004.02.015

[6] F.F. Duan, Y.Y. Yang, K. Wang, A.M. Moro, V. Guimarães, D.Y. Pang, J.S. Wang, *et al.*, Physics Letters B, **811**, 135942 (2020). https://doi.org/10.1016/j.physletb.2020.135942

[7] S.S. Godre and Y.R. Waghmare, Physical Review C, **36**(4), 1632 (1987). https://doi.org/10.1103/PhysRevC.36.1632

[8] P.R. Desai and S.S. Godre, The European Physical Journal A, **47**, 1-10 (2011). https://doi.org/10.1140/epja/i2011-11146-8

[9] A.H. Wapstra and K. Bos, Atomic Data and Nuclear Data Tables **19**(3), 177-214 (1977). https://doi.org/10.1016/0092-640X(77)90020-1

[10] J.S. Al-Khalili, J.A. Tostevin and I.J. Thompson, Physical review C, **54**(4), 1843 (1996). https://doi.org/10.1103/PhysRevC.54.1843

[11] H. De Vries, C.W. De Jager and C. De Vries, Atomic data and nuclear data tables, **36**(3), 495-536 (1987). https://doi.org/10.1016/0092-640X(87)90013-1

[12] V.B. Katariya and S.S. Godre, in: *65th DAE Symposium on Nuclear Physics*, (Mumbai, India, 2021), pp. 315-316. https://sympnp.org/proceedings/65/B56.pdf

[13] S.S. Godre, Nucl. Phys. A, 734, E17-E20 (2004). https://doi.org/10.1016/j.nuclphysa.2004.03.009

ЧАСТКИ ПОДІЙ ТА ЙМОВІРНОСТІ ДЛЯ РЕАКЦІЇ ^{11}Be + ^{209}Bi В БАГАТОЧАСТИНКОВОМУ 3-СТАДІЙНОМУ КЛАСИЧНОМУ МОЛЕКУЛЯРНОМУ ДИНАМІЧНОМУ ПІДХОДІ
Віпул Б. Катарія[a], Субодх С. Годре[a], Пінанк Х. Джарівала[b]
[a] Університет Віра Нармада Південного Гуджарата, Сурат - 395007, Індія
[b] Кафедра фізики, Науковий коледж Нав'юг, Сурат - 395009, Індія

Ядра гало продемонстрували унікальні структури, які радикально відрізняються від звичайної ядерної матерії. Серед інших ядер гало, ядро ^{11}Be є одним з найбільш вивчених ядер гало, і воно має добре встановлену структуру гало з одним нейтроном та енергією розділення нейтронів S_n = 0,501 МеВ. Ми досліджували реакцію ^{11}Be + ^{209}Bi в багаточастинковій 3-стадійній моделі класичної молекулярної динаміки (3S-CMD), де ^{11}Be побудовано як кластер щільно зв'язаного ^{10}Be та одного нейтрона. Відстань між ^{10}Be та нейтроном регулюється таким чином, щоб встановити іон-іонний потенціал між ними, рівний експериментальній енергії розділення нейтронів. Для цієї реакції ми розрахували частки подій $F(b)$ для заданого параметра удару, b та енергії зіткнення E_{CM}, а також ймовірності подій $P(E_{CM})$ шляхом інтегрування $F(b)$ за всіма значеннями $b \le b_{max}$ (b_{max} - параметр удару, вище якого всі траєкторії призводять до розсіювання) для заданого E_{CM}. У цих розрахунках виявлено, що для енергій поблизу бар'єру перенесення нейтронів є значним для нижчих параметрів удару, але при енергіях, що значно перевищують бар'єр, повне злиття домінує для нижчих параметрів удару, тоді як для дещо вищих параметрів удару перенесення нейтронів є відповідним.

Ключові слова: *реакції злиття; ядра гало; зіткнення важких іонів; слабкозв'язані ядра; класична молекулярна динаміка*

MODELING OF THE CHARACTERISTICS OF ELECTRON BEAMS AND GENERATED PHOTON FLUXES ON THE M-30 MICROTRON

Eugene V. Oleinikov[a]*, David Chvátil[b], Eugene Yu. Remeta[a], Aleksandr I. Gomonai[a], Yurii Yu. Bilak[c]

aInstitute of Electron Physics, National Academy of Sciences of Ukraine, Uzhhorod, Ukraine
bNuclear Physics Institute, Czech Academy of Sciences, Czech Republic
cUzhhorod National University, Uzhhorod, Ukraine
Corresponding Author e-mail: zheka.net.ua@gmail.com

Ensuring optimization of the radiation treatment process of experimental samples at electron accelerators and effective prediction of the results of the interaction of electron beams with irradiation objects requires the most accurate information about the characteristics of the beams. The initial (primary) characteristics of accelerator electron beams during transportation to irradiation objects will change due to their interaction with the external environment (air). Thus, secondary particles are also generated - bremsstrahlung photons, which also interact with samples. The paper presents the results of studies on modeling the influence of air layers on the change in the initial characteristics of electron beams during their transportation to irradiation objects and on the parameters of the generated bremsstrahlung photon fluxes in the plane of placement of experimental samples. The studies used the Monte Carlo code – GEANT4. The modeling was carried out for the electron accelerator of the IEP NAS of Ukraine - the M-30 microtron, taking into account its technical parameters. The results of studies of the characteristics (energy spectrum, their integral values, transverse distributions in the 10×10 cm plane) of the electron beam and secondary photons at the output of the electron accelerator are presented. The influence of the thicknesses of the air layers (0.1÷500 cm) between the electron output unit and the potential plane (100×100 cm) of the placement of experimental samples for irradiation on the characteristics of the primary electron beams and generated bremsstrahlung photons (for the energy range of 6÷20 MeV) is studied.

Keywords: *Microtron; GEANT4; Electron beam; Bremsstrahlung; Ti window; Air; Spectra; Spatial distributions*
PACS: 29.17.+w, 29.27._a

INTRODUCTION

Electron beams obtained from electron accelerators (linear, microtrons [1]) are used to solve both scientific [2] and a wide range of applied problems [3-9]. These problems are related to the improvement of radiation therapy protocols in the practice of treating oncological diseases [3]; to the protection of personnel during the operation of accelerators [4], sterilization of medical drugs and devices for their disinfection [5]; processing of food products to increase their shelf life [6]; creation of promising materials with predetermined technical parameters that are necessary for the development of modern innovative technologies [7], alternative methods of producing medical radioisotopes [8]; to non-destructive analysis of nuclear materials for the purpose of their control and non-proliferation [9] and many others. To solve these problems, it is necessary to have the most accurate information about the characteristics (energy spectra, their integral values, transverse distributions along the potential placement plane (PPP) of experimental samples [10,11]) of electron beams interacting with the irradiated objects. In this case, it is important to determine the factors that will influence these final characteristics of the beams during their transportation to the irradiated materials and interaction with them.

The initial (primary) characteristics of electron beams during transportation between the accelerator output unit and the irradiated sample PPP will change due to their interaction with the environment, usually air, due to the processes of inelastic collisions with atomic electrons and nuclei. These processes lead to ionization and excitation of atoms (ionization losses) and the formation of bremsstrahlung (radiation losses) [12]. That is, the initial energy of the beam electrons is lost (decreases) due to inelastic collisions - excitation, ionization, and the formation of bremsstrahlung photon fluxes. In elastic collisions, electrons' kinetic energy and momentum can be redistributed between particles [12]. We also note that secondary particles – photons and electrons – will be present in the electron beams, which are formed by the above processes during the transport of electrons in the layers of matter (air) [13,14].

To ensure the uniformity of the transverse distribution of electron beams along the PPP of the irradiation objects, the distance from the electron output blocks of the accelerators to them is increased, which leads to an increase in the thickness of the air layers and, accordingly, to an increase in the number of secondary photons [15-17]. Secondary photons will also be formed at the outputs of the electron output blocks (between vacuum and air) due to their interaction with the structural elements of the accelerators [18,19]. Reliable information about the characteristics of the secondary photon fluxes in electron beams and the relationships between them is necessary when planning and optimizing (observing the uniformity of the particle field in the PPP of the samples, taking into account their geometric dimensions) the process of irradiation of experimental samples on electron accelerators [15-17]. It should be noted that data on the characteristics of

secondary photon fluxes in electron beams are also used to develop methods for determining the characteristics (spectral, integral, and transverse distributions in the PPP of experimental samples) of electron beams when direct measurements are not possible [20,21].

Results of current research (both theoretical and experimental) into the process of transporting electron beams (with energies up to 20 MeV) from the accelerator output blocks to the irradiation objects indicate the influence of air layers (from 0.1 to 700 cm) on the specified final characteristics, as well as on the characteristics of the photon fluxes generated by them in the PPP of experimental samples [22,23]. With increasing distance to the irradiation objects, these characteristics of electron beams will change at fixed values of the initial electron energy [24,25]. Thus, electron energy's nominal values (in the PPP) will decrease relative to their initial values [24,25]. It should also be noted that the efficiency of generating bremsstrahlung photon fluxes by electron beams in the PPP will increase [26,27].

The final characteristics of electron beams and generated photon fluxes in the PPP are significantly influenced by the initial values of electron energies at fixed distances between the electron output units of the accelerators and the irradiation objects [26]. Thus, with an increase in beam energy (energy range 6÷20 MeV), electron scattering in air decreases [12,22], and the efficiency of secondary photon generation increases [12,15].

Analysis of the results of existing experimental and theoretical studies of the influence of air layers on the change in the final characteristics of electron beams and generated secondary photon fluxes in the PPP (under practically the same conditions of conducting experimental studies on electron accelerators with different technical parameters) indicates their dependence on the characteristics of the primary (initial) electron beams (their geometric dimensions, the shape of the spatial distributions at the accelerator output and energy) [28,29]. Any differences between the characteristics of primary electron beams on different types of accelerators depend on their technical parameters and design features of the output (electron) blocks, since they determine their initial characteristics [28,29].

Therefore, for the successful use of electron accelerators to ensure the experimental samples' irradiation process, reliable data on the characteristics of electron beams and secondary photon fluxes that interact with the irradiation objects are required for each type of accelerator. These data are necessary for optimizing the process of irradiation of experimental samples with electron beams - ensuring their uniformity in the PPP of experimental samples, obtaining the expected value of the absorbed dose (taking into account the energies, intensity, spatial and angular distributions of electron beams in the PPP, geometric dimensions of experimental samples), and reliable assessment of the contribution of the additional absorbed dose from the specified secondary, bremsstrahlung, photons.

The presented work aimed to study the influence of the initial parameters of electron beams (during their transportation to irradiation objects) and air layers on their final values and characteristics of the generated fluxes of secondary photons in the PPP of experimental samples.

The research was conducted using the electron accelerator of the Institute of Electron Physics of the National Academy of Sciences of Ukraine – the M-30 microtron. Its main technical parameters (design of the electron output unit, range of accelerated electron energies, average effective beam current) [30] are similar to those of most operating accelerators in our country [31].

MATERIALS AND METHODS

For computer calculations of the process of transporting electrons and the secondary photons generated by them in the titanium (Ti) window of the electron output unit of the M-30 microtron and the air layers between the output unit and the PPP of the irradiation materials, a program was developed based on the GEANT4 v11.1 toolkit [32]. The created program specified a list of physical processes FTFP_BERT_HP, which uses the physical model of electromagnetic interaction standard for GEANT4 [33,34]. The modeling took into account the design features of the electron output unit of the M-30 microtron [35,36] and the initial parameters of the electron beam that were defined in the DetectorConstruction and PrimaryGeneratorAction classes, respectively [3]. GEANT4 visualization methods based on the Win32 API were used to verify the irradiation scheme.

The simulations were performed for uncollimated electron beams with an equal probability distribution [22], which had the shape of an ellipse with axes of 22 and 6 mm [35,36]. The initial electron energy varied from 6 to 20 MeV. During the simulations, all electrons and the secondary photons, generated by them, that fell into planes perpendicular to the axis of the initial electron beam were recorded - 10×10 cm (at the accelerator output) and 100×100 cm (in the PPP of the materials for irradiation). Visualization of the results of modeling electron transport and secondary photon generation using the GEANT4 toolkit in the absence and presence of air layers is shown in Figure 1.

The modeling was carried out in two stages.

First stage: the characteristics (energy spectra, integral and transverse distribution) of electron beams and secondary photon fluxes generated in the Ti window and their content in the electron beam at 1 mm distance from the accelerator output unit in a 10×10 cm plane were studied.

The second stage is the study of the influence of air layers between the accelerator output unit and the PPP of the irradiation materials on the generation of secondary photon fluxes by the electron beam and their content in the beams that fell into the PPP of experimental samples (100×100 cm) at five fixed distances (100÷500 cm) from the output unit.

The simulated energy spectra of electrons and secondary photons falling into the PPP were normalized to one initial electron.

The integral values N of the number of electrons N_e and secondary photons N_γ were calculated according to formula (1) from the corresponding obtained energy spectra $\phi(E)$:

$$N = \int_0^{E_{max}} \phi(E)dE. \tag{1}$$

The percentage of secondary photons in the electron beam was determined by the formula

$$C = \frac{N_\gamma}{N_e} \cdot 100\%. \tag{2}$$

Based on the simulation results, probability heat maps of the transverse distribution of electron beams and secondary photon fluxes in the PPP were created using the ORIGIN package [7] for visualization.

a)

b)

c)

d)
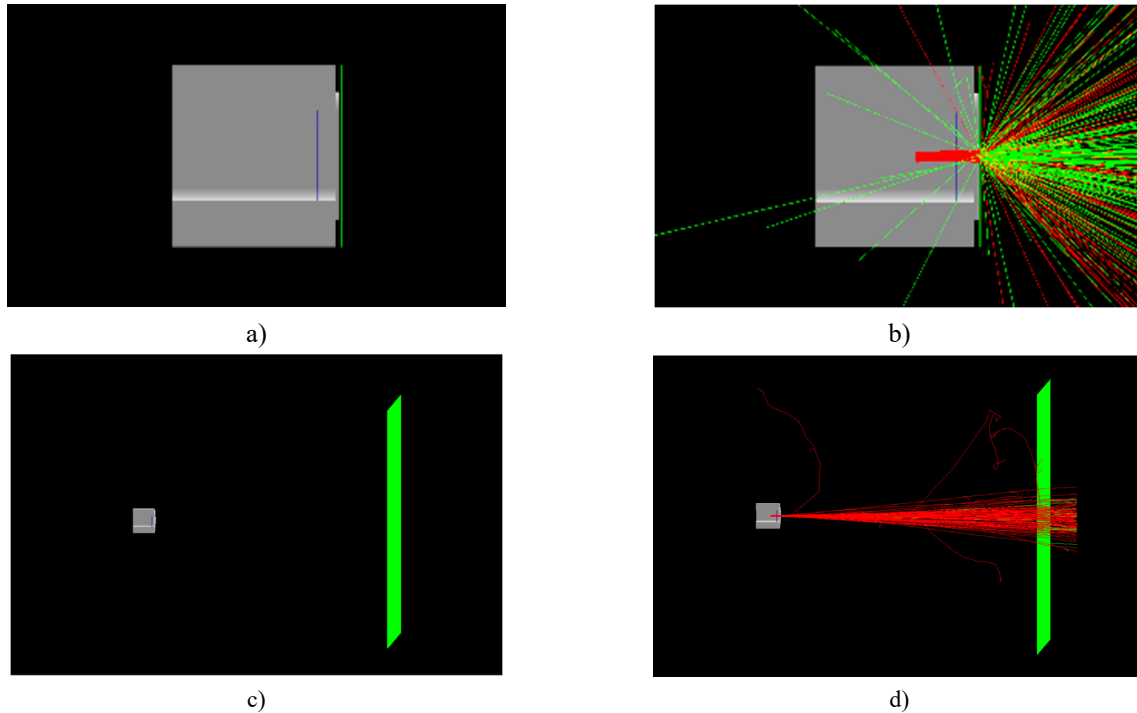
Figure 1. Visualization of modeling results for Ti windows in the absence (a, b) and presence (c, d) of air layers using the GEANT4 toolkit (grey – electron output unit; green square - PPP; red and green lines – electron and photons path).

RESULTS AND DISCUSSION

As a result of the simulations conducted, the following were investigated:

- changes in the characteristics (energy spectra, their integral values, and transverse distributions in the PPP) of the initial electron beam and photon fluxes generated by electrons during interaction with the Ti window of the output unit of the M-30 microtron and their content in the electron beam in the plane of the output unit;

- changes in the characteristics of electron beams and photon fluxes generated by electrons during interaction with air layers between the plane of the output unit and the PPR of the irradiated objects, and the relative content of photon fluxes in electron beams.

Effect of titanium window on electron beam characteristics and secondary photon generation

As a result of the simulations, the characteristics of the energy spectra of electron beams (after their interaction with the Ti layer) and the fluxes of secondary photons (generated by the Ti layer) in the plane of the output unit of the M-30 microtron (10×10 cm), perpendicular to the electron beam axis (Figure 2), were calculated. The calculations were performed for initial electron energies from 6 to 20 MeV.

It is established that the numerical integral values of the number of electrons $N_{e/e}$ in the beam after their interaction with the Ti layer are practically constant for the specified energy range. In contrast, the numerical integral values of the number of photons $N_{\gamma/e}$ in the fluxes increase with increasing initial electron energy from 8.117×10^{-4} γ/e (at 6 MeV) to 0.00101 γ/e (at 20 MeV). Their percentage content in electron beams C also increases slightly from 0.08061% to 0.1003% with increasing initial electron energy from 6 MeV to 20 MeV.

From the simulation results, the profiles of electron beams and bremsstrahlung photons on a plane measuring 10×10 cm at the accelerator output were obtained (Figure 3). From the obtained profiles, the transverse distribution of the intensity of electrons and secondary photons along the X axis perpendicular to the beam axis in the plane's center was taken (Figure 4). An increase in the energy of the initial electron beam from 6 MeV to 20 MeV does not affect the transverse distribution of the electron beam in the plane at the accelerator output (the numerical value is $\sim 6.1547 \times 10^5$),

whereas in the case of bremsstrahlung photon fluxes, their integral number increases by ~1.5 times (from ~419.3 to ~605.4), but this increase is not significant.

a)   b)
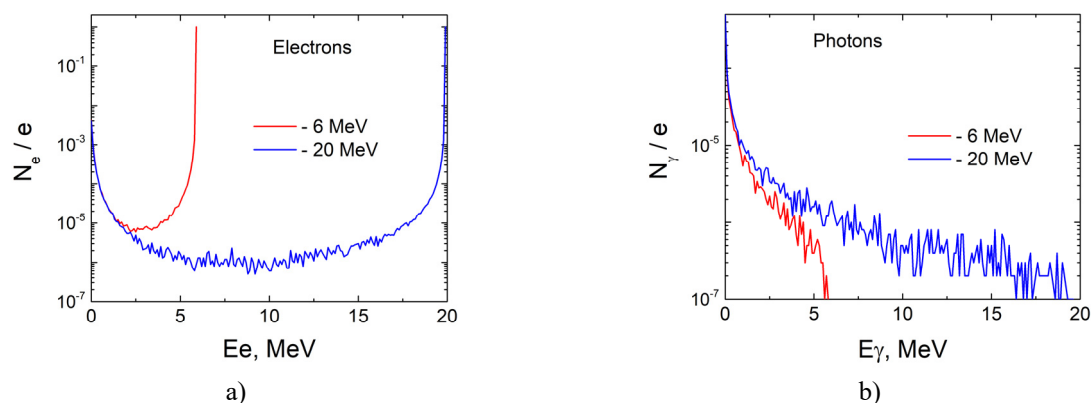
Figure 2. Dependence of the energy spectra of electron beams (a) and generated fluxes of secondary photons (b) on the initial energy of electrons after their interaction with the Ti layer.

a)   b)

c)   d)
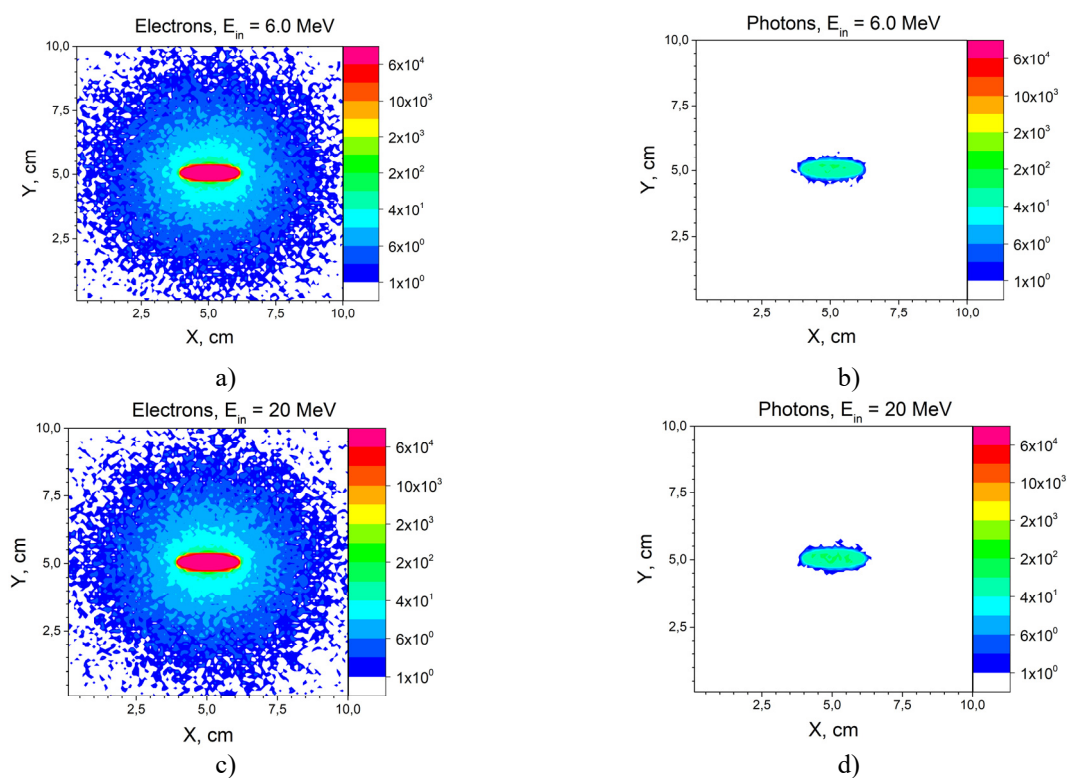
Figure 3. Profiles of electron beams (a, c) and secondary photon fluxes (b, d) at fixed values of initial electron energies of 6 MeV (a, b) and 20 MeV (c, d).

a)   b)
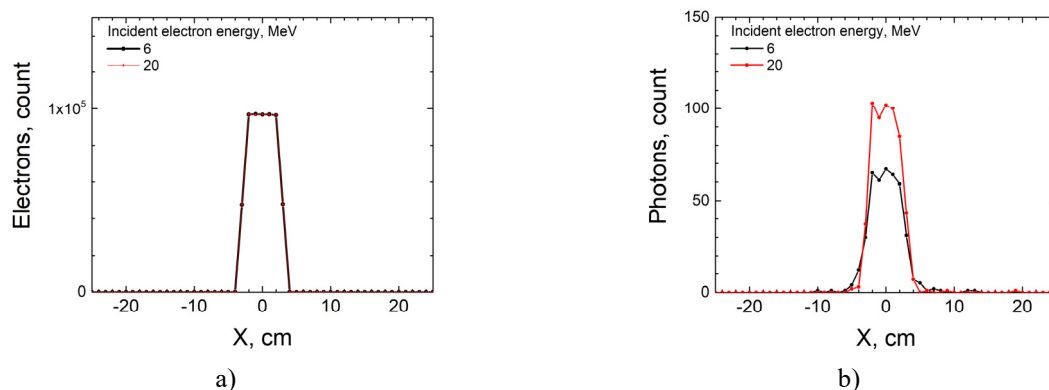
Figure 4. Transverse distributions of electron beams (a) and secondary photon fluxes (b) at fixed values of initial electron energies of 6.0 and 20.0 MeV.

The calculations reflect the general patterns of the characteristics of the electron beams at the output in different models of accelerators, where Ti plates are used for the electron extraction schemes from vacuum to air [18,19]. The same applies to the fluxes of secondary photons generated by electrons in Ti windows. Possible differences in the results may be associated with the difference in technical parameters (design features of the electron extraction units, geometric dimensions) and with the initial electron energies used.

The influence of air layers on the characteristics of the initial electron beams and the generation of secondary photons

The implemented modeling allowed us to investigate the influence of air layers located between the electron output unit of the accelerator - the M-30 microtron and the PPP of experimental samples on the change in the initial characteristics of electron beams during their transportation to the irradiation object and the generation of secondary photons by them. The dependences of the final characteristics of electron beams in the PPP and the fluxes of secondary photons in the air on the initial energies of the electrons were established.

Calculations of the parameters (energy spectra, their integral values, transverse particle distributions in the SPP) of electron beams and the secondary photons generated by them in the PPP of the irradiated objects were carried out for a wide range of initial electron energies - 6÷20 MeV and distances between the output unit and the PPP - 0.1÷500 cm. The established parameters of the initial electron beam at the output of the output unit of the M-30 microtron, which took into account its technical characteristics, were used as input data when conducting simulations.

The results of simulations of the energy spectra of electron beams entering the PPP, depending on their initial energies (E_{in} = 6, 8, 10, 12.5, 14.5, 17.5, and 20 MeV) at fixed values of the distance – 100, 300 and 500 cm, and similar dependencies for the generated fluxes of secondary photons are presented in panel Figure 5. The energy spectra of electron beams and generated secondary photons fluxes in the PPP, depending on the distance (0.1, 100, 200, 300, 400, and 500 cm) at fixed values of the initial electron energy of 6.0, 12.5, and 20.0 MeV, are presented in panel Figure 6.

The simulation results (see Figures 5 and 6) indicate the dependence of the final spectral characteristics of electron beams in the PPP of irradiated objects on the thicknesses of the air layers (between the electron output unit and the PPP) through which they are transported and on their initial energies.

Analysis of the obtained results indicates a decrease in the numerical values of the nominal energy of electron beams in the PPP of experimental samples with an increase in the distance from 0.1 cm to 500 cm. The dependence of the nominal energy of electrons on the distance at fixed values of their initial energy is presented in Table 1.

Calculations were performed using our program to compare the obtained data with the results of similar studies (with the same initial electron energies and distances between the electron output blocks and the PPP of the irradiation objects) [38-40]. The results of the calculations of the energy dependences of the deviations of the nominal values of electron energies from their initial values are presented in Figure 7. The obtained results are consistent with each other. The deviations are associated with the experimental uncertainty of the literature data [38-40].
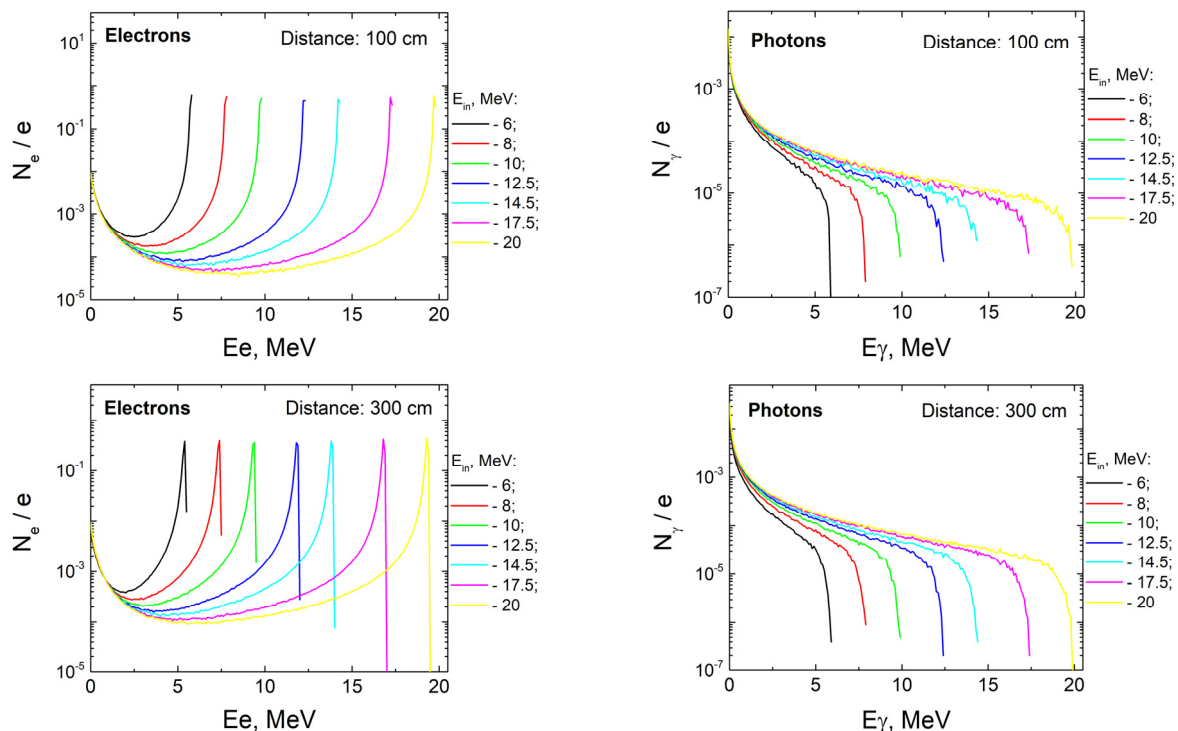
Figure 5. Energy spectra of electron beams and secondary photon fluxes in the PPP depending on the initial electron energy and fixed distance values – 100, 300, and 500 cm
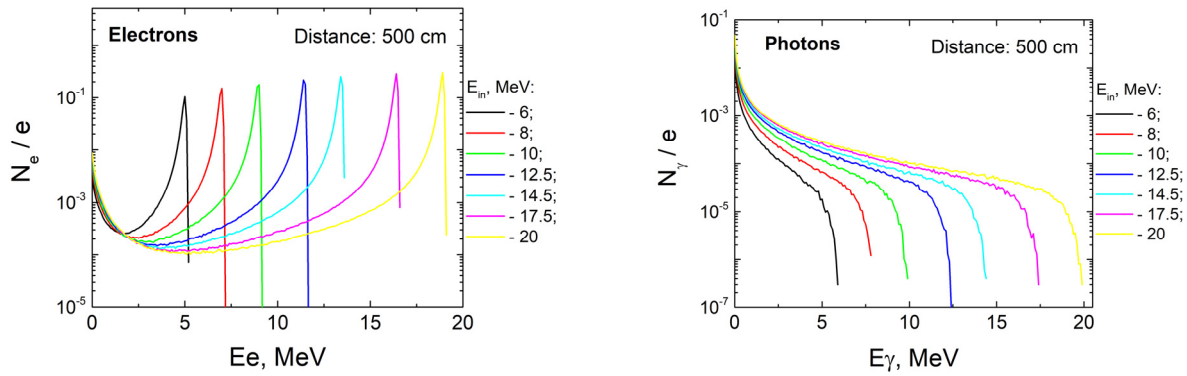
Figure 5. Energy spectra of electron beams and secondary photon fluxes in the PPP depending on the initial electron energy and fixed distance values – 100, 300, and 500 cm *(continued)*
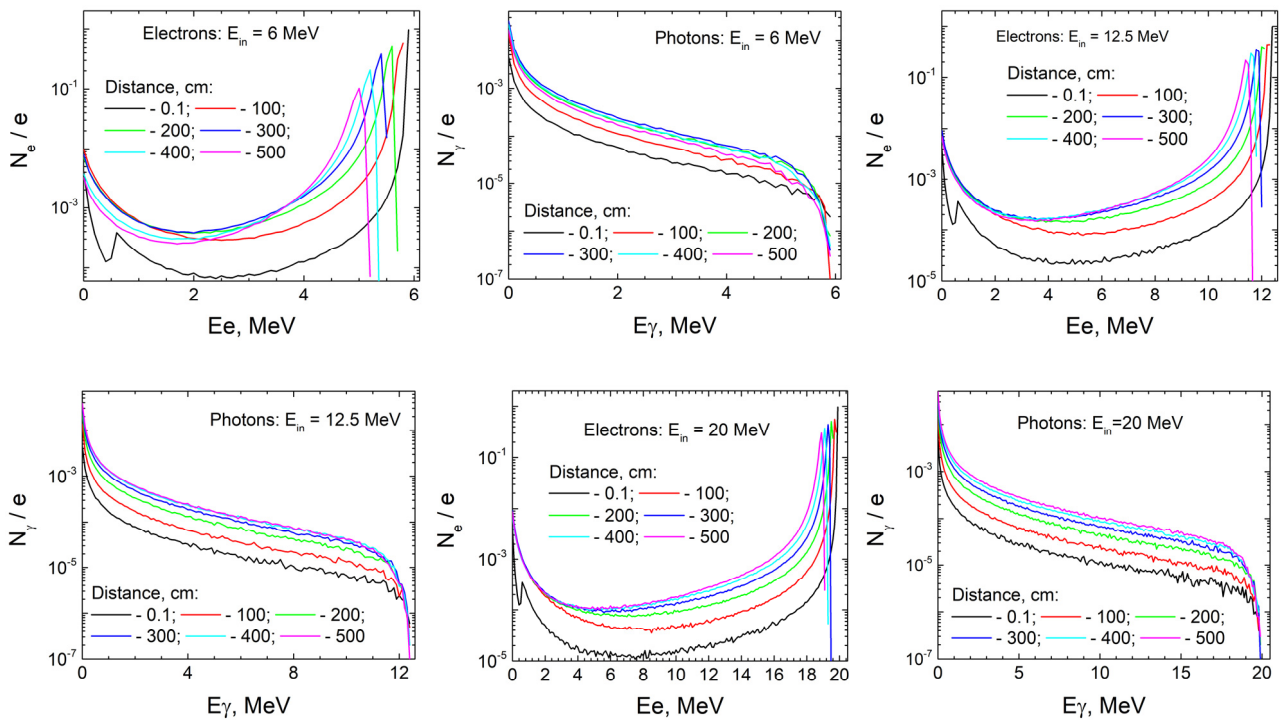
Figure 6. Energy spectra of electron beams and secondary photon fluxes depending on the distance at fixed values of initial electron energies – 6, 12.5, and 20 MeV

Table 1. Nominal value of electron beam energy in the PPP of experimental samples

Initial electron energy, MeV	Nominal energy change interval at distances 0.1–500 cm, MeV	Distances (cm)					
		0.1	100	200	300	400	500
		Nominal energy (MeV)					
6.0	~6.0 ÷ ~5.2	~ 5.9	~ 5.8	~ 5.7	~ 5.5	~ 5.3	~ 5.2
8.0	~8.0 ÷ ~7.2	~ 7.9	~ 7.8	~ 7.7	~ 7.5	~ 7.3	~ 7.2
10.0	~10.0 ÷ ~9.2	~ 9.9	~ 9.8	~ 9.7	~ 9.5	~ 9.3	~ 9.2
12.5	~12.5 ÷ ~11.6	~ 12.4	~ 12.3	~12.1	~ 12	~ 11.8	~ 11.6
14.5	~14.5 ÷ ~13.6	~ 14.4	~ 14.3	~14.1	~14.0	~13.8	~13.6
17.5	~17.5 ÷ ~16.6	~ 17.4	~ 17.3	~17.1	~16.9	~16.8	~16.6
20.0	~20 ÷ ~19.1	~ 19.9	~ 19.8	~19.6	~1 9.5	~19.3	~19.1

The obtained energy spectra of electron beams and secondary photon fluxes were used to calculate their integral values according to (1) and the percentage of secondary photons in the electron beam according to (2). Figure 8 shows the dependences of the integral quantitative values of electron beams and secondary photon fluxes on the initial electron energies (6 ÷ 20 MeV) at fixed distances 0.1÷500 cm, and the percentage of secondary photons in the electron beams.
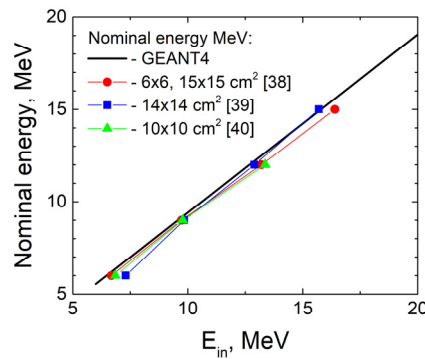
Figure 7. Dependence of the nominal values of electron energies on their initial values for different detection planes.
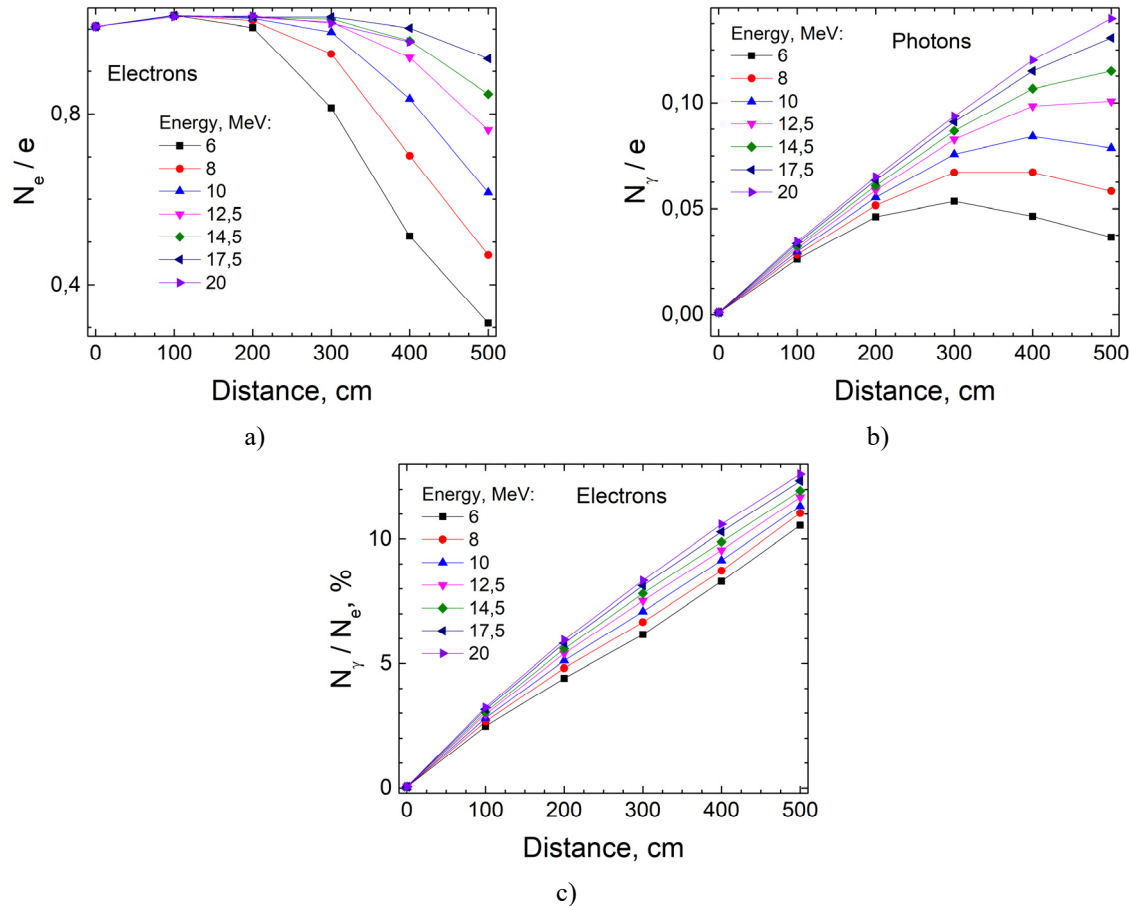

a)

b)

c)
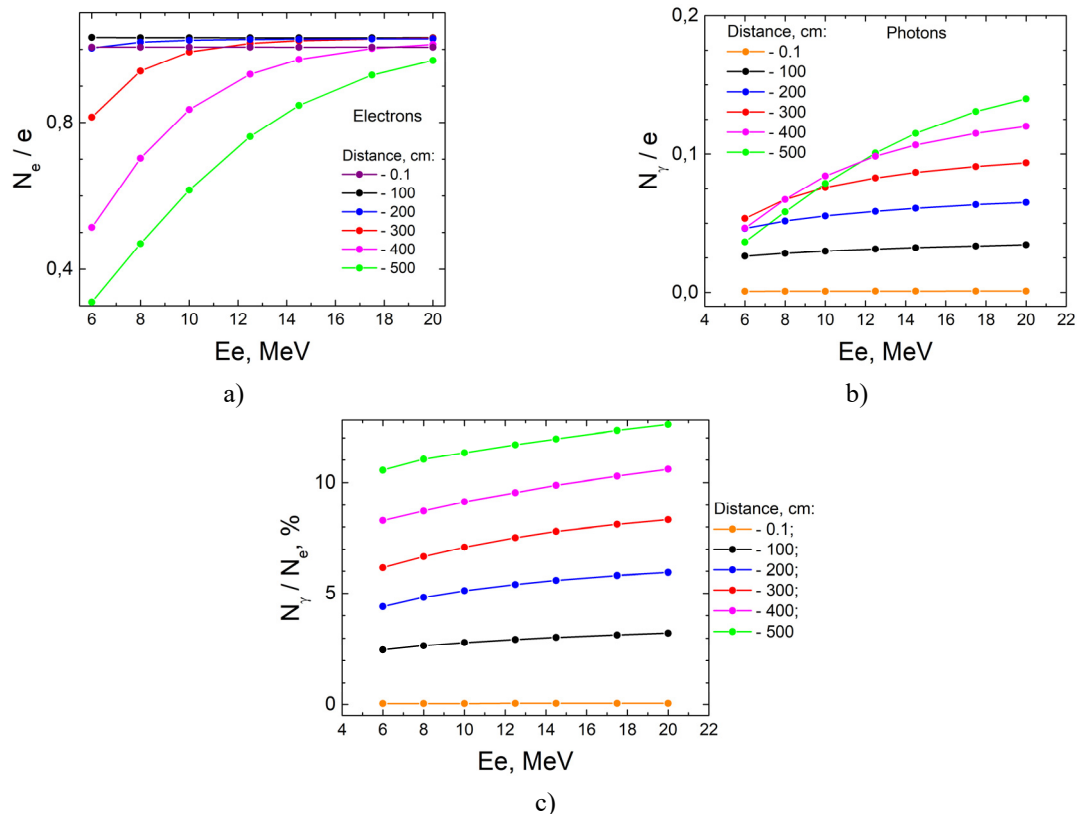
Figure 8. Dependence of the integral values of the quantities of electrons (a) and secondary photons (b), and the percentage of photons in the electron beam (c), on the initial energy of electrons at fixed distances

Similar dependences of the integral values of electron beams and secondary photon fluxes on the distances (0.1÷500 cm) at fixed initial electron energies 6÷20 MeV and the percentage of secondary photons in the electron beams are presented in Figure 9.

The dependence of integral quantitative values of electrons and secondary photons, falling on the PPP, on the energy at fixed distances and the percentage of secondary photons in the electron beam are given in Table 2.

Analysis of the calculated integral values of the electron beam N_e/e indicates their significant dependence on the thickness of the air layers through which the beam is transported and on its initial energy (Figure 8a, Figure 9a, Table 2). The integral values decrease at fixed initial electron energies with increasing distance to the irradiation objects. The initial energy of the beam at fixed distances significantly affects the rate of decrease of N_e/e. Thus, at a fixed initial energy of 6 MeV, the numerical values N_e/e decrease from 1.0060 to 0.3099 with a change in distance from 0.1 cm to 500 cm. And at a fixed initial energy of 20 MeV, the numerical values of N_e/e decrease slightly from 1.0060 to 0.9699 (with a similar change in distances from 0.1 cm to 500 cm).

The integral values of the bremsstrahlung photon fluxes N_γ/e generated by electron beams in the air layers between the output unit and the PPP of the experimental samples are determined by the thicknesses of the layers and the initial energies of the electrons (Figure 8b, Figure 9b, Table 2). The rate of change of N_γ/e is significantly affected by both the initial energy of the electrons and the distances. At a fixed initial energy of 6 MeV, the value of N_γ/e changes significantly from 8.117×10^{-4} to 0.0366, with a change in distances from 0.1 cm to 500 cm. And at a fixed initial energy of 20 MeV, the numerical values of N_γ/e change significantly from 0.0010 to 0.1399 with a similar change in distances from 0.1 cm to 500 cm.

With the increase in the initial electron energy and the increase in the distance, the probability of generating bremsstrahlung photons in the PPP of experimental samples increases. Therefore, the percentage content C (see (2)) of bremsstrahlung photon fluxes in electron beams increases (Figure 8c, Figure 9c, Table 2). It should be noted that the distance factor plays a key role here. With an increase in the distance from 0.1 cm to 500 cm, the numerical values of C increase from 0.04% to 10.55% at a fixed initial electron energy of 6 MeV. Almost similar changes occur at a fixed electron energy of 20 MeV. Here, the numerical values of C increase from 0.05% to 12.60%.

a)

b)

c)

Figure 9. Dependence of the integral values of the quantities of electrons (a) and secondary photons (b), and the percentage of photons in the electron beam (c), on the distance at fixed values of the initial electron energy

Table 2. The dependence of integral quantitative values of electrons, secondary photons falling on the PPP, and the percentage of secondary photons in the electron beam on the initial electron energy at fixed distances

Distance, cm		Initial electron energy, MeV						
		6	**8**	**10**	**12.5**	**14.5**	**17.5**	**20**
0.1	N_e/e	1.006 0	1.0060	1.0060	1.0060	1.0060	1.0060	1.0060
	N_γ/e	8.117E-4	8.645E-4	8.908E-4	9.338E-4	9.373E-4	9.826E-4	0.0010
	C	**0.04 %**	**0.04 %**	**0.04 %**	**0.05%**	**0.05%**	**0.05%**	**0.05 %**
100	N_e/e	1.0326	1.0319	1.0319	1.0316	1.0317	1.0317	1.0318
	N_γ/e	0.0263	0.0283	0.0298	0.03133	0.0323	0.0336	0.0345
	C	**2.48 %**	**2.67 %**	**2.81 %**	**2.95 %**	**3.04 %**	**3.15 %**	**3.23 %**
200	N_e/e	1.0033	1.0199	1.0249	1.0270	1.0278	1.0287	1.0290
	N_γ/e	0.0462	0.05160	0.0553	0.0586	0.0608	0.0634	0.0651
	C	**4.41 %**	**4.82 %**	**5.12 %**	**5.40 %**	**5.59 %**	**5.81 %**	**5.95 %**
300	N_e/e	0.8147	0.9409	0.9930	1.0164	1.0235	1.0284	1.0306
	N_γ/e	0.0535	0.0672	0.0758	0.0827	0.0867	0.0910	0.0937
	C	**6.16 %**	**6.66 %**	**7.09 %**	**7.52 %**	**7.81 %**	**8.13 %**	**8.33 %**
400	N_e/e	0.5137	0.7025	0.8358	0.9321	0.9725	1.0023	1.0135
	N_γ/e	0.0465	0.0672	0.0841	0.0985	0.1067	0.1149	0.1200
	C	**8.30 %**	**8.73 %**	**9.15 %**	**9.56 %**	**9.88 %**	**10.29 %**	**10.59 %**
500	N_e/e	0.3099	0.4694	0.6158	0.7621	0.8469	0.9298	0.9699
	N_γ/e	0.0366	0.0582	0.0786	0.1008	0.1149	0.1308	0.1399
	C	**10.55 %**	**11.04 %**	**11.32 %**	**11.68 %**	**11.95 %**	**12.33 %**	**12.60 %**

The calculated dependences N_e/e, N_γ/e, and C are consistent with the results of similar studies for the same initial electron energies and distances to the irradiation objects [11,26,27].

The simulation results allowed us to obtain profiles of electron beams and generated secondary photons in the PPP with size 100×100 cm (for a distance of 100 cm from the accelerator output unit) at initial electron energies of 6, 12.5, and 20 MeV (Figure 10). A heat map of electron and secondary photon distribution probability was made based on the results achieved. It was found that an increase in the initial energy of electrons leads to a decrease in the angular distribution of particles (electrons, bremsstrahlung photons) and to an increase in their concentration in the center of the PPP.
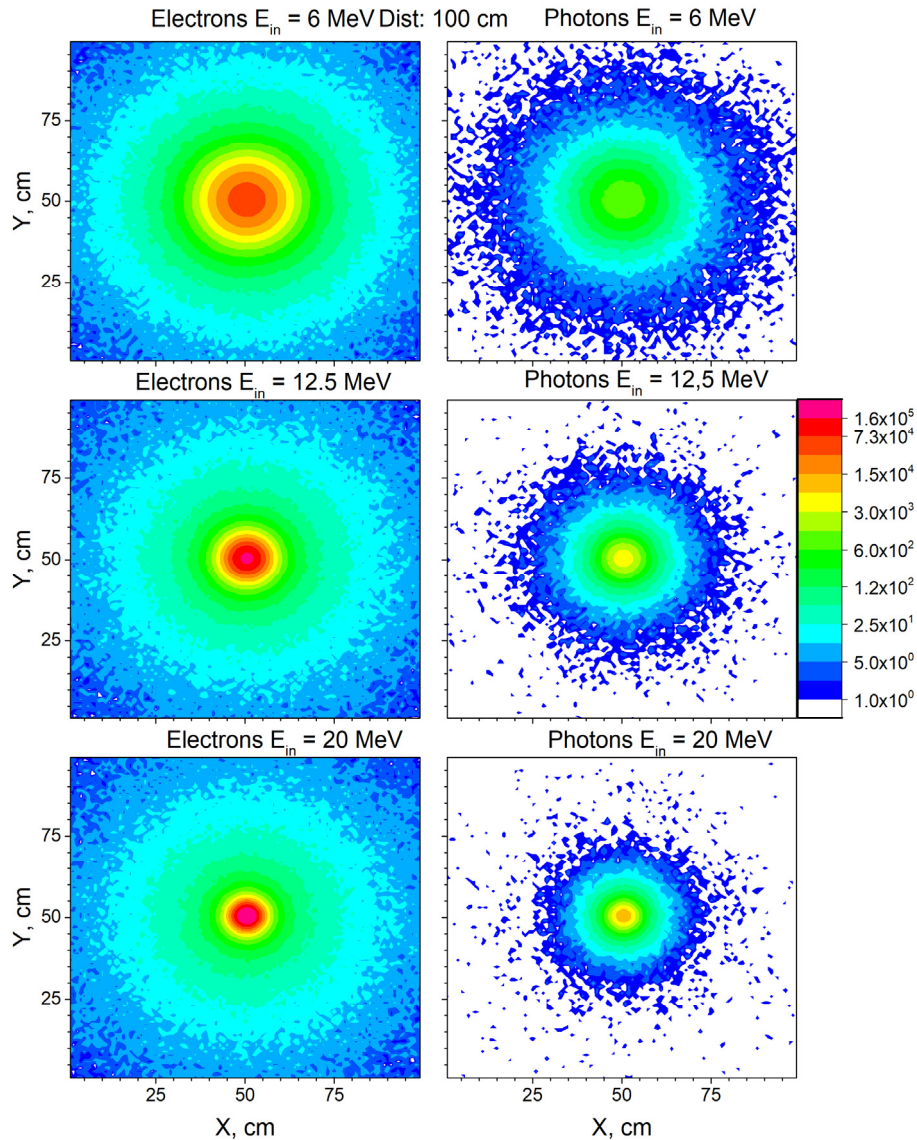
Figure 10. Profiles of electrons and secondary photons incident on a plane at fixed values of the initial electron energy

From the obtained profiles in the section on planes of size 100×100 cm (for a distance of 100 cm from the accelerator output unit) (Figure 10), transverse distributions of the intensity of electrons and secondary photons along the X axis perpendicular to the beam axis in the center of PPP (Figure 11) were taken. The cross-section graph confirms the conclusions mentioned above and clearly demonstrates the increase in particle concentration in the center of the irradiated plane. The numerical values of the calculated peak areas of the sections at the initial electron energies of 6, 12.5, and 20 MeV are 6.990×10^5, 1.381×10^6, 2.084×10^6 for electrons and 1.4469×10^4, 3.4537×10^4, 5.8380×10^4 for bremsstrahlung photons, respectively.

The obtained results reflect the general patterns of the influence of the initial energy of electron beams on their spatial distributions at fixed distances and the spatial distributions of secondary bremsstrahlung photons generated in air. The obtained results are consistent with similar studies [10,11,19,41].

Any differences between the investigated characteristics may be related to the technical parameters of the accelerators (electron ejection units). They can significantly affect the final characteristics of the electron beams and bremsstrahlung photon fluxes in the PPP of the samples [28,29].
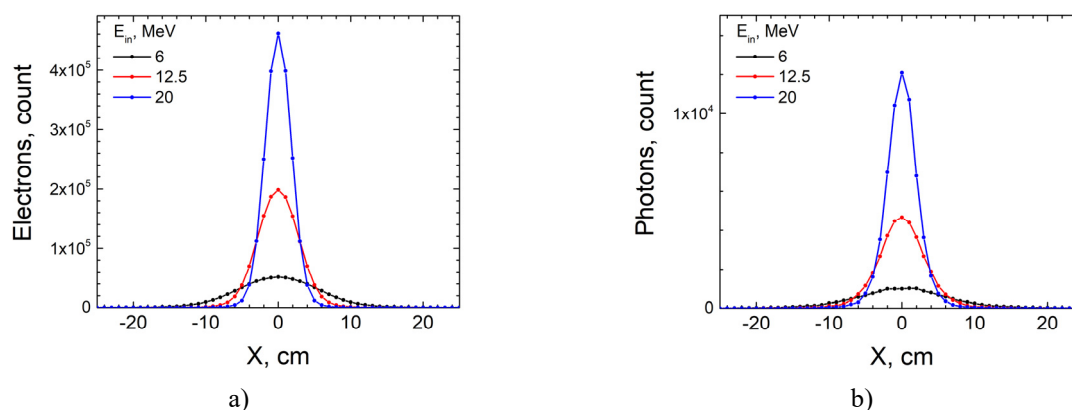
Figure 11. Transverse distributions of the intensity of the electron beam (a) and the generated secondary photons (b) on the central X axis (0 – the center of the PPP of the sample) at the initial electron energies.

CONCLUSIONS

The results of modeling studies using the Monte Carlo code GEANT4 made it possible to establish the influence of air layers on the change in the initial characteristics of electron beams during their transportation to irradiation objects and on the parameters of the generated bremsstrahlung photon fluxes in the plane of placement of experimental samples.

The computer simulations of changes in the characteristics of electron beams and bremsstrahlung photon fluxes generated in the air layers between the M-30 microtron output unit and the plane of placement of experimental samples will allow finding optimal schemes for their radiation treatment, for example, obtaining uniform particle fields in the plane of their location, taking into account their geometric dimensions. In addition, the simulation results will allow for the prediction of effective and optimal practical applications to conduct a reliable assessment of the absorbed dose during interaction with electron beams and the contribution of additional dose from interaction with bremsstrahlung photon fluxes.

The proposed simulation scheme can be used to optimize the irradiation processes of experimental samples on different types of accelerators with various technical parameters.

ORCID IDs
Eugene V. Oleinikov, https://orcid.org/0000-0003-0949-5145; **Eugene Yu. Remeta,** https://orcid.org/0000-0001-9799-7895
Yurii Yu. Bilak, https://orcid.org/0000-0001-5989-1643; **Aleksandr I. Gomonai,** https://orcid.org/0000-0003-4341-699X
David Chvatil, https://orcid.org/0009-0007-1821-5850

REFERENCES
[1] F. Méot. Understanding the Physics of Particle Accelerators. A Guide to Beam Dynamics Simulations Using ZGOUBI // Springer Cham. 2024. 636 p. https://doi.org/10.1007/978-3-031-59979-8
[2] F. Frei, S. Vörös, M. Lüthi, P. Peier, Nuclear Instruments and Methods in Physics Research A, **1077**, 170588 (2025). https://doi.org/10.1016/j.nima.2025.170588
[3] A. Ikhlaq, S.A. Buzdar, M. Aslam, M.U. Mustafa, S. Salahuddin, M. Nisa, Scientific Inquiry and Review, **5**(3), 13 (2021). https://doi.org/10.32350/sir/52
[4] S.D. Quoc, T. Fujibuchi, H. Arakawa, K. Hamada, D.H. Han, Applied Radiation and Isotopes, **219**, 111704 (2025). https://doi.org/10.1016/j.apradiso.2025.111704
[5] Md.K. Hasan, D. Staack, S.D. Pillai, L.S. Fifield, M. Pharr, Polymer Degradation and Stability, **221**, 110677 (2024). https://doi.org/10.1016/j.polymdegradstab.2024.110677
[6] Z. Chu, H. Wang, B. Dong, Molecules, **29**(14), 3318 (2024). https://doi.org/10.3390/molecules29143318
[7] A.G. Chmielewski, Radiation Physics and Chemistry, **213**, 111233 (2023). https://doi.org/10.1016/j.radphyschem.2023.111233
[8] Y. Wang, D. Chen, R.S. Augusto, J. Liang, Z. Qin, J. Liu, Z. Liu, Molecules, **27**(16), 5294 (2022). https://doi.org/10.3390/molecules27165294
[9] J. Bendahan, Nuclear Instruments and Methods in Physics Research Section A, **954**. 161120 (2020). https://doi.org/10.1016/j.nima.2018.08.079
[10] A. Ryczkowski, T. Piotrowski, M. Staszczak, M. Wiktorowicz, P. Adrich, Zeitschrift für Medizinische Physik, **34**(4), 510 (2024). https://doi.org/10.1016/j.zemedi.2023.03.003
[11] C. Oproiu, M.R. Nemţanu, M. Braşoveanu, and M. Oane, "Determination of absorbed dose distribution in technological accelerated electron beam treatments," in: *Practical Aspects and Applications of Electron Beam Irradiation*, ch. 2, edited by M.R. Nemtanu and M. Brasoveanu (Transworld Research Network, 2011). p. 17-41.
[12] W. Strydom, W. Parker, and M. Olivares, "Electron beams: Physical and clinical aspects," in: *Review of Radiation Oncology Physics: A Handbook for Teachers and Students*, Chapter 8, tech. editor E.B. Podgorsak, International Atomic Energy Agency Library Cataloguing in Publication Data. Vienna: 2005. p. 273-300. https://www-pub.iaea.org/MTCD/publications/PDF/Pub1196_web.pdf
[13] H.O. Tekin, T. Manici, E.E. Altunsoy, K. Yilancioglu, and B. Yilmaz, Acta Physica Polonica A, **132**(3-II), 967 (2017). https://doi.org/10.12693/APhysPolA.132.967
[14] M.K. Saadi, and R. Machrafi, Applied Radiation and Isotopes, **161**, 109145 (2020). https://doi.org/10.1016/j.apradiso.2020.109145

[15] G.X. Ding, S. Kucuker-Dogan, and I.J. Das, Medical Physics, **49**(2), 1297 (2022). https://doi.org/10.1002/mp.15433

[16] V.A. Shevchenko, A.Eh. Tenishev, V.L. Uvarov, and A.A. Zakharchenko, Problems of Atomic Science and Technology, (6), 163 (2019). https://doi.org/10.46813/2019-124-163

[17] V.L. Uvarov, A.A. Zakharchenko, L.V. Zarochintsev, *et al.*, Problems of Atomic Science and Technology, (3), 154 (2020). https://doi.org/10.46813/2020-127-154

[18] M.R.M. Chulan, M.F.M. Zin, L.K. Wah, M. Mokhtar, M.A. Ahmad, A.H. Baijan, R.M. Sabri, and K.A. Malik, IOP Conf. Series: Materials Science and Engineering, **785**, 012003 (2020). https://doi.org/10.1088/1757-899X/785/1/012003

[19] P. Apiwattanakul, and S. Rimjaem, Nuclear Inst. and Methods in Physics Research B, **466**, 69 (2020). https://doi.org/10.1016/j.nimb.2020.01.012

[20] R.I. Pomatsalyuk, V.A. Shevchenko, D.V. Titov, A.Eh. Tenishev, V.L. Uvarov, A.A. Zakharchenko, and V.N. Vereshchaka, Problems of Atomic Science and Technology, (6), 201 (2021). https://doi.org/10.46813/2021-136-201

[21] H. Kim, D.H. Jeong, S.K. Kang, M. Lee, H. Lim, S.J. Lee, and K.W. Jang, Nuclear Engineering and Technology, **55**, 3417 (2023). https://doi.org/10.1016/j.net.2023.05.033

[22] A. Toutaoui, A.N. Aichouche, K. Adjidir, and A.C. Chami, Journal of Medical Physics, **33**, 141 (2008). https://doi.org/10.4103/0971-6203.44473

[23] G.X. Ding, Z.(J) Chen, and K. Homann, Medical Physics, **51**, 5563 (2024). https://doi.org/10.1002/mp.17186

[24] J. Tertel, J. Wulff, H. Karle, and K. Zink, Zeitschrift für Medizinische Physik, **30**(10), 51 (2010). https://doi.org/10.1016/j.zemedi.2009.11.001

[25] M.R.S. Didi, M. Zerfaoui, M. Hamal, Y. Oulhouq, and A. Moussa, Radiation Physics and Chemistry, **207**, 110859 (2023). https://doi.org/10.1016/j.radphyschem.2023.110859

[26] G.X. Ding, S. Kucuker-Dogan, and I.J. Das, Medical Physics, **49**(2), 1297 (2022). https://doi.org/10.1002/mp.15433

[27] N. Khaledi, D. Sardari, M. Mohammadi, A. Ameri, and N. Reynaert, Journal of Radiotherapy in Practice, **17**, 319 (2018). https://doi.org/10.1017/S1460396917000711

[28] A. Ryczkowski, T. Piotrowski, M. Staszczak, M. Wiktorowicz, and P. Adrich, Zeitschrift für Medizinische Physik, **34**(4), 210 (2024). https://doi.org/10.1016/j.zemedi.2023.03.003

[29] A. Ryczkowski, B. Pawałowski, M. Kruszyna-Mochalska, A. Misiarz, A. Lenartowicz-Gasik, M. Wosicki, A. Jodda, *et al.*, Polish Journal of Medical Physics and Engineering, **30**, 177 (2024). https://doi.org/10.2478/pjmpe-2024-0021

[30] V.T. Maslyuk, Visnyk of the National Academy of Sciences of Ukraine, **11**, 46 (2016). https://doi.org/10.15407/visn2016.11.046

[31] Professional public organization «Ukrainian Association of Medical Physicists», Remote radiation therapy in Ukraine. https://uamp.org.ua/useful-information/radiotherapy-equipment-in-ukraine/external-radiotherapy/ (in Ukrainian)

[32] GEANT4 11.1 (9 December 2022). https://geant4.web.cern.ch/download/11.1.0.html

[33] S. Ashurov, S. Palvanov, A. Tuymuradov, and D. Tuymurodov, Bulletin of National University of Uzbekistan Mathematics and Natural Sciences, **6**(4), 179 (2023). https://doi.org/10.56017/2181-1318.1257

[34] T.V. Malykhinaa, V.E. Kovtuna, V.I. Kasilovb, and S.P. Gokov, East European Journal of Physics, **4**, 91 (2021). https://doi.org/10.26565/2312-4334-2021-4-10

[35] E. Oleinikov, I. Pylypchynets, and O. Parlag, Journal of Nuclear and Particle Physics, **13**, 7 (2023). https://doi.org/10.5923/j.jnpp.20231301.02

[36] E.V. Oleinikov, I.V. Pylypchynets, O.O. Parlag, and V.V. Pyskach, **153**(5), 148 (2024). https://doi.org/10.46813/2024-153-148

[37] OriginLab Corporation, One Roundhouse Plaza, Suite 303, Northampton, MA 01060, UNITED STATES, OriginPro, https://www.originlab.com/

[38] R. Maskani, M.J. Tahmasebibirgani, M.H. Ghahfarokhi, and J. Fatahias, Asian Pacific Journal of Cancer Prevention, **16**(17), 7795 (2015). https://doi.org/10.7314/APJCP.2015.16.17.7795

[39] M. Rezzoug, M. Zerfaoui, Y. Oulhouq, and A. Rrhioua, Reports of Practical Oncology & Radiotherapy, **28**(5), 592 (2023). https://doi.org/10.5603/rpor.96865

[40] M. Rezzoug, M. Zerfaoui, Y. Oulhouq, A. Rrhioua, S. Didi, M. Hamal, and A. Moussa, Radiation Physics and Chemistry, **207,** 110859 (2023). https://doi.org/10.1016/j.radphyschem.2023.110859

[41] M.A. Pagnan-González, J.O. Hernández-Oviedo, and E. Mitsoura, Revista de Medicina e Investigación, **3**(1), 22 (2015). https://doi.org/10.1016/j.mei.2015.02.002

МОДЕЛЮВАННЯ ХАРАКТЕРИСТИК ПУЧКІВ ЕЛЕКТРОНІВ ТА ЗГЕНЕРОВАНИХ ПОТОКІВ ФОТОНІВ НА МІКРОТРОНІ М-30

Євген В. Олейніков[a], Давід Хватіл[b], Євген Ю. Ремета[a], Олександр І. Гомонай[a], Юрій Ю. Білак[c]

[a]Інститут електронної фізики НАН України, Ужгород, Україна
[b]Інститут ядерної фізики Чеської Академії Наук, Чеська республіка
[c]ДВНЗ «Ужгородський національний університет», Ужгород, Україна

Забезпечення оптимізації процесу радіаційної обробки експериментальних зразків на електронних прискорювачах та ефективне прогнозування результатів взаємодії пучків електронів з об'єктами опромінення потребують максимально точної інформації про характеристики пучків. Початкові (первинні) характеристики пучків електронів прискорювачів при транспортуванні до об'єктів опромінювання будуть змінюватися внаслідок їх взаємодії з зовнішнім середовищем (повітрям). Так, додатково відбувається генерація вторинних частинок – гальмівних фотонів, які теж взаємодіють зі зразками. У роботі представлені результати досліджень з моделювання впливу шарів повітря на зміну початкових характеристик пучків електронів при їх транспортуванні до об'єктів опромінення та на параметри згенерованих потоків гальмівних фотонів у площині розміщення експериментальних зразків. У дослідженнях використовувався Монте-Карло код – GEANT4. Моделювання проводилося на прикладі електронного прискорювача ІЕФ НАН України – мікротрону М-30 з врахуванням його технічних параметрів. Представлено результати досліджень характеристик (енергетичні спектри, їх інтегральні значення, поперечні розподіли у площині 10×10 см) пучка електронів і вторинних фотонів на виході електронного прискорювача. Вивчено вплив товщин шарів повітря (0.1÷500 см) між блоком виводу електронів та потенційною площиною (100×100 см) розміщення експериментальних зразків для опромінення на характеристики первинних пучків електронів та згенерованих гальмівних фотонів (для області енергій 6÷20 МеВ).

Ключові слова: *мікротрон; GEANT4; пучок електронів; гальмівне випромінювання; Ті віконце; повітря; спектр; просторовий розподіл*

ON THE FEATURES OF OPEN MAGNETOACTIVE WAVEGUIDES EXCITATION

E.V. Poklonsky[a], V.M. Kuklin[b]

[a]V.N. Karazin Kharkiv National University, 4 Svobody Square, Kharkiv, 61022, Ukraine
[b]Semyon Kuznets Kharkiv National University of Economics. Department of Cybersecurity and Information Technologies, Nauky Ave., 2. 9 – A. 61165, Kharkiv, Ukraine
Corresponding Author E-mail: evpoklonsky@karazin.ua, volodymyr.kuklin@hneu.net

It is shown that in the volume of an open waveguide, each electron – oscillator rotating in a constant magnetic field is capable of generating a TE wave, for which this waveguide is transparent. The generation efficiency is determined by the rate of electron injection and their longitudinal velocity along the waveguide axis. The field generation mode near the cutoff frequency with a low group velocity comparable with the longitudinal velocity of the injected electrons is selected. In this case, the transverse velocity of the electrons significantly exceeds their longitudinal velocity and the group velocity of the wave. In the absence of field reflection from the waveguide ends, each electron makes its contribution to the total radiation field, i.e. it can be considered that the field generation occurs in the superradiance mode. It is shown that the total field of the electron flow is capable of forming a resonator field consisting of two waves propagating towards each other due to even partial reflections from the waveguide ends. With a small reflection of the fields from the ends and a small drift velocity of the rotating electrons, the superradiance mode dominates, similar to the case of excitation of a completely open waveguide. In the case of a noticeable reflection of the fields from the ends of the system at a relatively high velocity of their longitudinal injection, the reflected fields significantly exceed the total field of the emitters and the traditional mode of waveguide resonator field generation is formed. The zones where either resonator field generation or generation under superradiance conditions dominate are presented on the plane "longitudinal motion velocity – reflection coefficient". Two cases are considered: when reflected waves are formed only due to reflection from the ends, and also when the effect of rotating electrons on reflected waves in the waveguide volume is taken into account. It is essential that the average amplitude of the total particle radiation field changes slightly for all considered generation modes. Resonance effects during reflection from the ends lead to a significant increase in the amplitude of the waveguide – resonator field.
Keywords: *Rotating electrons – oscillators, magnetoactive waveguide, resonator field generation, TE wave superradiance mode.*
PACS: 05.45.Xt,52.40.Mj,84.30.Ng.

INTRODUCTION

The nature of excitation of oscillations in limited systems – waveguides and resonators – due to self-consistent [1] interaction with flows of charged particles and oscillators has been considered in a large number of different works (see, for example, [2 – 9]). Traditionally, problems of generation and amplification were solved in the paradigm of interaction of the field determined by the geometry of the waveguide or resonator with active particles according to the scheme proposed in [10]. In this approach to the description, there is no direct interaction between the active particles of the flow; each of them interacts only with the field of the waveguide.

On the other hand, each particle or oscillator in the active zone emits and it is possible to find the total field of these emitters. In the absence of a waveguide and a resonator at a low noise level [11-13], a system of such emitters under certain conditions is capable of generating radiation with a noticeable share of coherence, and such radiation is usually called superluminescence or superradiance mode. In the same way, in an open waveguide, in the absence of reflection from its ends or with a sufficiently small reflection, the superradiance mode can also be realized. In works [14-15] it is shown that the intensity of the eigenfield of particles in the modes of their arising synchronization is comparable with the intensity of traditional waveguide or resonator generation. Since the total field of the emitters (charged parts and oscillators) of the active zone in waveguide and resonator systems is always present and can be quite significant, it is rational to study the influence of this field on the formation of the resonator waveguide field under conditions of even partial reflection from the ends of the waveguide. This process of formation of the resonator waveguide field occurs due to the effects of reflection from the ends of the system and the interaction of the reflected waves with particles in the active zone. When the conditions of phase synchronization of particles and oscillators are met and the reflection of the field from the ends of the system increases, it is possible to observe the formation of a resonator waveguide field exceeding the total eigenfield of the active particles. At low reflection coefficients, the eigenfield of particles can dominate, which corresponds to the superradiance regime.

The aim of the work is to identify zones on the phase plane "injection velocity - reflection coefficient" where the conditions for generation in superradiance regimes are met and where the generation of a resonator waveguide field is realized.

1. PARTICLE OWN FIELD AND RESONATOR FIELD OF A WAVEGUIDE

Let us consider the excitation of a TE electromagnetic wave, the electric vector of which is perpendicular to the waveguide axis, with a frequency and a wave vector in a smooth metal cylindrical waveguide of radius by an electron

beam in resonance cases, where is the cyclotron frequency of electron rotation. Generation is considered near the cutoff frequency, where the group velocity of the wave is small. Induction of a constant magnetic field. The electron beam occupies a cylindrical layer in the cross-section of the waveguide, which we will assume to be sufficiently thin. All centers of Larmor rotation of electrons with radius are at the same distance from the waveguide axis. Each such electron rotating in a constant magnetic field (actually an oscillator) is capable of generating a TE wave, for which this waveguide is transparent.

The traditional description of the process of excitation of a resonator waveguide field (under conditions of field formation due to reflection from the boundaries - ends of the waveguide) assumes that the direct interaction of particles with each other in the active zone is neglected. Particles interact only with the waveguide field. It is obvious that in this traditional description the total field of particles – rotating electrons – during their interaction with each other is not taken into account at all. The equations for the longitudinal component of the magnetic field, electromagnetic waves propagating in both directions (the interference of which is the resonator waveguide field) have the form [16-17]

$$\frac{d\mathrm{B}_{wg\pm}}{d\tau} + \theta \cdot \mathrm{B}_{wg\pm} = \frac{i}{2} N^{-1} \cdot \sum_{j=1}^{N} a_j \cdot J_1'(a_j) \cdot \exp(-2\pi\mathrm{i}\zeta_j \mp 2\pi\mathrm{i}Z_j) , \tag{1}$$

here $\mathrm{B}_{wg\pm}$ are the dimensionless amplitudes of the longitudinal magnetic field of counterpropagating waves, θ is the decrement of absorption due to radiation, a_j is the radius of Larmor rotation (in fact, the amplitude of the oscillator), N is the number of modeling particles, $2\pi\zeta_j$ is the phase of the oscillator, $Z_j = k_z z_j$ is the dimensionless longitudinal coordinate. If the condition $|\partial \mathrm{B}_{wg\pm} / \partial \tau| << \theta | \mathrm{B}_{wg\pm} |$ is met, equation (1) can be rewritten as

$$\mathrm{B}_{wg\pm} = \frac{i}{2N\theta} \cdot \sum_{j=1}^{N} a_j \cdot J_1'(a_j) \cdot \exp(-2\pi\mathrm{i}\zeta_j \mp 2\pi\mathrm{i}Z_j) . \tag{2}$$

The resonator waveguide field can be represented in a simplified form using only the waves reflected from the ends of the system, which will be defined below

$$\mathrm{B}_{ref}(Z) = \mathrm{B}_{ref+} \exp(2\pi i Z) + \mathrm{B}_{ref-} \exp(-2\pi i Z) . \tag{3}$$

Then the resonator waveguide field can be written

$$\mathrm{B}_{wg+} = \mathrm{B}_{ref+}, \quad \mathrm{B}_{wg-} = \mathrm{B}_{ref-} . \tag{4}$$

If we take into account the influence of particles in the volume on the reflected waves, then the resonant waveguide field can be approximated by two waves

$$\begin{aligned} \mathrm{B}_w(Z) &= \mathrm{B}_{wg}(Z) + \mathrm{B}_{ref}(Z) = \mathrm{B}_{w+} \cdot e^{2\pi i Z} + \mathrm{B}_{w-} \cdot e^{-2\pi i Z} \\ \mathrm{B}_{w+} &= \mathrm{B}_{ref+} + 0.5\,\mathrm{B}_{wg+}, \quad \mathrm{B}_{w-} = \mathrm{B}_{ref-} + 0.5\,\mathrm{B}_{wg-} \end{aligned} \tag{5}$$

and the fields are presented in complex form $B_{\pm} = | B_{\pm} | \exp\{i\varphi_{\pm}\}$. The equations of motion for electrons rotating in a constant magnetic field

$$2\pi \frac{d\zeta_i}{d\tau} = \eta_i(1-\alpha) + \mathrm{Re}\{J_1(a_i) \cdot [1 - \frac{1}{a_i^2}] \cdot \exp(2\pi i \zeta_i) \cdot [\mathrm{B}(Z_i, \tau)]\} , \tag{6}$$

$$da_i / d\tau = \mathrm{Re}\{i \cdot J_1'(a_i) \cdot \exp(2\pi i \zeta_i) \cdot [\mathrm{B}(Z_i, \tau)]\} \tag{7}$$

should be supplemented with two more equations that take into account the longitudinal motion of the oscillators

$$d\eta_i / d\tau = 2\pi d^2 Z_i / d\tau^2 = \mathrm{Re}\{iR \cdot a_i \cdot J_1'(a_i) \exp(2\pi i \zeta_i) \cdot [\mathrm{B}(Z_i, \tau)]\} , \tag{8}$$

$$2\pi dZ_i / d\tau = \eta_i , \tag{9}$$

here - α takes into account the relativism of the electron, η_i - is the dimensionless longitudinal velocity of the electron, $R_e = k_z^2 \cdot \omega_B / k_{ms}^2 \cdot \delta_e$ - is the quantity that determines the orientation of the wave vector of the wave.

Total radiation fields of particles. Superradiance modes. However, in reality, first a total radiation field of electrons rotating in a constant magnetic field, actually oscillators, arises in the waveguide, and each such oscillator emits a TE

wave in both directions. Because an oscillator is capable of emitting only waves that are in the transparency zone of the medium (or system - in this case, the waveguide). In this case, the field of this radiation will act on all particles of the oscillator ensemble. In other words, all oscillators interact with each other.

If all these rotating electrons were outside the waveguide, this process would be called the superradiance mode, if, of course, the oscillators are subsequently synchronized in phase, which is observed in the absence of noise [7]. But even in an open waveguide, without reflection or with insignificant reflection from the ends, this process is also no different from the superradiance mode and, in all likelihood, is it. Let us assume that the resonator waveguide field (2) is absent, and that there is only a superradiance field, i.e. a field that is determined only by the interaction of rotating electrons. To describe the magnetic field of the TE wave excited by this ensemble of rotating electrons, we can use the expression [13]

$$\mathrm{B}_{sr}(Z) = \frac{i}{2N\theta}\sum_{j=1}^{N} a_j J_1^{'}(a_j)\exp\{-2\pi i\zeta_j\}\cdot\exp\{2\pi i\left|Z-Z_j\right|\} \tag{10}$$

We write the total field acting on the particles as

$$\mathrm{B}(Z,\tau) = \mathrm{B}_{sr}(Z,\tau) + \mathrm{B}_w(Z,\tau) \tag{11}$$

Equations (2), (10), and (11) with the equations of motion (6) – (9) use the following variables

where $\tau = \delta_e t$, $\delta_e^2 = 4e^2\cdot\omega_B\cdot\mathrm{N}_{b0}\cdot[m_e\cdot c\cdot k_{ms}^2\cdot r_w\cdot J_m^2(x_{ms})\cdot(1-m^2/x_{ms}^2)\cdot D_\omega]^{-1}\cdot J_{m-n}^2(k_{ms}\cdot r_C)$, $D_\omega = \partial D/\partial\omega = \partial\{[\omega^2-(k_z^2+k_{ms}^2)c^2]/[\omega^2-k_z^2 c^2]\}/\partial\omega|_{D=0}$, $B = e\cdot b_B\cdot J_{m+n}(k_{ms}\cdot r_C)/m_e\cdot c\cdot\delta_e$, $R_e = k_z^2\cdot\omega_B/k_{ms}^2\cdot\delta_e$, $Z_j = kz_j/2\pi$ is the position of the electron rotation center along the waveguide axis, $a = k_{ms}r_B = k_{ms}v_\Phi/\omega_B$, $\omega_B = eB_0/m_e c$, B_0 – is the constant magnetic field in the waveguide, N_{b0} – is the number of particles of the unperturbed beam per unit length. Here b_B is the wave amplitude, and t $B = B_z = b_B\cdot J_m(k_{ms}r)\cdot\exp\{-i\omega t+ik_z z+im\vartheta\}$ the longitudinal component of the magnetic field of the wave has the form in the cylindrical coordinate system $(r,\ \vartheta,\ z)$, m is an integer, and $J_m(x)$, $J_m^{'}(x) = dJ_m(x)/dx$ is the Bessel function and its derivative. The requirement that the tangential component of the field at the waveguide boundary vanishes determines the values of the transverse wave number $k_\perp = k_{ms} = x_{ms}/r_w$, where x_{ms} – is the root of the equation $dJ_m(x)/dx = 0$.

Reflection conditions. The reflected field amplitudes $\mathrm{B}_{ref\pm}$ are obtained from the equations of the balance of the incident/reflected field at the boundaries

$$\begin{aligned}\mathrm{B}_{ref+} &= -r_L\cdot\left(\mathrm{B}_{sr-}+0.5\mathrm{B}_{wg-}+\mathrm{B}_{ref-}\right), \quad Z=0 \\ \mathrm{B}_{ref-} &= -r_R\cdot\left(\mathrm{B}_{sr+}+0.5\mathrm{B}_{wg+}+\mathrm{B}_{ref+}\right), \quad Z=1\end{aligned}, \tag{12}$$

here $\mathrm{B}_{sr-} = \mathrm{B}_{sr}(0)$, $\mathrm{B}_{sr+} = \mathrm{B}_{sr}(1)$

$$\begin{aligned}\mathrm{B}_{ref+} &= \frac{r_l\left(r_r(\mathrm{B}_{sr+}+0.5\mathrm{B}_{wg+})-(\mathrm{B}_{sr-}+0.5\mathrm{B}_{wg-})\right)}{(1-r_l\cdot r_r)}, \\ \mathrm{B}_{ref-} &= \frac{r_r\left(r_l(\mathrm{B}_{sr-}+0.5\mathrm{B}_{wg-})-(\mathrm{B}_{sr+}+0.5\mathrm{B}_{wg+})\right)}{(1-r_l\cdot r_r)}\end{aligned}, \tag{13}$$

Expressions (13) take into account the effect of particles - electrons in the waveguide volume on the reflected waves. In the case where the effect of particles in the volume on the reflected waves is not taken into account, for the reflected field amplitudes determined only by the reflection processes at the ends of the system we obtain (see (5)).

$$\mathrm{B}_{ref+} = \frac{r_l\left(r_r\mathrm{B}_{sr+}-\mathrm{B}_{sr-}\right)}{(1-r_l\cdot r_r)}, \quad \mathrm{B}_{ref-} = \frac{r_r\left(r_l\mathrm{B}_{sr-}-\mathrm{B}_{sr+}\right)}{(1-r_l\cdot r_r)}. \tag{14}$$

2. NUMERICAL SOLUTION OF THE PROBLEM

A waveguide contains a given number of particles simulating an ensemble of electrons – N. At the initial moment, all particles have a given amplitude, velocity, and random phase $a_i(0) = a_0 = 1$, $\eta_i(0) = \eta_0$, $\zeta_j\in(0,2\pi)$.

Particles are injected into the beginning of the waveguide in such a way that their total number in the waveguide remains constant. Here is the oscillator amplitude, velocity, and phase of the new (replacement) particles are the same as those of the particles at the initial moment: $a_{new} = a_0 = 1$, $\eta_{new} = \eta_0$, $\zeta_{new}\in(0,2\pi)$.

Constant parameters $N = 500$, $\theta = 1$, $\alpha = 0.5$, $a_0 = 1$, $R = 0.1$, $r_L = 1$ (total reflection at the left edge) were used in the calculations. The velocity of the incoming particles and the reflection coefficient at the right edge η_0, r_L were changed. Particles with a random phase were injected in the region of the left end. Here a_i, ζ_i, η_i, Z_i is the amplitude (radius of rotation), phase, longitudinal velocity, and coordinate of the i-th particle. $B(Z_i)$ is the field acting on the particle at the point with coordinate Z_i. In the absence of reflection at the two ends of the waveguide, the ensemble of rotating electrons generates only their total radiation field, which can be considered a superradiance field (see Fig. 1).

It is worth noting that in the absence of reflection there is no wave field; only the presence of reflection effects allows the formation of a waveguide field.

Phase synchronization and formation of noticeable coherence of radiation of an ensemble of particles in the active zone of an open waveguide in superradiance mode with a large dispersion (scattering) of the initial amplitudes of the oscillators (here these are the Larmor rotation radii of the electrons) generally require an initiating external field and noise attenuation [9] to accelerate the generation process. It turned out that in the absence of a spread of the initial amplitudes of the oscillators, an external field is not required, the development of the generation process (see Fig. 1) occurs noticeably faster. Under the considered conditions, the proper field of rotating particles-electrons turns out to be large enough and can effectively form reflected waves of noticeable amplitude due to reflection from the ends. Reflection from the ends of the resonator leads to the appearance of reflected waves traveling in the opposite direction. Reflected waves can be formed due to reflections of the field from the ends according to (14). But, generally speaking, these waves can change when passing through the active zone under the influence of the fields of moving oscillators in the volume of the active zone. Therefore, it is useful to take into account the influence of the oscillators in the active zone on these reflected waves. And then the resonator field will consist of two waves traveling in different directions, where the amplitude of the reflected waves at the boundary is supplemented by a term that qualitatively takes into account the influence of the oscillators in the resonator volume on these waves (13).
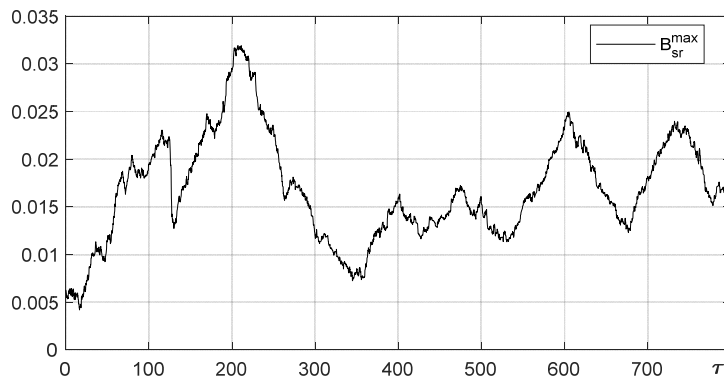
Figure 1. Time dependence of the particle field maximum for each moment of time at zero reflection coefficients

$$r_L = 0, \ r_R = 0$$

In the general case, $B_{sr}(Z)$ this field consists of the total field of the particles and $B_w(Z)$ the resonator (waveguide) field. Below, two mechanisms for the formation of reflected waves that make up the waveguide field are considered. The first is due only to reflections from the ends of the waveguide according to (14) and the second, where the influence of particles in the active zone volume on the reflected waves is additionally taken into account, that is, taking into account the corrections after formula (13).

The process of the emergence of a waveguide resonator field is associated with the formation of reflected waves at the boundaries. When reflecting from the ends of the resonator, reflected waves appear, running in the opposite direction: from the end Z=0, a reflected wave running to the right with the amplitude at the boundary B_{ref+} (Z=0), from the end Z=1, a wave running to the left with the amplitude at the other boundary B_{ref-} (Z=1). Generally speaking, these waves change under the influence of the fields of moving oscillators when passing through the active zone. Therefore, the effect of oscillators in the active zone on these reflected waves should be taken into account $B_{wg}(Z,\tau)$. And then the resonator field will consist of two waves running in different directions, where a term is added to the amplitude of the reflected waves at the boundary, qualitatively taking into account the influence of oscillators in the resonator volume on these waves.

After a certain period of establishing the generation in the waveguide, a quasi-stationary mode is formed, on which chaotic oscillations are superimposed due to incoming particles with a random phase. Therefore, after establishing this mode, the values of the squares of the resonator waveguide field and the total particle field, as well as their ratio K, averaged over the waveguide volume and time are calculated.

$$E_{sr}^{2} = <(E_{sr}^{2})_{av}>_{t}, \quad E_{w}^{2} = <(E_{w}^{2})_{av}>_{t}, \quad K = E_{w}^{2}/E_{sr}^{2} \tag{15}$$

Calculations show that for given reflection coefficients and an increase in the particle input velocity, both the total proper field of the particles and the waveguide field grow, but the waveguide field grows somewhat faster. Thus, the following operating modes can be observed: 1 – dominance of the generation of the proper field of the oscillators - the superradiance mode ($K < 1$), 2 – generation of the resonator field ($K > 1$). Fig. 2 shows the boundaries between the modes depending on the parameters changed in the calculations: the injection velocity and the reflection coefficient at the right edge of the waveguide.
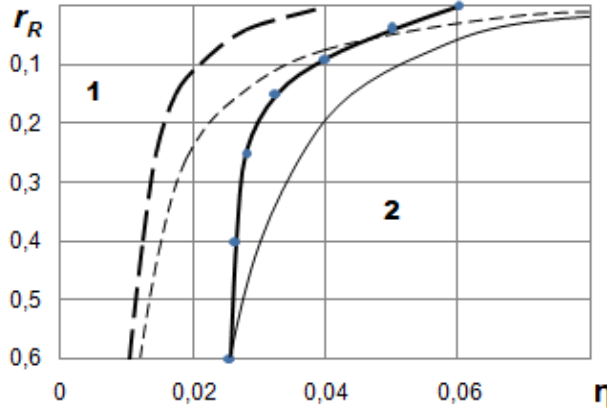
Figure 2. Boundaries between generation modes during correction of reflected waves, according to the conditions of taking into account the influence of particles in the active zone volume on reflected waves (13) (bold line), the thin line indicates the boundary of the regions in the absence of such consideration, according to conditions (14).

The dotted lines correspond to the boundary of the regions in the case when the average particle velocity in the waveguide volume is used, and not the initial velocity of the injected particles. In region 1, the generation of the intrinsic particle field dominates (in fact, the superradiance mode), in region 2 - the generation of a resonator waveguide field of the traditional type, caused by reflection processes from the ends.

In the developed mode 1 - dominance of superradiance - the intensity of the total particle field exceeds the intensity of the resonator waveguide field.

Fig. 3 shows the time dependence of the average particle field squared over the waveguide volume (solid lines) and the resonator waveguide field (dotted lines) in mode 1 ($\eta_0 = 0.02$, $r_R = 0.2$), taking into account the influence of particles in the waveguide volume on reflected waves, and in the absence of such an influence.
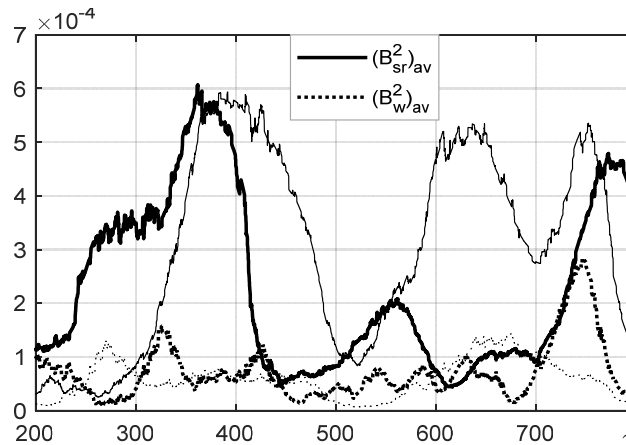
Figure 3. Time dependence of the averaged over the waveguide volume squares of the particle field (dotted line) and the resonator waveguide field (solid line) in mode 1 ($\eta_0 = 0.02$, $r_R = 0.2$) bold lines in the case of taking into account the influence of particles in the waveguide volume on the reflected waves, according to conditions (13). Th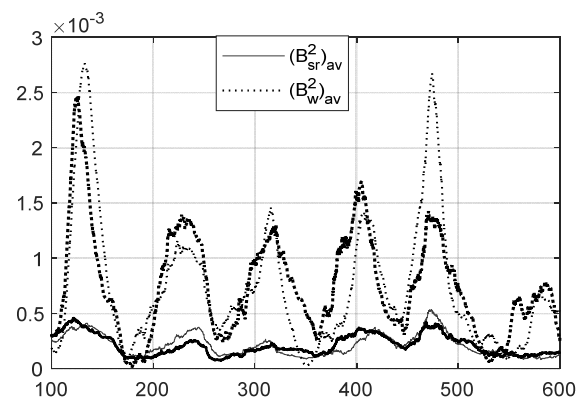in lines are the particle field and the reflected field in the absence of such an influence of particles in the volume on the reflected waves according to conditions (14).

A decrease in the drift velocity of electrons along the system in developed generation modes is characteristic. For mode 1 - superradiation: $\eta_0 = 0.02$, $r_R = 0.2$, Fig. 4 demonstrates the time dependence of the average particle velocity over the waveguide volume in mode 1, taking into account the influence of particles in the waveguide volume on reflected waves, and in the absence of such influence,
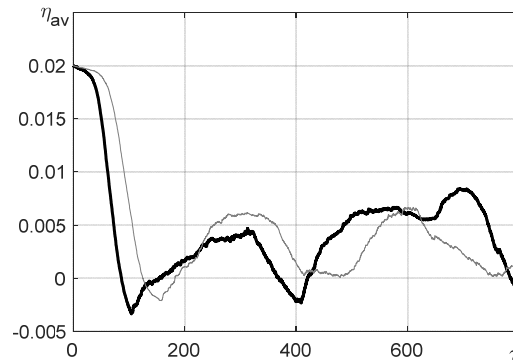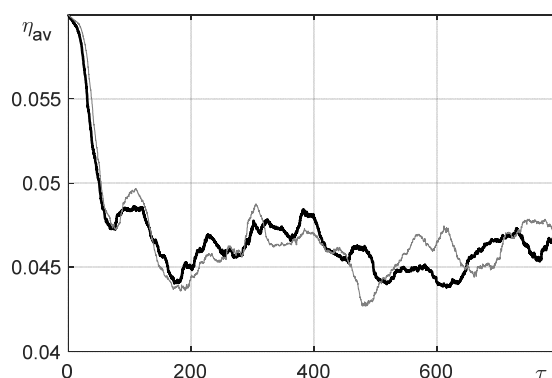
Figure 4. Time dependence of the average particle velocity over the waveguide volume in mode 1, $(\eta_0 = 0.02, r_R = 0.2)$ the thick line in the case of taking into account the influence of particles in the waveguide volume on the reflected waves, according to conditions (13). The thin line - in the absence of such influence, according to conditions (13).

We can give the form of the fields for this mode. It is seen that the resonant waveguide field retains the sinusoidal shape of the standing wave, the field of particles increases towards the left end of the system. The resonator waveguide field in this mode is less than the total field of particles, the attenuation coefficient is $K = 0.32$.

From Fig. 5 it is seen that if the waveguide field is distributed approximately uniformly along the length of the system, then the total electron field (superradiation field) increases significantly along the system. When generating a waveguide field, the contribution of each electron to the field amplitude is determined by its position in the active zone. However, it is important that the distribution of oscillators in the active zone and their phase synchronization do not change the spatial structure of the waveguide field. The growth of the particle field (superradiation) is associated with an increase in the fraction of rotating electrons locally synchronized with the total field along the length of the system. Thus, the advantage of generation in the radiation mode is an increase in the field amplitude at the end of the system in the direction of electron drift, which greatly simplifies energy extraction and increases the generation efficiency.

In the mode of traditional waveguide generation 2 ($\eta_0 = 0.06, r_R = 0.6$), the radiation field of particles changes weakly in relation to the field of the same type in the superradiance mode 1. However, due to the increase in reflection and acceleration of injection, the amplitudes of the resonator waveguide field increase noticeably. Below in Fig. 6 the dependence on time of the square of the particle field averaged over the waveguide volume (solid lines) and the waveguide field is shown with and without taking into account the influence of particles in the waveguide volume on reflected waves.
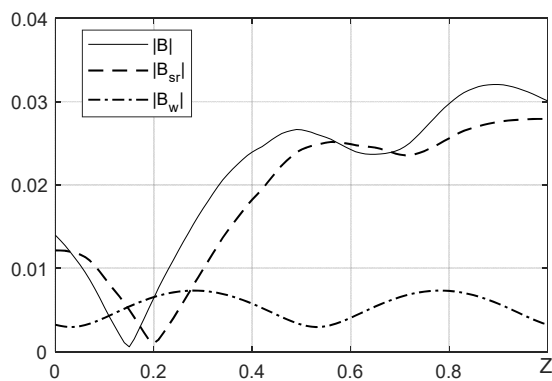
Figure 5. Distributions along the waveguide length of the amplitude modulus of the total field, the particle field, and the waveguide field in mode 1 at the moment τ=800 for the parameters in the case of the influence of particles in the waveguide volume on the reflected waves, according to conditions (13)

Figure 6. Time dependence of the averaged over the waveguide volume squares of the particle field (solid lines) and the waveguide field (dotted lines) in the waveguide generation mode 2 $(\eta_0 = 0.06, r_R = 0.2)$, thick lines in the case of the influence of particles in the waveguide volume on the reflected waves, according to conditions (13). Thin lines are the particle field and the reflected field in the absence of such influence according to conditions (14)

In the waveguide generation mode, i.e. in mode 2, the longitudinal velocity of electrons also decreases noticeably. In Fig. 7 it is not difficult to see the dependence on time of the average particle velocity over the volume of the waveguide in mode 2 ($\eta_0 = 0.06, r_R = 0.6$) the bold line in the case of taking into account the influence of particles on reflected waves, the thin line in the absence of such influence.

Figure 7. Time dependence of the average particle velocity over the waveguide volume in mode 2 ($\eta_0 = 0.06$, $r_R = 0.6$) the bold line in the case of taking into account the influence of particles on reflected waves, according to conditions (13). The thin line – in the absence of such influence, according to conditions (14).

Distributions of the amplitude moduli of the total field, particle field and waveguide field for mode 2, in particular, in the case of the influence of particles in the waveguide volume on reflected waves (see Fig. 8).
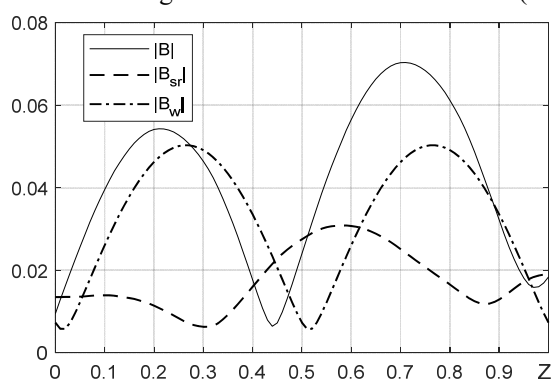
Figure 8. Distributions of the amplitude moduli of the total field, particle field and waveguide field in mode 2 at the moment $\tau=800$ along the waveguide length for the parameters in the case of the influence of particles in the waveguide volume on the reflected waves, according to conditions (13)

The waveguide-resonator field in this case is greater than the total particle field, the excess factor is $K = 2.77$.

3. CONCLUSIONS

In this paper, the generation process in a short cylindrical magnetoactive waveguide is considered. It is shown that even in the absence of reflection from the ends, a total radiation field of TM waves is formed in the waveguide by an ensemble of particles - rotating electrons, which corresponds to the superradiance mode. The possibility of generating a TM wave in a waveguide of the type under consideration - in a gyrotron in the superradiance mode was considered in [18-19]. However, a more general problem of forming a waveguide-resonance field, which is initiated by the field of an ensemble of particles - rotating electrons, is of interest. The appearance of a waveguide resonant field occurs due to reflection from the ends of the waveguide, taking into account the interaction of such reflected waves with particles in the volume of the active zone. It is these reflected waves that form a standing wave - a resonant waveguide field.

If the reflection coefficients from the waveguide ends are small and the particle injection rate is low, then the conditions for the dominant excitation of the total eigenfield of the particles are realized, which corresponds to the superradiance modes. The amplitudes of the resonator waveguide field are small. With increasing reflection from the ends and at a higher injection rate, the resonator waveguide field exceeds the total eigenfield of the electron oscillators in the active zone. That is, the traditional mode of generation of the resonator waveguide field is realized. Fig. 2 shows the zones of occurrence of the superradiance mode and excitation of the resonator waveguide field. The waveguide resonator field can be supported by particles in the waveguide volume, or it can be formed only due to reflection effects. It is important to note that the zones of dominance of superradiance and traditional resonator generation are always formed under different conditions of energy exchange between reflected waves and oscillators in the waveguide volume, described by conditions (13) and (14). Note that even with a decrease in the direct effect of oscillators in the volume on reflected waves, which meets conditions (14), the zones of different types of generation shift slightly. This is due to the presence of a total field of oscillators, which is capable of acting as an intermediary between the oscillators in the active zone and the waves reflected from the ends of the resonator, forming the waveguide resonator field. It is noted that the amplitudes of the eigenfields of electron oscillators in different modes differ slightly. The advantage of generation in the radiation mode is

an increase in the field amplitude at the end of the system in the direction of electron drift, which greatly simplifies energy extraction and increases the generation efficiency.

ORCID
Eugen Poklonskiy, https://orcid.org/0000-0001-5682-6694; **Volodymyr Kuklin,** https://orcid.org/0000-0002-0310-1582

REFERENCES
[1] J.W. Lord Rayleigh, "On Electrical Vibrations and the Constitution of the Atom," Philosophical magazine, vol. 6 ser. **11**, 117-122 (1906).
[2] A.V. Gaponov, M.I. Petelin, and V.K. Yulpatov, "The induced radiation of excited classical oscillators and its use in high-frequency electronics," Sov. Radiophysics and Quantum Electronics, **10**, 794–813 (1967). (in Russian)
[3] Ya.B. Fainberg, "Plasma electronics," Укр. Phis, J. **23**(11), 1885–1901 (1978). (in Russian)
[4] A.I. Akhiezer, I.A. Akhiezer, R.V. Polovin, A.G. Sitenko, and K.N. Stepanov, *Plasma Electrodynamics*, *Linear Theory*, vol. 1, (Pergamon Press, Oxford-New York, 1975) (International Series of Monographs in Natural Philosophy, vol.68).
[5] A.I. Akhiezer, I.A. Akhiezer, R.V. Polovin, A.G. Sitenko, and K.N. Stepanov, *Plasma Electrodynamics*, *Nonlinear theory and fluctuations*, vol. 2, (Pergamon Press, Oxford-New York, 1975) (International Series of Monographs in Natural Philosophy, vol. 69).
[6] V.A. Buts, A.N. Lebedev, and V.I. Kurilko, *The Theory of Coherent Radiation by Intense Electron Beams*, (Springer Berlin Heidelberg New York, 2006).
[7] V.A. Balakirev, N.I. Karbushev, A.O. Ostrovsky, and Yu.V. Tkach, *Theory of Cherenkov's Amplifiers and Generators on Relativistic Beams*, (Naukova Dumka, Kyiv, 1993).
[8] J. Weiland, and H. Wilhelmsson, *Coherent non-linear interaction of waves in plasmas*, (Pergamon Press, 1977).
[9] A. Dattner, "Resonance densities in a cylindrical plasma column," Phys. Rev. Lett. **10**, 205 (1963). https://doi.org/10.1103/PhysRevLett.10.205
[10] A. Nordsieck, "Theory of large signal behavior of travelingwave amplifiers," Proc. IRE, **41**(5), 630–631 (1953).
[11] V.A. Buts, "Stabilization of classic and quantum systems," PAST, (6), 146–148 (2012). https://vant.kipt.kharkov.ua/ARTICLE/VANT_2012_6/article_2012_6_146.pdf
[12] G.M. Zaslavsky, "Chaos, fractional kinetics, and anomalous transport," Phys. Rep. **371**, 461-580 (2002). https://doi.org/10.1016/S0370-1573(02)00331-9
[13] E.V. Poklonskiy, *et al.*, "On the development of super-radiation in noise condition," PAST, (3), 84-86 (2024). https://doi.org/10.46813/2024-151-084
[14] E.V. Poklonskiy, *et al.*, "On the wave generation in a magnetoactive waveguide," PAST, (5), 87-91 (2024). https://doi.org/10.46813/2024-153-087
[15] V.M. Kuklin, "The latest developments of the our Scientific Group of Kharkov University," PhysicalScience& Biophysics Journal (PSBJ) USA, **6**(2), (2022). https://doi.org/10.23880/psbj-16000218
[16] A.B. Kitsenko, and I.M. Pankratov, "Nonlinear stage of interaction of a flow of charged particles with plasma in a magnetic field," Sov. Plasma Physics, **4**(1), 227–234 (1978).
[17] V.M. Kuklin, *Selected chapters (theoretical physics)*, (V.N. Karazin KhNU, Kharkiv, 2021). http://dspace.univer.kharkov.ua/handle/123456789/16359
[18] A.G. Zagorodniy, P.I. Fomin, and A.P. Fomina, "Superradiation of electrons in a magnetic field and a nonrelativistic gyrotron," NAS of Ukraine, (4), 75–80 (2004).
[19] P.I. Fomin, and A.P. Fomina, "Dicke Superradiance on Landau Levels," PAST, (6), 45-48 (2001). https://vant.kipt.kharkov.ua/ARTICLE/VANT_2001_6/article_2001_6_45.pdf

ПРО ОСОБЛИВОСТІ ЗБУДЖЕННЯ ВІДКРИТИХ МАГНІТОАКТИВНИХ ХВИЛЕВОДІВ

Є.В. Поклонський[a], В.М. Куклін[b]
[a]Харківський національний університет імені В. Н. Каразіна, 61022, м. Харків, пл. Свободи, 4
[b]Харківський національний економічний університет імені С. Кузнеця. кафедра кібербезпеки та інформаційних технологій. пр. Науки, 2. 9 – А. 61165, Харків, Україна

Показано, що в об'ємі відкритого хвилеводу кожен електрон-осцилятор, що обертається в постійному магнітному полі, здатний генерувати хвилю ТЕ, для якої цей хвилевід прозорий. Ефективність генерації визначається швидкістю інжекції електронів і їх поздовжньою швидкістю вздовж осі хвилеводу. Вибрано режим генерації поля поблизу частоти відсічення з низькою груповою швидкістю, порівнянною з поздовжньою швидкістю інжектованих електронів. При цьому поперечна швидкість електронів значно перевищує їх поздовжню швидкість і групову швидкість хвилі. За відсутності відбиття поля від кінців хвилеводу кожен електрон вносить свій внесок у сумарне поле випромінювання, тобто можна вважати, що генерація поля відбувається в режимі надвипромінювання. Показано, що сумарне поле електронного потоку здатне утворювати резонаторне поле, яке складається з двох хвиль, що поширюються назустріч одна одній за рахунок навіть часткового відбиття від кінців хвилеводу. При малому відбитті полів від торців і малій дрейфовій швидкості електронів, що обертаються, домінує режим надвипромінювання, подібно до випадку збудження повністю відкритого хвилеводу. У разі помітного відбиття полів від торців системи при відносно високій швидкості їх поздовжньої інжекції відбиті поля значно перевищують сумарне поле випромінювачів і формується традиційний режим генерації поля хвилевідного резонатора. На площині «поздовжня швидкість руху – коефіцієнт відбиття» представлені зони, де домінує генерація резонаторного поля або генерація в умовах надвипромінювання. Розглянуто два випадки: коли відбиті хвилі утворюються тільки за рахунок відбиття від торців, а також коли враховується вплив активної зони електронів на відбиті хвилі в об'ємі хвилеводу. Суттєво, що середня амплітуда сумарного поля випромінювання частинок змінюється незначно для всіх розглянутих типів генерації. Резонансні ефекти при відбиванні від торців призводять до значного збільшення амплітуди поля хвилеводу.
Ключові слова: *електрони-осцилятори, що обертаються; магнітоактивний хвилевід; резонаторна генерація поля; режим надвипромінювання ТЕ хвилі.*

SPATIAL DYNAMICS OF A RADIALLY POLARIZED TERAHERTZ LASER BEAM WITH A PHASE SINGULARITY

Andrey V. Degtyarev, Mykola M. Dubinin, Vyacheslav A. Maslov*, Konstantin I. Muntean, Oleh O. Svystunov

V.N. Karazin Kharkiv National University, 4 Svoboda Sq., Kharkiv 61022, Ukraine
*Corresponding Author e-mail: v.a.maslov@karazin.ua
Received April 1, 2025; revised July 21, 2025; accepted August 4, 2025

Analytical expressions are obtained that describe the nonparaxial diffraction in free space of the TM_{01} mode with radial polarization of the field of the dielectric waveguide resonator of a terahertz laser during its interaction with a spiral phase plate with different topological charge (n). The physical features of the obtained vortex beams during their propagation and tight focusing are studied by numerical simulation. The integral diffraction Rayleigh-Sommerfeld transforms are used to simulate the propagation and focusing of the obtained beams. In free space the use of the spiral phase plate at the waveguide output with a topological charge of $n = 1$ leads to a change in the transverse beam profile from annular to a beam that has a field maximum on the axis, and then for $n = 2$ again to annular. During focusing the transverse distribution of the total field intensity in the absence of a spiral phase plate has a ring structure. In this case there is a slight intensity on the axis due to the contribution of the longitudinal component of the field. The transverse profile of the beam changes in the same way as during its propagation when using a phase plate. In this case the phase front changes from spherical to spiral with the presence of two ($n = 1$) and four ($n = 2$) branching vortices.

Keywords: *Terahertz laser; Dielectric waveguide resonator; Spiral phase plate; Vortex beams; Radial polarization; Radiation propagation; Tight focusing*
PACS: 42.55.Lt; 42.60.Da; 42.25.Bs; 47.32.C−

1. INTRODUCTION

Terahertz waves refer to electromagnetic radiation with frequencies in the range of 0.1 THz to 10 THz. These waves have unique characteristics such as high penetrating power, low ionizing power and small scattering. Due to these advantages terahertz waves have broad application prospects in imaging, communication and material characterization [1, 2].

Among the various structural beams vector beams with nonuniform polarization states have shown significant application value in many fields due to their unique light field distribution characteristics. Compared with spatially uniform polarized beams the polarization distribution of vector beams is spatially variable. Due to these properties, vector beams have a number of unique advantages such as precise focusing [3 – 6] and high image resolution [7, 8]. In the optical range, using the Richards-Wolf integral transforms [9 − 11], the features of focusing beams with nonuniform polarization were studied. It is shown that with tight focusing of radially polarized light a circular focal spot is observed. In this case the redistribution of energy between the components of the electric field strength occurs in such a way that the longitudinal component can make a significant contribution to the formation of the focal spot [12, 13].

Another type of structured optical fields with great potential for practical applications are vortex beams. Today optical vortices are used to manipulate microparticles, to enhance image contrast in microscopy, for metrology tasks, and, in particular, to increase the data transmission density in optical communication systems [14 − 17]. The expansion of vortex beam generation techniques into the terahertz (THz) spectral range has been expected to expand the scope of THz technologies. For example, THz vortex beams are attractive for wireless communications because they can support an infinite number of orbital angular momentum eigenstates characterized by their topological charges [18].

The study of the propagation of vortex laser beams in free space is important for understanding the features of their interaction with the environment. Such beams are characterized by the presence of orbital angular momentum, which affects their behavior during propagation. In free space vortices can demonstrate the stability of the wave front structure, which allows them to preserve their unique properties over long distances [19, 20].

Focusing of vortex laser beams in the terahertz range is a complex and at the same time promising area of research. Focused beams have unique properties that can be used to create super-dense foci, compact foci with dimensions below the diffraction limit, optical needles, light tunnels, flat-top foci, focal matrices, and others [21 − 23]. There are only a few works known in which the focusing of vortex beams in the terahertz range is studied. In [24, 25], a series of terahertz emitters with a spiral Fresnel zone plate was developed for direct generation of focused terahertz vortex beams. The authors [26, 27] proposed metasurfaces that can be used to focus incident waves with arbitrary polarization states into vortex beams carrying a certain topological charge.

It is well known that terahertz optically pumped molecular lasers have the advantages of high power, room temperature operation, and long-term stability over other practical terahertz radiation sources. Most optically pumped lasers use waveguide resonators, which make it possible to obtain sufficiently high powers (up to 1 W) in a continuous mode with relatively small cavity sizes [28]. Among the modes of such resonators the TM_{01} mode with radial field polarization, which has the lowest losses in this class of modes, is of interest.

A spiral phase plate (SPP) with an azimuthally varying thickness is one of the most well-known optical elements for the formation of vortex beams [29, 30]. The SPP works by directly imposing a helical phase shift on the incident laser beam, allowing almost 100 % of the incident radiation energy to be converted into the optical beam.

The aim of this work is to obtain analytical expressions for describing nonparaxial diffraction during propagation and focusing in free space of wave beams excited by the TM_{01} mode with radial polarization of the field of the waveguide resonator of a terahertz laser, during its interaction with a spiral phase plate. In addition, using numerical modeling, this work studies the physical properties of the resulting vortex beams during their propagation in free space and tight focusing.

2. THEORETICAL RELATIONSHIPS

We describe the propagation of laser radiation in free space along the $0z$ axis using the well-known integral Rayleigh-Sommerfeld transformations [31 − 33]. In a cylindrical coordinate system, we use the following expressions for the field components in different diffraction zones

$$E_r(\rho_1,\beta,z_1) = -\frac{i\,z_1}{\lambda r_1^2}\exp(ikr_1)\int_0^\infty\int_0^{2\pi}[E_r^0(\rho_0,\varphi)\cos(\varphi-\beta)-E_\varphi^0(\rho_0,\varphi)\sin(\varphi-\beta)]\times$$
$$\times\exp\left(ik\frac{\rho_0^2}{2r_1}\right)\exp\left[-ik\frac{\rho_1\rho_0\cos(\varphi-\beta)}{r_1}\right]\rho_0\,d\rho_0\,d\varphi, \tag{1.1}$$

$$E_\varphi(\rho_1,\beta,z_1) = -\frac{i\,z_1}{\lambda r_1^2}\exp(ikr_1)\int_0^\infty\int_0^{2\pi}[E_r^0(\rho_0,\varphi)\sin(\varphi-\beta)+E_\varphi^0(\rho_0,\varphi)\cos(\varphi-\beta)]\times$$
$$\times\exp\left(ik\frac{\rho_0^2}{2r_1}\right)\exp\left[-ik\frac{\rho_1\rho_0\cos(\varphi-\beta)}{r_1}\right]\rho_0\,d\rho_0\,d\varphi, \tag{1.2}$$

$$E_z(\rho_1,\beta,z_1) = \frac{-i}{\lambda r_1^2}\exp(ikr_1)\int_0^\infty\int_0^{2\pi}\left\{E_r^0(\rho_0,\varphi)[\rho_0-\rho_1\cos(\varphi-\beta)]+E_\varphi^0(\rho_0,\varphi)\rho_1\sin(\varphi-\beta)\right\}\times$$
$$\times\exp\left(ik\frac{\rho_0^2}{2r_1}\right)\exp\left[-ik\frac{\rho_1\rho_0\cos(\varphi-\beta)}{r_1}\right]\rho_0\,d\rho_0\,d\varphi, \tag{1.3}$$

where $k = 2\pi/\lambda$ is the wave number, λ is the wavelength, (ρ_0,φ) are the polar coordinates in the area where the input field is specified, (ρ_1,β,z_1) are the cylindrical coordinates in the observation plane, $E_r^0(\rho_0,\varphi)$ and $E_\varphi^0(\rho_0,\varphi)$ are the complex amplitudes r and φ components of the input electric field, $r_1 = \sqrt{\rho_1^2+z_1^2}$.

The modes of the studied dielectric resonator coincide with the modes of a hollow circular dielectric waveguide. Therefore, in the initial plane we specify radiation in the form of a symmetrical radially polarized TM_{01} mode. The normalized expressions for the cylindrical components of the electromagnetic field of this mode in the source plane $z = 0$ have the following form [34]

$$TM_{01}\text{ mode }\begin{cases}E_r^0(\rho_0,\varphi) = B_{01}J_1\left(U_{01}\dfrac{\rho_0}{a}\right), \\[2mm] E_\varphi^0(\rho_0,\varphi) = 0,\end{cases} \tag{2}$$

where a is the waveguide radius, J_1 is the Bessel function of the 1st kind of the first order, U_{01} is the first root of the equation $J_1(x) = 0$, $B_{01} = \dfrac{1}{a\sqrt{\pi}J_0(U_{01})}$ is the normalizing factor for TM_{01} mode.

Let us consider the interaction between of this mode and a spiral phase plate with its arbitrary topological charge (n) [35]. The SPP is positioned at the output of a waveguide with an aperture of the same diameter (Figure 1). The complex transmission function of this SPP with a radius a in polar coordinates has the form [36]:

$$T_n(\rho_0, \varphi) = \text{circ}\left(\frac{\rho_0}{a}\right) \exp(in\varphi), \tag{3}$$

where $\text{circ}(\cdot)$ is the circular function.
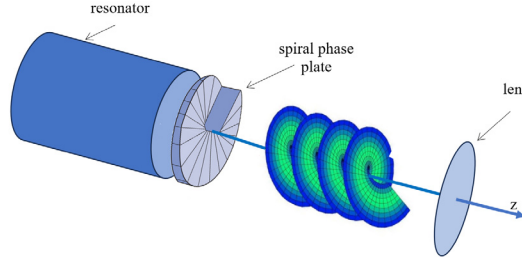
Figure 1. Topology of the model.

For simplifying calculations, integration over the angle φ in (1) can be performed using known relations for the integer $m \geq 0$ from [32]

$$\int_0^{2\pi} \cos(m\varphi + \varphi_0) \exp[-ix\cos(\varphi - \theta)d\varphi] = 2\pi(-i)^m J_m(x)\cos(m\theta + \varphi_0),$$

$$\int_0^{2\pi} \sin(m\varphi + \varphi_0) \exp[-ix\cos(\varphi - \theta)]d\varphi = 2\pi(-i)^m J_m(x)\sin(m\theta + \varphi_0).$$

Then from here we can obtain the following relation

$$\int_0^{2\pi} e^{-ix\cos(\varphi - \beta)} e^{in\varphi} d\varphi = 2\pi e^{in\beta}(-i)^n J_n(x). \tag{4}$$

Using Euler's formula for trigonometric functions and taking into account (4), we can obtain expressions for the following integrals:

$$\int_0^{2\pi} e^{-ix\cos(\varphi - \beta)} e^{in\varphi} \sin m\varphi\, d\varphi = -i\pi[e^{i(n+m)\beta}(-i)^{n+m} J_{n+m}(x) - e^{i(n-m)\beta}(-i)^{n-m} J_{n-m}(x)], \tag{5.1}$$

$$\int_0^{2\pi} e^{-ix\cos(\varphi - \beta)} e^{in\varphi} \cos m\varphi\, d\varphi = \pi[e^{i(n+m)\beta}(-i)^{n+m} J_{n+m}(x) + e^{i(n-m)\beta}(-i)^{n-m} J_{n-m}(x)], \tag{5.2}$$

$$\int_0^{2\pi} e^{-ix\cos(\varphi - \beta)} e^{in\varphi} \sin(\varphi - \beta)\, d\varphi = \pi(-i)^{n+2} e^{in\beta}[J_{n+1}(x) + J_{n-1}(x)], \tag{5.3}$$

$$\int_0^{2\pi} e^{-ix\cos(\varphi - \beta)} e^{in\varphi} \cos(\varphi - \beta)\, d\varphi = \pi(-i)^{n+1} e^{in\beta}[J_{n+1}(x) - J_{n-1}(x)]. \tag{5.4}$$

Also, using formulas (5.1 – 5.4), we obtain expressions for the field components describing the nonparaxial diffraction of vortex beams excited by the TM_{01} mode in free space. They have the following form:

$$E_r(\rho_1, \beta, z_1) = \frac{(-i)^{n+2} k z_1}{2r_1^2} e^{i(n\beta + kr_1)} B_{01}[I1_{1n+1}(\rho_1, z_1) - I1_{1n-1}(\rho_1, z_1)], \tag{6.1}$$

$$E_\varphi(\rho_1, \beta, z_1) = \frac{(-i)^{n+3} k z_1}{2r_1^2} e^{i(n\beta + kr_1)} B_{01}[I1_{1n+1}(\rho_1, z_1) + I1_{1n-1}(\rho_1, z_1)], \tag{6.2}$$

$$E_z(\rho_1, \beta, z_1) = \frac{(-i)^{n+1} k}{2r_1^2} e^{i(n\beta + kr_1)} B_{01}\{2I2_{1n}(\rho_1, z_1) + i\rho_1[I1_{1n+1}(\rho_1, z_1) - I1_{1n-1}(\rho_1, z_1)]\}, \tag{6.3}$$

where the following notations are introduced

$$I1_{1n}(\rho_1, z_1) = \int_0^a J_1\left(U_{01}\frac{\rho_0}{a}\right) J_n\left(\frac{k\rho_1\rho_0}{r_1}\right) \exp\left(ik\frac{\rho_0^2}{2r_1}\right) \rho_0\, d\rho_0,$$

$$I2_{1n}(\rho_1, z_1) = \int_0^a J_1\left(U_{01}\frac{\rho_0}{a}\right) J_n\left(\frac{k\rho_1\rho_0}{r_1}\right) \exp\left(ik\frac{\rho_0^2}{2r_1}\right)\rho_0^2 \, d\rho_0.$$

The field at the input and output of a lens with radius a_1 is described using the phase correction function [37] $U(\rho_1) = \exp\left(\frac{-i\pi\rho_1^2}{\lambda F}\right)$, where F is the focal length of a lens. By repeatedly applying the Rayleigh-Sommerfeld integral transformations (1) to the components of the electric field strength vector (6) found after phase correction, we obtain analytical expressions for the transverse and longitudinal components of the field in the focal region of the lens. These expressions for the components of the field of the vortex beam excited by the radially polarized TM_{01} mode at a distance z_2 from the lens have the form

$$E_r(\rho_2, \theta, z_2) = \frac{(-i)^{2n}k^2 z_1 z_2}{2r_2^2}\exp[i(n\theta + kr_2)]B_{01}\times$$

$$\times \int_0^{a_1}\left[I1_{1n+1}(\rho_1, z_1)J_{n+1}(x) + I1_{1n-1}(\rho_1, z_1)J_{n-1}(x)\right]\frac{\exp[ik(r_1 + \frac{\rho_1^2}{2r_2})]}{r_1^2}U(\rho_1)\rho_1 d\rho_1, \qquad (7.1)$$

$$E_\varphi(\rho_2, \theta, z_2) = \frac{(-i)^{2n+1}k^2 z_1 z_2}{2r_2^2}\exp[i(n\theta + kr_2)]B_{01}\times$$

$$\times \int_0^{a_1}\left[[I1_{1n+1}(\rho_1, z_1)J_{n+1}(x) - I1_{1n-1}(\rho_1, z_1)J_{n-1}(x)]\right]\frac{\exp[ik(r_1 + \frac{\rho_1^2}{2r_2})]}{r_1^2}U(\rho_1)\rho_1 d\rho_1, \qquad (7.2)$$

$$E_z(\rho_2, \theta, z_2) = \frac{(-i)^{2n-1}k^2 z_1}{2r_2^2}\exp[i(n\theta + kr_2)]B_{01}\times$$

$$\times \int_0^{a_1}\left\{\rho_1 J_n(x)[I1_{1n+1}(\rho_1, z_1) - I1_{1n-1}(\rho_1, z_1)] + i\rho_2[I1_{1n+1}(\rho_1, z_1)J_{n+1}(x) + I1_{1n-1}(\rho_1, z_1)J_{n-1}(x)\right\}\times \qquad (7.3)$$

$$\times\frac{\exp[ik(r_1 + \frac{\rho_1^2}{2r_2})]}{r_1^2}U(\rho_1)\rho_1 d\rho_1.$$

3. NUMERICAL RESULTS AND DISCUSSIONS

Using the obtained expressions, calculations were carried out to determine the distribution of the total intensity ($I = |E_r|^2 + |E_\varphi|^2 + |E_z|^2$) as well as the intensity and phase ($\varphi = \text{arctg}(\text{Im}(E_i)/\text{Re}(E_i)), i = x, y, z$) of individual field components of vortex laser beams excited by a radially polarized TM_{01} mode of a dielectric waveguide resonator of a terahertz laser, as they propagate in free space and under tight focus conditions. In the calculations the radiation wavelength was $\lambda = 0.4326$ mm, which corresponds to the generation line of a formic acid (HCOOH) terahertz laser with optical pumping [38]. The SPP was placed at the output of the waveguide resonator and formed the investigated vortex laser beams. The waveguide and SPP had identical diameters of $2a = 35$ mm, and the lens diameter was $2a_1 = 50$ mm. The focal length of the lens was $F = 36.36$ mm [39, 40] which provided the conditions for tight focusing (the numerical aperture of the lens was NA = 0.68, where NA = a_1 / F).

Figure 2 shows the longitudinal intensity distributions of the field (a1 – a3), as well as the transverse intensity distributions in the regions of maximum field intensity (b1 – b3) for laser beams without SPP ($n = 0$) and vortex beams ($n = 1, 2$) in free space. The longitudinal field intensity distributions are presented in the Fresnel diffraction zone for $z_1 = 100 – 1000$ mm.

From Figure 2 (a1, b1) it can be seen that for SPP with a topological charge of $n = 0$ in the absence of a phase plate the investigated beam has a ring-like shape in the cross-section. The maximum intensity I_{max} of the laser beam at $n = 0$ is observed at a distance of $z_1 = 175$ mm from SPP and it is equal to 0.0023 absolute units, which corresponds to the intensity at the output mirror of the waveguide resonator. The I_{max} values in the regions of maximum intensity remain almost unchanged when using SPP. Additionally, at the distances where the maximum intensity regions are observed, the effective beam diameter d_s was calculated for different topological charges using the formula:

$$d_s = 2\sqrt{\frac{2\int_0^{2\pi}\int_0^{\infty} \rho_1^2 I(\rho_1,\beta,z_1)\rho_1 d\rho_1 d\beta}{\int_0^{2\pi}\int_0^{\infty} I(\rho_1,\beta,z_1)\rho_1 d\rho_1 d\beta}}. \tag{8}$$

The value of d_s in the region of maximum intensity ($z_1 = 175$ mm) for $n = 0$ is equal to 21 mm.
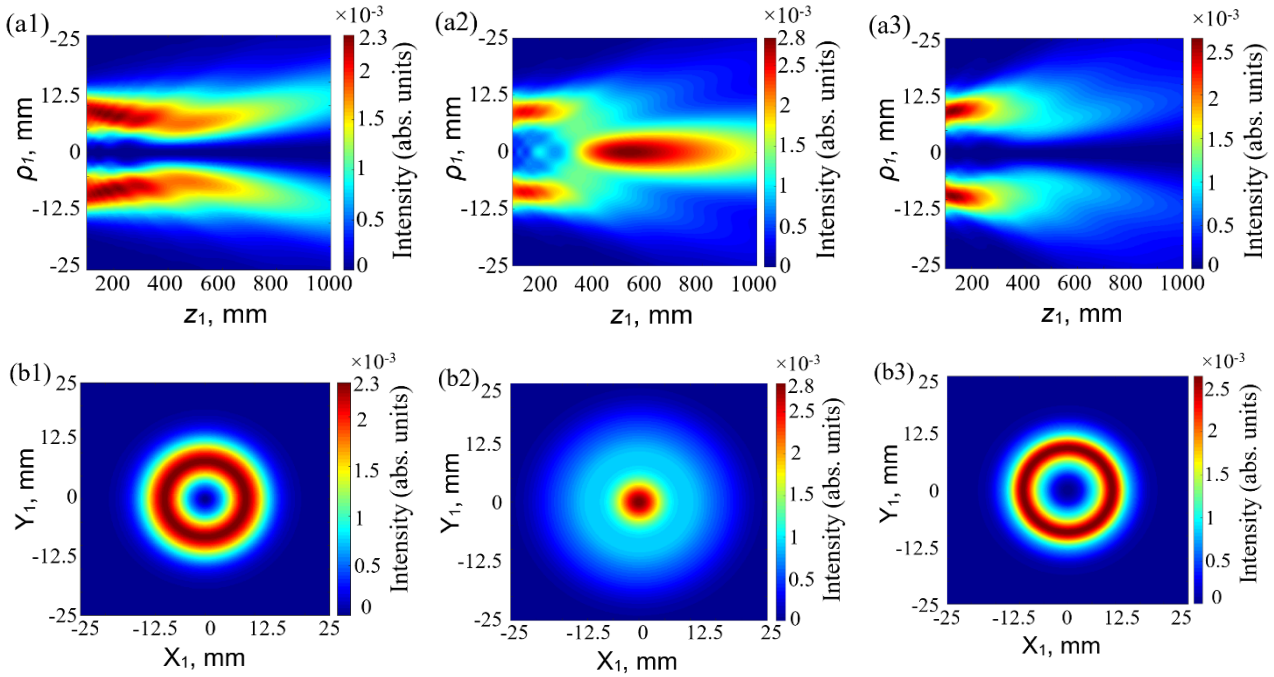
Figure 2. Longitudinal intensity distributions of the field (a1 – a3), as well as transverse intensity distributions in the regions of maximum field intensity (b1 – b3) for different values of the topological charge in free space. The first, second and third columns correspond to $n = 0$, $n = 1$ and $n = 2$, respectively.

The use of SPP with a topological charge of $n = 1$ at the waveguide output leads to a change in the beam profile from a ring-shaped structure to a profile with a field maximum on the axis (Figure 2 (b2)). This behavior of the beam profile change is due to the fact that, as can be seen from the integral expressions for the field components (6.1 – 6.3), these components have a minimum on the axis in the absence of SPP at the waveguide output. When SPP with $n = 1$ is installing, these field components reach their maximum value on the axis due to the influence of the second term in the expressions for these components. In this case the region of maximum intensity shifts to a distance of $z_1 = 527$ mm from SPP (Figure 2 (a2)) and the effective beam diameter increases to $d_s = 27.5$ mm.

A subsequent change in the value of the topological charge ($n = 2$) leads to a zero value of these field components on the axis. As the topological charge increases from $n = 1$ to $n = 2$, the beam profile restores its initial ring-shaped structure (Figure 2 (a3, b3)). The region of maximum intensity is located at a distance of $z_1 = 130.5$ mm (Figure 2 (a3)), and the effective beam diameter d_s in this region, as in the absence of SPP, is equal to 21 mm.

Additionally, the dependencies of the relative contribution η of the field components to the power of the laser beam in the Fresnel diffraction zone were calculated for topological charges $n = 1, 2$ according to the formula:

$$\eta(z_1) = \frac{\int_0^{2\pi}\int_0^{\infty} |E_{r,\phi,z}(\rho_1,\beta,z_1)|^2 \rho_1 d\rho_1 d\beta}{\int_0^{2\pi}\int_0^{\infty}\left[|E_r(\rho_1,\beta,z_1)|^2 + |E_\phi(\rho_1,\beta,z_1)|^2 + |E_z(\rho_1,\beta,z_1)|^2\right]\rho_1 d\rho_1 d\beta}. \tag{9}$$

In the absence of SPP the total field intensity is determined by the radial E_r component. The contribution of the E_z component to the total beam power is negligible; therefore, the graph of the field components contribution to the laser beam power is not presented.

The results of calculations of the dependence of the relative contribution η of the field components to the power of the laser beam during its propagation in free space for topological charges of SPP $n = 1, 2$ are shown in Figure 3. For $n = 1$ the contribution of the radial E_r component decreases with increasing distance from SPP, while the contribution of the azimuthal component E_φ gradually increases and begins to dominate at large distances (Figure 3a). The contribution of the longitudinal component E_z remains practically constant and has a negligible effect on the beam power over the entire studied range. For $n = 2$ an increase in the contribution of the azimuthal component to the beam power is observed, indicating a growing role of this component with increasing topological charge (Figure 3b).
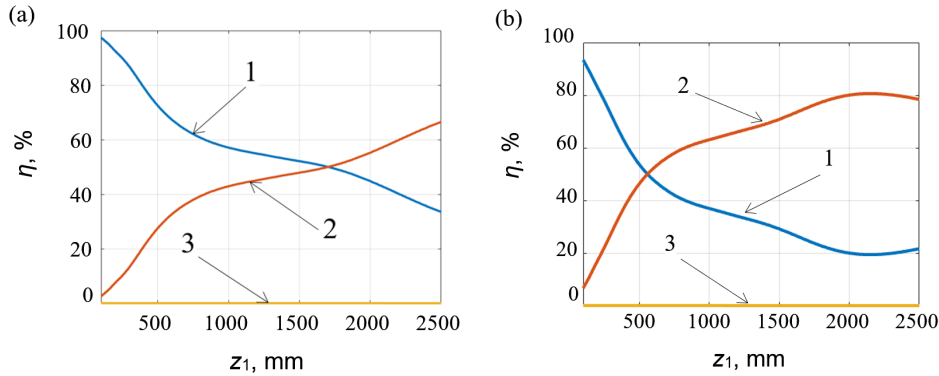
Figure 3. Dependencies of the relative contribution η of the field components $(1 - E_r, 2 - E_\varphi, 3 - E_z)$ to the power of the vortex laser beam on the function of the distance z_1 from SPP for topological charges $n = 1$ (a), $n = 2$ (b).

The spatial-energy characteristics of vortex laser beams in the focal region of the lens were also studied under the condition of tight focusing. A short focal length lens $(F = 36.36$ mm) was installed in the region of maximum field intensity for different topological beam charges to fulfill this condition. The longitudinal field intensity distributions of laser beams for various topological charge values ($n = 0, 1, 2$) are shown in Figure 4. The figures indicate that the maximum intensity value for these topological charges is observed at $n = 1$ and reaches 2.2 absolute units (Figure 4b).
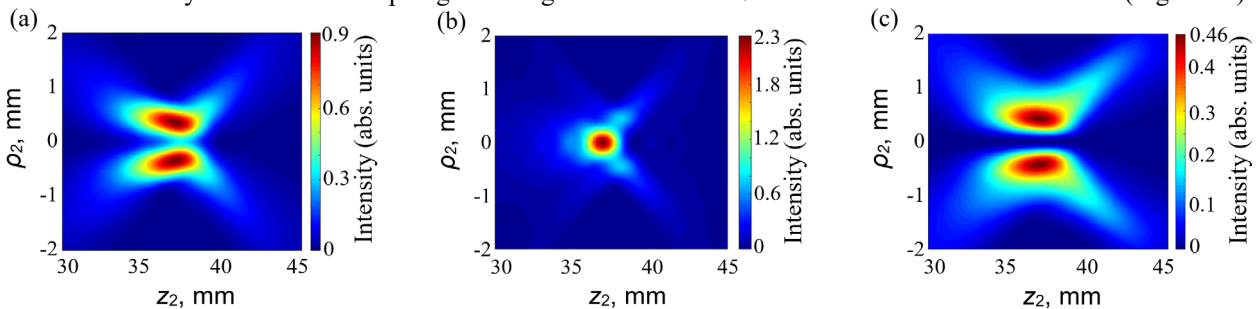
Figure 4. Longitudinal field intensity distributions of the laser beam without SPP ($n = 0$) and vortex beams ($n = 1, 2$) in the focal region of the lens.

The dependencies of the relative contribution η of the electric field components for focused laser beams to their total power were calculated for different topological charges. The results are shown in Figure 5.
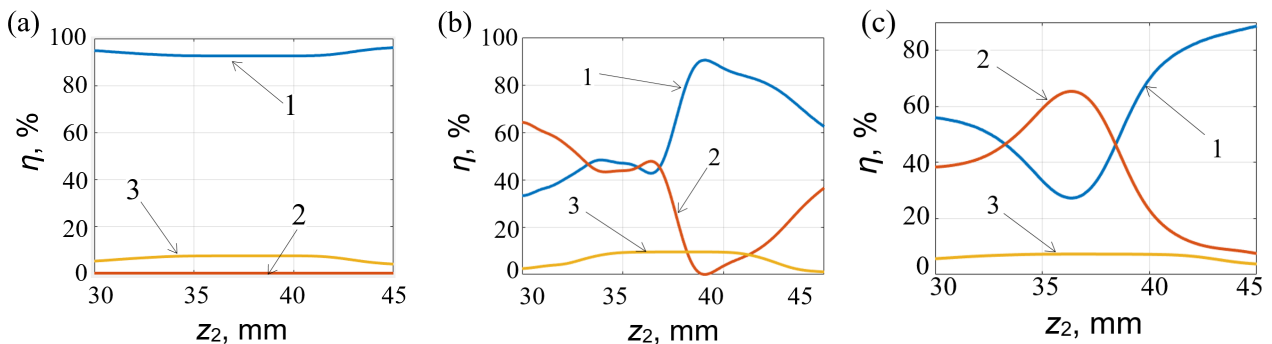
Figure 5. Dependencies of the relative contribution η of the field components $(1 - E_r, 2 - E_\varphi, 3 - E_z)$ to the power of the laser beam without SPP ($n = 0$) and vortex beams ($n = 1, 2$) on the function of the distance z_2 from the lens.

In the case of zero topological charge the radial component is dominant, which maintains a stable high level of relative contribution $\eta \approx 90$ % throughout the entire range of the focal region (Figure 5a). The contribution of the azimuthal component in this case is zero, and the longitudinal component has a small increase in the central part of the focal region, not exceeding 10 % of the beam total power. The introduction of a topological charge into the beam ($n = 1$) leads to a

significant redistribution of energy in the beam between the radial and azimuthal components of the electric field in the focal region (Figure 5b). The contribution of the azimuthal component is dominant at distances $z_2 \approx 30 - 35$ mm to the geometric focus, while the radial component has a smaller contribution to the total beam power in this region. However, the contribution of the azimuthal component significantly changes at a distance $z_2 \approx 36 – 40$ mm, while the contribution of the radial component begins to grow and reaches a maximum after the geometric focus of the lens. The contribution of the longitudinal component to the beam power, as in the case of $n = 0$, remains insignificant but it shows growth in the region of the geometric focus. The redistribution of the contribution to the total beam power for the radial and azimuthal components is observed even more for the topological beam charge $n = 2$. The contribution of the longitudinal component also shows an increase in the geometric focus region of the lens (Figure 5c).

Figure 6 shows the spatial transverse distributions of the total intensity, as well as the intensity and phase of individual components of the electric field for a tightly focused laser beam in the absence of SPP. In this case the total intensity distribution has a ring-shaped structure. However, there is a small field intensity on the axis (Figure 6(a1)), which is caused by the influence of the longitudinal component (Figure 6 (b2)). In this case the azimuthal component is zero. The phase front of both components is spherical (Figure 6 (c1, c2)), which is explained by the absence of orbital angular momentum in the radiation. As a result of focusing the effective beam diameter d_f defined similarly (8) in the region of maximum intensity ($z_2 = 37$ mm) decreases to $d_f = 2.4$ mm compared to the beam diameter d_s during propagation in free space ($z_1 = 175$).
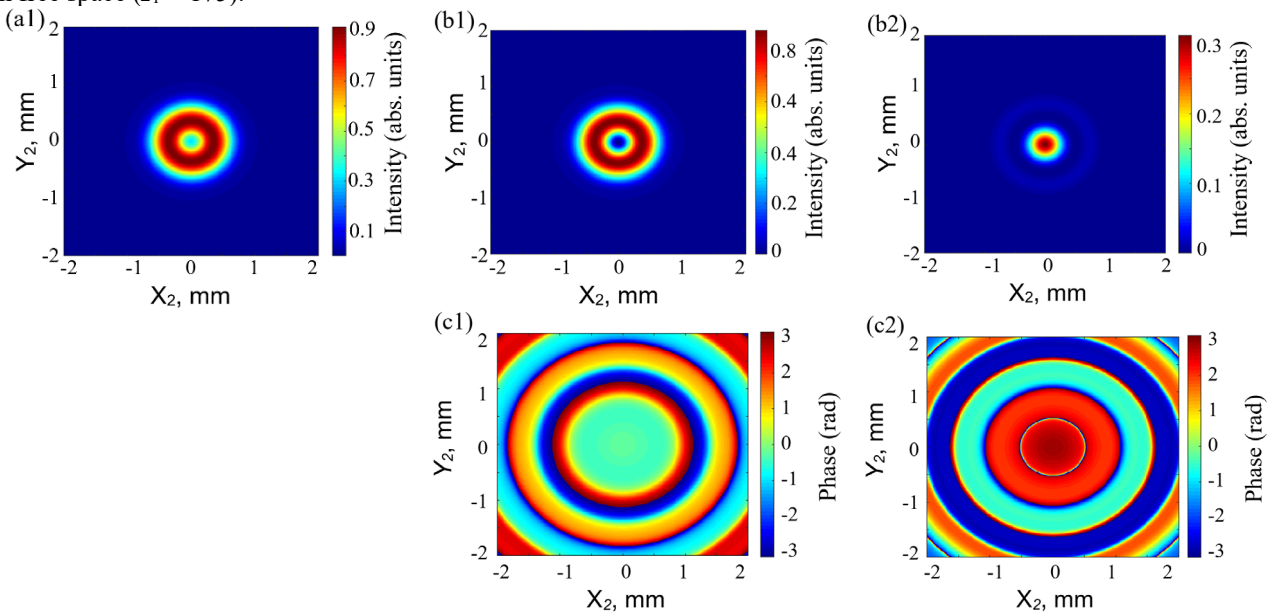
Figure 6. Transverse distributions of the total field intensity (a1), as well as the intensity (b1, b2) and phase (c1, c2) of the field for the E_r (b1, c1) and E_z (b2, c2) components of a tightly focused laser beam in the absence of SPP.

Analysis of the vortex laser beam for $n = 1$ shows that the total intensity distribution has a maximum on the axis (Figure 7(a1)).
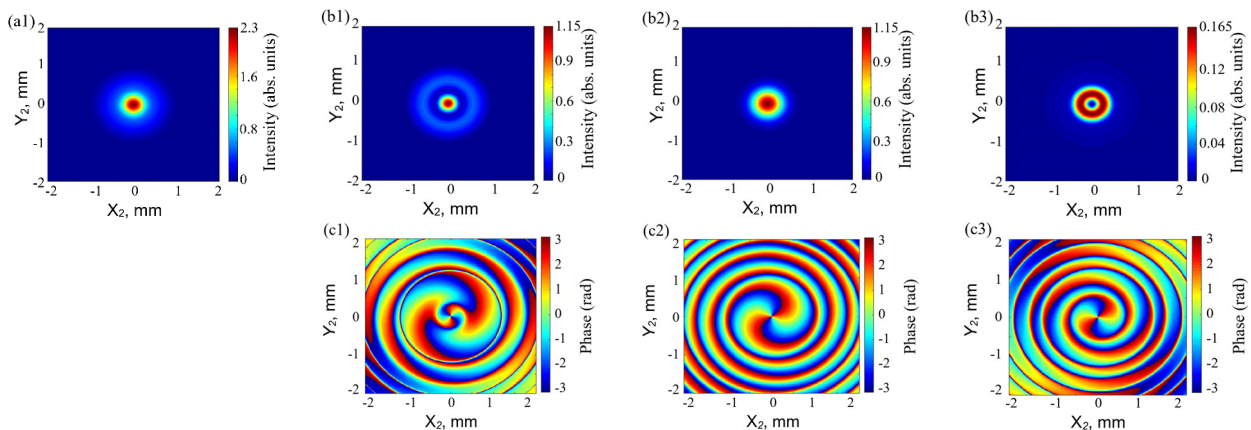
Figure 7. Transverse distributions of the total field intensity (a1), as well as the intensity (b1 – b3) and phase (c1 – c3) of the field for the E_r (b1, c1), E_ϕ (b2, c2) and E_z (b3, c3) components of a tightly focused vortex laser beam with a topological charge of $n = 1$.

The effective beam diameter d_f at $z_2 = 37$ mm compared to the beam diameter d_s during propagation in free space decreases to $d_f = 1.0$ mm. Radial and azimuthal components make equal contributions to the field intensity distribution

in the region of geometric focus (Figure 7 (b1, b2)). Meanwhile, the longitudinal component exhibits a ring-shaped field distribution and has almost no effect on the total intensity (Figure 7 (b3)). The phase distribution of all three field components represents a vortex with two branches (Figure 7 (c1 – c3)).

For the beam with a topological charge of $n = 2$ the total field intensity distribution has a pronounced ring-shaped structure (Figure 8 (a1)). The transverse intensity distribution for all three field components also has a ring-shaped profile in the focal region (Figure 8 (b2 – b3)). The effective beam diameter d_f at $z_2 = 37$ mm decreases to $d_f = 3.7$ mm compared to the beam diameter d_s during propagation in free space. The phase distribution of all three components shows the presence of a vortex with four branches (Figure 8 (c1 – c3)).
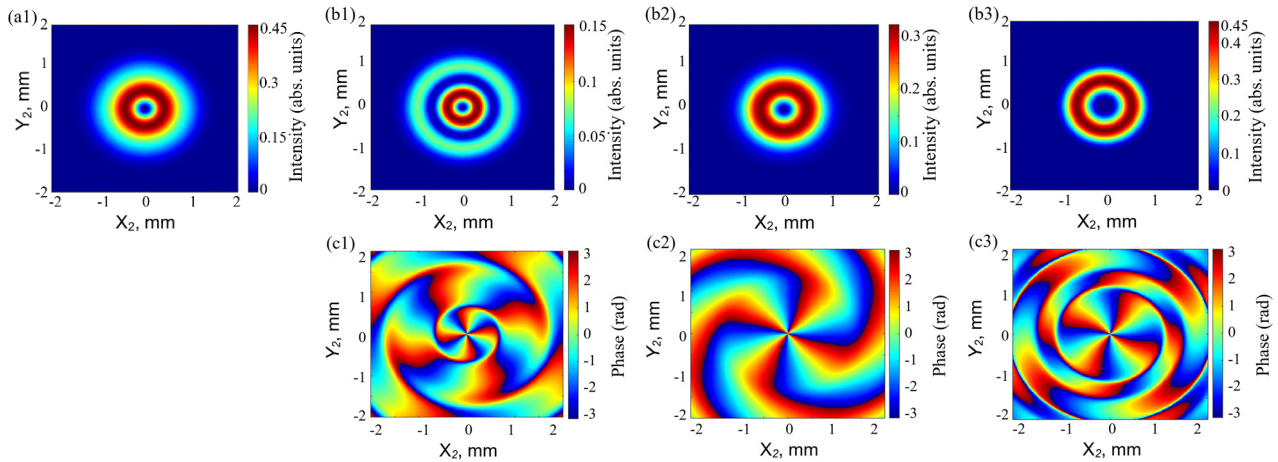
Figure 8. Transverse distributions of the total field intensity (a1), as well as the intensity (b1 – b3) and phase (c1 – c3) of the field for the E_r (b1, c1), E_ϕ (b2, c2) and E_z (b3, c3) components of a tightly focused vortex laser beam with a topological charge of $n = 2$

3. CONCLUSIONS

Analytical expressions have been obtained that describe nonparaxial diffraction in free space of the TM_{01} mode with radial polarization of the field of the dielectric resonator of a waveguide terahertz laser during its interaction with a spiral phase plate with different topological charges (n). Physical features of the obtained vortex beams during their propagation in free space and tight focusing are studied by numerical modeling.

It is shown that the use of SPP at the waveguide output with a topological charge $n = 1$ leads to a change in the beam profile during its propagation in free space from a ring-shaped beam to a beam having a field maximum on the axis. A subsequent change in the value of the topological charge ($n = 2$) leads to a zero value of these field components on the axis. In the absence of a spiral phase plate the total intensity of the beam field is determined by the radial and longitudinal components, whereas in its presence it is determined by all three components of the field.

The distribution of the total field intensity in the absence of a spiral phase plate has a ring structure with tight focusing. At the same time a slight field intensity is observed on the axis due to the contribution of the longitudinal component. The total distribution of field intensity has a maximum on the axis and the effective beam diameter d_f reaches a minimum value of 1 mm when using SPP with a topological charge $n = 1$. In this case the phase distribution of the field components is characterized by the presence of two vortices. For the beam with a topological charge of $n = 2$ the distribution of the total intensity has a clearly defined ring structure and the phase distribution of the field components demonstrates the presence of four vortices.

ORCID

Andrey V. Degtyarev, https://orcid.org/0000-0003-0844-4282; **Mykola M. Dubinin,** https://orcid.org/0000-0002-7723-9592
Vyacheslav O. Maslov, https://orcid.org/0000-0001-7743-7006; **Konstantin I. Muntean,** https://orcid.org/0000-0001-6479-3511
Oleh O. Svystunov, https://orcid.org/0000-0002-4967-5944

REFERENCES

[1] G.S. Park, M. Tani, J.S. Rieh, and S.Y. Park, *Advances in Terahertz Source Technologies*, (CRC Press, 2024).
[2] A. Saha, A. Biswas, K. Ghosh, and N. Mukhopadhyay, *Optical to Terahertz Engineering*, (Springer, 2023).
[3] B. Gu, Y. Hu, X. Zhang, M. Li, Z. Zhu, G. Rui, and Y. Cui, "Angular momentum separation in focused fractional vector beams for optical manipulation", Optics Express, **29**(10), 14705 (2021). https://doi.org/10.1364/OE.423357
[4] B. Gao, J. Wen, G. Zhu, L. Ye, and L.G. Wang, "Precise measurement of trapping and manipulation properties of focused fractional vortex beams", Nanoscale, **14**(8), 3123 (2022). https://doi.org/10.1039/D1NR06163A
[5] B. Pant, B.K. Mishra, S. Singh, and B.K. Singh, "Mode transformation and dark spot formation of cylindrical vector beams by thin dielectric film", Optics & Laser Technology, **180**, 111539 (2025). https://doi.org/10.1016/j.optlastec.2024.111539

[6] J. Ma, Z. Xie, and X. Yuan, "Tailoring arrays of optical stokes skyrmions in tightly focused beams", Laser & Photonics Reviews, **19**(3), 2401113 (2025). https://doi.org/10.1002/lpor.202401113

[7] M. Liu, Y. Lei, L. Yu, X. Fang, Y. Ma, L. Liu, and P. Gao, "Super-resolution optical microscopy using cylindrical vector beams", Nanophotonics, **11**(15), 3395 (2022). https://doi.org/10.1515/nanoph-2022-0241

[8] X. Yuan, H. Guo, S. Zhuang, and J. Hu, "Generation and high-resolution focusing of higher-order vector beam via metasurface", IEEE Photonics Journal, **16**, 2201206 (2024). https://doi.org/10.1109/JPHOT.2024.3406534

[9] S. Boichenko, "Fast-speed algorithm to compute tight focusing of laser beams: Effectiveness of circularly polarized vortex beam series as a mathematical basis", Physical Review A, **109**(4), 043501 (2024). https://doi.org/10.1103/PhysRevA.109.043501

[10] V.V. Kotlyar, S.S. Stafeev, V.D. Zaitsev, A.M. Telegin, and E.S. Kozlova, "Spin–orbital transformation in a tight focus of an optical vortex with circular polarization", Applied Sciences, **13**(14), 8361 (2023). https://doi.org/10.3390/app13148361

[11] Y. Miao, L. Wang, Q. Zhang, X. Sun, X. Gao, J. Wan, and S. Zhuang, "Tight-focusing properties of propagable fractional-order vector vortex beams", Journal of the Optical Society of America B, **40**(5), 1113 (2023). https://doi.org/10.1364/JOSAB.485509

[12] D. Maluenda, M. Aviñoá, K. Ahmadi, R. Martínez-Herrero, and A. Carnicer, "Experimental estimation of the longitudinal component of a highly focused electromagnetic field", Scientific Reports, **11**(1), 17992 (2021). https://doi.org/10.1038/s41598-021-97164-z

[13] Z. Qing, W. Yan, X. Long, Z. Yuan, Z.C. Ren, X.L. Wang, and H.T. Wang, "Longitudinal manipulation of local nonseparability in vector beams", Optics Letters, **49**(10), 2557 (2024). https://doi.org/10.1364/OL.524647

[14] D.A. Ikonnikov, S.A. Vyunisheva, D.V. Prokopova, N.N. Losevsky, S.A. Samagin, S.P. Kotova, and A.M. Vyunishev, "Configurable vortex laser beams for optical manipulations of microparticle ensembles", Laser Physics Letters, **20**(8), 086002 (2023). https://doi.org/10.1088/1612-202X/ace0af

[15] J. Zeng, Y. Dong, Y. Wang, J. Zhang, and J. Wang, "Optical imaging using orbital angular momentum: interferometry, holography and microscopy", Journal of Lightwave Technology, **41**(7), 2025 (2022). https://doi.org/10.1109/JLT.2022.3225214

[16] M. Cheng, W. Jiang, L. Guo, J. Li, and A. Forbes, "Metrology with a twist: probing and sensing with vortex light", Light: Science & Applications, **14**(1), 4 (2025). https://doi.org/10.1038/s41377-024-01665-1

[17] F. Pang, L. Xiang, H. Liu, L. Zhang, J. Wen, X. Zeng, and T. Wang, "Review on fiber-optic vortices and their sensing applications", Journal of Lightwave Technology, **39**(12), 3740 (2021). https://opg.optica.org/jlt/abstract.cfm?URI=jlt-39-12-3740

[18] S.K. Noor, M.N.M. Yasin, A.M. Ismail, M.N. Osman, P.J. Soh, N.Ramli, and A.H. Rambe, "A review of orbital angular momentum vortex waves for the next generation wireless communications", Ieee Access, **10**, 89465 (2022). https://doi.org/10.1109/ACCESS.2022.3197653

[19] D. Bongiovanni, D. Li, M. Goutsoulas, H. Wu, Y. Hu, D. Song, and Z. Chen, "Free-space realization of tunable pin-like optical vortex beams", Photonics Research, **9**(7), 1204 (2021). https://doi.org/10.1364/PRJ.420872

[20] G. Wang, X. Weng, X. Kang, Z. Li, K. Chen, X. Gao, and S. Zhuang, "Free-space creation of a perfect vortex beam with fractional topological charge", Optics Express, **31**(4), 5757 (2023). https://doi.org/10.1364/OE.483304

[21] Z. Shen, and S. Huang, "Generation of subdiffraction optical needles by simultaneously generating and focusing azimuthally polarized vortex beams through Pancharatnam–Berry metalenses", Nanomaterials, **12**(22), 4074 (2022). https://doi.org/10.3390/nano12224074

[22] J. Chen, and Q. Xu, "Superlong uniform light tunnel created by focusing radially polarized vortex beam", Journal of Applied Physics, **124**, 4 (2018). https://doi.org/10.1063/1.5033926

[23] P.B. Singh, and B. Kumar, "Formation of subwavelength tunable flat-top focus with double foci characteristic by tightly focused cylindrical vector beams", Optics Communications, **572**, 130972 (2024). https://doi.org/10.1016/j.optcom.2024.130972

[24] X. Zhang, Y. Xu, B. Hong, F. Zhang, A. Wang, and W. Zhao, "Generation of a focused THz vortex beam from a spintronic THz emitter with a helical Fresnel zone plate", Nanomaterials. **13**(14), 2037 (2023). https://doi.org/10.3390/nano1314203

[25] X. Feng, X. Chen, Y. Lu, Q. Wang, L. Niu, Q. Xu, and W. Zhang, "Direct emission of focused terahertz vortex beams using Indium-Tin-Oxide-based Fresnel zone plates", Advanced Optical Materials, **11**(1), 2201628 (2023). https://doi.org/10.1002/adom.202201628

[26] M. Zhong, and J.S. Li, "Terahertz vortex beam and focusing manipulation utilizing a notched concave metasurface", Optics Communications, **511**, 127997 (2022). https://doi.org/10.1016/j.optcom.2022.127997

[27] H. Li, C. Zheng, H. Xu, J. Li, C. Song, F. Yang, and J. Yao, "All-graphene geometric terahertz metasurfaces for generating multi-dimensional focused vortex beams", Opt. Laser Technol, **159**, 108986 (2023). https://doi.org/10.1016/j.optlastec.2022.108986

[28] J. Farhoomand, and H.M. Pickett, "Stable 1.25 watts CW far infrared laser radiation at the 119 μm methanol line", Int. J. Infrared Millim. Waves, **8**, 441 (1987). https://doi.org/10.1007/BF01013257

[29] M.W. Beijersbergen, R.P.C. Coerwinkel, M. Kristensen, and J.P. Woerdman, "Helical-wavefront laser beams produced with a spiral phase plate", Opt. Commun., **112**(5-6), 321 (1994). https://doi.org/10.1016/0030-4018(94)90638-6

[30] A.V. Ustinov, S.N. Khonina, P.A. Khorin, and A.P. Porfirev, "Control of the intensity distribution along the light spiral generated by a generalized spiral phase plate", Journal of the Optical Society of America B, **38**(2), 420 (2021). https://doi.org/10.1364/JOSAB.408884

[31] V.V. Kotlyar, and A.A. Kovalev, "Nonparaxial propagation of a Gaussian optical vortex with initial radial polarization", J. Opt. Soc. Am. A, **27**(3), 372 (2010). https://doi.org/10.1364/JOSAA.27.000372

[32] B. Gu, and Y. Cui, "Nonparaxial and paraxial focusing of azimuthal-variant vector beams", Opt. Express, **20**(16), 17684 (2012). https://doi.org/10.1364/OE.20.017684

[33] Y. Zhang, L. Wang, and C. Zheng, "Vector propagation of radially polarized Gaussian beams diffracted by an axicon", J. Opt. Soc. Am. A, **22**(11), 2542 (2005). https://doi.org/10.1364/JOSAA.22.002542

[34] E.A.J. Marcatili, and R.A. Schmeltzer, "Hollow metallic and dielectric waveguides for long distance optical transmission and lasers", Bell Syst. Tech. J., **43**(4), 1783 (1964). https://doi.org/10.1002/j.1538-7305.1964.tb04108.x

[35] J.F. Nye, and M.V. Berry, "Dislocations in wave trains", Proceedings of the Royal Society of London. A. Mathematical and Physical Sciences, **336**(1605), 165 (1974). https://doi.org/10.1098/rspa.1974.0012

[36] H. Wang, Q. Song, Y. Cai, Q. Lin, X. Lu, H. Shangguan, Y. Ai, and S. Xu, "Recent advances in generation of terahertz vortex beams and their applications", Chin. Phys. B, **29**(9), 097404 (2020). https://doi.org/10.1088/1674-1056/aba2df

[37]   J.W. Goodman, *Introduction to Fourier optics*, (Roberts and Company Publishers, 2005).
[38]   O.V. Gurin, A.V. Degtyarev, N.N. Dubinin, M.N. Legenkiy, V.A. Maslov, K.I. Muntean, V.N. Ryabykh and V.S. Senyuta, "Formation of beams with nonuniform polarisation of radiation in a cw waveguide terahertz laser", Quantum Electron., **51**(4), 338 (2021). https://doi.org/10.1070/QEL17511
[39]   A.V. Degtyarev, M.M. Dubinin, O.V. Gurin, V.A. Maslov, K.I. Muntean, V.N. Ryabykh, V.S. Senyuta, "Control of tightly focused laser beams in the THz range", Microwave and Optical Technology Letters, **63**(11), 2888 (2021). https://doi.org/10.1002/mop.32946
[40]   A.V. Degtyarev, M.M. Dubinin, O.V. Gurin, V.A. Maslov, K.I. Muntean, V.M. Ryabykh, V.S. Senyuta, and O.O. Svystunov, "Control over higher-order transverse modes in a waveguide-based quasi-optical resonator", Radio Physics and Radio Astronomy, **27**(2**)**, 129 (2022). https://doi.org/10.15407/rpra27.02.129

ПРОСТОРОВА ДИНАМІКА РАДІАЛЬНО ПОЛЯРИЗОВАНОГО ТЕРАГЕРЦЕВОГО ЛАЗЕРНОГО ПУЧКА З ФАЗОВОЮ СИНГУЛЯРНІСТЮ

Андрій В. Дегтярьов, Микола М. Дубінін, Вячеслав О. Маслов, Костянтин І. Мунтян, Олег О. Свистунов
Харківський національний університет імені В.Н. Каразіна, майдан Свободи, 4, Харків, Україна, 61022

Отримано аналітичні вирази, що описують непараксіальну дифракцію у вільному просторі TM_{01} моди з радіальною поляризацією поля діелектричного хвилевідного резонатора терагерцового лазера при її взаємодії зі спіральною фазовою пластинкою з різним топологічним зарядом (n). Шляхом чисельного моделювання вивчено фізичні особливості отриманих вихрових пучків при їх поширенні та гострому фокусуванні. Для моделювання поширення пучків та фокусування отриманих пучків використані інтегральні дифракційні перетворення Релея–Зоммерфельда. У вільному просторі використання спіральної фазової пластинки на виході хвилеводу при топологічному заряді $n = 1$ призводить до зміни поперечного профілю пучка з кільцеподібного на пучок, який має максимум поля на осі, а далі ($n = 2$) знов на кільцеподібний. При фокусуванні розподіл сумарної інтенсивності поля за відсутності спіральної фазової пластинки має кільцеву структуру. Водночас на осі є незначна інтенсивність, що зумовлена вкладом повздовжньої компоненти поля. При використанні фазової пластинки поперечний профіль пучка змінюється так само як і при його поширенні. При цьому фазовий фронт змінюється із сферичного на спіральний з наявністю двох ($n = 1$) та чотирьох ($n = 2$) гілкових вихорів.
Ключові слова: *терагерцовий лазер; діелектричний хвилевідний резонатор; спіральна фазова пластинка; вихрові пучки; радіальна поляризація; поширення випромінювання; гостре фокусування*

WAVE PROPAGATION IN ANISOTROPIC MAGNETICALLY QUANTIZED ION PLASMA WITH TRAPPED ELECTRON AND POSITRON

Balaram Pradhan[a], Apul Narayan Dev[b*], Manoj Kumar Deka[c]

aCenter for Data science, Siksha 'O' Anusandhan (Deemed to be University),
Khandagiri, Bhubneswar 751030, Odisha, India
bDepartment of Mathematics, Siksha 'O' Anusandhan (Deemed to be University),
Khandagiri, Bhubneswar 751030, Odisha, India
cDepartment of Radiography and Imaging Technology, Srimanta Sankaradeva University of Health Sciences,
Guwahati 781032, India
*Corresponding Author E-mail: apulnarayan@gmail.com; apulnarayandev@soa.ac.in
Received June 8, 2025; revised July 6, 2025; in final form August 8, 2025; accepted August 18, 2025

This study examines the effects of magnetically quantized degenerate trapped electrons and positrons on small-amplitude ion acoustic shock waves (IAShWs) in a pair ion plasma using the Zakharov-Kuznetsov Burger (ZKB) equation. It focuses on how factors like magnetic quantization, degenerate temperature, normalized negative ions, electrons, positrons, anisotropic pressure, and other relevant physical parameters from an astrophysical plasma environment influence the propagation of IAShWs, particularly in the nonlinear regime. This research explores that there exist two distinct wave propagation modes—subsonic and supersonic which shows few distinct characteristics in different physical plasma environment of astrophysical origin. The results could aid in understanding the nonlinear dynamics and wave propagation characteristics in superdense plasmas found in white dwarfs and neutron stars, where the effects of trapped electrons and positrons, as well as ionic pressure anisotropy, are significant which is yet to be explored in detail.
Keywords: *Magnetized plasma; Subsonic and supersonic modes; Reductive perturbation method (RPT); Degenerate trapped electrons and positrons; ZKB equation; Phase plane analysis*
PACS: 52.35. Fp, 52.35. Mw, 52.27. Ep, 52.25. Xz, 52.27.Cm, 52.35.Ra

1. INTRODUCTION

The field of degenerate dense plasmas is attracting more attention, resulting in a significant amount of research activity. As scientists explore this area further, new insights and discoveries are being made [1-3]. These plasmas are found in highly dense astrophysical environments, including white dwarf stars [4, 5, 6] and neutron stars [7, 8, 9], among other locations. In these extreme settings, the physical conditions allow for the formation and stability of such plasmas. Several researchers have explored nonlinear waves in degenerate plasma systems (DPS) that include both positive and negative ions, as well as electrons and positrons [10-14]. Their studies focus on understanding the complex interactions within these plasmas, which can lead to fascinating phenomena such as solitons and wave packets. Jahangir R. et al. [15] investigate the nonlinear dynamics of IAShWs in a magnetized plasma with trapped electrons. Their study examines how degenerate electrons and temperature influence the amplitude and width of shock waves. Nonlinear localized wave excitation in non-equilibrium plasmas with particle flow have been investigated in [16-19] kinetic approximation with trapped electrons. Kaur R. et al. [20] explore the characteristics of IAShWs and the structure of oscillatory shock waves in ion beam plasma, which contains positive ions and trapped electrons within a quantizing magnetic field. They found that the amplitude of the oscillatory shock waves increases as the quantizing parameter rises. Iqbal M. J. et al. [21] examine the solitary wave structures in a plasma made up of degenerate electrons and positrons in the presence of a quantizing magnetic field. El-Borie M. A. et al. [22] study the properties of ion-acoustic waves in a magnetized plasma made up of positively and negatively charged fluid ions and trapped electrons. They analyze how various plasma parameters, including electron degenerate temperature, electron trapping effects, and viscosity, influence the profile of small yet finite amplitude solitary and shock waves. Shah H. A. et al. [23] examine the impact of trapping in a degenerate quantum plasma that includes nondegenerate ions and degenerate electrons. They found solitary wave structures when the electrons are fully degenerate, while in weakly nondegenerate plasma, both rarefactive and compressive solitary wave structures appear with changes in temperature. In a multi-ion plasma composed of positive and negative ions and trapped electrons, the nonlinear propagation of ion acoustic solitary waves (IASWs) and IAShWs are investigated by El-Monier S. Y. et al [24]. They noticed the effect of different plasma parameters on IASWs and IAShWs profile. IAShWs in a pair of ion magnetized plasma is investigated by Yeashna T. et al [25]. They observed both compressive and rarefactive shock potentials and the effect of oblique angle and kinematic viscosity on that profile. Zedan N. A. et al. [26] examined IASWs in a collisionless magnetized plasma that includes a degenerate pair of ions and trapped electrons within a quantizing magnetic field. In a theoretical investigation on dust ion acoustic waves in a degenerate electron-positron-ion (EPI) plasma the influence of viscosity on shock wave profile is studied by Halder et. al. [27]. Hussian S. et al. [28] investigated electron-ion degenerate plasma considering trapping effects and Landau quantization. They concluded that increasing kinematic viscosity and obliqueness strengthens the shock. In a theoretical investigation of shock waves in a degenerate magnetized plasma, Asaduzzaman M. et al. [29] analysed

---

how variations in kinematic viscosity, obliqueness, and number density significantly affect the characteristics of amplitude and steepness. Small amplitude IASWs are studied by Deka M. K. & Dev A. N. [30] on a magnetically quantized degenerate plasma consisting trapped electrons and positrons.

In a strong magnetic field, plasma exhibits anisotropic pressure characterized by distinct parallel and perpendicular components. This occurs under adiabatic conditions, influenced by rapid changes in plasma density as waves propagate. These variations in density can significantly affect the plasma's behavior, leading to unique wave dynamics and interactions that are crucial for understanding plasma stability and confinement in various astrophysical and laboratory settings. Irfan M. et al [31] studied characteristics of the ion-acoustic waves (IAWs) in the presence of ionic pressure anisotropy and electron trapping effects in a dense magnetoplasma consisting of degenerate relativistic trapped electrons and they reported that ionic pressure anisotropy has a significant effect on the amplitude of solitary potential both in relativistic and non-relativistic cases. Jahan. S. et al [32] studied the IAShWs in a degenerate magnetoplasma consisting of degenerate electrons, inertial nonrelativistic partially charged heavy and light ions. In their observation, it was concluded that the number density of non-relativistic heavy and light ions enhances the amplitude of IAShWs and the steepness of the shock profile is decreased with kinematic viscosity. In a rigorous investigation on degenerate EPI plasma, Rahman A. U. et al [33] studied the effect of key plasma parameters such as ion-electron temperature ratio, positron-electron density ratio and degeneracy parameter on solitary wave structure. The effect of anisotropic pressure and viscosity on the propagation of shock waves in a degenerate quantum magneto plasma is studied by Deka M. K. et al [34]. The aim of this manuscript is to investigate the propagation of IAShWs in magnetoplasma which consists of degenerate electrons, positrons, and ions, with the effects of viscosity. As far as we know, no one has yet made an effort to explore the nonlinear structures of IAShWs in the current context. This lack of investigation highlights a significant gap in our understanding, which could potentially hinder the progress in this field. The manuscript is arranged as follows. The basic equations are normalized by using normalized parameter in Sec. 2. In Sec. 3 the ZKB equation is derived from normalised equation. The influence of physical parameter on the profile of shock waves are discussed in Sec. 4. In Sec. 5 the phrase portrait analysis is performed by using Galian transformation. Finally, the brief conclusion is provided in Sec. 6.

2. MATHEMATICAL MODEL FOR DYNAMIC EQUATIONS

Let us consider a collision-less magneto plasma consisting of positive and negative ions along with trapped electrons and positrons is considered in the current investigation. The presence of external magnetic field ($B = B_o \hat{x} \neq 0$, where $\hat{x}$ is the unit vector along the x-axes) causes the inertial ions to exhibit pressure anisotropy.

The occupation number density of degenerate electrons and positrons can be expressed as [20,23,24,27,30]

$$N_j = \frac{p_{F_j}^2 \eta_j}{2\pi^2 \hbar^3} \sqrt{\frac{m_j}{2}} \sum_{l=0}^{\infty} \int_0^{\infty} \frac{\varepsilon^{-\frac{1}{2}}}{1+\exp\left((\varepsilon - U)/T\right)} d\varepsilon \tag{1}$$

Here, μ is the chemical potential, $\eta = \hbar \omega_{ce}/\varepsilon_{Fe}$ is representing the effect of the quantizing magnetic field appears though the modified electron Fermi energy $\varepsilon_{Fe} = \left(\hbar^2/2m_e\right)\left(3\pi^2 n_{e0}\right)^{2/3}$ and $n_{e0} = \left(p_{Fe}^3/3\pi^2\hbar^3\right)$. Again, the momentum of the fermi surface is denoted by p_{Fe}, the degenerate temperature is $T = \left(\pi T_e/2\sqrt{2}\,\varepsilon_{Fe}\right)$ and the potential is $\Psi = e\psi/\varepsilon_{Fe}$. By adopting the standard procedures for replacing the summation by integration of Eq. (1) for electron density, we obtain

$$N_e = N_{e0}\left\{\frac{3}{2}H(1+\Psi)^{\frac{1}{2}} + (1+\Psi-H)^{\frac{3}{2}} - \frac{HT^2}{2}(1+\Psi)^{-\frac{3}{2}} + T^2(1+\Psi-H)^{-\frac{1}{2}}\right\}$$

Which on expanding becomes

$$n_e = \frac{\eta}{2}(3-T^2) + (1-\eta)^{\frac{3}{2}} + T^2(1-\eta)^{-\frac{1}{2}} + \frac{3\psi}{2}\left\{\frac{\eta}{2}(1+T^2) + (1-\eta)^{\frac{1}{2}} - \frac{T^2}{3}(1-\eta)^{-\frac{3}{2}}\right\}$$
$$+ \frac{3\psi^2}{8}\left\{-\frac{\eta}{2}(1+5T^2) + (1-\eta)^{-\frac{1}{2}} + T^2(1-\eta)^{-\frac{5}{2}}\right\} \tag{2}$$

Similarly, we obtain the expression for positron density as

$$N_p = N_{p0}\left\{\frac{3}{2}\frac{\eta}{2}\mu_p^{-\frac{2}{3}}\left(1-\psi\mu_p^{-\frac{2}{3}}\right)^{\frac{1}{2}} - \frac{\eta T^2}{2}\mu_p^{-2}\left(1-\psi\mu_p^{-\frac{2}{3}}\right)^{-\frac{3}{2}} + \left(1-\psi\mu_p^{-\frac{2}{3}} - \eta\mu_p^{-\frac{2}{3}}\right)^{\frac{3}{2}}\right.$$
$$\left. + \mu_p^{-\frac{4}{3}}T^2\left(1-\psi\mu_p^{-\frac{2}{3}} - \eta\mu_p^{-\frac{2}{3}}\right)^{-\frac{1}{2}}\right\}$$

On expanding, the above equations become

$$
\begin{aligned}
n_p = &\frac{\eta \mu_p^{-\frac{2}{3}}}{2}\left(3 - \mu_p^{-\frac{4}{3}}T^2\right) + \left(1 - \mu_p^{-\frac{2}{3}}\eta\right)^{\frac{3}{2}} + \mu_p^{-\frac{4}{3}}T^2\left(1 - \mu_p^{-\frac{2}{3}}\eta\right)^{-\frac{1}{2}} \\
&+ \frac{3\psi}{2}\left\{-\frac{\eta\mu_p^{-\frac{4}{3}}}{2}\left(1 + \mu_p^{-\frac{4}{3}}T^2\right) - \mu_p^{-\frac{2}{3}}\left(1 - \mu_p^{-\frac{2}{3}}\eta\right)^{\frac{1}{2}} + \frac{\mu_p^{-2}T^2}{3}\left(1 - \mu_p^{-\frac{2}{3}}\eta\right)^{-\frac{3}{2}}\right\} \\
&+ \frac{3\psi^2}{8}\left\{-\frac{\eta\mu_p^{-2}}{2}\left(1 + 5\mu_p^{-\frac{4}{3}}T^2\right) + \mu_p^{-\frac{4}{3}}\left(1 - \mu_p^{-\frac{2}{3}}\eta\right)^{-\frac{1}{2}} + \mu_p^{-\frac{8}{3}}T^2\left(1 - \mu_p^{-\frac{2}{3}}\eta\right)^{-\frac{5}{2}}\right\}
\end{aligned}
\tag{3}
$$

The unnormalized govern equations for such plasma are read as

$$
\frac{\partial N_\pm}{\partial T} + \nabla\left(N_\pm V_\pm\right) = 0
\tag{4}
$$

$$
\left(\frac{\partial}{\partial T} + \vec{V}_\pm \nabla\right)\vec{V}_\pm = \frac{Z_\pm e}{m_\pm}\left(\mp\vec{\nabla}\Psi + \vec{V}_\pm \times B\right) - \frac{1}{m_\pm n_\pm}\nabla P_\pm + \delta_\pm \vec{\nabla}^2 \vec{V}_\pm + \left(\delta_\pm + \rho_\pm\right)\vec{\nabla}\left(\vec{\nabla}\vec{V}_\pm\right)
\tag{5}
$$

$$
\nabla^2 \Psi = 4\pi e\left(N_e + Z_- N_- - Z_+ N_+ - N_p\right)
\tag{6}
$$

In the above plasma system, $N_\pm$ is ion fluid density (+ sign represents for positive ion and – sign represents for negative ion) which is normalized by equilibrium unperturbed number density $N_{\pm 0}$, $V_\pm$ is the positive and negative ion fluid velocity which is normalized by ion acoustic speed C_s $\left(v_\pm = V_\pm \times C_s\right)$, the corresponding space variable is normalized by Debye length $\left(\lambda_D = \sqrt{K_B T_e / 4\pi N_e e^2}\right)$ and the time variable is by plasma frequence $\left(\omega_{pi} = \sqrt{4\pi N_{+0} e^2 / m_+}\right)$. The external magnetic field $\left(\Omega_\pm = Z_\pm e B \lambda_D / m_\pm C_s\right)$, kinematic viscosity $\left(\delta_\pm = \delta_\pm' / C_s \lambda_D\right)$ and bulk viscosity $\left(\rho_\pm = \rho_\pm' / C_s \lambda_D\right)$ is normalized by λ_D and C_s. The other plasma parameter such as potential function is normalized by $\Psi = e\psi / \varepsilon_{Fe}$, the pressure term along the parallel direction is $P_{\pm ll} = P_{\pm ll0}\left(N_\pm / N_{\pm 0}\right)^3$ and along the perpendicular direction is $P_{\pm\perp} = P_{\pm\perp}\left(N_\pm / N_{\pm 0}\right)$. Thus, at equilibrium the charge neutrality condition of our plasma model can be written as $\mu_m + \mu_e = 1 + \mu_p$.

After normalization, the basic set of equations for positive and negative ions are expressed as

$$
\frac{\partial n_+}{\partial t} + \frac{\partial}{\partial x}\left(n_+ u_{+x}\right) + \frac{\partial}{\partial y}\left(n_+ u_{+y}\right) + \frac{\partial}{\partial Z}\left(n_+ u_{+z}\right) = 0
\tag{7}
$$

$$
\begin{aligned}
&\frac{\partial u_{+x}}{\partial t} + \left(u_{+x}\frac{\partial}{\partial x} + u_{+y}\frac{\partial}{\partial y} + u_{+z}\frac{\partial}{\partial z}\right)u_{+x} = -Z_+\frac{\partial\phi}{\partial x} + \left(\vec{u}_{+x} \times \Omega_+\right) - \bar{P}_{+\|}n_+\frac{\partial n_+}{\partial x} \\
&+ \delta_{+\|}'\left(\frac{\partial^2}{\partial x^2} + \frac{\partial^2}{\partial y^2} + \frac{\partial^2}{\partial z^2}\right)\left(u_{+x}\right) + \left(\delta_{+\|}' + \rho_{+\|}'\right)\left(\frac{\partial^2 u_{+x}}{\partial x^2} + \frac{\partial^2 u_{+y}}{\partial x\partial y} + \frac{\partial^2 u_{+z}}{\partial x\partial z}\right)
\end{aligned}
\tag{8}
$$

$$
\begin{aligned}
&\frac{\partial u_{+y}}{\partial t} + \left(u_{+x}\frac{\partial}{\partial x} + u_{+y}\frac{\partial}{\partial y} + u_{+z}\frac{\partial}{\partial z}\right)u_{+y} = -Z_+\frac{\partial\phi}{\partial y} + \left(\vec{u}_{+y} \times \Omega_+\right) - \bar{P}_{+\perp}\frac{1}{n_+}\frac{\partial n_+}{\partial y} \\
&+ \delta_{+\perp}'\left(\frac{\partial^2}{\partial x^2} + \frac{\partial^2}{\partial y^2} + \frac{\partial^2}{\partial z^2}\right)\left(u_{+y}\right) + \left(\delta_{+\perp}' + \rho_{+\perp}'\right)\left(\frac{\partial^2 u_{+x}}{\partial y\partial x} + \frac{\partial^2 u_{+y}}{\partial y^2} + \frac{\partial^2 u_{+z}}{\partial y\partial z}\right)
\end{aligned}
\tag{9}
$$

$$
\begin{aligned}
&\frac{\partial u_{+z}}{\partial z} + \left(u_{+x}\frac{\partial}{\partial x} + u_{+y}\frac{\partial}{\partial y} + u_{+z}\frac{\partial}{\partial z}\right)u_{+z} = -Z_+\frac{\partial\phi}{\partial z} + \left(\vec{u}_{+z} \times \Omega_+\right) - \bar{P}_{+\perp}\frac{1}{n_+}\frac{\partial n_+}{\partial z} \\
&+ \delta_{+\perp}'\left(\frac{\partial^2}{\partial x^2} + \frac{\partial^2}{\partial y^2} + \frac{\partial^2}{\partial z^2}\right)\left(u_{+z}\right) + \left(\delta_{+\perp}' + \rho_{+\perp}'\right)\left(\frac{\partial^2 u_{+x}}{\partial z\partial x} + \frac{\partial^2 u_{+y}}{\partial z\partial y} + \frac{\partial^2 u_{+z}}{\partial z^2}\right)
\end{aligned}
\tag{10}
$$

$$\frac{\partial n_-}{\partial t} + \frac{\partial}{\partial x}\left(n_- u_{-x}\right) + \frac{\partial}{\partial y}\left(n_- u_{-y}\right) + \frac{\partial}{\partial z}\left(n_- u_{-z}\right) = 0 \tag{11}$$

$$\left.\begin{aligned}
&\frac{\partial u_{-x}}{\partial t} + \left(u_{-x}\frac{\partial}{\partial x} + u_{-y}\frac{\partial}{\partial y} + u_{-z}\frac{\partial}{\partial z}\right)u_{-x} = \gamma Z_-\frac{\partial \phi}{\partial x} - \left(\vec{u}_{-x}\times\Omega_-\right) - \gamma\bar{P}_{-\|}n_-\frac{\partial n_-}{\partial x} \\
&+\delta'_{-\|}\left(\frac{\partial^2}{\partial x^2} + \frac{\partial^2}{\partial y^2} + \frac{\partial^2}{\partial z^2}\right)\left(u_{-x}\right) + \left(\delta'_{-\|} + \rho'_{-\|}\right)\left(\frac{\partial^2 u_{-x}}{\partial x^2} + \frac{\partial^2 u_{-y}}{\partial x\partial y} + \frac{\partial^2 u_{-z}}{\partial x\partial z}\right)
\end{aligned}\right\} \tag{12}$$

$$\left.\begin{aligned}
&\frac{\partial u_{-y}}{\partial t} + \left(u_{-x}\frac{\partial}{\partial x} + u_{-y}\frac{\partial}{\partial y} + u_{-z}\frac{\partial}{\partial z}\right)u_{-y} = \gamma Z_-\frac{\partial \phi}{\partial y} - \left(\vec{V}_{-z}\times\Omega_-\right) - \gamma\bar{P}_{-\perp}\frac{1}{n_-}\frac{\partial n_-}{\partial y} \\
&+\delta'_{-\perp}\left(\frac{\partial^2}{\partial x^2} + \frac{\partial^2}{\partial y^2} + \frac{\partial^2}{\partial z^2}\right)\left(u_{-y}\right) + \left(\delta'_{-\perp} + \rho'_{-\perp}\right)\left(\frac{\partial^2 u_{-x}}{\partial y\partial x} + \frac{\partial^2 u_{-y}}{\partial y^2} + \frac{\partial^2 u_{-z}}{\partial y\partial z}\right)
\end{aligned}\right\} \tag{13}$$

$$\left.\begin{aligned}
&\frac{\partial u_{-z}}{\partial t} + \left(u_{-x}\frac{\partial}{\partial x} + u_{-y}\frac{\partial}{\partial y} + u_{-z}\frac{\partial}{\partial z}\right)u_{-z} = \gamma Z_-\frac{\partial \phi}{\partial z} - \left(\vec{u}_{-z}\times\Omega_-\right) - \gamma\bar{P}_{-\perp}\frac{1}{n_-}\frac{\partial n_-}{\partial z} \\
&+\delta'_{-\perp}\left(\frac{\partial^2}{\partial x^2} + \frac{\partial^2}{\partial y^2} + \frac{\partial^2}{\partial z^2}\right)\left(u_{-z}\right) + \left(\delta'_{-\perp} + \rho'_{-\perp}\right)\left(\frac{\partial^2 u_{-x}}{\partial z\partial x} + \frac{\partial^2 u_{-y}}{\partial z\partial y} + \frac{\partial^2 u_{-z}}{\partial z^2}\right)
\end{aligned}\right\} \tag{14}$$

$$\frac{\partial^2\psi}{\partial x^2} + \frac{\partial^2\psi}{\partial y^2} + \frac{\partial^2\psi}{\partial z^2} = \left(n_e\mu_e + Z_- n_-\mu_m - Z_+ n_+ - n_P\mu_p\right) \tag{15}$$

Where, $\mu_e\left(n_{e0}/n_{+0}\right)$ is electron to positive ion density ratio, $\mu_m\left(n_{-0}/n_{+0}\right)$ is negative to positive ion density ratio and $\mu_p\left(n_{p0}/n_{+0}\right)$ is the positron to positive ion density ratio.

3. DERIVATION OF TKDVB EQUATION

To study the nonlinear properties of ion-acoustic shock waves (IAShWs) in a collisionless pair of ion plasma (PIP), we adopt the method of reductive perturbation (MRP). According to this method for small amplitude waves the following stretched variables are used to derived ZKB equation [14,15]

$$\left.\begin{aligned}
&\xi = \varepsilon^{1/2}\left(X - \lambda T\right), \eta = \varepsilon^{1/2}Y\ , \ \zeta = \varepsilon^{1/2}Z,\ \ \tau = \varepsilon^{3/2}T \\
&\delta'_{\pm} = \varepsilon^{1/2}\delta_{\pm}\ \ and\ \ \rho'_{\pm} = \varepsilon^{1/2}\rho_{\pm}
\end{aligned}\right\} \tag{16}$$

Where λ shows the linearized phase velocity of the IAShWs and its perturbed amplitude is measuring by the real small dimensionless parameter $\varepsilon\left(<<1\right)$.

The dependent physical variables of the above equation such as density $\left(n\right)$, velocity $\left(u\right)$ and potential function $\left(\psi\right)$ are expanded asymptotically as a power series near the equilibrium state as follows:

$$\left.\begin{aligned}
&n_{\pm} = 1 + \sum_{j=1}^{\infty}\varepsilon^j n_{\pm}^{(1)},\qquad u_{\pm x} = \sum_{j=1}^{\infty}\varepsilon^j u_{\pm x}^{(1)} \\
&u_{\pm y,z} = \sum_{j=1}^{\infty}\sum_{k=0}^{\infty}\varepsilon^{1+\frac{j}{2}}u_{\pm y,z}^{(1+k)},\quad \psi = \sum_{j=1}^{\infty}\varepsilon^j\psi^{(j)}
\end{aligned}\right\} \tag{17}$$

Now, substituting the above perturbation scheme (Eqs. 16 & 17) in the set of normalized equations (7)-(15) and collecting the coefficients of lower order of $\varepsilon\left(\sim\varepsilon^{3/2}\right)$ as follows:

$$\left.\begin{aligned}
&N_+^{(1)} = \frac{-Z_+}{\left(\bar{P}_{+\|} - \lambda^2\right)}\psi^{(1)}, N_-^{(1)} = \frac{\gamma Z_-}{\left(\gamma\bar{P}_{-\|} - \lambda^2\right)}\psi^{(1)}, N_e^{(1)} = \frac{\psi^{(1)}}{\alpha_1}, N_p^{(1)} = \frac{\psi^{(1)}}{\Upsilon_1} \\
&V_{+x}^{(1)} = \lambda N_+^{(1)}, V_{+y}^{(1)} = \frac{1}{\Omega_+}\left(Z_+\frac{\partial\psi^{(1)}}{\partial\eta} + \bar{P}_{+\perp}\frac{\partial N_+^{(1)}}{\partial\eta}\right), V_{+z}^{(1)} = \frac{1}{\Omega_+}\left(Z_+\frac{\partial\psi^{(1)}}{\partial\zeta} + \bar{P}_{+\perp}\frac{\partial N_+^{(1)}}{\partial\zeta}\right) \\
&V_{-x}^{(1)} = \lambda N_-^{(1)}, V_{-y}^{(1)} = \frac{\gamma}{\Omega_-}\left(Z_-\frac{\partial\psi^{(1)}}{\partial\eta} - \bar{P}_{-\perp}\frac{\partial N_-^{(1)}}{\partial\eta}\right), V_{-z}^{(1)} = \frac{\gamma}{\Omega_-}\left(Z_-\frac{\partial\psi^{(1)}}{\partial\zeta} - \bar{P}_{-\perp}\frac{\partial N_-^{(1)}}{\partial\zeta}\right)
\end{aligned}\right\} \tag{18}$$

Where, $\alpha_1 = \dfrac{3}{2}\left\{\dfrac{\eta}{2}\left(1+T^2\right)+\left(1-\eta\right)^{\frac{1}{2}}-\dfrac{T^2}{3}\left(1-\eta\right)^{-\frac{3}{2}}\right\}$ and $\Upsilon_1 = \dfrac{\eta\delta^{-\frac{2}{3}}}{2}\left(3-\delta^{-\frac{4}{3}}T^2\right)+\left(1-\delta^{-\frac{2}{3}}\eta\right)^{\frac{3}{2}}+\delta^{-\frac{4}{3}}T^2\left(1-\delta^{-\frac{2}{3}}\eta\right)^{-\frac{1}{2}}$

Proceeding in same way from lowest order of poissons equation we obtain the expression for phase velocity as:

$$\lambda^2 = \frac{q \pm \sqrt{q^2-4pr}}{2p}. \tag{19}$$

Here,

$p = \left(\Upsilon_1\mu_e - \alpha_1\mu_P\right)$;

$q = \left(\alpha_1\Upsilon_1\left(Z_+^2+\gamma\mu_m Z_-^2\right)+\left(\Upsilon_1\mu_e-\alpha_1\mu_P\right)\left(\overline{P}_{+\parallel}+\gamma\overline{P}_{-\parallel}\right)\right)$;

$r = \left(\gamma\overline{P}_{+\parallel}\overline{P}_{-\parallel}\left(\Upsilon_1\mu_e-\alpha_1\mu_P\right)+\alpha_1\Upsilon_1\left(Z_+^2\gamma\overline{P}_{-\parallel}+\gamma\mu_m\overline{P}_{+\parallel}Z_-^2\right)\right)$

Similarly, continuing the same process for next higher order of ε gives rise the expression for the second order perturbation terms. After a few algebraic operations with the help of Eq. (18), we obtain the ZKB equation as:

$$\left. \begin{aligned} &\frac{\partial\psi^{(1)}}{\partial\tau}+B\psi^{(1)}\frac{\partial\psi^{(1)}}{\partial\xi}+C\frac{\partial^3\psi^{(1)}}{\partial\xi^3}-D_2\left(\frac{\partial^2\psi^{(1)}}{\partial\xi^2}+\frac{\partial^2\psi^{(1)}}{\partial\eta^2}+\frac{\partial^2\psi^{(1)}}{\partial\zeta^2}\right) \\ &-D_1\frac{\partial^2\psi^{(1)}}{\partial\xi^2}+F\frac{\partial}{\partial\xi}\left(\frac{\partial^2\psi^{(1)}}{\partial\eta^2}+\frac{\partial^2\psi^{(1)}}{\partial\zeta^2}\right)=0 \end{aligned} \right\} \tag{20}$$

Where the nonlinearity of the system is $B=b/a$, the dispersion term $C=-1/a$, the dissipation coefficient due to bulk viscosity and kinematic viscosity are respectively $D_1=d_1/a$, $D_2=d_2/a$ and $F=f/a$ is the transverse term.

While $a = \left(-\dfrac{2\lambda Z_+^2}{\left(\overline{P}_{+\parallel}-\lambda^2\right)^2}-\dfrac{2\lambda\gamma\mu_m Z_-^2}{\left(\gamma\overline{P}_{-\parallel}-\lambda^2\right)^2}\right)$,

$b = \left(\alpha_2\mu_e-\Upsilon_2\mu_P+Z_+^3\dfrac{3\lambda^2+\overline{P}_{-\parallel}}{\left(\overline{P}_{-\parallel}-\lambda^2\right)^3}-\mu_m Z_-^3\dfrac{3\lambda^2+\gamma\overline{P}_{-\parallel}}{\left(\gamma\overline{P}_{-\parallel}-\lambda^2\right)^3}\right)$

$\alpha_2 = \dfrac{3}{8}\left\{-\dfrac{\eta}{2}\left(1+5T^2\right)+\left(1-\eta\right)^{-\frac{1}{2}}+T^2\left(1-\eta\right)^{-\frac{5}{2}}\right\}$

$\Upsilon_2 = \dfrac{3}{2}\left\{-\dfrac{\eta\delta^{-\frac{4}{3}}}{2}\left(1+\delta^{-\frac{4}{3}}T^2\right)-\delta^{-\frac{2}{3}}\left(1-\delta^{-\frac{2}{3}}\eta\right)^{\frac{1}{2}}+\dfrac{\delta^{-2}T^2}{3}\left(1-\delta^{-\frac{2}{3}}\eta\right)^{-\frac{3}{2}}\right\}$

$d_1 = \left(Z_+^2\dfrac{\left(\delta_{+\parallel}+\rho_{+\parallel}\right)}{\left(\overline{P}_{+\parallel}-\lambda^2\right)^2}+\lambda Z_-^2\dfrac{\left(\delta_{-\parallel}+\rho_{-\parallel}\right)}{\left(\gamma\overline{P}_{-\parallel}-\lambda^2\right)^2}\right)$

$d_2 = \left(\dfrac{Z_+^2\delta_{+\parallel}}{\left(\overline{P}_{+\parallel}-\lambda^2\right)^2}-\dfrac{\lambda\mu_m Z_-^2\delta_{-\parallel}}{\left(\gamma\overline{P}_{-\parallel}-\lambda^2\right)^2}\right)$

$f = \left(-\dfrac{\lambda^2}{\Omega_+^2}\dfrac{Z_+^2}{\left(\overline{P}_{+\parallel}-\lambda^2\right)}-\dfrac{\lambda^2}{\Omega_-^2}\dfrac{\gamma\mu_m Z_-^2}{\left(\gamma\overline{P}_{-\parallel}-\lambda^2\right)}+\dfrac{\lambda^2}{\Omega_+^2}\dfrac{\overline{P}_{+\perp}Z_+^2}{\left(\overline{P}_{+\parallel}-\lambda^2\right)^2}+\dfrac{\lambda^2}{\Omega_-^2}\dfrac{\gamma^2\mu_m Z_-^2\overline{P}_{-\perp}}{\left(\gamma\overline{P}_{-\parallel}-\lambda^2\right)^2}-1\right)$

4. RESULTS AND DISCUSSIONS

In this section, we investigate the effects of variations of different plasma parameters on the characteristics of IAShWs governed by Eq. (20). For that purpose, we have considered the range of some typical physical parameters in dense astrophysical environments (neutron stars and white dwarfs) in which degenerate EPI is important. The well-defined parameters are considered as the equilibrium density $\eta_{io} = 10^{26} - 10^{29} cm^{-3}$, $n_{eo(p0)} = 10^{28} - 10^{30} cm^{-3}$ [9,14,15,23], $B_o = 10^9 - 10^{12} G$ [15,20,23] and the Fermi temperature for those parameters in the range of $3.6277 \times 10^7 K$ [20,30].
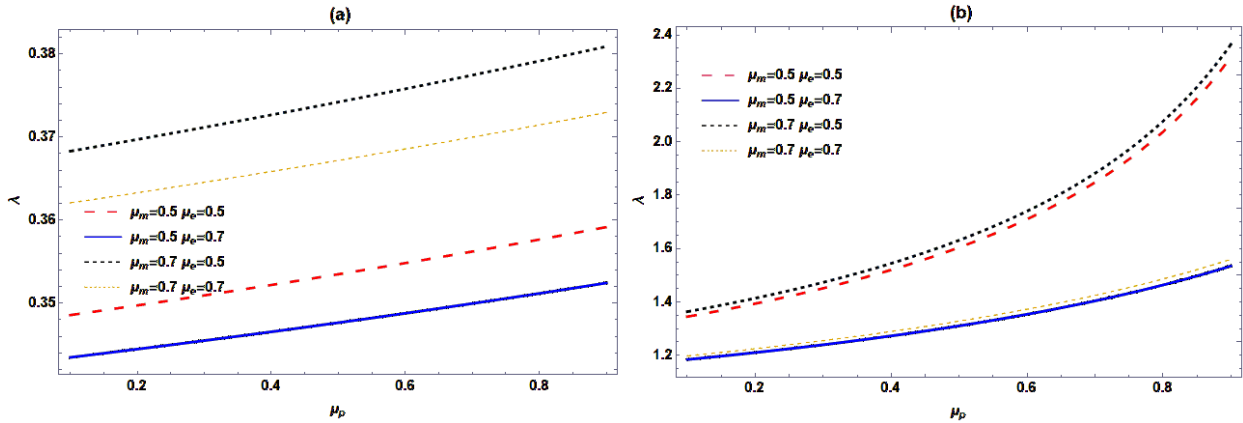
Figure 1 The variation of normalized phase speed λ represented by Eq. (19) is depicted against μ_p for (a) subsonic $(\lambda < 1)$ and (b) supersonic $(\lambda > 1)$ situations with several values of μ_m and μ_e

We have investigated the impact of critical plasma parameters on phase speed, as our goal is to analyze the characteristics of ion acoustic modes in the plasma system under consideration. The plasma model being analysed can have both fast and slow modes. Fig.1 presents the normalized phase velocity (λ) of the wave as a function of the ratio of positron-to-positive ion equilibrium density (μ_p). This data is displayed for various values of the electron-to-positive ion equilibrium density ratio (μ_e) and the negative-to-positive ion equilibrium density ratio (μ_m), covering both (a) subsonic and (b) supersonic mode. The Fig. 1(a) reveals that λ decreases as the μ_e increases. In contrast, it rises with higher ratios of μ_p and μ_m. In both figures, the phase velocity is lowest when the electron density μ_e is higher than the electron μ_m density. This happens because, as positron density increases, electron density may also increase due to matter-antimatter annihilation. As a result, the concentration of heavier negative ions increases, which reduces the phase velocity. On the other hand, if electron density decreases while negative ion density increases with positron density, the total positive ion density becomes higher, causing the phase velocity to increase. This situation corresponds to the black dashed curve in Fig. 1(a) and Fig. 1(b).
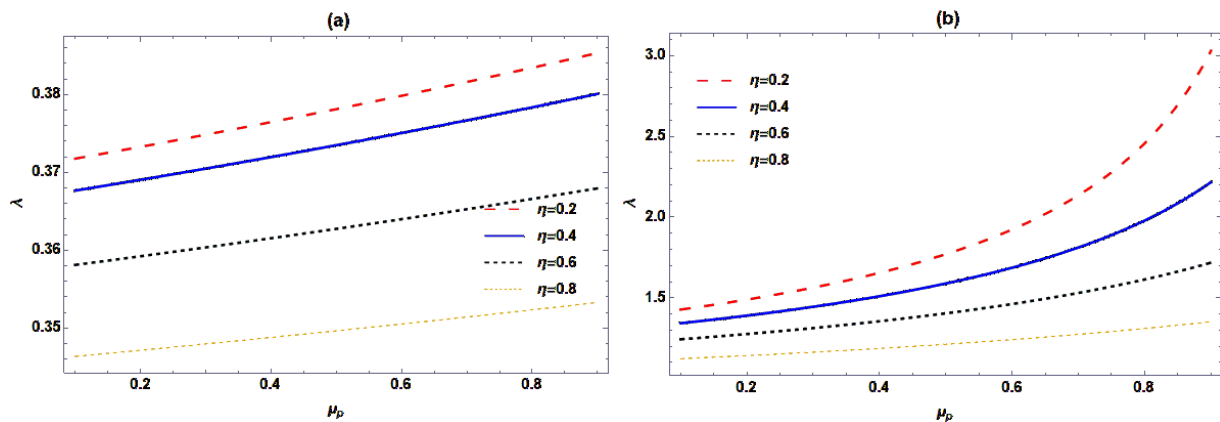
Figure 2. The variation of normalized phase speed λ represented by Eq. (19) is depicted against μ_p for (a) subsonic $(\lambda < 1)$ and (b) supersonic $(\lambda > 1)$ situations with several values of η.

The Fig. 2 shows the variation of normalized phase velocity (λ) by changing the quantization parameter (η) for two ion acoustic modes (a) subsonic and (b) supersonic. From both Fig. 2, it is observed that the λ decreases with

increasing η [26]. This is because as the quantization parameter increase which eventually means an increase in the strength of magnetic field, more and more electron will be trapped and hence phase velocity will be reduced.
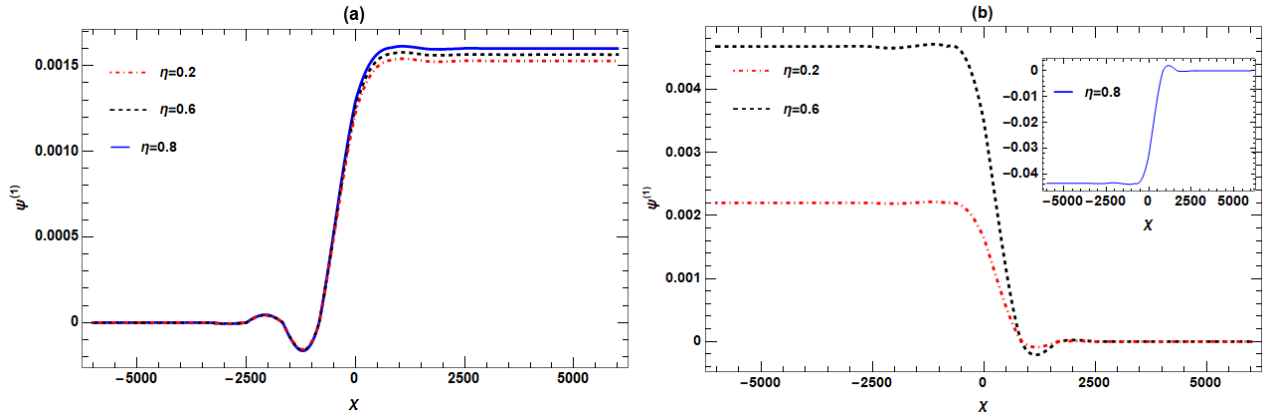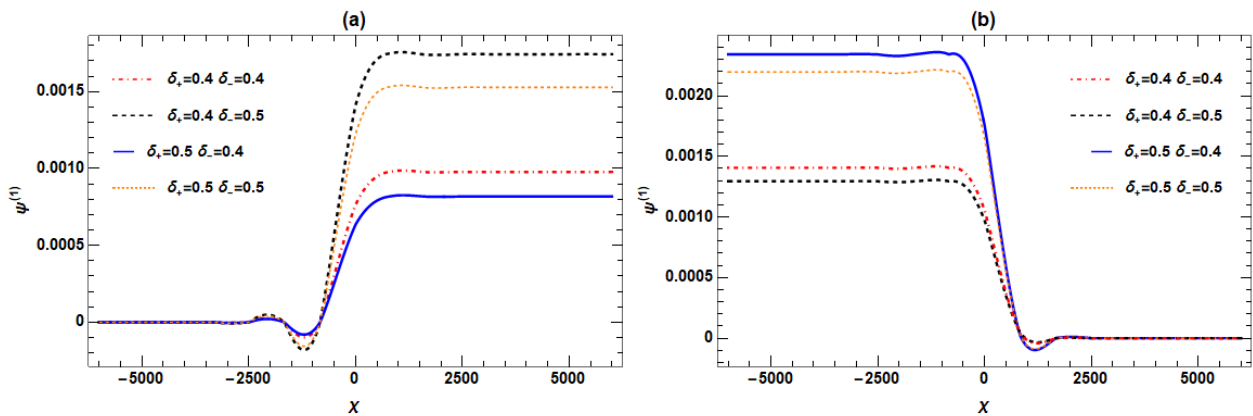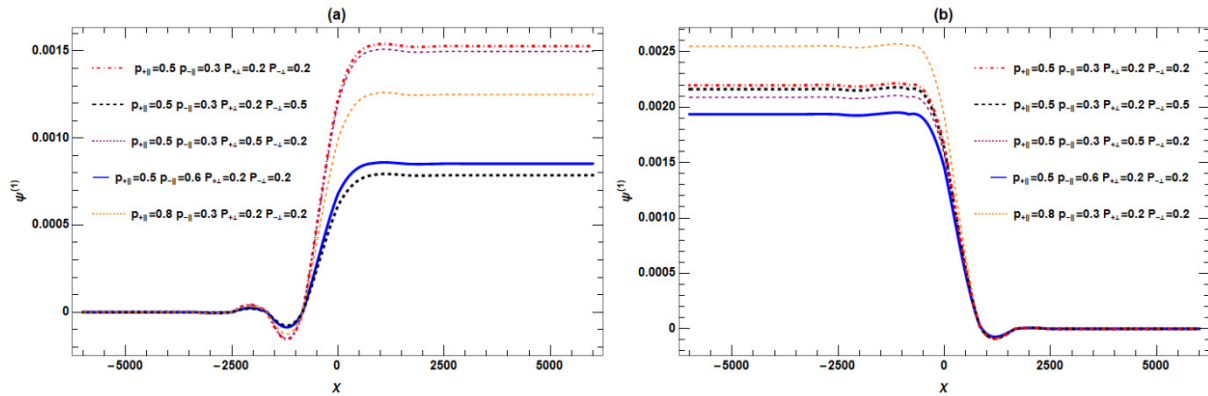

Figure 3. Showing the profile $\psi^{(1)}$ of IAShWs that represented by Eq. (20) against χ with combination of different normalized density values $\mu_m,$ μ_e and μ_p for $(a)\lambda < 1$ and $(b)\lambda > 1$, while the values of other parameter is considered as $\delta_+ = 0.5,$ $\delta_- = 0.5,$ $\Omega_+ = 0.6, \Omega_+ = 0.16,$ $l = 0.3,$ $p_{+\|} = 0.5, p_{+\perp} = 0.2, p_{-\|} = 0.3$ & $p_{-\perp} = 0.2$

Fig. 3 demonstrates the graphical representation of normalized potential function $\psi^{(1)}$ (as a function of spatial distance χ) with different values of quantizing magnetic field effect appears through the parameter (η) and temperature (T) for (a) subsonic and (b) supersonic modes respectively. From Fig. 3(a), it is noticed that when the normalized phase speed is in subsonic mode, the increase in η increases the steepness of shock wave without affecting the amplitude of the waves. However, from Fig. 3(b), it is observed that as η increases the amplitude and steepness of shock wave increase, but after a particular value of $\eta \geq 0.8$ the polarity of shock potential changes from positive to negative. The quantizing parameters influence both the phase velocity of the shock wave and the nonlinearity within the plasma system. Next, we investigate the influence of obliqueness parameter l on the profile of IAShWs potential profile $\psi^{(1)}$ for both (a) subsonic and (b) supersonic normalized phase velocity λ . Fig. 4(a) shows that the amplitude of IAShWs is strongly dependent on l and it is observed that as l increases, the amplitude as well as steepness of shock profile decreases rapidly. However, when the phase speed is in supersonic range the increase in l initially increases the amplitude and steepness, after a certain value it reduced the shock profile (Fig. 4(b)) [20, 29]. It can be concluded that obliqueness of the propagation has a strong effect over propagation with subsonic speed as compared to supersonic speed.
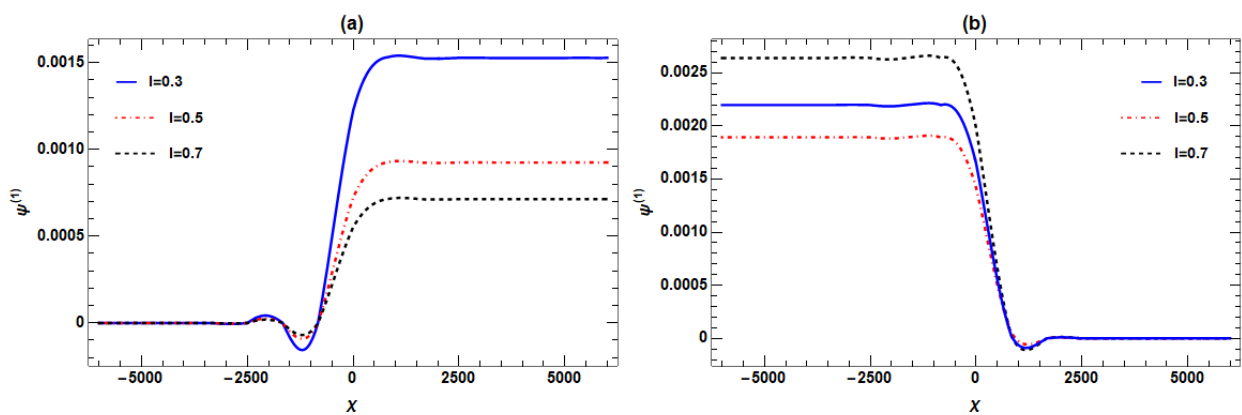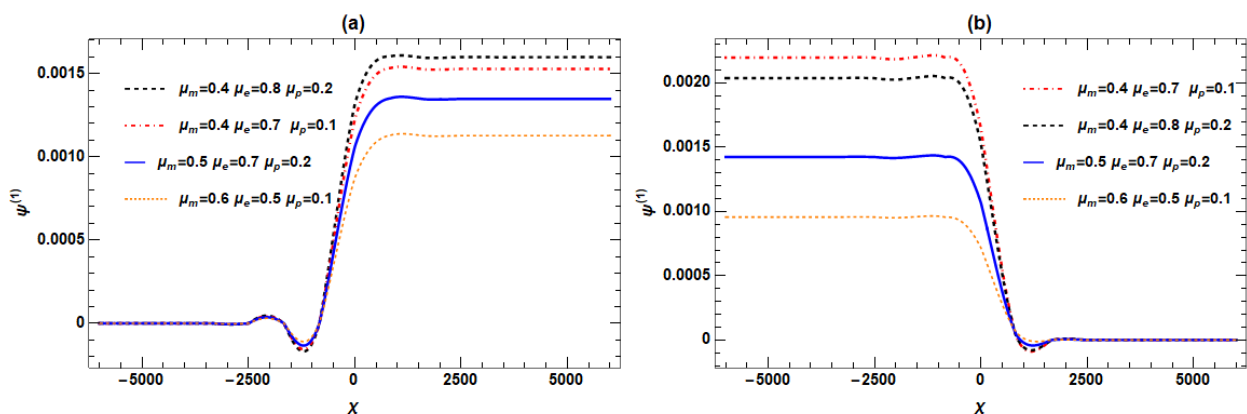

Figure 4. Showing the profile $\psi^{(1)}$ of IAShWs that represented by Eq. (20) against χ with combination of different normalized density values $\mu_m,$ μ_e and μ_p for $(a)\lambda < 1$ and $(b)\lambda > 1$, while the values of other parameter is considered as $\delta_+ = 0.5,$ $\delta_- = 0.5,$ $\Omega_+ = 0.6, \Omega_+ = 0.16,$ $l = 0.3,$ $p_{+\|} = 0.5, p_{+\perp} = 0.2, p_{-\|} = 0.3$ & $p_{-\perp} = 0.2$

Fig. 5 shows the graphical presentation of IAShWs profile of normalized potential function $\psi^{(1)}$ against χ with different combination of external magnetic field provided to positive (Ω_+) and negative (Ω_-) ions for both (a) subsonic and (b) supersonic modes of normalized phase velocity. Fig 5(a) & 5(b) clearly show that as the strength of the external magnetic field increases, both the amplitude and steepness of the shock wave also rise. Moreover, the sharpness of the

shock wave becomes increasingly noticeable. It is clear from both the figures that as the cyclotron frequency of positive ion's increases significantly compared to electron's cyclotron frequency, and as we know, higher magnetic field is required to magnetize the positive ions than compared to electrons, all the low energy electrons can escape such high magnetic field there causing enhancement in the energy of the wave and thus amplitude of the wave increases significantly. This research explores how the strength of the magnetic field affects the properties of the IAShWs profile by examining the dispersion coefficient in relation to the normalized cyclotron frequency [35,38].
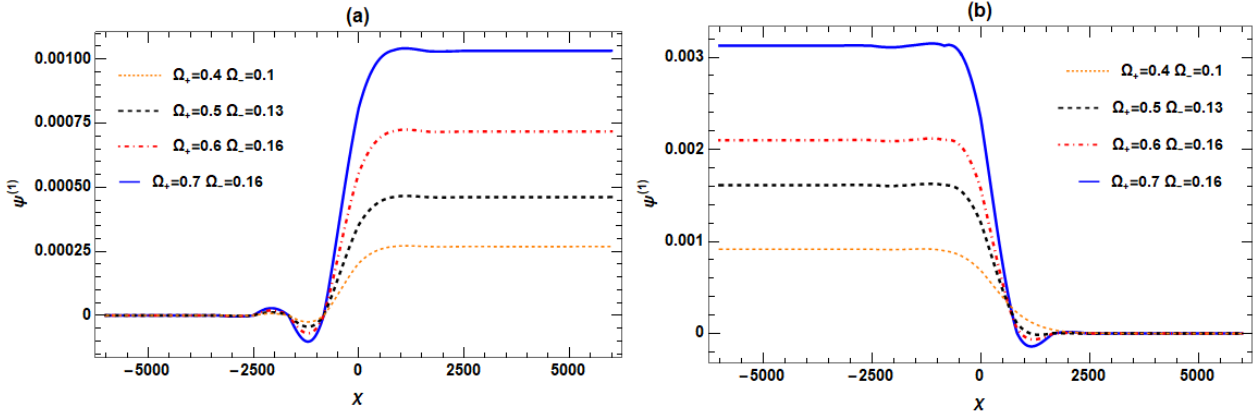
Figure 5. The profile $\psi^{(1)}$ of IAShWs with respect to χ for a combination of different normalized density values μ_m, μ_e and μ_p for $(a)\lambda<1$ and $(b)\lambda>1$, the values of other parameters are considered as $\delta_+ = 0.5$, $\delta_- = 0.5$, $\Omega_+ = 0.6, \Omega_+ = 0.16$, $l = 0.3$, $p_{+\parallel} = 0.5, p_{+\perp} = 0.2, p_{-\parallel} = 0.3$ & $p_{-\perp} = 0.2$

Fig. 6 shows the graphical presentation of IAShWs profile of normalized potential function $\psi^{(1)}$ against χ with different kinematic and bulk viscosity of the pair of ions (as dissipative parameter δ_+ and δ_-) for both (a) subsonic and (b) supersonic phase speed. From Fig. 6(a) (Subsonic phase speed), it is clearly seen that viscosity of positive ion reduces the IAShWs profile, while negative ion viscosity enhances the profile. It might be because, as the negative ion viscosity increases (i.e. overall reduction in the velocity of the negative ions), the more and more low energy electrons will be captured in the surface of the heavy negative ions, and eventually, the left behind electrons will be of only high energy, and this enhances the amplitude of the wave. On the other hand, from Fig. 6(b) (Supersonic phase speed), it is seen that the profile of IAShWs profile enhances with positive ion viscosity which is reduces for negative ion viscosity [34,36,37].

Figure 6. Showing the profile $\psi^{(1)}$ of IAShWs that represented by Eq. (20) against χ with combination of different normalized density values μ_m, μ_e and μ_p for $(a)\lambda<1$ and $(b)\lambda>1$, while the values of other parameter is considered as $\delta_+ = 0.5$, $\delta_- = 0.5$, $\Omega_+ = 0.6$, $\Omega_+ = 0.16$, $l = 0.3$, $p_{+\parallel} = 0.5, p_{+\perp} = 0.2, p_{-\parallel} = 0.3$ & $p_{-\perp} = 0.2$.

To know the effect of pressure anisotropy on the characteristics of IAShWs, we depict the variation of $\psi^{(1)}$ w.r.t χ for different values of $p_{+\parallel}, p_{+\perp}, p_{-\parallel}$ and $p_{+\perp} = 0.2$ (for fixed values of other parameter). From Fig.7(a) i.e. when the normalized phase speed is in subsonic mode, we have observed that when the thermal pressure of positive ions increases in both parallel and perpendicular direction $(p_{+\parallel}$ & $p_{+\perp})$ increases the amplitude and steepness of the shock profiles whereas the increase in thermal pressure of negative ion in perpendicular direction decreases the amplitude and steepness of the wave. However, from Fig.7(b) i.e. when the normalized phase speed is in supersonic mode, it is noticed that

increasing the parallel thermal pressure of positive ion $\left(p_{+\parallel}\right)$ enhances the amplitude as well as steepness of shock waves profile, but increasing the parallel thermal pressure of negative ion $\left(p_{-\parallel}\right)$ reduces the amplitude of the shock structure [34,38].

Figure 7. Showing the profile $\psi^{(1)}$ of IAShWs that represented by Eq. (20) against χ with combination of different normalized density values $\mu_{m,}$ μ_e and μ_p for $(a)\lambda<1$ and $(b)\lambda>1$, while the values of other parameter is considered as $\delta_+=0.5,$ $\delta_-=0.5,$ $\Omega_+=0.6, \Omega_+=0.16$ & $l=0.3$

Fig.8 shows the graphical presentation of IAShWs profile of normalized potential function $\psi^{(1)}$ against χ with different combination of density ratio of negative ion $\left(\mu_m\right)$, electron $\left(\mu_e\right)$ and positron $\left(\mu_p\right)$ w.r.t positive ion for both (a) subsonic and (b) supersonic modes of normalized phase velocity. It can be noticed from both figures that as we increases μ_e from 0.7 to 0.8 and μ_p from 0.1 to 0.2 by keeping μ_m as 0.4 (red dot dashed & black dashed) the amplitude and steepness of IAShWs increases when the phase speed is in subsonic mode, which on the other hand reduces for supersonic mode. In similar manner we see for other curves of Fig. 8(a) & 8(b) as we increasing the values of any two parameter μ_m, μ_p and μ_e by keeping third one same value, it is observed that amplitude and steepness of the shock structure declines. An oscillating shock wave pattern is linked to the potential profile when the electron density achieves a critical threshold. When the electron count is insufficient to shield against the potential, positive ions work to increase the electron pressure, facilitating the formation of an oscillating structure. However, the potential of this structure remains unshielded. As a result, a reduction in electron density within the plasma leads to a decrease in both the amplitude and steepness of the wave. This relationship highlights the delicate balance between electron density and the stability of oscillatory structures, illustrating the dynamic interplay between charged particles in the plasma environment. [32,39]

Figure 8. Showing the profile $\psi^{(1)}$ of IAShWs that represented by Eq. (20) against χ with combination of different normalized density values $\mu_{m,}$ μ_e and μ_p for $(a)\lambda<1$ and $(b)\lambda>1$, while the values of other parameter is considered as $\delta_+=0.5,$ $\delta_-=0.5,$ $\Omega_+=0.6, \Omega_+=0.16,$ $l=0.3,$ $p_{+\parallel}=0.5,$ $p_{+\perp}=0.2, p_{-\parallel}=0.3$ & $p_{-\perp}=0.2$.

5. PHASE PORTRAIT ANALYSIS

The results of travelling wave solutions of a differential equation (DE) can also be analyzed through phase portrait analysis. For this phase portrait analysis, we convert the second order DE into two first order ordinary DEs in a system as follows [8,35,40]:

$$\left.\begin{array}{l} \dfrac{d\psi^{(1)}}{d\chi} = y \\[3mm] \dfrac{dy}{d\chi} = \dfrac{U}{G}\psi^{(1)} - \dfrac{Bl}{2G}\left(\psi^{(1)}\right)^2 + \dfrac{H}{G}y \end{array}\right\} \tag{21}$$

From this planner dynamical system (PDS)(Eq.21) the corresponding Jacobian matrix is

$$J = \begin{pmatrix} 0 & 1 \\[2mm] \dfrac{U}{G} - \dfrac{Bl}{2G}\psi^{(1)} & \dfrac{H}{G} \end{pmatrix} \tag{22}$$

The system (21) has two equilibrium points which are stated as $\left(\psi_i^{(1)},0\right)$ for $i=0$ and 1. The trace (T_i) and determinant (Δ_i) of the above Jacobian matrix decides the stability of the system at these equilibrium points. Let the elements of the Jacobian matrix be $\Delta_i = \det\left(J\left(\psi_i^{(1)},0\right)\right)$ and $T_i = trace\left(J\left(\psi_i^{(1)},0\right)\right)$. Then using the concept of dynamical systems [31,37-40], the equilibrium points $\left(\psi_i^{(1)},0\right)$ is a saddle point for $\Delta_i < 0$, a center point for $\Delta_i > 0, T_i = 0$, a stable spiral for $T_i < 0$ and $T_i^2 - 4\Delta_i < 0$, an unstable spiral for $T_i > 0$ and $T_i^2 - 4\Delta < 0$, and node for $T_i^2 - 4\Delta > 0$.

Figure 9(a) subsonic and 9(b) supersonic shown that the PDS (22) has two equilibrium configurations at $C_0(0,0)$ and $C_1\left(\left(2U/Bl\right)^2,0\right)$. To examine the stability of the system (22), we use the values of some typical parameter as $\beta_e = 0.2$, $\beta_p = 0.2$, $\delta_+ = 0.1$, $\delta_- = 0.1$, $\mu_m = 0.4, \mu_p = 0.7$ and $U > 0$, the critical point C_1 has $\Delta < 0$, thus this is a saddle point. Again, the critical C_0 satisfies $T_1 = 0$ and $\Delta_i > 0$.Thus the critical point $C_0(0,0)$ is a center. From both the figure we conclude that there are trajectories from $(-0.005,0)$ and $(0.005,0)$ connecting two saddle points. The existence of these heteroclinic orbit corresponds to occurrence of shock wave profile.
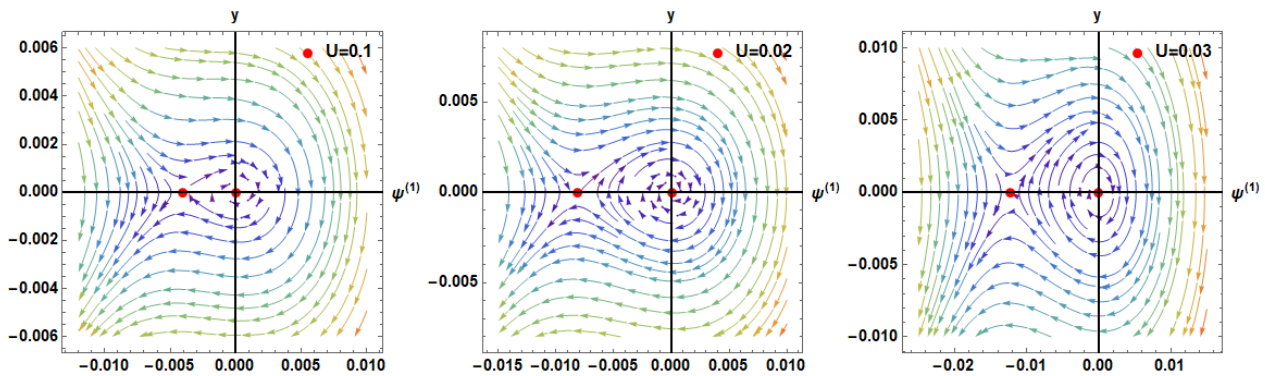
Figure 9(a). Phase portrait of the system (Eq. (21)) for different values of travelling wave speed U while $\delta_+ = 0.5$, $\delta_- = 0.5$, $\Omega_+ = 0.4, \Omega_+ = 0.1$, $l = 0.3$, $p_{+\parallel} = 0.5, p_{+\perp} = 0.2, p_{-\parallel} = 0.3$ & $p_{-\perp} = 0.2$ for the lower Mach number
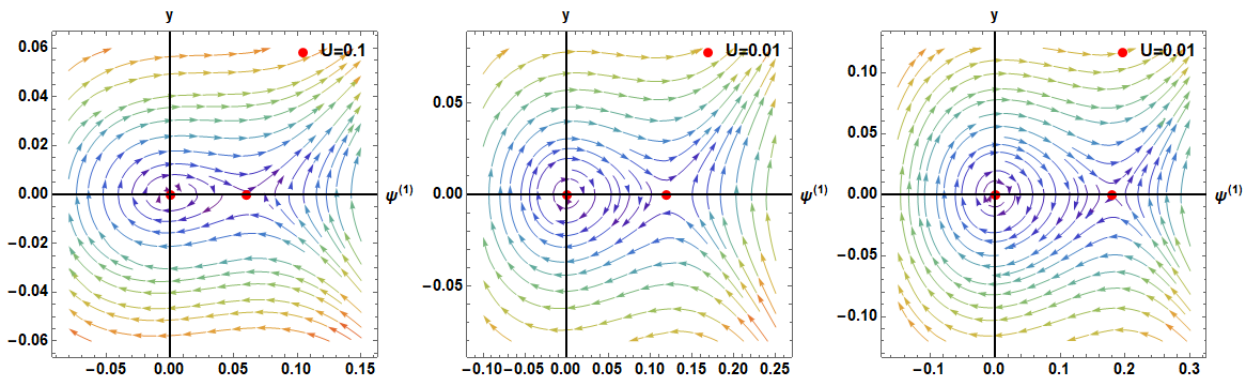
Figure 9(b). Phase portrait of the system (Eq. (21)) for different values of travelling wave speed U while $\delta_+ = 0.5$, $\delta_- = 0.5$, $\Omega_+ = 0.4, \Omega_+ = 0.1$, $l = 0.3$, $p_{+\parallel} = 0.5$, $p_{+\perp} = 0.2$, $p_{-\parallel} = 0.3$ & $p_{-\perp} = 0.2$ for the lower Mach number

6. CONCLUSION

In conclusion, we investigate the effect of trapping of electron & positron and anisotropic pressure as well as viscosity on IAShWs in degenerate plasma. With the help of method of reductive perturbation, we derived the well-known ZKB equation. The effect of density ratio of negative ion, electron and positron w.r.t positive ions, magnetic field, anisotropic pressure & viscosity for both positive and negative ions are investigated briefly. Next, we will convert our evolutionary equation into a two-dimensional dynamical system and conduct a phase-plane analysis. The results of our research could have practical applications in several situations involving space observation and astrophysics, particularly when dealing with trapped electrons and pressure anisotropy.

Declarations
Availability of data and materials: Not applicable. No new data were created or analyzed in this study.
Competing interests: The authors declare that they have no competing interests.
Authors' contributions: BP contributed in Plotting Graphs and writing the manuscript, AND contributed in forming model, methodology and supervised the manuscript. MKD contributed in editing of the manuscript.

ORCID
 Balaram Pradhan, https://orcid.org/0009-0005-8093-8035; **Apul Narayan Dev,** https://orcid.org/0000-0002-4478-5204
 Manoj Kumar Deka, https://orcid.org/0000-0001-8011-9930

REFERENCE
[1] A.A. Mamun, and P.K. Shukla, "Solitary waves in an ultrarelativistic degenerate dense plasma," Phys. Plasmas, **17**, 104504 (2010). https://doi.org/10.1063/1.3491433
[2] W.M. Moslem, "Self-similar expansion of white dwarfs. Astrophys," Space Sci. **342**, 351-355 (2012). https://doi.org/10.1007/s10509-012-1185-4
[3] N. Roy, S. Tasnim, and A.A. Mamun, "Solitary waves and double layers in an ultra-relativistic degenerate dusty electron-positron-ion plasma," Phys. Plasmas, **19**, 033705 (2012). https://doi.org/10.1063/1.3688877
[4] I. Zeba, W.M. Moslem, and P.K. Shukla, "Ion solitary pulses in warm plasmas with ultrarelativistic degenerate electrons and positrons," Astrophys. J. **750**, 72 (2012). https://doi.org/10.1088/0004-637X/750/1/72
[5] S.A. Shan, A. Ur-Rehman, and A. Mushtaq, "Ion-acoustic solitary waves in a positron beam plasma with electron trapping and nonextensivity effects," Phys. Plasmas, **24**, 032104 (2017). https://doi.org/10.1063/1.4978294
[6] A.U. Rahman, S. Ali, A. Mushtaq, and A. Qamar, "Nonlinear ion acoustic excitations in relativistic degenerate, astrophysical electron–positron–ion plasmas," J. Plasma Phys. **79**, 817-823 (2013). https://doi.org/10.1017/S0022377813000524
[7] B. Hosen, M.G. Shah, R.M. Hossen, and A.A. Mamun, "Ion-acoustic solitary waves and double layers in a magnetized degenerate quantum plasma," IEEE Trans. Plasma Sci. **45**, 3316-3327 (2017). https://doi.org/10.1109/TPS.2017.2766167
[8] A. Abdikian, A. Saha, and S. Alimirzaei, "Bifurcation analysis of ion-acoustic waves in an adiabatic trapped electron and warm ion plasma." J. Taibah Univ. Sci. **14**, 1051-1058 (2020). https://doi.org/10.1080/16583655.2020.1798062
[9] M.K. Islam, S. Biswas, N.A. Chowdhury, A. Mannan, M. Salahuddin, and A.A. Mamun, "Obliquely propagating ion-acoustic shock waves in a degenerate quantum plasma," Contrib. Plasma Phys. **62**, 202100073 (2022). https://doi.org/10.1002/ctpp.202100073
[10] M.M. Haider, and A.A. Mamun, "Ion-acoustic solitary waves and their multi-dimensional instability in a magnetized degenerate plasma," Phys. Plasmas. **19**, 102105 (2012). https://doi.org/10.1063/1.4757218
[11] A. Abdikian, and B. Ghanbari, "On a modified Korteweg–de Vries equation for electrostatic structures in relativistic degenerate electron–positron plasma," Results Phys. **48**, 106399 (2023). https://doi.org/10.1016/j.rinp.2023.106399
[12] M. Adnan, G. Williams, A. Qamar, S. Mahmood, and I. Kourakis, "Pressure anisotropy effects on nonlinear electrostatic excitations in magnetized electron-positron-ion plasmas," Eur. Phys. J. D, **68**, 1-15 (2014). https://doi.org/10.1140/epjd/e2014-50384-y
[13] M.K. Deka, B. Pradhan, A.N. Dev, D. Mahanta, J. Manafian, and K.H. Mahmoud, "Shock Waves in Ion-Beam-Depleted Spin-Polarized Quantum Plasma with Ionic Pressure Anisotropy," Plasma, **8**, 3 (2025). https://doi.org/10.3390/plasma8010003
[14] M. Ahmad, M. Adnan, and A. Qamar, "Magnetosonic shock waves in degenerate electron–positron–ion plasma with separated spin densities," Phys. Fluids, **36**, 087115 (2024). https://doi.org/10.1063/5.0216452
[15] R. Jahangir, and S. Ali, "Nonlinear ion-acoustic waves in degenerate plasma with landau quantized trapped electrons," Front. Phys. **9**, 622820 (2021). https://doi.org/10.3389/fphy.2021.622820
[16] H. Schamel, and B. Sarbeswar, "Analytical double layers," Phys. Fluids, **26**, 190-193 (1983). https://doi.org/10.1063/1.864006
[17] H. Schamel, "Weak double layers: Existence, stability, evidence," Z. fur Naturforsch. - J. Phys. Sci. **38**, 1170-1183 (1983). https://doi.org/10.1515/zna-1983-1102
[18] H. Schamel, and V.I. Maslov, "Adiabatic growth of electron holes in current-carrying plasmas," Phys. Scr. **50**, 42 (1994). https://doi.org/10.1088/0031-8949/1994/T50/006
[19] V. Maslov, and H. Schamel, "Growing electron holes in drifting plasmas," Phys. Lett. A, **178**, 171-174 (1993). https://doi.org/10.1016/0375-9601(93)90746-M
[20] R. Kaur, and N.S. Saini, "Ion acoustic shocks in a weakly relativistic ion-beam degenerate magnetoplasma," Galaxies, **9**, 64 (2021). https://doi.org/10.3390/galaxies9030064
[21] M.J. Iqbal, W. Masood, H.A. Shah, and N.L. Tsintsadze, "Nonlinear density excitations in electron-positron-ion plasmas with trapping in a quantizing magnetic field," Phys. Plasmas, **24**, 014503 (2017). https://doi.org/10.1063/1.4973830
[22] M.A. El-Borie, M. Abd-Elzaher, and A. Atteya, "Obliquely propagating ion-acoustic solitary and shock waves in magnetized quantum degenerate multi-ions plasma in the presence of trapped electrons," Chin. J. Phys. **63**, 258-270 (2020). https://doi.org/10.1016/j.cjph.2019.10.004

[23] H.A. Shah, M.N.S. Qureshi, and N. Tsintsadze, "Effect of trapping in degenerate quantum plasmas," Phys. Plasmas, **17**, 032312 (2010). https://doi.org/10.1063/1.3368831

[24] S.Y. El-Monier, and A. Atteya, "Dynamics of ion-acoustic waves in nonrelativistic magnetized multi-ion quantum plasma: the role of trapped electrons," Waves Random Complex Media, **32**, 299-317 (2022). https://doi.org/10.1080/17455030.2020.1772522

[25] T. Yeashna, R.K. Shikha, N.A. Chowdhury, A. Mannan, S. Sultana, and A. Mamun, "Ion-acoustic shock waves in magnetized pair-ion plasma," Eur. Phys. J. D, **75**, 1-7 (2021). https://doi.org/10.1140/epjd/s10053-021-00139-y

[26] N.A. Zedan, A. Atteya, W.F. El-Taibany, and S.K. El-Labany, "Stability of ion-acoustic solitons in a multi-ion degenerate plasma with the effects of trapping and polarization under the influence of quantizing magnetic field," Waves Random Complex Media, **32**, 728-742 (2022). https://doi.org/10.1080/17455030.2020.1798560

[27] P. Halder, K.N. Mukta, and A.A. Mamun, "Nonlinear propagation of dust-ion-acoustic shock waves in a degenerate multi-species plasma," Int. J. Cosmol. Astron. Astrophys. **1**, 81-87 (2019). http://dx.doi.org/10.18689/ijcaa-1000119

[28] S. Hussain, H. Ur-Rehman, and S. Mahmood, " The effect of magnetic field quantization on the propagation of shock waves in quantum plasmas," Phys. Plasmas. 26, 052105 (2019). https://doi.org/10.1063/1.5090181

[29] M. Asaduzzaman, M.A.A. Mamun, and A.A. Mamun, "Obliquely Propagating Self-Gravitational Shock Waves in Non-Relativistic Degenerate Quantum Plasmas," J. Eng. Sci. Technol. Rev. **15**(1), 21-29 (2024). https://doi.org/10.3329/jes.v15i1.76030

[30] M.K. Deka, and A.N. Dev, "Wave propagation with degenerate electron–positron in magnetically quantised ion beam plasma," Pramana, **95**, 65 (2021). https://doi.org/10.1007/s12043-021-02081-5

[31] M. Irfan, S. Ali, and A.M. Mirza, "Solitary waves in a degenerate relativistic plasma with ionic pressure anisotropy and electron trapping effects," Phys. Plasmas. **24**, 052108 (2017). https://doi.org/10.1063/1.4981932

[32] S. Jahan, T.S. Roy, B.E. Sharmin, N.A. Chowdhury, A. Mannan, and A.A. Mamun, "Magnetized ion-acoustic shock waves in degenerate quantum plasma," arXiv preprint arXiv 2103, 15863 (2021). https://doi.org/10.48550/arXiv.2103.15863

[33] A. Ur-Rahman, I. Kourakis, and A. Qamar, "Electrostatic solitary waves in relativistic degenerate electron–positron–ion plasma," IEEE Trans. Plasma Sci. **43**, 974-984 (2015). https://doi.org/10.1109/TPS.2015.2404298

[34] M.K. Deka, D. Mahanta, A.N. Dev, J. Sarma, S.K. Mishra, E. Saikia, "Features of shock wave in a quantized magneto plasma under the influence of ionic pressure anisotropy and anisotropic viscosity," AIP Conf. Proc. **2819**, 070005 (2023). https://doi.org/10.1063/5.0137746

[35] I. Alazman, B.S.T. Alkahtani, M. Ur-Rahman, and M.N. Mishra, "Nonlinear complex dynamical analysis and solitary waves for the (3+1)-D nonlinear extended Quantum Zakharov–Kuznetsov equation," Results Phys. **58**, 107432 (2024). https://doi.org/10.1016/j.rinp.2024.107432

[36] W. Albalawi, M.M. Hammad, M. Khalid, A. Kabir, C.G. Tiofack, and S.A. El-Tantawy, "On the shock wave structures in anisotropy magnetoplasmas," AIP Advances, **13**, 105309 (2023). https://doi.org/10.1063/5.0173000

[37] B. Boro, A.N. Dev, B.K. Saikia, and N.C. Adhikary, "Nonlinear dust ion acoustic shock wave structures in solar F corona region," Phys. Plasmas, **27**, 122901 (2020). https://doi.org/10.1063/5.0023283

[38] B. Pradhan, B. Boro, A.N. Dev, J. Manafian, and N.A. Alkader, "Effect of ion anisotropy pressure in viscous plasmas: evolution of shock wave," Nonlinear Dyn. **112**, 17403-17416 (2024). https://doi.org/10.1007/s11071-024-09994-x

[39] S. Jahan, B.E. Sharmin, N.A. Chowdhury, A. Mannan, T.S. Roy, and A.A. Mamun, "Electrostatic ion-acoustic shock waves in a magnetized degenerate quantum plasma," Plasma, **4**, 426-434 (2021). https://doi.org/10.3390/plasma4030031

[40] T. Sarkar, S. Roy, S. Raut, and P.C. Mali, "Studies on the dust acoustic shock, solitary, and periodic waves in an unmagnetized viscous dusty plasma with two-temperature ions," Braz. J. Phys. **53**, 12 (2023). https://doi.org/10.1007/s13538-022-01221-5

[41] Z. Iqbal, H.A. Shah, M.N.S. Qureshi, W. Masood, and A. Fayyaz, "Nonlinear dynamical analysis of drift ion acoustic shock waves in Electron-Positron-Ion plasma with adiabatic trapping," Results Phys. **41**, 105948 (2022). https://doi.org/10.1016/j.rinp.2022.105948

[42] A. Atteya, M.A. El-Borie, G.D. Roston, A.A.S. El-Helbawy, P.K. Prasad, and A. Saha, "Ion-acoustic stable oscillations, solitary, periodic and shock waves in a quantum magnetized electron–positron–ion plasma," Z. fur Naturforsch. - J. Phys. Sci. **76**, 757-768 (2021). https://doi.org/10.1515/zna-2021-0060

[43] S.N. Chow, and J.K. Hale, *Methods of bifurcation theory*, (Springer Science & Business Media, 2012).

[44] J. Guckenheimer, and P. Holmes, *Nonlinear oscillations, dynamical systems, and bifurcations of vector fields*, (Springer Science & Business Media, 2013).

ПОШИРЕННЯ ХВИЛЬ В АНІЗОТРОПНІЙ МАГНІТНО-КВАНТОВАНІЙ ІОННІЙ ПЛАЗМІ З ЗАХОПЛЕНИМИ ЕЛЕКТРОНАМИ ТА ПОЗИТРОНАМИ

Баларам Прадхан[a], Апул Нарайан Дев[b], Манодж Кумар Дека[c]
[a]Центр науки про дані, Сікша «О» Анусандхан (вважається університетом), Хандагірі, Бхубнешвар 751030, Одіша, Індія
[b]Кафедра математики, Сікша «О» Анусандхан (вважається університетом), Хандагірі, Бхубнешвар 751030, Одіша, Індія
[c]Кафедра радіографії та технологій візуалізації, Університет медичних наук імені Шріманти Шанкарадеви, Гувахаті 781032, Індія

Це дослідження розглядає вплив магнітно квантованих вироджених захоплених електронів та позитронів на іонно-акустичні ударні хвилі (ІАУХ) малої амплітуди в парній іонній плазмі за допомогою рівняння Захарова-Кузнецова-Бюргера (ZKB). Воно зосереджується на тому, як такі фактори, як магнітне квантування, вироджена температура, нормалізовані негативні іони, електрони, позитрони, анізотропний тиск та інші відповідні фізичні параметри з астрофізичного плазмового середовища, впливають на поширення ІАУХ, особливо в нелінійному режимі. Це дослідження досліджує, що існують два різних режими поширення хвиль — дозвуковий та надзвуковий, які демонструють мало відмінних характеристик у різних фізичних плазмових середовищах астрофізичного походження. Результати можуть допомогти в розумінні нелінійної динаміки та характеристик поширення хвиль у надщільній плазмі, що зустрічається в білих карликах та нейтронних зірках, де вплив захоплених електронів та позитронів, а також анізотропія іонного тиску, є значним, що ще потребує детального вивчення.

Ключові слова: *намагнічена плазма; дозвуковий та надзвуковий режими; метод відновних збурень (RPT); вироджені захоплені електрони та позитрони; рівняння ZKB; аналіз фазової площини*

MODELLING OF MHD MICROPOLAR NANO FLUID FLOW IN AN INCLINED POROUS STENOSED ARTERY WITH DILATATION

 Narender Satwai[a,b], Karanamu Maruthi Prasad[a]*

[a]*Department of Mathematics, School of Science, GITAM (Deemed to be University), Hyderabad, Telangana State, India–502329*
[b]*Department of Mathematics, B V Raju Institute of Technology, Vishnupur, Narsapur, Telangana State, India-502313*
*Corresponding author e-mail: mkaranam@gitam.edu
Received April 20, 2025; revised June 1, 2025; Accepted June 9, 2025

In this paper, the impact of a magnetic field on blood flow with nanofluid particles through an inclined porous stenosed artery and dilatation was studied. Here blood is treated as micropolar fluid. The equations are solved by using Homotopy perturbation method [HPM] under the assumption of mild stenosis. The closed form solutions of velocity, temperature profile, and concentration distribution are obtained. The effects of pertinent parameters on flow phenomena have been observed and results are analyzed graphically. This study examines the impact of the magnetic parameter on flow characteristics and reveals that the presence of a magnetic field increases resistance to the flow while decreasing shear stress at the wall. A result is found that the flow resistance and shear stress at the wall decreased for heights of the stenosis dilatation. Additionally, the study finds that resistance to the flow increases and shear stress at the wall decreases with viscosity. The stream lines are drawn to examine the flow pattern and properties of momentum transfer.
Keywords: *Stenosis; Dilatation; Micropolar fluid; Flow resistance; Wall shear stress; Brownian motion parameter; Thermophoresis parameter*
PACS: 47.15.-x, 47.63.-b, 47.63.Cb

1. INTRODUCTION

Atherosclerosis, which is the narrowing of the blood vessel lumen, or the inner open space or lumen of an artery, due to fatty substance formation, is one of the most dangerous health risks in the modern world. This may result in hypertension, myocardial infarction, and further complications. Consequently, stenosis occurs when abnormal and irregular growth impedes normal blood circulation, with significant research indicating that hydrodynamic characteristics, including wall shear and flow resistance, contribute to the onset and progression of this medical condition. A comprehensive understanding of the blood flow dynamics in a stenosed vessel would facilitate precise diagnosis and treatment of cardiovascular conditions.

As a result, several researchers have explored mathematical models for confined duct flows [1,2,3,4,5]. All these mathematical analyses have characterized blood as a Newtonian fluid. Moreover, when the diameters of the artery or tube are small and the shear rate is low, blood demonstrates non-Newtonian behavior. The quantity of red blood cells (RBCs) in erythrocytes affects this behavior. Young D. F., Tsai F. Y., and P. Chaturani and R. P. Samy [6,4] conducted theoretical and experimental investigations on blood flow in arteries exhibiting mild stenosis. All these investigations aim to elucidate how stenosis influences the properties of blood flow, encompassing velocity profile, wall shear stress, and resistive impedance. Prasad K.M. and Yasa P.R. [7] developed a mathematical explanation for the flow of a micropolar fluid within a tapering stenosed artery including porous walls.

However, all these investigations concentrated on the effects of individual arterial stenosis assuming a uniform cross-section of the tube. It is acknowledged that many blood arteries display small changes in cross-section over their length and can develop multiple segments, especially at bends and junctions (Schneck et al. [8]). Addressing this complexity, Maruthi Prasad, and Radhakrishnamacharya [9] investigated blood flow in arteries with multiple stenoses and a non-uniform cross-section, modeling blood as a Herschel-Bulkley fluid.

A Cemal Eringen's [10] described simple microfluids as concentrated suspensions of neutrally buoyant deformable particles in a viscous fluid, in which the individuality of substructures influences the physical outcome of the flow. Such fluid models can be used to rheologically characterize polymeric suspensions and normal human blood, and they have been used to physiological and technical concerns Micropolar fluids are a subclass of microfluids characterized by rigid fluid microelements. Basically, these fluids may support couple strains and body couples while also exhibiting micro rotational and micro inertial effects. The fundamental benefit of using a micropolar fluid model to analyze blood flow in comparison to other types of non-Newtonian fluids is that it takes care of the rotation of fluid particles by means of an independent kinematic vector known as the microrotation vector. G. R. Charya [11] described blood flow as micropolar fluid flow through a constricted channel. Fluid circulation in a non-symmetric vessel with continuous, constrained borders is investigated in this paper. Theoretical velocity profiles are calculated using the micropolar fluid to simulate blood flow in small arteries, and the results show good agreement with the experimental data. Ariman et al. [12] presented a comprehensive examination of microcontinuum fluid mechanics, illustrating numerous applications in physiological phenomena. Prasad, K. M. et al. [13] examined a mathematical explanation for two-layered fluid flow through a stenotic

artery, in which the core region contains a micropolar fluid with nanoparticles, acting as a non-Newtonian fluid, while the peripheral region behaves as a Newtonian fluid. Srinivasacharya, D, et al. [14] studied the peristalsis of a micropolar fluid in a tube. Prasad, K. M. & Yasa, P. R. [15] examined the micropolar fluid flow through a permeable artery.

Blood is appropriately described as a micropolar fluid due to its complicated and changeable rheological behaviour, which is heavily influenced by changes in artery diameter. As arteries contract, microelements like red blood cells (RBCs) become compressed, increasing collision impacts and frictional interactions. These microstructural dynamics have a major effect on the viscosity and velocity profiles of blood flow [16]. Furthermore, the formation of cholesterol plaques over time can constrict the carotid artery, increasing the risk of stroke or temporary vision loss caused by disturbed or misdirected blood flow. Because plaque development and progression are controlled by local flow conditions, a micropolar fluid model is appropriate for illustrating blood's crucial micro rotational and shear-dependent behaviour in such pathological conditions [17].

Fluids that contain nanoparticles, which are incredibly tiny particles with a nanometer scale, are known as nanofluids. Nano-fluids have generated significant interest from researchers because of their increased thermal conductivity, a concept first introduced by Choi [18]. Nadeem and Noreen Sher Akbar [19] studied the flow of a micropolar fluid infused with nanoparticles in the smaller intestine. Many researchers focused on this field because of its significance in the biomedical field [20,21,22]. Maruthi Prasad and Prabhakar Reddy [23] studied the thermal effects of two immiscible fluids within a permeable stenosed artery having Newtonian fluid in the peripheral region and a nano-fluid in the core region. Prasad, K. M. et al. [24] explored a mathematical model peristaltic pumping of Jeffrey model with nanoparticles in an inclined tube. Dawood, A. S. et al. [25] investigates nanofluid behavior in stenosed arteries by introducing a variable pressure gradient and analyzing the impact of magnetic fields on nano-blood flow. The presence of nanoparticles suspended in the base fluid is insufficient to improve thermal conductivity, as this enhancement is contingent upon the particles' shape and size of the particles.

In the human vascular system, magnetic fields are essential for controlling blood flow. Magnetohydrodynamic (MHD) applications have been demonstrated to lower blood artery fluid flow rates and aid in the treatment of cardiovascular diseases. Numerous biological uses, including drug administration, cell separation, and cancer treatment, have led to the development of magnetic devices. Ikbal et al. [26], Bali and Awasthi [27] and Misra et al. [28] have all done significant work on biofluid dynamics in the context of magnetic fields, while He [29,30] investigated the application of Homotopy perturbation method. A moving electrically conducting fluid will produce both electric and magnetic fields when exposed to a magnetic field. A body force called the Lorentz force is created when these fields interact, and it tends to oppose the liquid's movement [31]. When Sud et al. [32] investigated how a moving magnetic field affected blood flow, they found that a suitable moving magnetic field accelerated blood flow. Utilizing a long wavelength approximation technique and a fundamental mathematical model for blood flow in a uniformly branching channel with flexible walls. Agrawal and Anwaruddin [33] examined the influence of a magnetic field on blood flow. The research demonstrated that a magnetic field could serve as a blood pump in cardiac processes to improve blood circulation in arteries impacted by arterial abnormalities such as stenosis or arteriosclerosis.

The various uses of porous medium, such as fluid filtration, water flow across riverbeds, surface water and oil transportation, bile duct fluid mechanics, and blood circulation in small arteries, make their impact on fluid dynamics noteworthy. Researchers have been inspired by these real-world uses to study flow dynamics in various geometries that incorporate porous media [34]. The impact of magnetic forces on the fluid flow of a nanofluid through an inclined channel with permeable walls and different constrictions, located within a porous medium, was investigated by Prasad, K. M., and Yasa, P. R. [35]. Azmi, W. F. W. et al. [36] studied fractional Casson fluid flow in small arteries, highlighting the impact of slip conditions and cholesterol porosity on blood flow dynamics.

In the human body, arteries are rarely aligned horizontally or vertically. Many arteries, including the carotid, femoral, and coronary arteries, are naturally inclined as a result of anatomical form and posture. Modelling the artery as inclined allows us to include gravitational forces that influence blood flow and pressure distribution. According to studies, arterial inclination has a considerable impact on velocity profiles, wall shear stress, and pressure gradients, all of which are important in diagnosing vascular disorders like stenosis. Therefore, including an inclined configuration in cardiovascular models provides a more realistic and comprehensive knowledge of blood flow dynamics under various physiological conditions. Prasad, K.M. and Yasa, P.R. [37] investigated micropolar fluid behavior in an inclined permeable tube with a non-uniform cross-section with an explanation for non-newtonian fluid flow in tubes with multiple stenoses. Their results illustrate the importance of fluid dynamics in the development and potential treatment of cardiovascular diseases.

Many researchers describe the stenosis as mild and single or multiple, but arterial disease often involves a combination of stenotic and post-stenotic dilated segments. Sudha, T. et al. [38] analyzed the impact of stenosis and dilatation on arterial blood flow with suspended nanoparticles utilizing the Homotopy method. Maruthi Prasad, K. et al. [39] investigates the impact of stenosis and post-stenotic dilatation on Jeffrey fluid flow in arteries. Pincombe et al. [40] investigated the effects of post-stenotic enlargements in coronary arteries, emphasizing the need for a more comprehensive approach to modeling arterial disease. While considering the issue of post-stenotic dilations as an interesting mathematical problem with applications frequently in the vascular system, this article focuses on post-stenotic dilatations since they have more medicinal significance.

Motivated from the above investigations a mathematical model has been developed for fluid flow across an inclined stenosis and dilatation with the influence of a magnetic field through a porous medium. Blood has been described as a micropolar fluid flow that contains nanoparticles.

2. MATHEMATICAL MODEL

A Cylindrical polar coordinate system (r, θ, z) is considered, where the Z−axis coincides with the center line of the tube, and flow is assumed to be axisymmetric. Consider the flow of a micropolar fluid across an inclined stenosed artery with dilatation, characterized by fluid viscosity μ and density ρ.
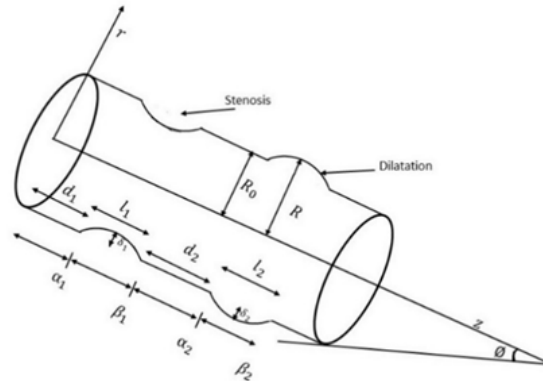
Figure 1. Geometry of the problem

The geometry of the problem, as shown in Figure 1, is given as

$$h(z) = \begin{cases} R_0 - \frac{\delta_i}{2}\left(1 + Cos\frac{2\pi}{l_i}\left(z - \alpha_i - \frac{l_i}{2}\right)\right), & for \ \alpha_i \leq z \leq \beta_i \\ R_0 & ; elsewhere \end{cases} \tag{1}$$

Where the maximum distance of the ith abnormal segment is denoted by δ_i, while R and R_0 signifies the radius of the affected artery and normal artery, respectively. The length of the ith abnormal segment is given by l_i, and the distance between the origin to the start of this segment is denoted by α_i as defined (Maruthi Prasad K. et al. [39] & Dhange M. et. al [41])

$$\alpha_i = \left(\sum_{j=1}^{i}(d_j + l_j)\right) - l_i \tag{2}$$

And β_i denotes the distance from the origin to the end of the ith abnormal segment and is given by

$$\beta_i = \left(\sum_{j=1}^{i}(d_j + l_j)\right) \tag{3}$$

The distance between the start of the ith abnormal section from the end of the (i-1)th segment is represent by d_i, for from the start of the segment if i =1

Accordingly, these are the governing equations for the fluid flow (Prasad, K. M. et al. [42])

$$\frac{\partial w_r}{\partial r} + \frac{w_r}{r} + \frac{\partial w_z}{\partial z} = 0 \tag{4}$$

$$R_e\delta\left(w_r\frac{\partial w_z}{\partial r} + w_z\frac{\partial w_z}{\partial z}\right) = -\frac{\partial p}{\partial z} + \frac{1}{N-1}\left(\frac{N}{r}\frac{\partial(rv_\theta)}{\partial r} + \frac{\partial^2 w_z}{\partial r^2} + \frac{1}{r}\frac{\partial w_z}{\partial r} + \delta^2\frac{\partial^2 w_z}{\partial z^2}\right) + (G_r\theta + B_r\sigma) + \frac{sin[\emptyset]}{F} - \frac{\mu\bar{w}}{K} + \bar{J}\times\bar{B} \tag{5}$$

$$R_e\delta^3\left(w_r\frac{\partial w_r}{\partial r} + w_z\cdot\frac{\partial w_r}{\partial z}\right) = -\frac{\partial p}{\partial r} + \frac{\delta^2}{N-1}\left(-N\frac{\partial v_\theta}{\partial z} + \frac{\partial^2 w_r}{\partial r^2} + \frac{1}{r}\frac{\partial w_r}{\partial r} - \frac{w_r}{r^2} + \delta^2\frac{\partial^2 w_z}{\partial z^2}\right) - \frac{cos[\emptyset]}{F} \tag{6}$$

$$\frac{jR_e\delta(1-N)}{N}\left(w_r\frac{\partial v_\theta}{\partial r} + w_z\frac{\partial v_\theta}{\partial z}\right) = -2v_\theta + \left(\delta^2\frac{\partial w_r}{\partial z} - \frac{\partial w_z}{\partial r}\right) + \frac{2-N}{m^2}\left(\frac{\partial}{\partial r}\left(\frac{1}{r}\frac{\partial(rv_\theta)}{\partial r}\right) + \delta^2\frac{\partial^2 v_\theta}{\partial z^2}\right) \tag{7}$$

$$\frac{R_e\delta\mu\overline{T_0}}{2\rho a^2}\left(w_r\frac{\partial\theta_t}{\partial r} + w_z\frac{\partial\theta_t}{\partial z}\right) = \frac{\overline{T_0}}{a^2}\left(\frac{1}{r}\frac{\partial}{\partial r}\left(r\frac{\partial\theta_t}{\partial r}\right)\right) + \frac{N_b\overline{T_0}}{a^2}\left(\frac{\partial\sigma}{\partial r}\right)\left(\frac{\partial\theta_t}{\partial r}\right) + \frac{N_t}{a^2}\left(\frac{\partial\theta_t}{\partial r}\right)^2 \tag{8}$$

$$\frac{4R_e\mu\overline{C_0}}{\rho a^2}\left(w_r\frac{\partial\sigma}{\partial r} + w_z\frac{\partial\sigma}{\partial z}\right) = \frac{(\rho c)_f}{(\rho c)_p}\frac{1}{a^2}\left[N_b\left(\frac{1}{r}\frac{\partial}{\partial r}\left(r\frac{\partial\sigma}{\partial r}\right)\right) + N_t\left(\frac{1}{r}\frac{\partial}{\partial r}\left(r\frac{\partial\theta_t}{\partial r}\right)\right)\right] \tag{9}$$

where $T = \frac{(\rho c)_f}{(\rho c)_p}$ is the ratio between the effective heat capacity of the nano particle material and heat capacity of the fluid. Here $F = \frac{1}{\rho g}$, $N = \frac{\mu}{\mu+K}$ is the coupling number $(0 \leq N \leq 1)$, $m = \frac{a^2K(2\mu+K)}{\gamma(\mu+K)}$ is the micro polar parameter. v_θ is the micro rotation in the θ direction.

In this context, ρ denotes fluid density, p represents fluid pressure, K indicates the permeability of the porous media, j micro gyration parameter, (μ) refers to viscosity, and F corresponds to body force. $\bar{J} \times \bar{B}$ represents the Lorentz force term in magnetohydrodynamics (where $\bar{J}$ denotes the current density vector and $\bar{B}$ signifies the magnetic field vector). Here, the microrotation vector and velocity are represented by $V = (0, v_\theta, 0)$ & $W = (w_r, 0, w_z)$ respectively

The non-dimensional variables are

$$\bar{\delta} = \frac{\delta}{R_0}, \bar{z} = \frac{z}{L}, \bar{r} = \frac{r}{R_0}, \overline{W}_z = \frac{w_z}{w_0}, \overline{W_r} = \frac{Lw_r}{w_0\delta}, \overline{W_\theta} = \frac{R_0\vartheta_\theta}{w_0}, \bar{J} = \frac{j}{R_0^2}, \bar{p} = \frac{P}{\frac{\mu w_0 L}{R_0^2}}, \bar{q} = \frac{q}{\pi R_0^2 w}, R_e = \frac{2\rho c_1 R_0}{\mu}, F = \frac{\mu U^h}{\rho g R_0^{h+1}},$$

$$N_b = \frac{(\rho c)_p D_{\bar{B}}\bar{C}_0}{(\rho c)_f}, N_t = \frac{(\rho c)_p D_T \bar{T}_0}{(\rho c)_f \beta}, G_r = \frac{g\beta\bar{T}_0 R_0^3}{\gamma^2}, B_r = \frac{g\beta\bar{C}_0 R_0^3}{\gamma^2}, \theta_t = \frac{T - \bar{T}_0}{\bar{T}_0}, \sigma = \frac{C - \bar{C}_0}{\bar{C}_0}, \bar{F} = \frac{F}{\mu W \lambda'}, M = \frac{\sigma R_0^2 B_0^2}{\rho\vartheta},$$

By using mild stenosis approximation, $\left(\frac{\delta}{R_0} \ll 1, Re * (2\delta/L0) \ll 1 \text{ and } 2R_0/L_0(1)\right)$ and non-dimensional scheme to the equations (4) to (9), the equations become

$$\frac{\partial P}{\partial r} = -\frac{\cos\alpha}{F} \tag{10}$$

$$\frac{N}{r}\frac{\partial}{\partial r}(rV_\theta) + \frac{\partial^2 w}{\partial r^2} + \frac{1}{r}\frac{\partial w}{\partial r} + (1-N)\frac{\sin[\phi]}{F} + (1-N)(G_r\theta + B_r\sigma) - \frac{\mu w}{k} - Mw = (1-N)\frac{\partial P}{\partial z} \tag{11}$$

$$2V_\theta + \frac{\partial w}{\partial r} - \frac{2-N}{m^2}\frac{\partial}{\partial r}\left(\frac{1}{r}\frac{\partial}{\partial r}(rV_\theta)\right) = 0 \tag{12}$$

$$\frac{1}{r}\frac{\partial}{\partial r}\left(r\frac{\partial\theta}{\partial r}\right) + N_b\frac{\partial\sigma}{\partial r}\frac{\partial\theta}{\partial r} + N_t\left(\frac{\partial\theta}{\partial r}\right)^2 = 0 \tag{13}$$

$$\frac{1}{r}\frac{\partial}{\partial r}\left(r\frac{\partial\sigma}{\partial r}\right) + \frac{N_t}{N_b}\left(\frac{1}{r}\frac{\partial}{\partial r}\left(r\frac{\partial\theta}{\partial r}\right)\right) = 0 \tag{14}$$

The axial velocity, denoted by w, has a radius of R_0. The temperature profile, nanoparticle phenomena, local temperature, and local nanoparticle Grashof numbers, Brownian motion number, Thermophoresis parameter, micropolar parameter and coupling number are represented by $\theta, \sigma, B_r, G_r, N_b, N_t, m$ and N. Additionally, $M = \sigma B_0^2$ is the magnetic parameter, μ is the viscosity, and k is the porous medium permeability.

The non-dimensional boundary conditions (Prasad, K. M., & Sudha, T. [43])

$$w = 0, V_\theta = 0, \theta = 0, \sigma = o \text{ at } r = h(z) \tag{15}$$

$$\frac{\partial w}{\partial r} = 0, \frac{\partial\theta}{\partial r} = 0, \frac{\partial\sigma}{\partial r} = 0 \text{ at } r = 0 \tag{16}$$

$$V_\theta \text{ is finite at } r = h(z) \tag{17}$$

3. METHOD OF SOLUTION

The coupled equations are solved using the Homotopy Perturbation Method (HPM). The Homotopy perturbation method (HPM) has been used to determine the solutions of the coupled equations (13) and (14).

$$H(q, \theta) = (1-q)[L(\theta) - L(\theta_{10})] + q\left[L(\theta) + N_b\frac{\partial\sigma}{\partial r} \cdot \frac{\partial\theta}{\partial r} + N_t\left(\frac{\partial\theta}{\partial r}\right)^2\right] \tag{18}$$

$$H(q, \theta) = L(\theta) - L(\theta_{10}) + qL(\theta_{10}) + q\left[N_b\frac{\partial\sigma}{\partial r} \cdot \frac{\partial\theta}{\partial r} + N_t\left(\frac{\partial\theta}{\partial r}\right)^2\right] \tag{19}$$

$$H(q, \sigma) = (1-q)[L(\sigma) - L(\sigma_{10})] + q\left[L(\sigma) + \frac{N_t}{N_b}\left(\frac{1}{r}\frac{\partial}{\partial r}\left(r\frac{\partial\theta}{\partial r}\right)\right)\right] \tag{20}$$

$$H(q, \sigma) = L(\sigma) - L(\sigma_{10}) + qL(\sigma_{10}) + q\left[\frac{N_t}{N_b}\left(\frac{1}{r}\frac{\partial}{\partial r}\left(r\frac{\partial\theta}{\partial r}\right)\right)\right] \tag{21}$$

Where, q is the embedding parameter $(0 \le q \le 1)$, $L \equiv \frac{1}{r}\frac{\partial}{\partial r}\left(r \cdot \frac{\partial}{\partial r}\right)$ is a linear operator, θ_0 ahd σ_0 are the initial guesses, given by

$$\theta_0(r, z) = \left(\frac{r^2 - h^2}{4}\right), \quad \sigma_0(r, z) = -\left(\frac{r^2 - h^2}{4}\right) \tag{22}$$

Define

$$\theta(r, z) = \theta_0 + q\theta_1 + q^2\theta_2 + \cdots \tag{23}$$

$$\sigma(r,z) = \sigma_0 + q\sigma_1 + q^2\sigma_2 + \cdots \qquad (24)$$

The Convergence of equations (23) and (24) is depending up on the non – linear component of the expression. Utilizing the same procedure as applied by (30), the solutions for temperature profile (θ) and nanoparticle phenomenon (σ) for $q = 1$ are

$$\theta(r,z) = \frac{1}{64}(N_b - N_t)(r^2 - h^2) - \left(\frac{1}{18}N_b(r^3 - h^3) + \frac{N_t}{36864}(N_b^2 + N_t^2)(r^4 - h^4)(r^6 - h^6)\right) \qquad (25)$$

$$\sigma(r,z) = \frac{-1}{4}(r^2 - h^2)\frac{N_t}{N_b} + \frac{N_t}{N_b}\left(\frac{1}{18}N_b(r^3 - h^3) + \frac{1}{36864}(N_b^2 + N_t^2)(r^6 - h^6)\right). \qquad (26)$$

Substituting equations (25) and (26) in (11) and using boundary conditions

$$\frac{\partial w}{\partial r} = -NV_\theta + (1-N)\frac{r}{2}\frac{dP}{dz} - (1-N)\frac{r}{2}\frac{sin[\emptyset]}{F} - (1-N)\left[G_r\left(\frac{1}{64}(N_b - N_t)\left(\frac{r^3}{4} - \frac{h^2 r}{2}\right) - \right.\right.$$
$$\left(\frac{1}{18}N_b\left(\frac{r^4}{5} - \frac{h^3 r}{2}\right) + \frac{N_t(N_t^2 + N_b^2)}{36864}\left(\frac{r^{11}}{12} - \frac{r^5 h^6}{6} - \frac{r^7 h^4}{8} + \frac{rh^{10}}{2}\right)\right)\right) + B_r\left(\frac{-1}{4}\left(\frac{r^3}{4} - \frac{h^2 r}{2}\right)\frac{N_t}{N_b} + $$
$$\left.\left.\frac{N_t}{N_b}\left(\frac{N_b}{18}\left(\frac{r^4}{5} - \frac{h^3 r^2}{2}\right) + \frac{(N_b^2 + N_t^2)}{3686u}\left(\frac{r^7}{8} - \frac{h^6 r}{2}\right)\right)\right)\right] + \left(\frac{\mu}{k} + M\right)\frac{wr}{2} \qquad (27)$$

Substitute (27) and (12), we get the expression for V_θ

$$V_\theta = C_2(z)I_1(mr) + C_3(z)K_1(mr) - \frac{(1-N)r}{2(2-N)}\left(\frac{dP}{dz} - \frac{sin[\emptyset]}{F}\right) + \left(\frac{1-N}{2-N}\right)\left[G_r(N_b - N_t)\left(\frac{r}{32m^2} - \frac{h^2 r}{128} + \frac{r^3}{256}\right) - \right.$$
$$G_r N_b\left(\frac{1}{2m^4} - \frac{rh^3}{36} + \frac{r^2}{6m^2} + \frac{r^4}{90}\right) - \frac{G_r N_t(N_b^2 + N_t^2)}{36864}\left(\frac{7372800r}{m'^0} - \frac{1152h^4 r}{m^6} - \frac{32h^6 r}{m^4} + \frac{h^{10}r}{2} + \frac{921600r^3}{m^8} - \frac{144h^4 r^3}{m^4} - \right.$$
$$\left.\frac{4h^6 r^3}{m^2} + \frac{38400r^5}{m^6} - \frac{6h^4 r^5}{m^2} - \frac{h^6 r^5}{6} + \frac{800r^7}{m^4} - \frac{h^4 r^7}{8} + \frac{10r^9}{m^2} + \frac{r^{11}}{12}\right) - \frac{B_r N_t}{N_b}\left(\frac{r}{2m^2} - \frac{rh^2}{8} + \frac{r^3}{16}\right) + $$
$$B_r N_t\left(\frac{1}{2m^4} - \frac{rh^3}{36} + \frac{r^2}{6m^2} + \frac{r^4}{90}\right) + \frac{B_r(N_b^2 + N_t^2)}{36864}\left(\frac{N_t}{N_b}\right)\left(\frac{1152^r}{m^6} - \frac{h^6 r}{2} + \frac{144r^3}{m^4} + \frac{6r^5}{m^2} + \frac{r^7}{8}\right) - \frac{wr}{2(2-N)}\left(\frac{\mu}{k} + M\right)\right] \qquad (28)$$

where, $I_1(mr)$ and $K_1(mr)$ the 1st and 2nd order modified Bessel functions, respectively.
Substitute equation (28) into equation (27), and by applying the boundary conditions (15-17), the velocity is

$$w[z,r] = \frac{1}{\left[1 - \left(\frac{\mu}{k} + M\right)\frac{r^2}{2(2-N)}\right]}\left[-NC_2(z)\frac{I_0(mr)}{m} + \frac{(1-N)}{(2-N)}\frac{r^2}{2}\left(\frac{dP}{dz} - \frac{sin[\emptyset]}{F}\right) - \frac{(1-N)}{(2-N)}\left(G_r(N_b - N_t)\left(\frac{Nr^2}{64m^2} + \frac{r^4}{512} - \right.\right.\right.$$
$$\frac{r^2 h^2}{128}\right) - G_r N_b\left(\frac{Nr}{2m^4} + \frac{Nr^3}{18m^2} + \frac{r^5}{225} - \frac{r^2 h^2}{36}\right) - \frac{G_r N_t(N_b^2 + N_t^2)}{36864}\left(\frac{7372800Nr^2}{2m^{10}} + \frac{230400Nr^4}{m^8} - \frac{576Nr^2 h^2}{m^6} + \frac{6400Nr^6}{m^6} - \right.$$
$$\frac{16h^6 Nr^2}{m^4} - \frac{36h^4 r^4}{m^4} + \frac{100Nr^8}{m^4} - \frac{Nh^6 r^4}{m^2} + \frac{Nr^{10}}{m^2} - \frac{Nh^4 r^6}{m^2} + \frac{r^{12}}{72} - \frac{r^6 h^6}{18} - \frac{r^8 h^4}{32} + \frac{r^2 h^{10}}{2}\right) - \frac{B_r N_t}{N_b}\left(\frac{Nr^2}{4m^2} + \frac{r^4}{32} - \right.$$
$$\frac{r^2 h^2}{8}\right) + B_r N_t\left(\frac{Nr}{2m^4} + \frac{Nr^3}{18m^2} + \frac{r^5}{225} - \frac{r^2 h^3}{36}\right) + \frac{B_r(N_t^2 + N_b^2)}{36864}\frac{Nt}{Nb}\left(\frac{576Nr^2}{m^6} + \frac{36Nr^4}{m^4} + \frac{Nr^6}{m^2} - \frac{r^8}{32} - \frac{h^6 r^2}{2}\right)\right) + C_4\right] \qquad (29)$$

where,

$$C_4 = NC_2\frac{I_0(mh)}{m} - \frac{(1-N)}{(2-N)}\frac{h^2}{q}\left(\frac{dP}{dz} - \frac{sin[\emptyset]}{F}\right) + \frac{(1-N)}{(2-N)}\left(G_r(N_b - N_t)\left(\frac{Nh^2}{64m^2} - \frac{3h^4}{512}\right) - G_r N_b\left(\frac{Nh}{2m^4} + \frac{Nh^3}{18m^2} - \frac{7h^5}{300}\right) - \right.$$
$$\frac{G_r N_t(N_b^2 + N_t^2)}{36864}\left(\frac{3686400Nh^2}{m^{10}} + \frac{230400Nh^4}{m^{10}} + \frac{5824Nh^6}{m^6} + \frac{48Nh^8}{m^4} - \frac{Nh'^0}{m^2} + \frac{41h^{12}}{96}\right) - \frac{B_r N_t}{Nb}\left(\frac{Nh^2}{4m^2} - \frac{3h^4}{8}\right) + $$
$$\left.B_r N_t\left(\frac{Nh}{2m^4} + \frac{Nh^3}{18m^2} - \frac{7h^5}{300}\right) + \frac{B_r(N_t^2 + N_b^2)}{36864}\frac{Nt}{Nb}\left(\frac{576Nh^2}{m^6} + \frac{36Nh^4}{m^4} + \frac{Nh^6}{m^2} - \frac{15h^8}{32}\right)\right)$$

$$C_2 = \frac{1}{I_1(mh)}\left[\frac{(1-N)}{(2-N)}\left(\frac{dP}{dz} - \frac{sin[\emptyset]}{F}\right)\frac{h}{2} - \frac{(1-N)}{(2-N)}\left(G_r(N_b - N_t)\left(\frac{h}{2m^2} - \frac{h^3}{256}\right) - G_r N_b\left(\frac{1}{2m^4} + \frac{h^2}{6m^2} - \frac{h^4}{60}\right) - \right.\right.$$
$$\frac{G_r N_b(N_b^2 + N_t^2)}{36864}\left(\frac{7372800h}{m^{10}} + \frac{921600h^3}{m^8} + \frac{37248h^5}{m^6} + \frac{624h^7}{m^4} + \frac{7h^{11}}{24}\right) - \frac{B_r N_t}{N_b}\left(\frac{h}{2m^2} - \frac{h^3}{16}\right) + B_r N_t\left(\frac{1}{2m^4} + \frac{h^2}{6m^2} - \frac{h^4}{60}\right) + $$
$$\left.\left.\frac{B_r(N_b^2 + N_t^v)}{36864}\frac{Nt}{Nb}\left(\frac{1152h}{m^6} + \frac{144h^3}{m^4} + \frac{6h^5}{m^2} - \frac{3h^7}{8}\right)\right)\right]$$

Dimension less flux (Q) can be determined as follows:

$$Q = \int_0^h 2rw \, dr \tag{30}$$

$$Q = \left[\left(\frac{Nh^2}{m} \frac{I_0(mh)}{I_1(mh)} - \frac{2Nh}{m} \right) + \frac{\left(\frac{\mu}{k}+M\right)}{(2-N)} \left(\frac{N}{m} \frac{I_0(mh)}{I_1(mh)} \frac{h^4}{4} - \frac{Nh^3}{m} + \frac{2Nh^2}{m} \frac{I_2(mh)}{I_1(mh)} \right) \right) \left(\frac{(1-N)}{(2-N)} \left(\frac{dP}{dz} - \frac{\sin[\emptyset]}{F} \right) \frac{h}{2} - \right.$$

$$\frac{(1-N)}{(2-N)} \left(G_r(N_b - N_t) \left(\frac{h}{32m^2} - \frac{h^3}{256} \right) - G_r N_b \left(\frac{1}{2m^4} + \frac{h^2}{6m^2} - \frac{h^4}{60} \right) - \frac{G_r N_t (N_b^2 + N_t^2)}{36864} \left(\frac{7372800h}{m^{10}} + \frac{37248h^5}{m^6} + \frac{6244^7}{m^4} + \right.$$

$$\frac{7h^{11}}{24} + \frac{921600h^3}{m^8} \right) - \frac{B_r N_t}{N_b} \left(\frac{h}{2m^2} - \frac{h^3}{16} \right) + B_r N_t \left(\frac{1}{2m^4} + \frac{h^2}{6m^2} - \frac{h^4}{60} \right) + \frac{B_r(N_b^2 + N_t^2)}{36864} \left(\frac{N_t}{N_b} \right) \left(\frac{1152h}{m^6} + \frac{144h^3}{m^4} + \frac{6h^5}{m^2} - \right.$$

$$\left. \left. \frac{3h^7}{8} \right) \right) \right] + \frac{(1-N)}{(2-N)} \left(\frac{-h^4}{4} - \frac{h^6}{24} \frac{\left(\frac{\mu}{k}+M\right)}{(2-N)} \right) \left(\frac{dP}{dz} - \frac{\sin\alpha}{F} \right) - \frac{(1-N)}{(2-N)} \left[G_r(N_b - N_t) \left(\left(\frac{-Nh^4}{128m^2} + \frac{379h^6}{1536} \right) + \right. \right.$$

$$\left(\frac{-Nh^6}{768m^2} + \frac{755h^6}{12288} \right) \frac{\left(\frac{\mu}{k}+M\right)}{(2-N)} \right) - G_r N_b \left(\left(-\frac{Nh^3}{6m^4} - \frac{Nh^5}{30m^2} + \frac{3h^7}{280} \right) + \left(\frac{-Nh^5}{40m^4} - \frac{Nh^7}{168m^2} + \frac{11h^9}{6480} \right) \frac{\left(\frac{\mu}{k}+M\right)}{(2-N)} \right) -$$

$$\frac{G_r N_t(N_t^2 + N_b^2)}{36864} \left(\left(\frac{-1843200Nh^4}{m^{10}} - \frac{153600Nh^6}{m^8} - \frac{2255Nh^8}{m^6} - \frac{24Nh^{10}}{m^4} + \frac{7Nh^{12}}{24m^2} - \frac{73h^{14}}{210} \right) + \left(\frac{-307200Nh^6}{m^{10}} - \frac{28800Nh^8}{m^8} - \right.$$

$$\left. \frac{912Nh^6}{m^6} - \frac{65Nh^{12}}{6m^4} + \frac{27Nh^{14}}{280m^2} - \frac{59h^{16}}{1920} \right) \frac{\left(\frac{\mu}{k}+m\right)}{(2-N)} \right) - \frac{B_r Nt}{N_b} \left(\left(\frac{-Nh^4}{8m^2} + \frac{31h^4}{192} \right) + \left(\frac{-Nh^6}{48m^2} + \frac{59h^8}{768} \right) \frac{\left(\frac{\mu}{k}+M\right)}{(2-N)} \right) +$$

$$B_r N_t \left(\left(-\frac{Nh^3}{6m^4} - \frac{Nh^5}{30m^2} + \frac{3h^7}{280} \right) + \left(\frac{-Nh^5}{40m^4} - \frac{Nh^7}{168m^2} + \frac{11h^9}{6480} \right) \frac{\left(\frac{\mu}{k}+M\right)}{(2-N)} \right) + \frac{B_r(N_t^2 + N_b^2)}{36864} \left(\frac{N_t}{N_b} \right) \left(\left(\frac{-288Nh^4}{m^6} - \frac{24Nh^6}{m^4} - \right. \right.$$

$$\left. \left. \left. \frac{3Nh^8}{4m^2} + \frac{19h^{10}}{80} \right) + \left(\frac{-48Nh^6}{m^6} - \frac{9Nh^8}{2m^4} - \frac{3Nh^{10}}{20m^2} + \frac{h^{12}}{32} \right) \frac{\left(\frac{\mu}{k}+M\right)}{(2-N)} \right) \right] \tag{31}$$

From equation (31), $\frac{dP}{dz}$ is

$$\frac{dP}{dz} = \frac{\sin[\emptyset]}{F} + \left[\frac{1}{\left(\left(\frac{Nh^3 I_0(mh)}{2m \, I_1(mh)} - \frac{Nh^2}{m} - \frac{h^4}{4} \right) + \left(\frac{N}{m} * \frac{I_0(mh)h^5}{I_1(mh)} \frac{h^5}{8} - \frac{Nh^4}{2m} - \frac{Nh^3}{m} * \frac{I_2(mh)}{I_1(mh)} - \frac{h^6}{24} \right) \frac{\left(\frac{\mu}{k}+M\right)}{(2-N)} \right) \right] \left(\frac{Q(2-N)}{(1-N)} + \right.$$

$$\left(\left(\frac{Nh^2}{2m} * \frac{I_0(mh)}{I_1(mh)} - \frac{2Nh}{m} \right) + \left(\frac{N}{m} * \frac{I_0(mh)}{I_1(mh)} \frac{h^4}{4} - \frac{Nh^3}{m} - \frac{2Nh^2}{m} \frac{I_2(mh)}{I_1(mh)} \right) \left(\frac{\left(\frac{\mu}{k}+M\right)}{(2-N)} \right) \right) \left(G_r(N_b - N_t) \left(\frac{h}{32m^2} - \frac{h^3}{256} \right) - \right.$$

$$G_r N_b \left(\frac{1}{2m^4} + \frac{h^2}{6m^2} - \frac{h^4}{60} \right) - \frac{G_r N_t(N_b^2 + N_t^2)}{36864} \left(\frac{7372800h}{m^{10}} + \frac{37248h^5}{m^6} + \frac{6244^7}{m^4} + \frac{7h^{11}}{24} + \frac{921600h^3}{m^8} \right) -$$

$$\frac{B_r N_t}{N_b} \left(\frac{h}{2m^2} - \frac{h^3}{16} \right) + B_r N_t \left(\frac{1}{2m^4} + \frac{h^2}{6m^2} - \frac{h^4}{60} \right) + \frac{B_r(N_b^2 + N_t^2)}{36864} \left(\frac{N_t}{N_b} \right) \left(\frac{1152h}{m^6} + \frac{144h^3}{m^4} + \frac{6h^5}{m^2} - \frac{3h^7}{8} \right) \right) +$$

$$\left(G_r(N_b - N_t) \left(\left(\frac{-Nh^4}{128m^2} + \frac{379h^6}{1536} \right) + \left(\frac{-Nh^6}{768m^2} + \frac{755h^6}{12288} \right) \frac{\left(\frac{\mu}{k}+M\right)}{(2-N)} \right) - G_r N_b \left(\left(-\frac{Nh^3}{6m^4} - \frac{Nh^5}{30m^2} + \frac{3h^7}{280} \right) + \right.$$

$$\left(\frac{-Nh^5}{40m^4} - \frac{Nh^7}{168m^2} + \frac{11h^9}{6480} \right) \frac{\left(\frac{\mu}{k}+M\right)}{(2-N)} \right) - \frac{G_r N_t(N_t^2 + N_b^2)}{36864} \left(\left(\frac{-1843200Nh^4}{m^{10}} - \frac{153600Nh^6}{m^8} - \frac{2255Nh^8}{m^6} - \frac{24Nh^{10}}{m^4} + \frac{7Nh^{12}}{24m^2} - \right. \right.$$

$$\left. \frac{73h^{14}}{210} \right) + \left(\frac{-307200Nh^6}{m^{10}} - \frac{28800Nh^8}{m^8} - \frac{912Nh^6}{m^6} - \frac{65Nh^{12}}{6m^4} + \frac{27Nh^{14}}{280m^2} - \frac{59h^{16}}{1920} \right) \frac{\left(\frac{\mu}{k}+m\right)}{(2-N)} \right) - \frac{B_r Nt}{N_b} \left(\left(\frac{-Nh^4}{8m^2} + \frac{31h^4}{192} \right) + \right.$$

$$\left. \left(\frac{-Nh^6}{48m^2} + \frac{59h^8}{768} \right) \frac{\left(\frac{\mu}{k}+M\right)}{(2-N)} \right) + B_r N_t \left(\left(-\frac{Nh^3}{6m^4} - \frac{Nh^5}{30m^2} + \frac{3h^7}{280} \right) + \left(\frac{-Nh^5}{40m^4} - \frac{Nh^7}{168m^2} + \frac{11h^9}{6480} \right) \frac{\left(\frac{\mu}{k}+M\right)}{(2-N)} \right) +$$

$$\left. \left. \frac{B_r(N_t^2 + N_b^2)}{36864} \left(\frac{N_t}{N_b} \right) \left(\left(\frac{-288Nh^4}{m^6} - \frac{24Nh^6}{m^4} - \frac{3Nh^8}{4m^2} + \frac{19h^{10}}{80} \right) + \left(\frac{-48Nh^6}{m^6} - \frac{9Nh^8}{2m^4} - \frac{3Nh^{10}}{20m^2} + \frac{h^{12}}{32} \right) \frac{\left(\frac{\mu}{k}+M\right)}{(2-N)} \right) \right) \right) \tag{32}$$

The pressure drop per wave length $\quad \Delta p = p(0) - p(\lambda) \quad$ is

$$\Delta p = -\int_0^1 \frac{dP}{dz} \, dz$$

$$\Delta p = -\int_0^1 \left[\frac{Sin[\emptyset]}{F} + \left[\frac{1}{\left(\left(\frac{Nh^3 I_0(mh)}{2m\, I_1(mh)} - \frac{Nh^2}{m} - \frac{h^4}{4} \right) + \left(\frac{N}{m} * \frac{I_0(mh)h^5}{I_1(mh)\, 8} - \frac{Nh^4}{2m} - \frac{Nh^3}{m} * \frac{I_2(mh)}{I_1(mh)} - \frac{h^6}{24} \right) \left(\frac{\left(\frac{\mu}{\kappa} + M \right)}{(2-N)} \right) \right)} \right] \left(\frac{Q(2-N)}{(1-N)} + \right. \right.$$

$$\left(\left(\frac{Nh^2}{2m} * \frac{I_0(mh)}{I_1(mh)} - \frac{2Nh}{m} \right) + \left(\frac{N}{m} * \frac{I_0(mh)}{I_1(mh)} \frac{h^4}{4} - \frac{Nh^3}{m} - \frac{2Nh^2}{m} \frac{I_2(mh)}{I_1(mh)} \right) \left(\frac{\left(\frac{\mu}{\kappa} + M \right)}{(2-N)} \right) \right) \left(G_r(N_b - N_t) \left(\frac{h}{32m^2} - \frac{h^3}{256} \right) - \right.$$

$$G_r N_b \left(\frac{1}{2m^4} + \frac{h^2}{6m^2} - \frac{h^4}{60} \right) - \frac{G_r N_t (N_b^2 + N_t^2)}{36864} \left(\frac{7372800h}{m^{10}} + \frac{37248h^5}{m^6} + \frac{624h^7}{m^4} + \frac{7h^{11}}{24} + \frac{921600h^3}{m^8} \right) -$$

$$\frac{B_r N_t}{N_b} \left(\frac{h}{2m^2} - \frac{h^3}{16} \right) + B_r N_t \left(\frac{1}{2m^4} + \frac{h^2}{6m^2} - \frac{h^4}{60} \right) + \frac{B_r (N_b^2 + N_t^2)}{36864} \left(\frac{N_t}{N_b} \right) \left(\frac{1152h}{m^6} + \frac{144h^3}{m^4} + \frac{6h^5}{m^2} - \frac{3h^7}{8} \right) \right) +$$

$$\left(G_r(N_b - N_t) \left(\left(\frac{-Nh^4}{128m^2} + \frac{379h^6}{1536} \right) + \left(\frac{-Nh^6}{768m^2} + \frac{755h^6}{12288} \right) \frac{\left(\frac{\mu}{k} + M \right)}{(2-N)} \right) - G_r N_b \left(\left(-\frac{Nh^3}{6m^4} - \frac{Nh^5}{30m^2} + \frac{3h^7}{280} \right) + \right. \right.$$

$$\left(\frac{-Nh^5}{40m^4} - \frac{Nh^7}{168m^2} + \frac{11h^9}{6480} \right) \frac{\left(\frac{\mu}{k} + M \right)}{(2-N)} \right) - \frac{G_r N_t (N_t^2 + N_b^2)}{36864} \left(\left(\frac{-1843200Nh^4}{m^{10}} - \frac{153600Nh^6}{m^8} - \frac{2255Nh^8}{m^6} - \frac{24Nh^{10}}{m^4} + \frac{7Nh^{12}}{24m^2} - \right.$$

$$\left. \frac{73h^{14}}{210} \right) + \left(\frac{-307200Nh^6}{m^{10}} - \frac{28800Nh^8}{m^8} - \frac{912Nh^6}{m^6} - \frac{65Nh^{12}}{6m^4} + \frac{27Nh^{14}}{280m^2} - \frac{59h^{16}}{1920} \right) \frac{\left(\frac{\mu}{k} + m \right)}{(2-N)} \right) - \frac{B_r Nt}{N_b} \left(\left(\frac{-Nh^4}{8m^2} + \frac{31h^4}{192} \right) + \right.$$

$$\left(\frac{-Nh^6}{48m^2} + \frac{59h^8}{768} \right) \frac{\left(\frac{\mu}{k} + M \right)}{(2-N)} \right) + B_r N_t \left(\left(-\frac{Nh^3}{6m^4} - \frac{Nh^5}{30m^2} + \frac{3h^7}{280} \right) + \left(\frac{-Nh^5}{40m^4} - \frac{Nh^7}{168m^2} + \frac{11h^9}{6480} \right) \frac{\left(\frac{\mu}{k} + M \right)}{(2-N)} \right) +$$

$$\left. \left. \left. \frac{B_r (N_t^2 + N_b^2)}{36864} \left(\frac{N_t}{N_b} \right) \left(\left(\frac{-288Nh^4}{m^6} - \frac{24Nh^6}{m^4} - \frac{3Nh^8}{4m^2} + \frac{19h^{10}}{80} \right) + \left(\frac{-48Nh^6}{m^6} - \frac{9Nh^8}{2m^4} - \frac{3Nh^{10}}{20m^2} + \frac{h^{12}}{32} \right) \frac{\left(\frac{\mu}{k} + M \right)}{(2-N)} \right) \right) \right) \right] dz \quad (33)$$

Also, flow resistance λ is defined as

$$\lambda = \frac{\Delta p}{Q}$$

$$\lambda = \frac{-1}{Q} \int_0^1 \left[\frac{Sin[\emptyset]}{F} + \left[\frac{1}{\left(\left(\frac{Nh^3 I_0(mh)}{2m\, I_1(mh)} - \frac{Nh^2}{m} - \frac{h^4}{4} \right) + \left(\frac{N}{m} * \frac{I_0(mh)h^5}{I_1(mh)\, 8} - \frac{Nh^4}{2m} - \frac{Nh^3}{m} * \frac{I_2(mh)}{I_1(mh)} - \frac{h^6}{24} \right) \left(\frac{\left(\frac{\mu}{k} + M \right)}{(2-N)} \right) \right)} \right] \left(\frac{Q(2-N)}{(1-N)} + \right. \right.$$

$$\left(\left(\frac{Nh^2}{2m} * \frac{I_0(mh)}{I_1(mh)} - \frac{2Nh}{m} \right) + \left(\frac{N}{m} * \frac{I_0(mh)}{I_1(mh)} \frac{h^4}{4} - \frac{Nh^3}{m} - \frac{2Nh^2}{m} \frac{I_2(mh)}{I_1(mh)} \right) \left(\frac{\left(\frac{\mu}{k} + M \right)}{(2-N)} \right) \right) \left(G_r(N_b - N_t) \left(\frac{h}{32m^2} - \frac{h^3}{256} \right) - \right.$$

$$G_r N_b \left(\frac{1}{2m^4} + \frac{h^2}{6m^2} - \frac{h^4}{60} \right) - \frac{G_r N_t (N_b^2 + N_t^2)}{36864} \left(\frac{7372800h}{m^{10}} + \frac{37248h^5}{m^6} + \frac{624h^7}{m^4} + \frac{7h^{11}}{24} + \frac{921600h^3}{m^8} \right) -$$

$$\frac{B_r N_t}{N_b} \left(\frac{h}{2m^2} - \frac{h^3}{16} \right) + B_r N_t \left(\frac{1}{2m^4} + \frac{h^2}{6m^2} - \frac{h^4}{60} \right) + \frac{B_r (N_b^2 + N_t^2)}{36864} \left(\frac{N_t}{N_b} \right) \left(\frac{1152h}{m^6} + \frac{144h^3}{m^4} + \frac{6h^5}{m^2} - \frac{3h^7}{8} \right) \right) +$$

$$\left(G_r(N_b - N_t) \left(\left(\frac{-Nh^4}{128m^2} + \frac{379h^6}{1536} \right) + \left(\frac{-Nh^6}{768m^2} + \frac{755h^6}{12288} \right) \frac{\left(\frac{\mu}{k} + M \right)}{(2-N)} \right) - G_r N_b \left(\left(-\frac{Nh^3}{6m^4} - \frac{Nh^5}{30m^2} + \frac{3h^7}{280} \right) + \right. \right.$$

$$\left(\frac{-Nh^5}{40m^4} - \frac{Nh^7}{168m^2} + \frac{11h^9}{6480} \right) \frac{\left(\frac{\mu}{k} + M \right)}{(2-N)} \right) - \frac{G_r N_t (N_t^2 + N_b^2)}{36864} \left(\left(\frac{-1843200Nh^4}{m^{10}} - \frac{153600Nh^6}{m^8} - \frac{2255Nh^8}{m^6} - \frac{24Nh^{10}}{m^4} + \frac{7Nh^{12}}{24m^2} - \right.$$

$$\left. \frac{73h^{14}}{210} \right) + \left(\frac{-307200Nh^6}{m^{10}} - \frac{28800Nh^8}{m^8} - \frac{912Nh^6}{m^6} - \frac{65Nh^{12}}{6m^4} + \frac{27Nh^{14}}{280m^2} - \frac{59h^{16}}{1920} \right) \frac{\left(\frac{\mu}{k} + m \right)}{(2-N)} \right) - \frac{B_r Nt}{N_b} \left(\left(\frac{-Nh^4}{8m^2} + \frac{31h^4}{192} \right) + \right.$$

$$\left(\frac{-Nh^6}{48m^2} + \frac{59h^8}{768} \right) \frac{\left(\frac{\mu}{k} + M \right)}{(2-N)} \right) + B_r N_t \left(\left(-\frac{Nh^3}{6m^4} - \frac{Nh^5}{30m^2} + \frac{3h^7}{280} \right) + \left(\frac{-Nh^5}{40m^4} - \frac{Nh^7}{168m^2} + \frac{11h^9}{6480} \right) \frac{\left(\frac{\mu}{k} + M \right)}{(2-N)} \right) +$$

$$\left. \left. \left. \frac{B_r (N_t^2 + N_b^2)}{36864} \left(\frac{N_t}{N_b} \right) \left(\left(\frac{-288Nh^4}{m^6} - \frac{24Nh^6}{m^4} - \frac{3Nh^8}{4m^2} + \frac{19h^{10}}{80} \right) + \left(\frac{-48Nh^6}{m^6} - \frac{9Nh^8}{2m^4} - \frac{3Nh^{10}}{20m^2} + \frac{h^{12}}{32} \right) \frac{\left(\frac{\mu}{k} + M \right)}{(2-N)} \right) \right) \right) \right] dz \quad (34)$$

Equation Δp is used to calculate the pressure drop when there is no stenosis h = 1, which is indicated by Δp_n.
The normal artery's flow resistance is represented by

$$\lambda_n = \frac{\Delta p_n}{q} \tag{35}$$

The Normalized flow resistance denoted by

$$\bar{\lambda} = \frac{\lambda}{\lambda_n} \tag{36}$$

Dimensionless shear stresses can be determined as follows

$$\tau_{rz} = \frac{1}{(1-N)}\frac{\partial w}{\partial r} + \frac{N}{(1-N)}V_\theta \tag{37}$$

$$\tau_{zr} = \frac{\partial w}{\partial r} - \frac{1}{(1-N)}V_\theta \tag{38}$$

$$\tau_{rz} = \frac{r}{2}\left(\frac{dp}{dz} - \frac{\sin\emptyset}{F}\right) - \left[G_r\left(\frac{1}{64}(N_b - N_t)\left(\frac{r^3}{4} - \frac{h^2 r}{2}\right) - \left(\frac{1}{18}N_b\left(\frac{r^4}{5} - \frac{h^3 r}{2}\right) + \frac{N_t(N_t^2+N_b^2)}{36864}\left(\frac{r^{11}}{12} - \frac{r^5 h^6}{6} - \frac{r^7 h^4}{8} + \right.\right.\right.$$

$$\left.\left.\left.\frac{rh^{10}}{2}\right)\right)\right) + B_r\left(\frac{-1}{4}\left(\frac{r^3}{4} - \frac{h^2 r}{2}\right)\frac{N_t}{N_b} + \frac{N_t}{N_b}\left(\frac{N_b}{18}\left(\frac{r^4}{5} - \frac{h^3 r^2}{2}\right) + \frac{(N_b^2+N_t^2)}{36864}\left(\frac{r^7}{8} - \frac{h^6 r}{2}\right)\right)\right)\right] + \left(\frac{\mu}{k} + M\right)\frac{wr}{2(1-N)} \tag{39}$$

$$\tau_{zr} = \frac{-N(2-N)r}{(1-N)}C_2(z)I_1(mr) + \frac{r}{2}\left(\frac{dP}{dz} - \frac{\sin\emptyset}{F}\right) - G_r(N_b - N_t)\left(\frac{Nr}{32m^2} - \frac{h^2 r}{128} + \frac{r^3}{256}\right) + G_r N_b\left(\frac{N}{2m^4} - \frac{rh^3}{36} + \right.$$

$$\frac{Nr^2}{6m^2} + \frac{r^4}{90}\right) + \frac{G_r N_t(N_b^2+N_t^2)}{36864}\left(\frac{7372800Nr}{m^{10}} - \frac{1152Nh^4 r}{m^6} - \frac{32Nh^6 r}{m^4} + \frac{921600r^3}{m^8} - \frac{144Nh^4 r^3}{m^4} - \frac{4Nh^6 r^3}{m^2} + \frac{38400Nr^5}{m^6} - $$

$$\frac{6Nh^4 r^5}{m^2} + \frac{800Nr^7}{m^4} + \frac{10Nr^9}{m^2} - \frac{h^4 r^7}{8} - \frac{h^6 r^5}{6} + \frac{h^{10}r}{2} + \frac{r^{11}}{12}\right) + \frac{B_r N_t}{N_b}\left(\frac{Nr}{2m^2} - \frac{rh^2}{8} + \frac{r^3}{16}\right) - B_r N_t\left(\frac{N}{2m^4} - \frac{rh^3}{36} + \frac{Nr^2}{6m^2} + \right.$$

$$\frac{r^4}{90}\right) - \frac{B_r(N_b^2+N_t^2)}{36864}\left(\frac{N_t}{N_b}\right)\left(\frac{1152Nr}{m^6} + \frac{144Nr^3}{m^4} + \frac{6Nr^5}{m^2} - \frac{h^6 r}{2} + \frac{r^7}{8}\right) + \frac{wr}{2(1-N)}\left(\frac{\mu}{k} + M\right) \tag{40}$$

where

$$C_2 = \frac{1}{I_1(mh)}\left[\frac{(1-N)}{(2-N)}\left(\frac{dP}{dz} - \frac{\sin\emptyset}{F}\right)\frac{h}{2} - \frac{(1-N)}{(2-N)}\left(G_r(N_b - N_t)\left(\frac{h}{2m^2} - \frac{h^3}{256}\right) - G_r N_b\left(\frac{1}{2m^4} + \frac{h^2}{6m^2} - \frac{h^4}{60}\right) - \right.\right.$$

$$\frac{G_r N_b(N_b^2+N_t^2)}{36864}\left(\frac{7372800h}{m^{10}} + \frac{921600h^3}{m^8} + \frac{37248h^5}{m^6} + \frac{624h^7}{m^4} + \frac{7h^{11}}{24}\right) - \frac{B_r N_t}{N_b}\left(\frac{h}{2m^2} - \frac{h^3}{16}\right) + B_r N_t\left(\frac{1}{2m^4} + \frac{h^2}{6m^2} - \frac{h^4}{60}\right) + $$

$$\frac{B_r(N_b^2+N_t^v)}{36864}\frac{N_t}{N_b}\left(\frac{1152h}{m^6} + \frac{144h^3}{m^4} + \frac{6h^5}{m^2} - \frac{3h^7}{8}\right)\right)\right]$$

4. RESULT AND ANALYSIS

The pressure drop, resistance of the flow, and wall shear stress are denoted by Equations (33), (36) and (39 & 40), respectively. The impact of various flow characteristics on flow resistance and wall shear stress have been studied by considering the parameter values as $d_1 = 0.2, d_2 = 0.2, L_1 = 0.2, L_2 = 0.2, L = 1, N = 0.1, q = 0.3, F = 0.3, B_r = 0.3, G_r = 0.2, N_b = 0.3, N_t = 0.8, \alpha = \pi/6, k = 0.05$. (Prasad, K. M., & Sudha, T. [43]).

Figures (2-10) depict the impact of various parameters on flow resistance $(\bar{\lambda})$ for various values of stenoses (δ_1) and dilatation heights (δ_2), inclination $(\emptyset)$, Thermophoresis parameter (N_t), Local Nanoparticle Grashof number (B_r), Brownian motion number (N_b), local temperature Grashof number (G_r), Viscosity (μ), Permeability of Porous medium (k) and Magnetic parameter (M).

From the Figures (2-10), it is observed that when the height of the stenosis (δ_1) increases the resistance of the flow increases and height of the dilatation (δ_2) increases the flow resistance decreases.
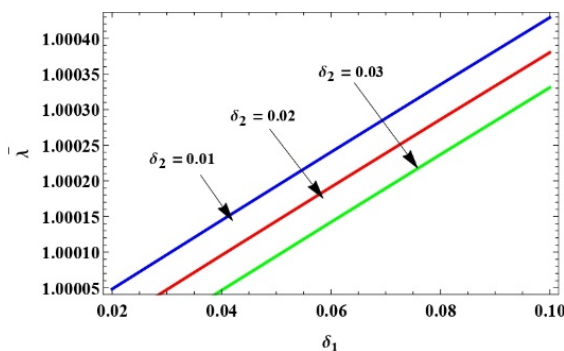
Figure. 2. Variation of $\bar{\lambda}$ with for δ_1 varying of δ_2
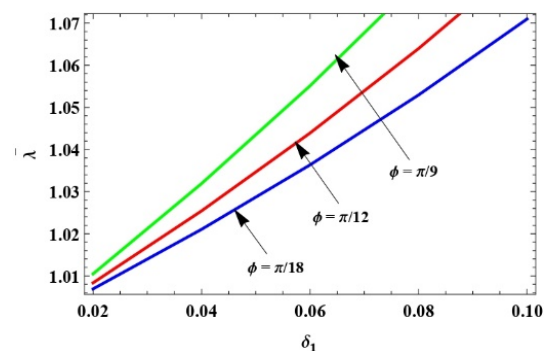
Figure 3. Variation of $\bar{\lambda}$ with for δ_1 varying of $\emptyset$

It is also observed from the Figures (2-10) that, the flow resistance $(\bar{\lambda})$ increases with Inclination $(\emptyset)$, Local Nanoparticle Grashof number (B_r), Magnetic Parameter (M) and Viscosity (μ) and the flow resistance $(\bar{\lambda})$ decreases

with thermophoresis parameter (N_t), Brownian motion parameter (N_b), Local Temperature Grashof number (G_r) and Permeability of Porous medium (k).

From the Fig. 5 and Fig. 8, it is interesting to observe that the flow resistance increases with increasing of Local Nanoparticle Grashof number (B_r) and viscosity (μ). Because of variation in temperature, buoyancy forces become more significant than viscous forces, influencing flow behaviour. Whereas buoyancy increases fluid motion, the combined impacts of viscosity and nanoparticle interactions contribute to increased flow resistance.
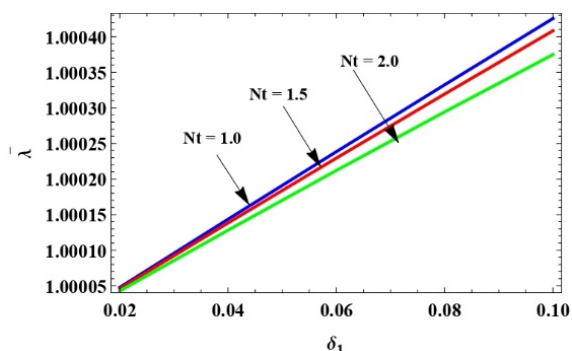
Figure.4. Variation of $\bar{\lambda}$ with for δ_1 varying of N_t
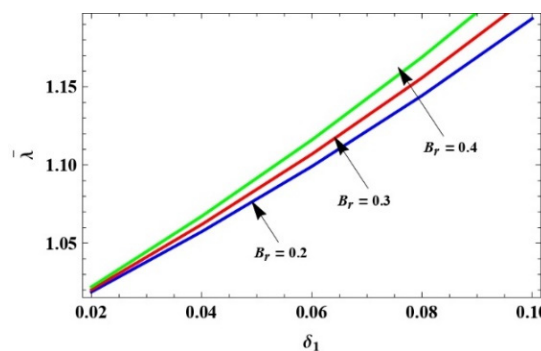
Figure. 5. Variation of $\bar{\lambda}$ with for δ_1 varying of B_r
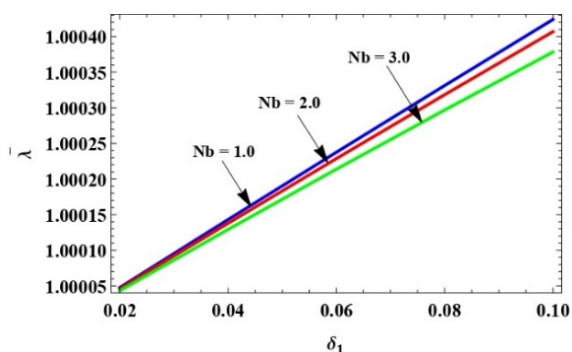
Figure. 6. Variation of $\bar{\lambda}$ with for δ_1 varying of N_b
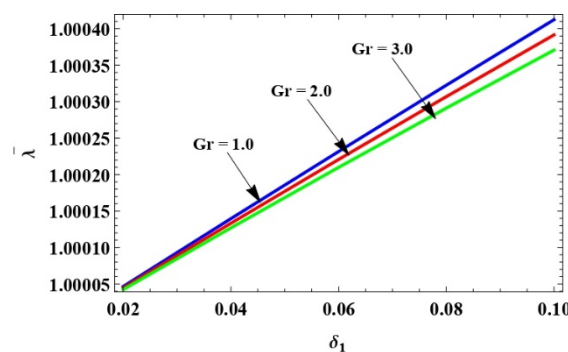
Figure. 7. Variation of $\bar{\lambda}$ with for δ_1 varying of G_r

From the Fig. 9, it is interested to notice that the impedance to the flow increases with stenosis height (δ_1) and permeability (k) this increase is significant when stenosis height(δ_1) exceeds the value 0.03. i.e in small arteries, the permeability effect is less than plaque deposition.
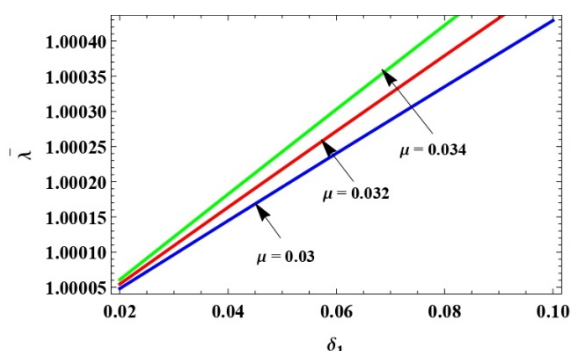
Figure. 8. Variation of $\bar{\lambda}$ with for δ_1 varying of μ
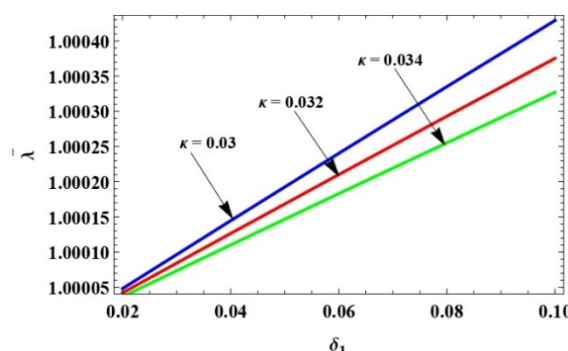
Figure. 9. Variation of $\bar{\lambda}$ with for δ_1 varying of k

From the Fig. 10, it is interesting to observe that the flow resistance increases with increase in magnetic parameter (M), However it is noticed that this increase is only significance when the stenosis height (δ) exceeds the value 0.03.

A magnetic field applied perpendicular to the flow interacts with charged nanoparticles, causing a drag force that reduces the fluid and increases flow resistance. However, by controlling the magnetic field appropriately, it becomes possible to control blood pressure and improve conditions such as poor circulation

Nanoparticles in a fluid strengthen the thermal properties by enhancing molecular collisions, however they also introduce increased flow resistance. Temperature fluctuations produce buoyancy effects, defined by the local nanoparticle Grashof number, while the permeability of porous medium affects blood flow efficiency. In systems such as vascular networks and drug delivery devices, the optimization of blood flow can be obtained through systematic adjustment of these parameters.

Figures (11-19) demonstrate the effect of velocity profiles for various values of Brownian motion number (N_b), Magnetic parameter (M), Local temperature Grashof number (G_r), micropolar parameter (m), local nanoparticle Grashof number (B_r), Permeability of porous medium (k), Thermophoresis parameter (N_t), Viscosity (μ) and Inclination ($\emptyset$).

It is noted that from the Figures (11-19) the velocity profiles increase with the increase of local nanoparticle Grashof number (B_r), Permeability of porous medium (k) and Thermophoresis parameter (N_t), but decreases with the increasing of brownian motion parameter (N_b), Local temperature Grashof number (G_r), Micropolar parameter (m), Viscosity (μ) and Inclination ($\emptyset$).
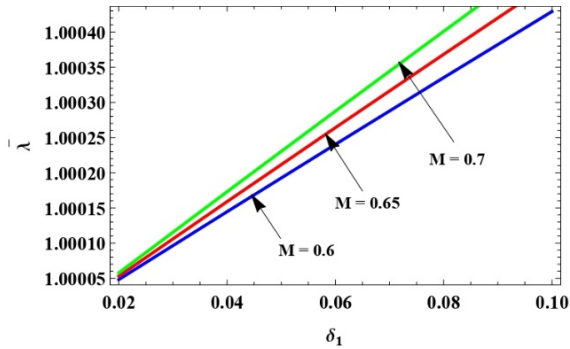
Figure 10. Variation of $\bar{\lambda}$ with for δ_1 varying of M
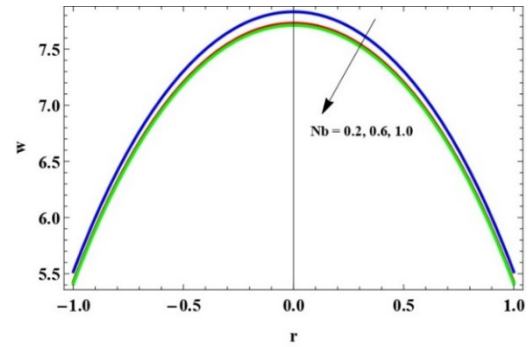
Figure 11. Variation of w with. N_b
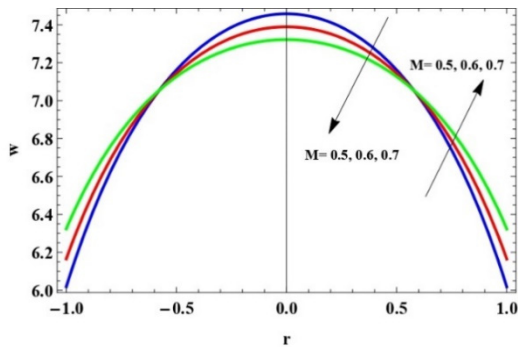
Figure 12. Variation of w with M
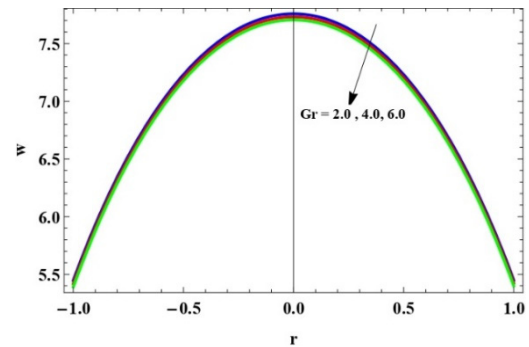
Figure 13. Variation of w with G_r
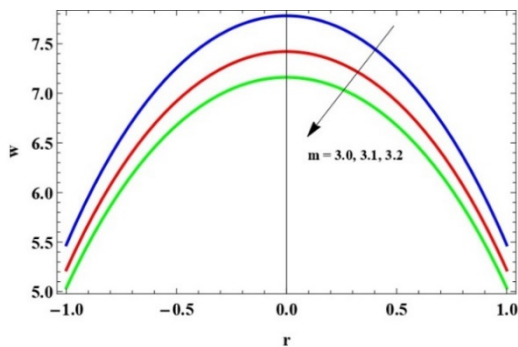
Figure 14. Variation of w with m
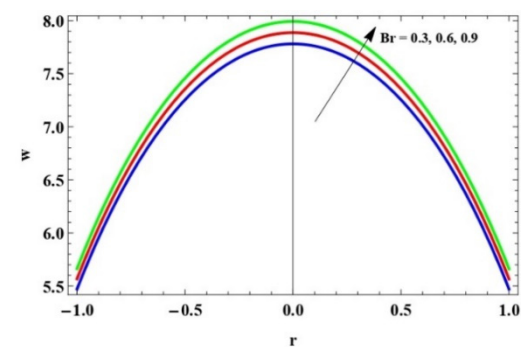
Figure 15. Variation of w with B_r
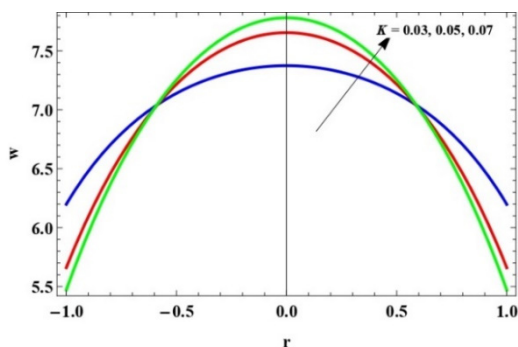
Figure 16. Variation of w with k
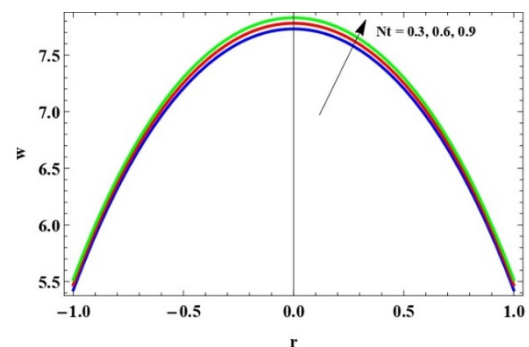
Figure 17. Variation of w with N_t
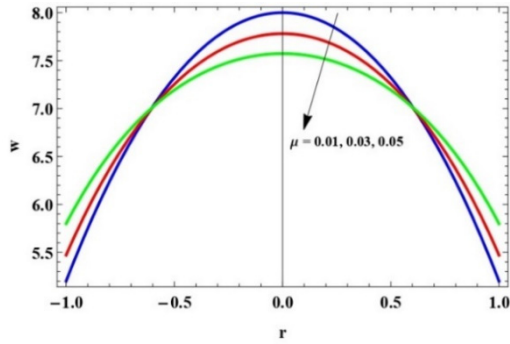
Figure 18. Variation of w with μ **Figure 19.** Variation of w with $\emptyset$
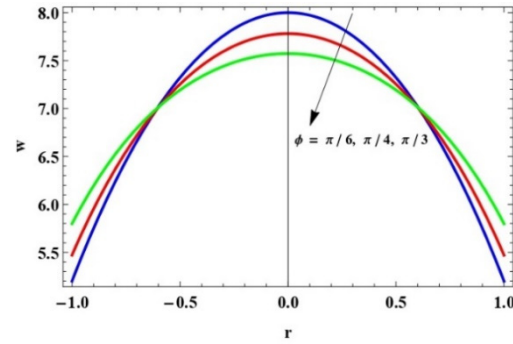
From the Fig. 12. It is interesting to identified that, the effect velocity profile decreases in the range of −0.5 to 0.5 with an increase of magnetic parameter (M) is and increasing in the other region.

Figures (20-37) demonstrate the variations of wall shear stress (τ_{rz} & τ_{zr}) versus z are shown to understand the progression of arterial disorders with various flow parameters for various values of micropolar parameter (m), Magnetic parameter (M), Brownian motion number (N_b), local temperature Grashof number (G_r), Thermophoresis parameter (N_t), Local Nanoparticle Grashof number (B_r), Viscosity (μ), Inclination $(\emptyset)$ and Permeability of Porous medium (k)

It is noticed that from the Figures (20-37) micropolar parameter (m), Magnetic parameter (M), Brownian motion parameter (N_b), local temperature Grashof number (G_r), Thermophoresis parameter (N_t), and Local Nanoparticle Grashof number (B_r) Inclination $(\emptyset)$, Permeability of Porous medium (k) decrease with the wall shear stress.

Increasing magnetic field effect, which produce a Lorentz force that decreases the flow momentum. Consequently, wall shear stress values decrease along z at every position.

The viscosity (μ), thermophoresis parameter (N_t), and magnetic parameter (M) all lead to the minimized wall shear stress, which is favourable in systems where excessive shear stress may be harmful. This is particularly relevant in delicate microfluidic devices and the human circulatory system, where maintaining optimal shear stress is required to minimize tissue injury and provide effective fluid flow.
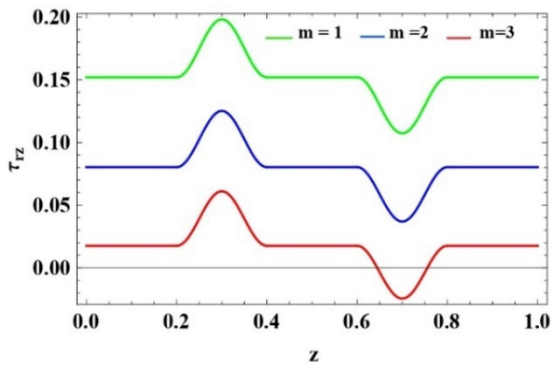
Figure 20. Variation of z on τ_{rz} with m varying   **Figure 21.** Variation of z on τ_{rz} with M varying
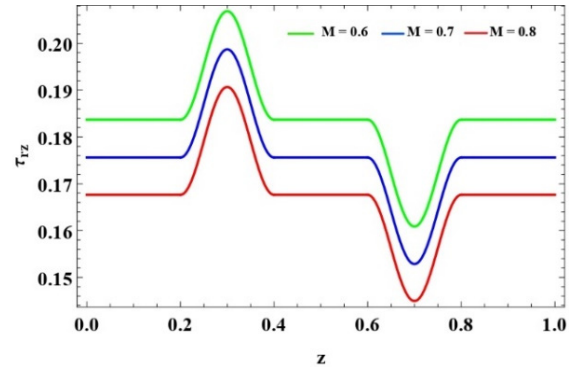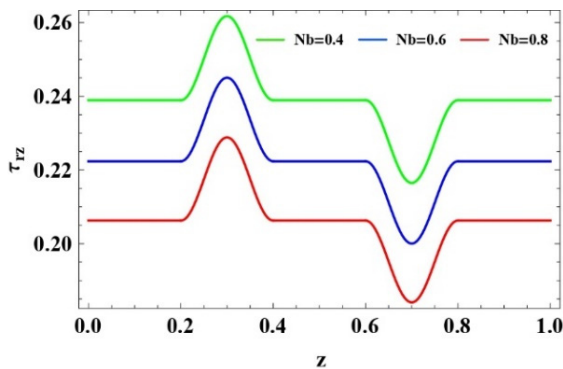
Figure 22. Variation of z on τ_{rz} with N_b varying   **Figure 23.** Variation of z on τ_{rz} with G_r varying
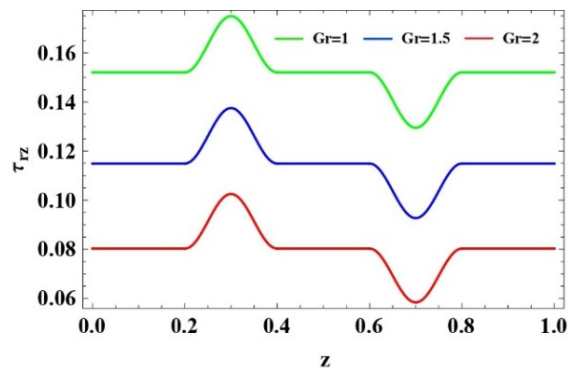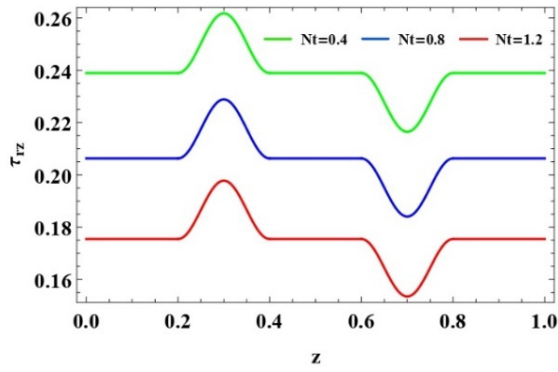
Figure 24. Variation of z on τ_{rz} with N_t varying
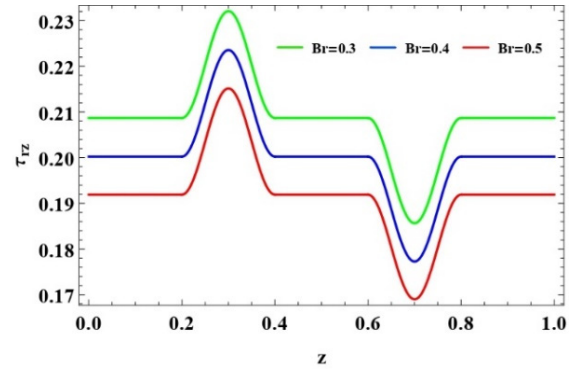
Figure 25. Variation of z on τ_{rz} with B_r varying
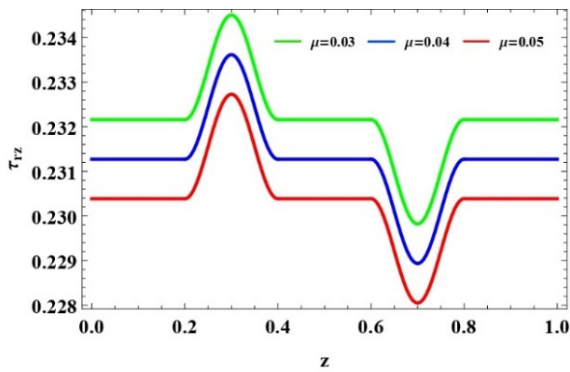
Figure 26. Variation of z on τ_{rz} with μ varying
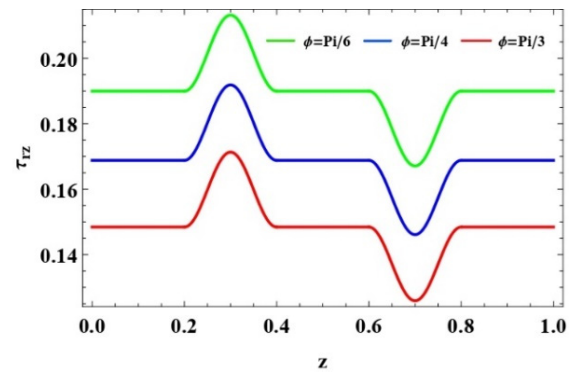
Figure 27. Variation of z on τ_{rz} with $\emptyset$ varying
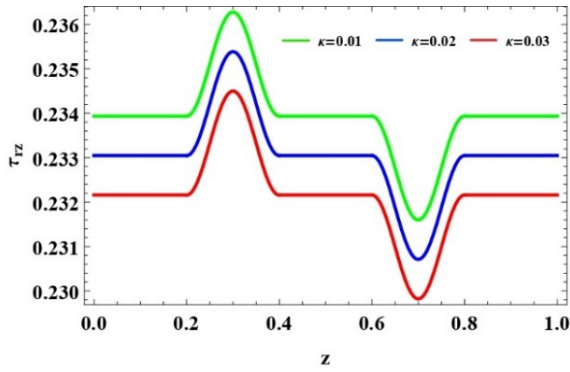
Figure 28. Variation of z on τ_{rz} with k varying
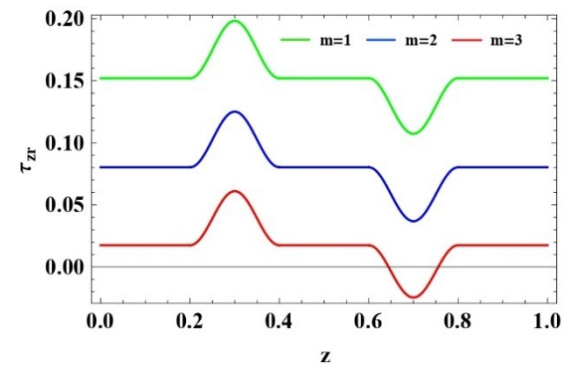
Figure 29. Variation of z on τ_{zr} with m varying
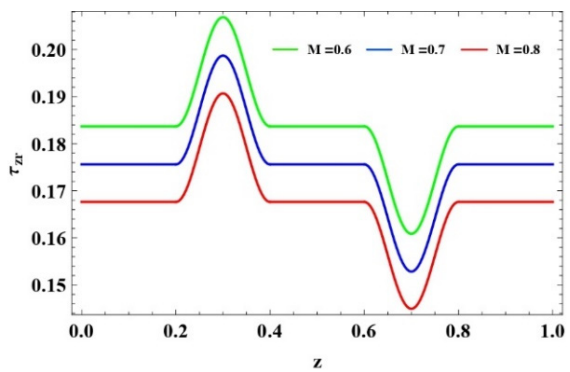
Figure 30. Variation of z on τ_{zr} with M varying
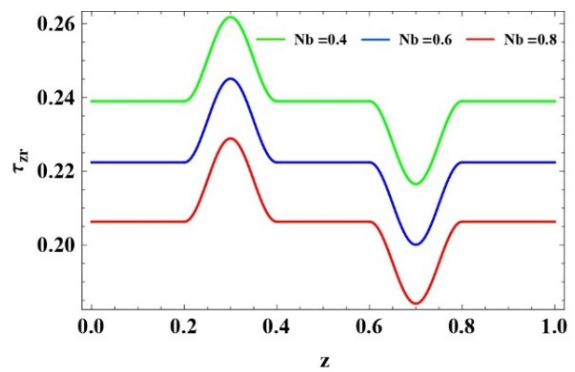
Figure 31. Variation of z on τ_{zr} with N_b varying
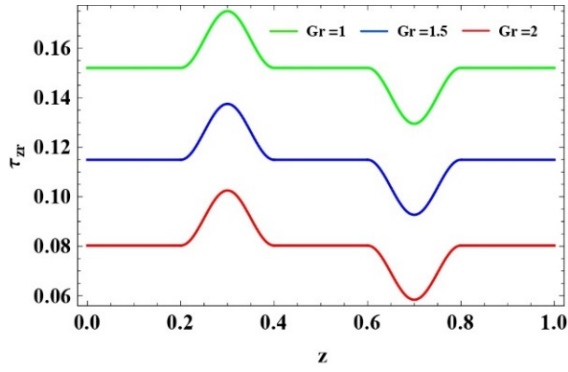
Figure 32. Variation of z on τ_{zr} with G_r varying
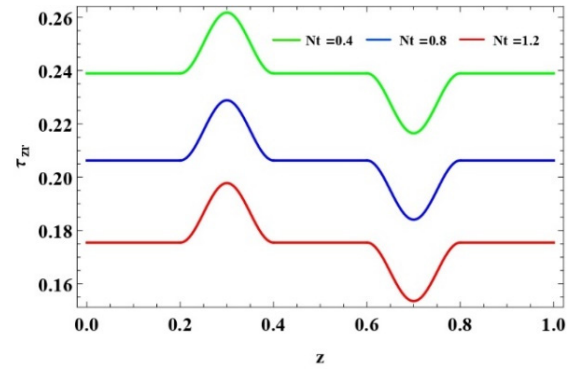
Figure 33. Variation of z on τ_{zr} with N_t varying
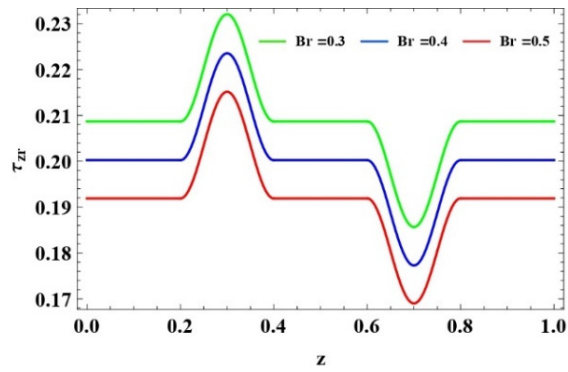
Figure 34. Variation of z on τ_{zr} with B_r varying
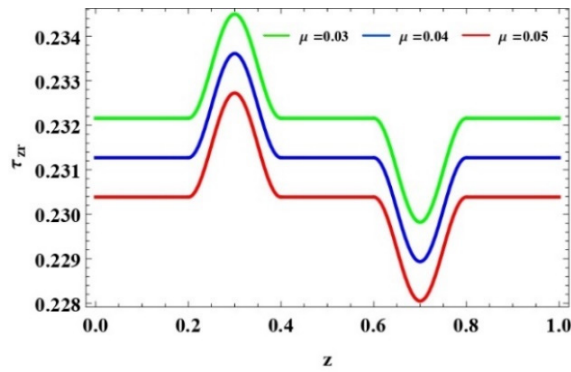
Figure 35. Variation of z on τ_{zr} with μ varying
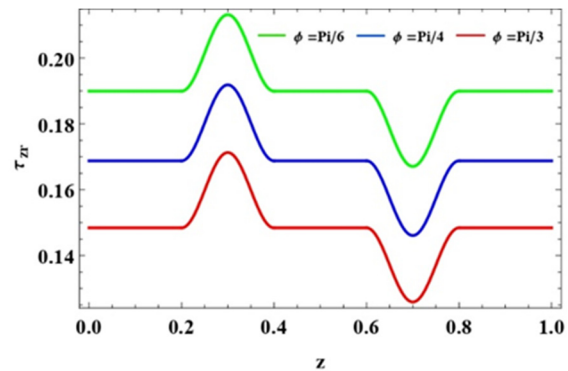
Figure 36. Variation of z on τ_{zr} with $\emptyset$ varying
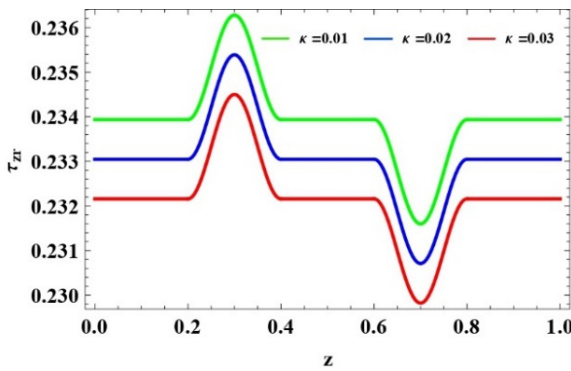
Figure 37. Variation of z on τ_{zr} with k varying

Figures (38-40) displays the streamlines for various values of k, M and B_r , It has been seen that the stream lines are getting closure with increase of k, M and B_r. It is seen that, the streamlines in the middle are becoming widen, it shows that the blood velocity is increasing and these reduces the resistance to flow decreases with the increase in values of k, M.
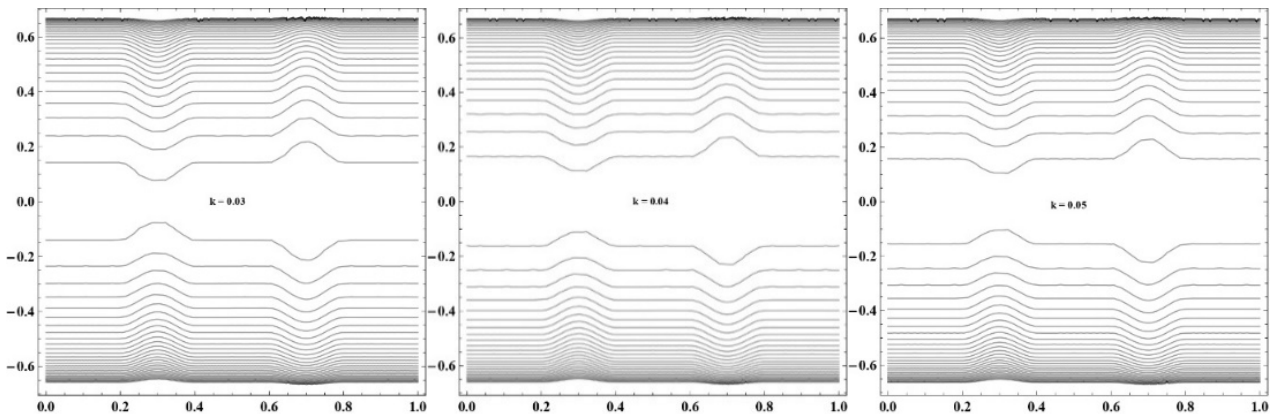
Figure 38. Streamlines for $k = 0.03, 0.04$ and 0.05
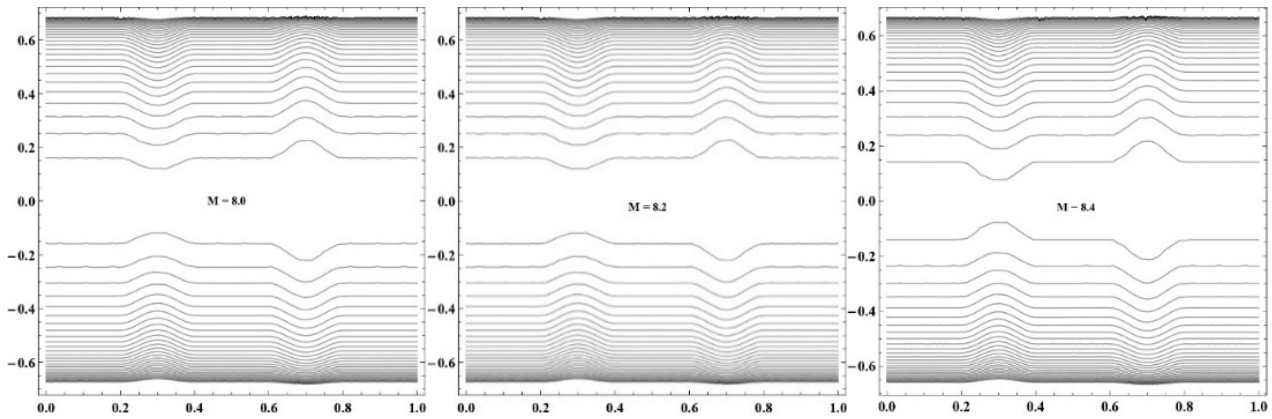
Figure 39. Streamlines for $M = 8.0, 8.2$ *and* 8.4
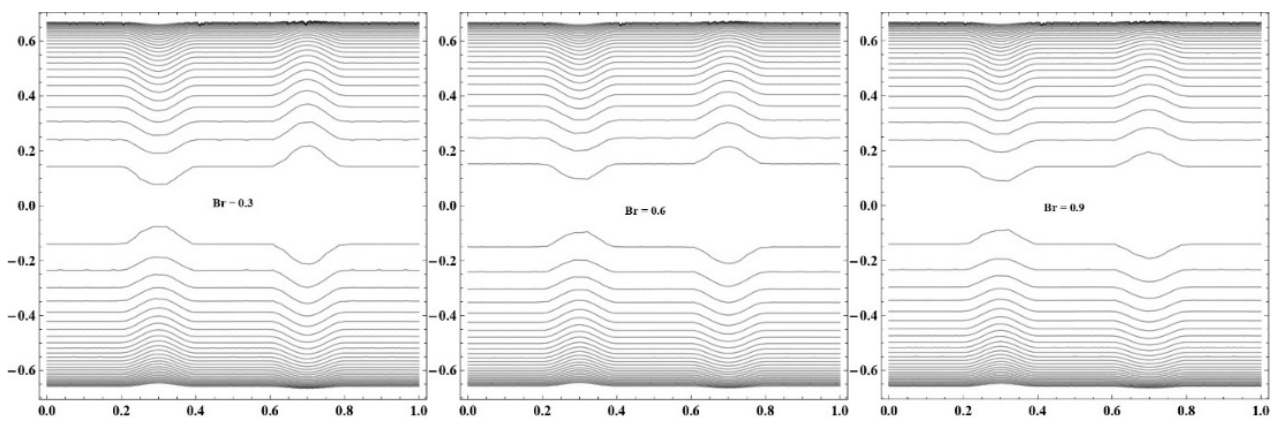
Figure 40. Streamlines for $B_r = 0.3, 0.6$ *and* 0.9

5. CONCLUSIONS

The influence of magnetic field on a micropolar fluid through an inclined porous medium with multiple abnormal segments has been studied. It was possible to evaluate the impact of various factors with different stenosis heights on the flow impedance and shear stress at the wall by finding solutions to the flow characteristic expressions.

The Observations are:

- Magnetic Parameter, Inclination, Local Nanoparticle Grashof number and Viscosity increases with flow resistance.
- The heights of stenotic dilatation, Thermophoresis parameter, Permeability of Porous medium, Local Temperature Grashof number and Brownian motion parameter decreases with the flow resistance.
- The resistance of the flow and shear stress at the wall decreasing for the values of heights of the stenosis dilatation
- It is identified that the effect of velocity profile with the increase of magnetic parameter (M) is decreasing in the region -0.5 to 0.5 and increasing in the other region.
- The heights of stenotic dilatation, Magnetic Parameter, Brownian motion number, Inclination, Local Temperature Grashof number, Thermophoresis parameter, Local Nanoparticle Grashof number and Permeability of Porous medium decreases with the shear stress at the wall.
- Study on micropolar nanofluids improves understanding of blood's microstructure and particle behaviour in magnetic fields. Incorporating micropolarity, magnetic effects, and nanoparticle dynamics (such Brownian motion and thermophoresis) improves the accuracy of blood flow models, especially for arterial stenosis or dilatation. These advanced simulations can enhance the design of medical devices such as stents and blood pumps, enable more precise targeted drug delivery systems, and support advanced diagnostic tools that simulate pathological blood flow conditions.
- The study demonstrates that blood flow resistance and wall shear stress in stenosed and dilated arteries are influenced by important factors such magnetic field strength, nanoparticle dynamics, and arterial geometry. Significantly, these results have direct applications in hematology and biomedical engineering. Controlling the external magnetic field can be used to optimize treatment techniques for cardiovascular disorders such as hypertension, atherosclerosis, and arterial blockages by regulating blood flow and shear stress.
- The streamlines lines are getting closure with the increase of Permeability of Porous medium, Magnetic parameter, Local Nanoparticle Grashof number.

ORCID
◉**Narender Satwai,** https://orcid.org/0000-0003-1466-4556; ◉**K. Maruthi Prasad,** https://orcid.org/0000-0002-9010-6452

REFERENCES

[1] D.F. Young, "Effect of a time dependent stenosis of flow through a tube," Journal of Engineering for Industry, **90**(2), 248-254 (1968). https://doi.org/10.1115/1.3604621

[2] J.B. Shukla, R.S. Parihar and B.R.P. Rao, "Effects of stenosis on non-newtonian flow of the blood in an artery," Bulletin of Mathematical Biology, **42**(3), 283–294 (1980). https://doi.org/10.1016/s0092-8240(80)80051-6

[3] J.-S. Lee and Y.-C. Fung, "Flow in Locally Constricted Tubes at Low Reynolds Numbers," Journal of Applied Mechanics, **37**(1), 9–16 (1970). https://doi.org/10.1115/1.3408496

[4] P. Chaturani and R.P. Samy, "Pulsatile flow of Casson's fluid through stenosed arteries with applications to blood flow," Biorheology, **23**(5), 499–511 (1986). https://doi.org/10.3233/bir-1986-23506

[5] G. Radhakrishnamacharya and S. Rao, "Flow of a magnetic fluid through a non-uniform wavy tube," Proceedings of the National Academy of Sciences, India. Section A. Physical Sciences, 77, (2007).

[6] D.F. Young and F.Y. Tsai, "Flow characteristics in models of arterial stenosis-I: steady flow," Journal of Biomechanics, **6**, 395-410 (1973). https://doi.org/10.1016/0021-9290(79)90004-6

[7] K.M. Prasad and P.R. Yasa, "Micropolar fluid flow in tapering stenosed arteries having permeable walls," Malaysian Journal of Mathematical Sciences, **15**(1), 147–160 (2021).

[8] D.J. Schneck and S. Ostrach, "Pulsatile blood flow in a channel of small exponential divergence-I. The linear approximation for low mean Reynolds number," J. Fluids Eng. **16**, 353–360 (1975). https://doi.org/10.1115/1.3447314

[9] K.M. Prasad and G. Radhakrishnamacharya, "Effect of multiple stenoses on Herschel–Bulkley fluid through a tube with non-uniform cross-section," International e-journal of engineering mathematics: Theory and Application, 1, 69–76 (2007).

[10] A.C. Eringen, "Theory of micropolar fluids," Journal of Mathematics and Mechanics, **16**(1), 1–18 (1966). https://www.jstor.org/stable/24901466

[11] G.R. Charya, "Flow of micropolar fluid through a constricted channel," In International Journal of Engineering Science, **15**(12), 719–725 (1977). https://doi.org/10.1016/0020-7225(77)90022-2

[12] T. Ariman, M.A. Turk, and N. Sylvester, "Application of microcontinum fluid mechanics," Int. J. Eng. Sci. **12**, 273–293 (1974). http://dx.doi.org/10.1016/0020-7225(74)90059-7

[13] K.M. Prasad, B. Sreekala and P.R. Yasa, "Analysis of micropolar fluid with nanoparticles flow through a core region in a stenosed artery having mild stenoses," Palestine Journal of Mathematics, **12**(4) (2023).

[14] D. Srinivasacharya, M. Mishra and A. Rao, "Peristaltic pumping of a micropolar fluid in a tube," Acta Mechanica, **161**, 165–178 (2003). https://doi.org/10.1007/s00707-002-0993-y

[15] K.M. Prasad and P.R. Yasa, "Flow of non-Newtonian fluid through a permeable artery having non-uniform cross section with multiple stenosis," Journal of Naval Architecture and Marine Engineering, **17**(1), 31–38 (2020). https://doi.org/10.3329/jname.v17i1.40942

[16] E. Yeom, Y.J. Kang and S.J. Lee, "Changes in velocity profile according to blood viscosity in a microchannel," Biomicrofluidics, **8**, 034110 (2014). https://doi.org/10.1063/1.4883275

[17] E. Karvelas, G. Sofiadis, T. Papathanasiou and I. Sarris, "Effect of micropolar fluid properties on the blood flow in a human carotid model," Fluids, **5**(3), 125 (2020).

[18] S.U.S. Choi and J.A. Eastman, "Enhancing thermal conductivity of fluids with nanoparticles," in: *ASME International Mechanical Engineering Congress & Exposition*, (San Francisco, United States, 1995).

[19] Noreen Sher Akbar and S. Nadeem, "Peristaltic Flow of a Micropolar Fluid with Nanoparticles in Small Intestine," Applied Nanoscience, **3**(6), 461-468 (2013). https://doi.org/10.1007/s13204-012-0160-2

[20] S. Nadeem and S. Ijaz, "Theoretical analysis of metallic nanoparticles on blood flow through stenosed artery with permeable walls," Physics Letters A, **379**(6), 542-554 (2015). https://doi.org/10.1016/j.physleta 2014.12.013

[21] A.M. Abd-Alla, E.N. Thabet and F.S. Bayones, "Numerical solution for MHD peristaltic transport in an inclined Nano fluid symmetric channel with porous medium," Sci. Rep. **12**(1), 1-11 (2022). https://doi.org/10.1038/s41598-022-07193-5

[22] J. He, N.S. Elgazery, K. Elagamy and A.N.Y. Elazem, "Efficacy of a modulated viscosity-dependent temperature/nanoparticles concentration parameter on a nonlinear radiative electromagnetic-Nano fluid flow along an elongated stretching sheet," J. Appl. Comput. Mech. **9**(3), 848-860 (2023). https://doi.org/10.22055/jacm. 2023 42294.3905

[23] K. Prasad, Y. Prabhaker and A.R. Mohammed, "Thermal effects of two immiscible fluids through a permeable stenosed artery having nanofluid in the core region," Heat Transfer, **51**(5), 4562-4583 (2022). https://doi.org/10.1002/htj.22513

[24] K.M. Prasad, N. Subadra, P.R. Shekhar and R.B. Vijaya, "Jeffrey fluid flow driven by peristaltic pumping with nanoparticles in an inclined tube," Journal of Naval Architecture & Marine Engineering, **20**(2), 165–175 (2023). https://doi.org/10.1002/htj.22513N

[25] A.S. Dawood, F.A. Kroush, R.M. Abumandour, and I.M. Eldesoky, "Multi-effect analysis of nanofluid flow in stenosed arteries with variable pressure gradient: analytical study," SN Applied Sciences, **5**(12), 382 (2023). https://doi.org/10.1007/s42452-023-05567-6

[26] Md.A. Ikbal, S. Chakravarty, K.K.L. Wong, J. Mazumdar and P.K. Mandal, "Unsteady response of non-Newtonian blood flow through a stenosed artery in magnetic field," In Journal of Computational and Applied Mathematics, **230**(1), 243–259 (2009). https://doi.org/10.1016/j.cam.2008.11.010

[27] R. Bali and U. Awasthi, "Effect of a magnetic field on the resistance to blood flow through stenotic artery," Applied Mathematics and Computation, **188**(2), 1635–1641 (2007). https://doi.org/10.1016/j.amc.2006.11.019

[28] J.C. Misra, A. Sinha and G.C. Shit, "Mathematical modelling of blood flow in a porous vessel having double stenoses in the presence of an external magnetic field," International Journal of Biomathematics, **04**(02), 207–225 (2011). https://doi.org/10.1142/s1793524511001428

[29] J.-H. He, "A coupling method of a Homotopy technique and a perturbation technique for non-linear problems," In International Journal of Non-Linear Mechanics, **35**(1), 37–43 (2000). https://doi.org/10.1016/s0020-7462(98)00085-7

[30] J.-H. He, "Application of homotopy perturbation method to nonlinear wave equations," Chaos, Solitons & Fractals, **26**(3), 695–700 (2005). https://doi.org/10.1016/j.chaos.2005.03.006

[31] I.J.D. Craig and P.G. Watson, "Magnetic reconnection solutions based on a generalized Ohm's law," Solar Phys. **214**, 131–150 (2003). https://doi.org/10.1023/A:1024075416016

[32] V.K. Sud, G.S. Sephon and R.K. Mishra, "Pumping action on blood flow by a magnetic field," Bull. Math. Biol. **39**, 385 (1977). https://doi.org/10.1007/BF02462917

[33] H.L. Agrawal and B. Anwaruddin, "Peristaltic flow of blood in a branch," Ranchi Univ. Math. J. **15**, 111–121 (1984).

[34] T. Sochi, "Non-Newtonian flow in porous media," Polymer, **51**(22), 5007–5023 (2010). https://doi.org/10.1016/j.polymer.2010.07.047

[35] K.M. Prasad and P.R. Yasa, "Mathematical Modelling on an Electrically Conducting Fluid Flow in an Inclined Permeable Tube with Multiple Stenoses," International Journal of Innovative Technology and Exploring Engineering, **9**(1), 3915–3921 (2019). https://doi.org/10.35940/ijitee.a4989.119119

[36] W.F.W. Azmi, A.Q. Mohamad, L.Y. Jiann and S. Shafie, "Mathematical fractional analysis on blood Casson fluid in slip and small arteries with the cholesterol porosity effect," Malaysian Journal of Mathematical Sciences, **18**(4), 755–774 (2024). https://doi.org/10.47836/mjms. 18.4.05

[37] K.M. Prasad, and P.R. Yasa, "Flow of non-Newtonian fluid through a permeable artery having non-uniform cross section with multiple stenosis," Journal of Naval Architecture and Marine Engineering, **17**(1), 31–38 (2020). https://doi.org/10.3329/jname.v17i1.40942

[38] T. Sudha, C. Umadevi, M. Dhange, S. Manna, and J.C. Misra, "Effects of stenosis and dilatation on flow of blood mixed with suspended nanoparticles: A study using Homotopy technique," **26**(1), 251-265 (2021). https://doi.org/10.2478/ijame-2021-0015

[39] M.K. Prasad, R.B. Vijaya and C. Umadevi, "Effects of Stenosis and Post Stenotic Dilatations on Jeffrey Fluid Flow in Arteries," International Journal of Research in Engineering and Technology, **4**, 195-201 (2015). https://doi.org/10.15623/ijret.2015.0413032

[40] B. Pincombe, B. Mazumdar, and J. Hamilton-Craig, "Effects of multiple stenoses and post- stenotic dilation on non- Newtonian blood flow in small arteries," Medical & Biological Engineering & Computing, **37**(5), 595–599 (1999). https://doi.org/10.1007/bf02513353

[41] M. Dhange, G. Sankad, R. Safdar, W. Jamshed, M.R. Eid, U. Bhujakkanavar, *et al*., "A mathematical model of blood flow in a stenosed artery with post-stenotic dilatation and a forced field," PLoS ONE, **17**(7), e0266727 (2022). https://doi.org/10.1371/journal.pone.0266727

[42] K.M. Prasad, N. Subadra and M.A.S. Srinivas, "Peristaltic transport of a micropolar fluid with nanoparticles in an inclined tube with permeable walls," International Journal of Advanced Research Trends in Engineering and Technology (IJARTET), **4**(10), (2017). https://ijartet.com/2750/v4i10/journal

[43] K.M. Prasad and T. Sudha, "The effects of post-stenotic dilatations on the flow of micropolar fluid through stenosed artery with suspension of nanoparticles," AIP Conference Proceedings, **2246**(1), 020082 (2000). https://doi.org/10.1063/5.0014455

МОДЕЛЮВАННЯ МГД ПОТОКУ МІКРОПОЛЯРНОЇ НАНОРИДИНИ В ПОХИЛІЙ ПОРИСТІЙ СТЕНОЗОВАНІЙ АРТЕРІЇ З ДИЛАТАЦІЄЮ

Нарендер Сатвай[a,b], Каранаму Маруті Прасад[a]

[a]Кафедра математики, Школа наук, GITAM (Вважається університетом), Хайдерабад, штат Телангана, Індія – 502329
[b]Кафедра математики, Технологічний інститут Б. В. Раджу, Вішнупур, Нарсапур, штат Телангана, Індія – 502313

У цій статті досліджується вплив магнітного поля на кровотік з частинами нанорідини через похилу пористу стенозовану артерію та дилатацію. Тут кров розглядається як мікрополярна рідина. Рівняння розв'язуються за допомогою методу гомотопічних бурень [HPM] у припущенні легкого стенозу. Отримано розв'язки замкнутої форми швидкості, профілю температури та розподілу концентрації. Спостерігався вплив відповідних параметрів на явища потоку, а результати аналізуються графічно. Це дослідження розглядає вплив магнітного параметра на характеристики потоку та показує, що наявність магнітного поля збільшує опір потоку, одночасно зменшуючи напруження зсуву на стінці. В результаті виявлено, що опір потоку та напруження зсуву на стінці зменшується з високою дилатацією стенозу. Крім того, дослідження показує, що опір потоку збільшується, а напруження зсуву на стінці зменшується зі збільшенням в'язкості. Лінії потоку побудовані для вивчення картини потоку та властивостей передачі імпульсу.

Ключові слова: *стеноз; дилатація; мікрополярна рідина; опір потоку; напруження зсуву на стінці; параметр броунівського руху; параметр термофорезу*

HEAT AND MASS TRANSFER IN STRATIFIED MHD FLOW UNDER AN INCLINED MAGNETIC FIELD

Mukul Medhi[*], Rudra Kanta Deka

Mathematics Department, Gauhati University, Guwahati-781014, Assam, India
[*]Corresponding Author e-mail: mukulmedhi2@gmail.com

This study investigates how thermal and mass stratification influence unsteady magnetohydrodynamic fluid flow through a permeable medium over an inclined parabolic plate when a slanted magnetic field is present. Laplace transform method is used to find closed-form analytical benchmark solutions for flow governing equations. The study compares the results obtained from thermal and mass stratification with scenarios where both forms of stratification are not present. Non-stratified cases demonstrate elevated velocities in comparison. Also the presence of both stratifications increases skin friction by 33.42%, the heat transfer rate by 97.54%, and the mass transfer rate by 36.91%. The biggest influence on fluid flow arises when the magnetic field is orthogonal to the flow direction. This study's conclusions are pertinent for optimising fluid dynamics in engineering and environmental applications.

Keywords: *MHD; Porous medium; Parabolic inclined plate; Thermal Stratification; Mass Stratification; Inclined magnetic field*

PACS: 44.05.+e, 47.11.-j, 47.65.-d, 47.56.+r

Nomenclature

α	Thermal diffusivity (m²/s)
β	Volumetric coefficient of thermal expansion (1/K)
γ'	Thermal stratification parameter
γ	Dimensionless thermal stratification parameter
λ	Inclination angle of the plate
ϕ	Angle of inclination of magnetic field
ν	Kinematic viscosity (m²/s)
σ	Electrical conductivity. (1/ohm.m)
τ	Non-dimensional skin friction
ξ'	Mass stratification parameter
ξ'	Dimensionless mass stratification parameter
C	Non-dimensional concentration
C'	Species concentration in the fluid (mol/m³)
C'_∞	Concentration far from the plate (mol/m³)
C'_w	Concentration at the plate (mol/m³)
D	Mass diffusion coefficient (m²/s)
g	Gravitational acceleration (m/s²)
Gc	Mass Grashof number
β^*	Expansion coefficient with concentration (m²/h)
Gr	Thermal Grashof number
Nu	Nusselt number
Pr	Prandtl number
t	Non-dimensional time
T'	Temperature of the fluid (K)
t'	Time (s)
T'_∞	Temperature far from the plate (K)
T'_w	Temperature at the plate (K)
T	Non-dimensional temperature
k'_p	Dimensional permeability
k_p	Permeability
u	Non-dimensional velocity
u'	Velocity in x direction (m/s)
u_0	Reference velocity
b'	Dimensional acceleration parameter

b	Accelerating parameter
y'	Non-dimensional coordinate normal to the plate
y	Dimensional coordinate normal to the plate (m)
B_0	Magnetic field strength
M	Magnetic parameter

1. INTRODUCTION

MHD focusses on the interaction of magnetic fields with electrically conducting fluids in motion. MHD exhibits application across a range of disciplines, encompassing plasma physics, astrophysics, and the design of MHD generators and pumps. Beyond the areas already mentioned, it holds immense potential across a broad spectrum of disciplines, including aeronautics, chemical engineering, electrical engineering, medicine, and the biological sciences. The field of magnetohydrodynamics was pioneered by the prominent Swiss physicist Hannes Alfvén [1]. Significant contributions from scholars such as [2], [3], [4], and [5] have shaped the current state of MHD. [6] investigated how MHDs are used practically in biological systems. According to [7], one of the most vital uses of MHD is the pumping of materials that are challenging to pump using ordinary pumps. [8] conducted a numerical investigation of the electroosmotic-driven transport of MHD Casson fluid via an exponential stretching sheet. Recent academic investigations by scholars including [9], [10], [11], [12], [13], [14], [15], [16], [17] and [18] have explored magnetohydrodynamic flows across a range of geometric contexts.

A material characterised by voids or pore spaces, devoid of solid, contained inside a solid or semisolid matrix is referred to as porous material. The permeability of porous materials is a defining characteristic, enabling the passage of various fluids from one side to the other. As a result, these materials are prevalent in both natural and technological contexts. Numerous fields, including hydrology and petroleum engineering, rely extensively on porous media. Consequently, the study of fluid dynamics within porous environments has garnered significant scholarly attention. A model addressing the boundary conditions of a porous material in relation to viscous fluid flow around a porous solid has been examined by [19] and [20]. [21] examined the heat generation and chemical reaction impact on MHD flow of Jeffrey nanofluid through a porous medium. It was examined by [22] how thermal radiation and chemical reactions affected Williamson MHD fluid flow embedded in porous environment. [23] conducted an analytical examination of the impacts of Soret effect and thermal generation on the unsteady magnetohydrodynamic flow of radiating and electrically conducting nanofluid across an oscillating vertical plate within a porous media. Furthermore, the subsequent researchers, [24], [25], [26], [27] and [28] are extensively engaged in the investigation of porous medium transport phenomena.

An inclined magnetic field serves as an important factor, especially in industrial applications and biological studies.Between 0 and 90 degrees is the range of this magnetic field's inclination angle. The impact of a tilted magnetic field on hydromagnetic flow across an oblique oscillating plate and a linearly accelerating plate was examined by [29] and [30]. [31] examined the influence of an angled magnetic field on the time-dependent squeezing flow between parallel plates with suction and injection. [32] investigated the flow and temperature distribution of MHD Casson fluid via a permeable extended surface within laminar flow regime. The unsteady hydro magnetic couette flow in the presence of a variable inclined magnetic field was analysed by [33]. The study of heat and mass transfer in unstable magnetohydrodynamic flow in two non-conducting infinite vertical plates with an slanted magnetic field is studied by [34]. In a perforated medium with a changing temperature, an angled magnetic field, and stable mass diffusion, [35] examined unsteady free-convection MHD fluid flow in conjunction with an exponentially accelerating plate. [36] investigated time variation measurements by the influence of Dufour, Hall, and ion-slip currents in unsteady magneto-hydrodynamic fluid flow across an inclined plate with an inclined generated magnetic field.

Research on MHD flow problems related to the motion induced by the sudden initiation of endless vertical plates exhibiting parabolic velocity has been extensively conducted, owing to their prospective uses in domains like astrophysics, geophysics, and missile technology. [37], [38], [39], and [40] are among them. [41] started their research by examining parabolic flow over an upright plate with uniform heat flux and variable mass diffusion, establishing a foundation for comprehending such intricate fluid dynamics. [42] recently conducted a numerical study on the MHD fluid's parabolic flow via an upright plate in a porous medium. [43] has examined the issue of the effects of a angled magnetic field on a transit radiative hydromagnetic flow across an oblique parabolic accelerating plate inside a porous medium, including chemical reactions and heat-generating parameters. Further [44] extended this by considering thermal diffusion effect. [45] examined how radiation and Hall current, in addition to a changing temperature, affected MHD flow over an inclined parabolic accelerating plate through a porous media. When rotation and the first chemical substance reaction were present, [46] examined parabolic flow via an isothermal perpendicular plate with heat and mass scattering.

None of the studies mentioned previously included thermal and mass stratification, which is crucial for weather and climatic prediction, comprehension of natural systems, engineering applications, and environmental and safety aspects. In the complex realm of fluid dynamics, thermal stratification and mass stratification are crucial factors. Thermal Stratification arises from resistance to heat transport, resulting in discrete layers within a fluid, whereas Mass Stratification occurs owing to density variations caused by differing solute concentrations. [47] and [48] developed analytical solutions for unsteady flow across an endless upright plate under various surface conditions. [49] and [50] investigated the impacts of mass and

thermal stratification on a upright wavy truncated cone and a wavy vertical surface within saturated porous media of a non-Newtonian fluid. [51] established the analytical solution for the simultaneous influences of mass and thermal stratification on unsteady flow via exponential mass diffusion and an accelerating plate inside a porous medium exhibiting variable temperatures. [52] examined the unsteady parabolic flow in a porous media over an endless upright plate, characterized by exponential temperature decay and variable mass diffusion, considering the effects of thermal and mass stratification. [53] and [54] developed solutions addressing the impacts of mass and thermal stratification on unsteady magnetohydrodynamic flow under various surface conditions.

Inspired by the aforementioned literary works, we endeavoured to conduct a precise examination of the matter concerning the effects of a slanted magnetic field, as well as thermal and mass stratification, on a transit hydromagnetic flow over a tilted parabolic accelerated plate within a porous medium. Based on the authors' knowledge, no studies have been conducted on the impact of inclined magnetic field, thermal and mass stratification on hydromagnetic flow past a parabolic accelerating inclined plate through a porous media. So, the novelty of concepts and physical facts presented in this study is anticipated to significantly influence and facilitate interactions across many domains. This problem is resolved in a closed form with a potent method, namely the Laplace transform approach. Subsequently, the results for the fluid with two stratifications are contrasted with those for the specific scenario devoid of stratification. The effects of various physical entities on the non-dimensional velocity of fluid, temperature distribution, fluid concentration, shear stress, and rates of heat and mass transfer are illustrated graphically and through tabulated data. The practical relevance of this study's conclusions pertains to the optimization of fluid dynamics in engineering and environmental applications. Both stratification's effects on magnetohydrodynamic flow in porous media may increase the effectiveness of mass transfer and heat transfer systems, which can be used in energy system design, industrial cooling, and pollution control.

2. MATHEMATICAL FORMULATION

Consider the unsteady MHD flow of a viscous, incompressible, stratified fluid past an inclined parabolic accelerated plate within the porous medium. We employ a rectangular Cartesian coordinate system in which the y-axis is orthogonal to the plate and the x-axis extends uprightly along the plate. The magnetic field vector affecting the flow is given by $B = (B_0 \cos\phi, B_0 \sin\phi, 0$ when a constant magnetic field B_0 is applied at an arbitrary angle ϕ with the axis x. Furthermore, the plate is intended to be inclined at an arbitrary angle λ. Both inclinations are expected to be oriented vertically. At the initial time ($t' = 0$), the plate is stationary. However, the plate begins to move parabolically with velocity $u' = u_0(b't'^2)$ in its own plane at $t' > 0$. Due to the infinite length of the plate, all flow variables are independent of x and depend solely on y and t'. The induced magnetic field is to be disregarded due to the consideration of a very small magnetic Reynolds number. Furthermore, it is considered that the viscous dissipation of energy is negligible. Figure 1 clearly illustrates the geometry of the problem.
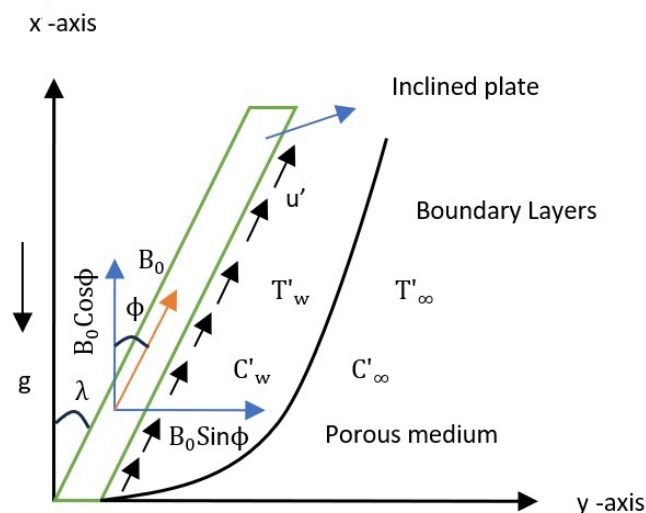
Figure 1. Flow geometry .

Consequently, according to Boussinesq's approximation, the equations delineated in refs [43], [44] and [52] are employed to characterise the unsteady flow.

$$\frac{\partial u'}{\partial t'} = g\beta(T' - T'_\infty)\cos\lambda + g\beta^*(C' - C'_\infty)\cos\lambda + \nu\frac{\partial^2 u'}{\partial y^2} - \left(\frac{\sigma\beta_0^2\sin^2\phi}{\rho} + \frac{\nu}{k'_p}\right)u' \qquad (1)$$

$$\frac{\partial T'}{\partial t'} = \alpha \frac{\partial^2 T'}{\partial y^2} - \gamma' u' \tag{2}$$

$$\frac{\partial C'}{\partial t'} = D \frac{\partial^2 C'}{\partial y^2} - \xi' u' \tag{3}$$

with following initial and boundary condition [44] and [55]:

$$t' \leq 0 : \quad u' = 0, \quad T' = T'_\infty, \quad C' = C'_\infty, \quad \forall \quad y$$

$$t' > 0 : \quad u' = u_0(b't'^2), \quad T' = T'_w, \quad C' = C'_w \quad at \quad y = 0$$

$$u' \to 0, \quad T' \to T'_\infty, \quad C' \to C'_\infty \quad as \quad y \to \infty \tag{4}$$

where "thermal stratification parameter" and "mass stratification paramter are termed as $\gamma' = \frac{dT'_\infty}{dx} + \frac{g}{C_p}$ and $\xi' = \frac{dC'_\infty}{dx}$. The phrase "thermal stratification" denotes the interplay of vertical temperature advection $\left(\frac{dT'_\infty}{dx}\right)$, wherein the temperature of the surrounding fluid is height-dependent, and the work of compression $\left(\frac{g}{C_p}\right)$ represents the rate at which particles in a fluid perform reversible work as a result of compression.

Introducing dimensionless variables:

$$u = \frac{u'}{u_0}, \quad t = \frac{t'u_0^2}{\nu}, \quad y' = \frac{u_0 y}{\nu}, \quad C = \frac{C' - C'_\infty}{C'_w - C'_\infty}, \quad \theta = \frac{T' - T'_\infty}{T'_w - T'_\infty},$$

$$Gr = \frac{g\beta\nu(T'_w - T'_\infty)}{u_0^3}, \quad M = \frac{\sigma\beta_0^2\nu}{\rho u_0^2}, \quad Gc = \frac{g\beta^*\nu(C'_w - C'_\infty)}{u_0^3}, \quad Sc = \frac{\nu}{D}$$

$$k_p = \frac{k'_p u_0^2}{\nu^2}, \quad \gamma = \frac{\gamma'\nu}{u_0(T'_w - T'_\infty)}, \quad \xi = \frac{\xi'\nu}{u_0(C'_w - C'_\infty)}, \quad Pr = \frac{\nu}{\alpha}, \quad b = \frac{b'\nu^2}{u_0^4} \tag{5}$$

The transformed governing equation in dimensionless form are:

$$\frac{\partial u}{\partial t} = \frac{\partial^2 u}{\partial y'^2} + Gr\,T\cos\lambda + Gc\,C\cos\lambda - \left(M\,\sin^2\phi + \frac{1}{k_p}\right)u \tag{6}$$

$$\frac{\partial\theta}{\partial t} = \frac{1}{Pr}\frac{\partial^2\theta}{\partial y'^2} - \gamma\,u \tag{7}$$

$$\frac{\partial C}{\partial t} = \frac{1}{Sc}\frac{\partial^2 C}{\partial y'^2} - \xi\,u \tag{8}$$

and the dimensionless initial and boundary constraints are:

$$t \leq 0 : \quad u = 0, \quad \theta = 0, \quad C = 0 \quad \forall \quad y'$$

$$t > 0 : \quad u = b\,t^2, \quad \theta = 1, \quad C = 1 \quad at \quad y' = 0$$

$$u \to 0, \quad \theta \to 0, \quad C \to 0 \quad as \quad y' \to \infty \tag{9}$$

3. METHOD OF SOLUTION

The use of the Laplace transform method yields an equation of non-tractable form for any given Prandtl or Schmidt number. The non-dimensional governing equations from (6) to (8), along with the boundary conditions (9), are solvable when the conditions are reduced to $Pr = 1$, $Sc = 1$. Consequently, we get

$$\frac{d^2\bar{u}}{dy'^2} - \left(s + h_1\right)\bar{u} + Gr\,\bar{T}\cos\lambda + Gc\,\bar{C}\cos\lambda = 0 \tag{10}$$

$$\frac{d^2\bar{T}}{dy'^2} - s\,\bar{T} - \gamma\,\bar{u} = 0 \tag{11}$$

$$\frac{d^2\bar{C}}{dy'^2} - s\,\bar{C} - \xi\,\bar{u} = 0 \tag{12}$$

where $h_1 = M\,\sin^2\phi + \frac{1}{k_p}$ and s denotes the Laplace transform parameter.

This set of ordinary differential equations is solved alongside the initial boundary conditions, employing the inverse Laplace transform technique as facilitated by [56] and [57] . Consequently, we derive the subsequent profiles of velocity, temperature, and concentration:

$$u = \frac{2\,b}{h_3}\left(h_4\,L_2(h_4) - h_5\,L_2(h_5)\right) + \frac{h_6}{h_3}\left(L_1(h_5) - L_1(h_4)\right) \tag{13}$$

$$\theta = \frac{(\xi - \gamma)\,Gc\,\cos\phi}{h_5 h_4}erfc\left(\frac{y'}{2\sqrt{t}}\right) + \frac{2\,\gamma\,b}{h_3}\left(L_2(h_4) - L_2(h_5)\right) + \frac{\gamma\,h_6}{h_3}\left(\frac{L_1(h_5)}{h_5} - \frac{L_1(h_4)}{h_4}\right) \tag{14}$$

$$C = \frac{(\gamma - \xi)\,Gr\,\cos\phi}{h_5 h_4}erfc\left(\frac{y'}{2\sqrt{t}}\right) + \frac{2\,\xi\,b}{h_3}\left(L_2(h_4) - L_2(h_5)\right) + \frac{\xi\,h_6}{h_3}\left(\frac{L_1(h_5)}{h_5} - \frac{L_1(h_4)}{h_4}\right) \tag{15}$$

where

$$h_2 = Gr\,\gamma\,\cos\phi + Gc\,\xi\,\cos\phi, \quad h_3 = \sqrt{h_1^2 - 4h_2}, \quad h_4 = \frac{h_1 + h_3}{2}, \quad h_5 = \frac{h_1 - h_3}{2}$$
$$h_6 = Gr\,\cos\phi + Gc\,\cos\phi$$

$L_i's$ indicate inverse Laplace's transforms as stated below

$$L_1(p) = L^{-1}\left\{\frac{e^{-y'\sqrt{s+p}}}{s}\right\}, \quad L_2(p) = L^{-1}\left\{\frac{e^{-y'\sqrt{s+p}}}{s^3}\right\},$$

4. CLASSICAL CASE ($\gamma = 0$, $\xi = 0$)

Solutions have been derived for the unique scenario in which stratification is absent. We aim to compare the outcomes of the fluid exhibiting thermal and mass stratification with the scenario devoid of stratification. Therefore, the solutions for the classical scenario with boundary conditions (9) via the Laplace transformation are as follows:

$$\theta_c = erfc\left(\frac{y'}{2\sqrt{t}}\right) \tag{16}$$

$$C_c = erfc\left(\frac{y'}{2\sqrt{t}}\right) \tag{17}$$

$$u_c = 2\,b\,L_2(h_1) - \frac{h_6}{h_1}L_1(h_1) + \frac{h_6}{h_1}\,erfc\left(\frac{y'}{2\sqrt{t}}\right) \tag{18}$$

Skin Friction

We obtained the non-dimensional skin-friction from the velocity field, which represents the shear stress at the surface, as follows:

$$\tau = -\left.\frac{\partial u}{\partial y'}\right|_{y'=0}$$

$$= \frac{2\,b}{h_3}\left(h_4\,g_2(h_4) - h_5\,g_2(h_5)\right) + \frac{h_6}{h_3}\left(g_1(h_5) - g_1(h_4)\right) \tag{19}$$

Skin Friction for special case:

$$\tau_c = -\left.\frac{\partial u_c}{\partial y'}\right|_{y'=0}$$

$$= 2\,b\,g_2(h_1) - \frac{h_6}{h_1}g_1(h_1) + \frac{h_6}{h_1}\left(\frac{1}{\sqrt{\pi}\,\sqrt{t}}\right) \tag{20}$$

Nussely Number

We obtained the non-dimensional Nusselt number from the temperature field, which represents the rate of heat transfer, as follows:

$$Nu = -\frac{\partial \theta}{\partial y'}\bigg|_{y'=0}$$

$$= \frac{(\xi - \gamma)\,Gc\,\cos\phi}{h_5 h_4}\left(\frac{1}{\sqrt{\pi}\,\sqrt{t}}\right) + \frac{2\,\gamma\,b}{h_3}\left(g_2(h_4) - g_2(h_5)\right) + \frac{\gamma\,h_6}{h_3}\left(\frac{g_1(h_5)}{h_5} - \frac{g_1(h_4)}{h_4}\right) \tag{21}$$

Nusselt number for special case:

$$Nu_c = -\frac{\partial \theta_c}{\partial y'}\bigg|_{y'=0}$$

$$= \frac{1}{\sqrt{\pi}\,\sqrt{t}} \tag{22}$$

Sherwood Number

We obtained the non-dimensional Sherwood number from the concentration field, which represents the rate of mass transfer, as follows:

$$Sh = -\frac{\partial C}{\partial y'}\bigg|_{y'=0}$$

$$= \frac{(\gamma - \xi)\,Gr\,\cos\phi}{h_5 h_4}\left(\frac{1}{\sqrt{\pi}\,\sqrt{t}}\right) + \frac{2\,\xi\,b}{h_3}\left(g_2(h_4) - g_2(h_5)\right) + \frac{\xi\,h_6}{h_3}\left(\frac{g_1(h_5)}{h_5} - \frac{g_1(h_4)}{h_4}\right) \tag{23}$$

Sherwood number for special case:

$$Sh_c = -\frac{\partial C_c}{\partial y'}\bigg|_{y'=0}$$

$$= \frac{1}{\sqrt{\pi}\,\sqrt{t}} \tag{24}$$

where,

$$g_1(x) = \frac{e^{-xt}}{\sqrt{\pi\,t}} + \sqrt{x}\,erf(\sqrt{x\,t})$$

$$g_2(x) = \frac{(4tx(tx+1) - 1)\,erf\left(\sqrt{tx}\right)}{8x^{3/2}} + \frac{\sqrt{t}e^{-tx}(2tx+1)}{4\sqrt{\pi}x}$$

5. RESULTS AND DISCUSSION

Utilising the solutions established in earlier sections, we computed numerical values for a range of physical parameters, including concentration, skin friction, velocity, temperature, and Nusselt and Sherwood number. This study enabled us to explore the physical dimensions of the problem more thoroughly. Additionally, we used MATHEMATICA to generate plots shown in Figures 2-26. This research considers the following parameters: $M = 1$, $k_p = 0.5$, $Gr = 5$, $Gc = 5$, $t = 2$, $b = 0.2$, $y' = 1.5$, $\gamma = 0.5$, $\xi = 0.3$, $\phi = \frac{\pi}{3}$, $\theta = \frac{\pi}{3}$. Parameters ranges are: $0 \le \gamma \le 1$, $0 \le \xi \le 1$, $2 \le Gr \le 10$, $2 \le Gc \le 10$, $0.5 \le k_p \le 2.3$, $0.5 \le M \le 5$, $\frac{\pi}{9} \le \phi \le \frac{\pi}{2}$, $\frac{\pi}{9} \le \lambda \le \frac{\pi}{3}$, $0.1 \le b \le 0.4$. To validate the accuracy of the the approach, the temperature profile produced by [55] is juxtaposed with the temperature profile derived from the scenario of no thermal stratification, as seen in Figure 2. The findings are in strong agreement.

Graphs showing the impacts of γ and ξ on the velocity, temperature, and concentration profile are shown in Figures 3, 10, and 17. Thermal and mass stratification lowers the flow velocity, as seen in Figure 3. As the stratification parameters (γ, &, ξ) rise, the convective interaction between the ambient fluid and the hot plate falls. Because of this reduction in buoyancy force, the flow velocity therefore decreases. Figure 10 illustrates that the classical scenario has a greater temperature compared to the nonclassical circumstance. It illustrates that temperature increases owing to mass stratification, but decreases due to thermal stratification. The temperature difference between the vertical plate and the surrounding fluid diminishes in the presence of thermal stratification. This results in an increase in the thickness of the heat boundary layer, hence reducing the temperature. Figure 17 demonstrates that fluid concentration increases with a higher thermal stratification parameter, while it decreases with an increasing mass stratification parameter.

Graphs showing the influences of Gr and Gc on the velocity, temperature, and concentration profile are shown in Figures 4, 11, and 18. Figure 4 shows that when both Grashof numbers increase, the velocity profiles also increase,

which is because the buoyancy force is directly proportional to the Grashof numbers. Figure 11 shows that temperature decreases as Gr and Gc increase, suggesting that heat dissipation away from the heated surface is increased by improved buoyancy-driven fluid flow. The impacts of Gr and Gc on concentration have been shown to be identical to those seen for Figure 18's temperature profiles.

Graphs showing the effect of k_p on the velocity, temperature, and concentration profile are shown in Figures 5, 12, and 19. Permeability, determined by the geometry of the medium rather than the characteristics of the fluid. It quantifies formation's ability to transmit fluids, directly relating to the interconnectedness of pores, which influences fluid movement within the medium. The larger the interconnectedness of void spaces, the more easily fluid can traverse the medium. Hence, the increase in medium permeability results in enhanced fluid flow. Consequently, the velocity field increases with larger pore sizes in the medium, as illustrated in the provided Figure 5. Figures 12 and 19 indicate that temperature and concentration diminish as the permeability parameter elevates. This occurs as the pore sizes in the medium increases, allowing for greater mobility of the fluid's particles.

Graphs showing the influence of M on the velocity, temperature, and concentration profile are shown in Figures 6, 13, 20. In the study of magnetohydrodynamic (MHD) flow, the Lorentz force has a prominent influence on the motion of particles of an electrically conducting fluid, naturally tending to diminish fluid velocity. The Lorentz force is exactly proportional to the magnetic field. Consequently, when the magnetic field intensifies, the resistance to fluid motion inside the flow domain escalates. Hence, velocity profiles decrease as M increases, as seen in Figure 6. Furthermore, as M is increased, the temperature rises as shown in Figure 13. Because of improved confinement, resistive heating, suppression of cooling systems, and higher energy absorption from the field, an increase in M usually causes a rise in temperature. Figure 20 illustrates how M affects the concentration profile. The figure shows that the concentration of shear layers is improved by elevating M. This is caused by the Lorentz force, which opposes the direction of flow as the intensity of the magnetic field rises.

Graphs showing the effect of ϕ on the velocity, temperature, and concentration profile are shown in Figures 7, 14, and 21. Figure 7 illustrates the impact of an arbitrary magnetic field inclination angle on nondimensional velocity. It is evident that a rise in the tilt of the magnetic field results in a drop in fluid velocity. This occurs because the resistive force, known as the Lorentz force, intensifies with an elevated in the inclination angle. When the direction of the magnetic field is orthogonal to the flow of the fluid, it has the greatest impact on the flow. However, increase in ϕ escalates temperature and concentration profile of the fluid as seen in Figures 14, and 21.

Graphs showing the impact of λ on the velocity, temperature, and concentration profile are shown in Figures 8, 15, and 22. As the plate's inclination angle rises, we can see that the fluid flow decreases. It is well known that the frictional force acting on the fluid dramatically rises across the flow domain when the plate is angled with respect to the flow direction. The provided Figure 8 illustrates how this physical fact results in a drop in fluid velocity. However, rise in λ escalates temperature and concentration profile of the fluid as seen in Figures 15, and 22.

Graphs showing the effect of b on the velocity, temperature, and concentration profile are shown in Figures 9, 16, and 23. Figure 9 shows that velocity increases as b increases. This is due to the fact that a stronger propulsive force applied on the fluid is implied by an increase in acceleration. Figure 16 illustrates how temperature drops as b increases. The way that acceleration affects the fluid's energy distribution helps to understand this tendency. Increased acceleration imparts additional kinetic energy to the fluid, especially in the vicinity of the surface, which is converted to thermal energy via fluid friction and viscous dissipation. By increasing the base temperature throughout the fluid, this improved energy conversion raises the system's minimum temperature. Also concentration profile decreases as rise in b as seen in Figure 23.

Graphs showing the effect of γ and ξ on the Skin Friction, Nusselt Number and Sherwood Number are shown in Figures 24, 25, and 26. In Figure 24, the skin friction curve shows a noticeable increase over time, especially in cases where both thermal (γ) and mass (ξ) stratification are present. In contrast to the scenario devoid of stratification, the upward trend signifies that the combined effect of temperature and mass stratification amplifies the fluid's resistance over the surface, resulting in elevated skin friction. Figures 25 and 26 illustrate an upward trend in the Nusselt and Sherwood values over time, suggesting enhanced mass and heat transmission. The increase is more significant with higher values of thermal stratification (γ) and mass stratification (ξ), as seen by the steeper curves. This behaviour indicates that enhanced stratification significantly improves the efficiency of heat and mass transfer in the fluid.

Table 1 shows how different parameters affect Skin friction (τ), Nusselt number (Nu), and Sherwood number (Sh). When the magnetic parameter (M) increases, the skin friction also increases because the magnetic force resists the fluid flow by inducing the Lorentz force, this also reduces heat and mass transfer, lowering Nu and Sh. On the other hand, increasing the permeability of the medium (k_p) allows the fluid to pass through more easily, which reduces skin friction but improves heat and mass transfer. Higher values of the thermal and mass Grashof numbers (Gr and Gc) increase Nu and Sh, showing stronger buoyancy-driven flow. But very high values can cause flow reversal near the plate, which lowers skin friction. Changing the angles of the magnetic field (ϕ) and the plate (λ) slightly reduces skin friction while helping heat and mass transfer. Finally, increasing the acceleration parameter (b) increases all three values, showing that unsteady motion boosts shear stress and improves both heat and mass transfer. Table 2 indicates that the presence of both stratifications increases skin friction by 33.42%, the heat transfer rate by 97.54%, and the mass transfer rate by 36.91%.

The Nusselt number (Nu) represents the ratio of convective to conductive heat transfer across a fluid boundary and is a fundamental parameter in the analysis of thermal transport phenomena. Similarly, the Sherwood number (Sh) quantifies the ratio of convective to diffusive mass transfer, serving as its mass transfer analogue. These dimensionless numbers

are critical in characterizing transport processes and evaluating the influence of various physical effects, such as thermal and solutal stratification or magnetohydrodynamic (MHD) forces. A detailed analysis of Nu and Sh provides insights into the enhancement or suppression of energy and mass transport under complex flow conditions. In practical systems, such understanding supports the optimization of engineering applications including heat exchangers, chemical processing units, and environmental control systems. Therefore, exploring the interplay between convective transport mechanisms and external effects is essential for the development of more efficient and purpose-specific thermal and mass transfer systems.
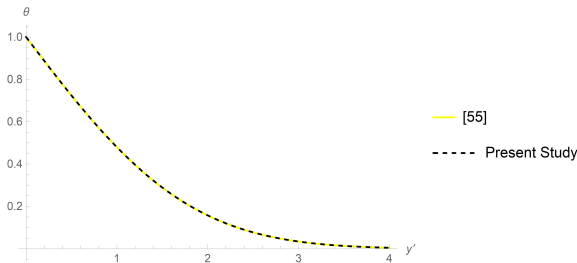
Figure 2. Comparison of temperature profile in the absence of γ
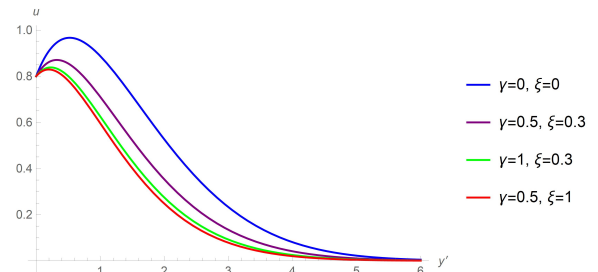
Figure 3. Effects of γ & ξ on velocity profile
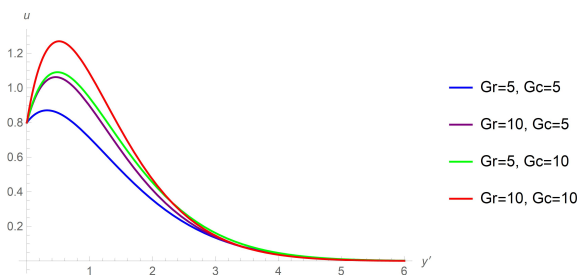
Figure 4. Effects of Gr & Gc on velocity profile
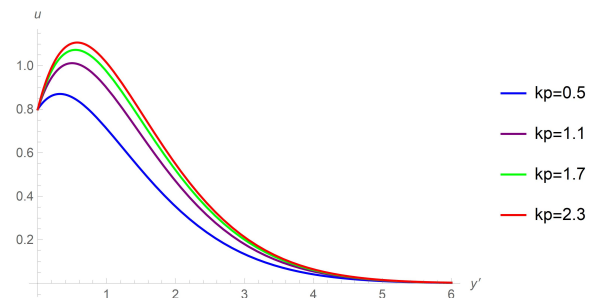
Figure 5. Effect of k_p on velocity profile
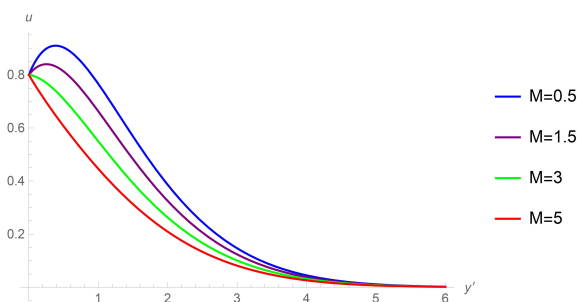
Figure 6. Effect of M on velocity profile
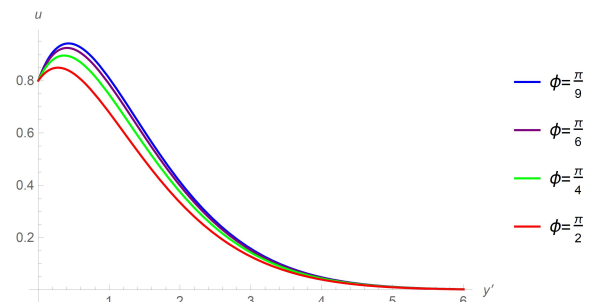
Figure 7. Effect of ϕ on velocity profile
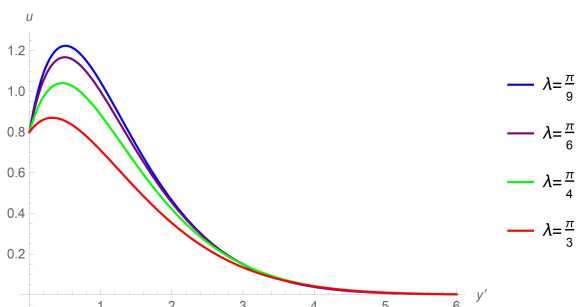
Figure 8. Effect of λ on velocity profile
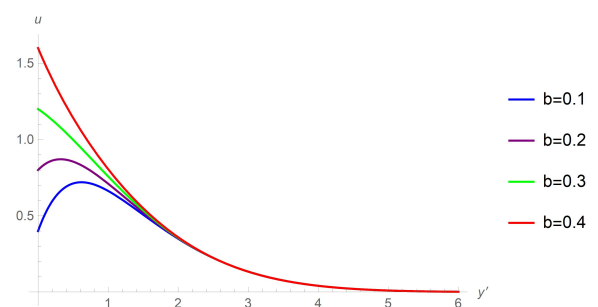
Figure 9. Effect of b on velocity profile
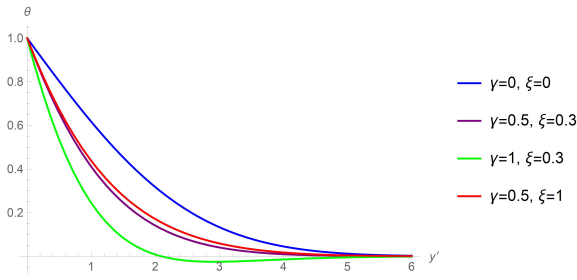
Figure 10. Effects of γ & ξ on temperature profile
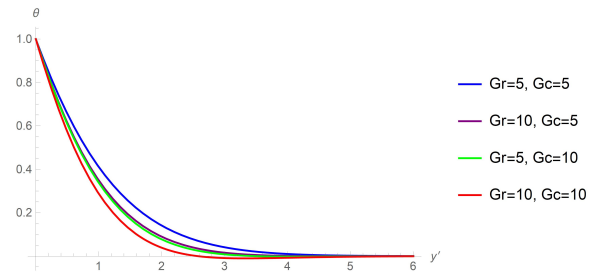
Figure 11. Effects of Gr & Gc on temperature profile
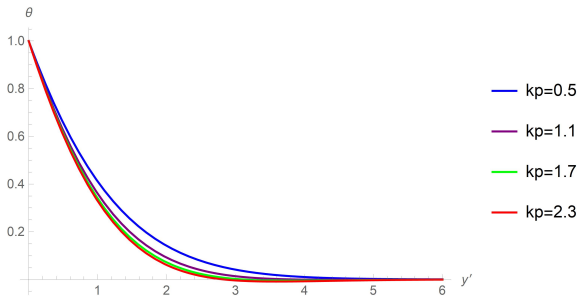
Figure 12. Effect of k_p on temperature profile
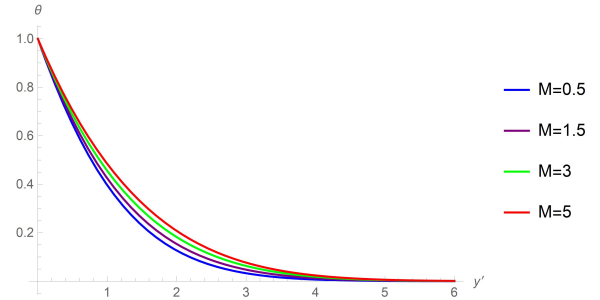
Figure 13. Effect of M on temperature profile
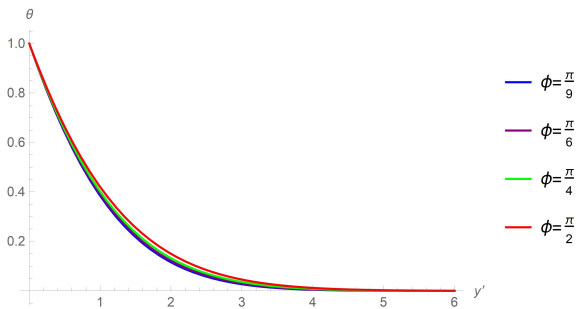
Figure 14. Effect of ϕ on temperature profile
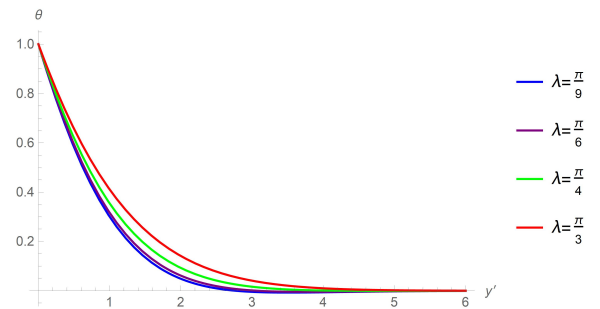
Figure 15. Effect of λ on temperature profile
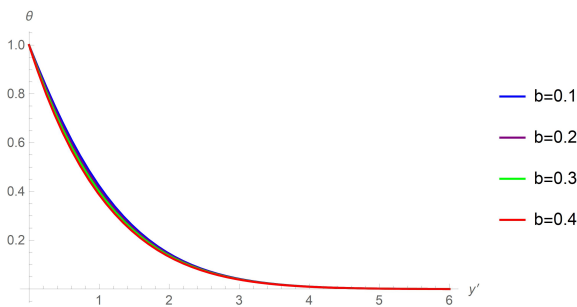
Figure 16. Effect of b on temperature profile
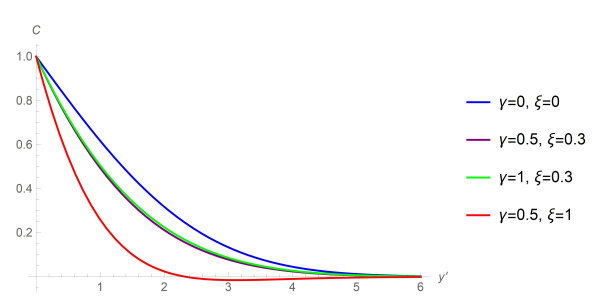
Figure 17. Effects of γ & ξ on concentration profile
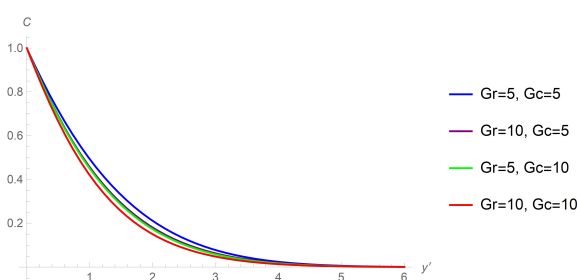
Figure 18. Effects of Gr & Gc on concentration profile
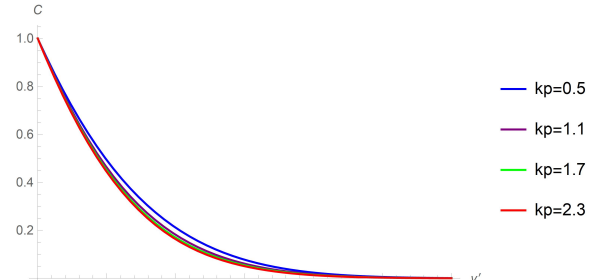
Figure 19. Effect of k_p on concentration profile
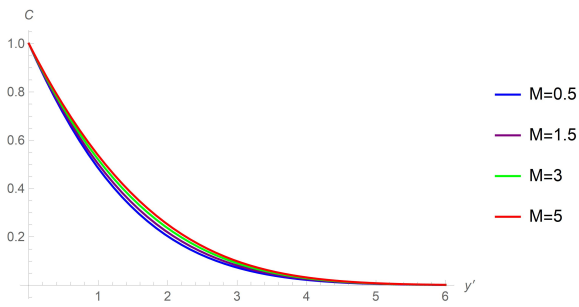
Figure 20. Effect of *M* on concentration profile
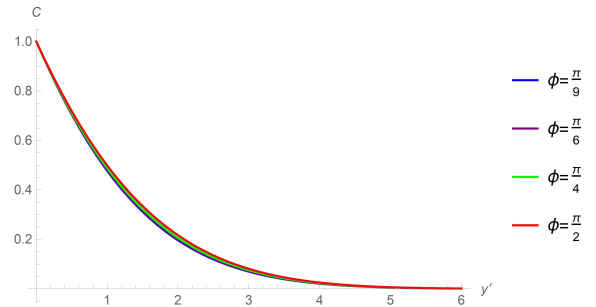
Figure 21. Effect of ϕ on concentration profile
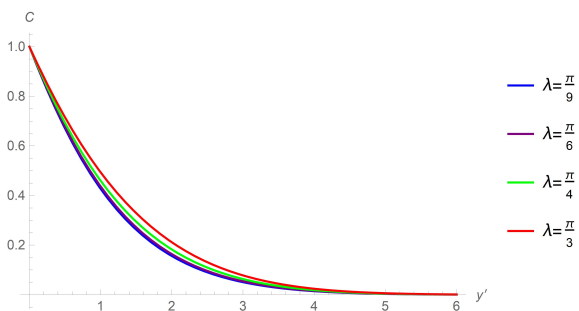
Figure 22. Effect of λ on concentration profile
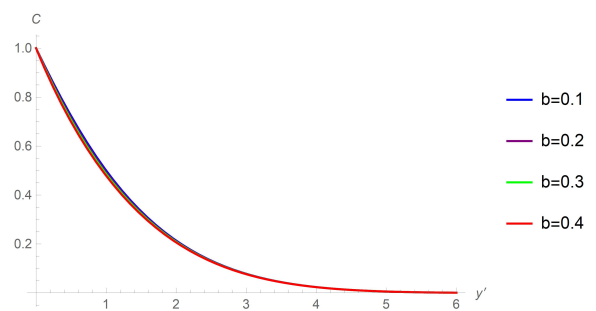
Figure 23. Effect of *b* on concentration profile
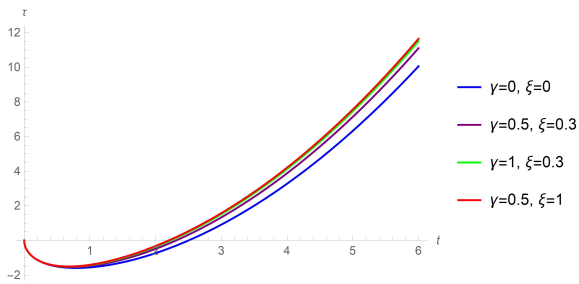
Figure 24. Effects of γ & ξ on Skin Friction
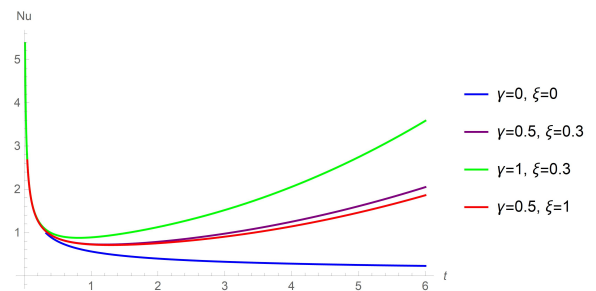
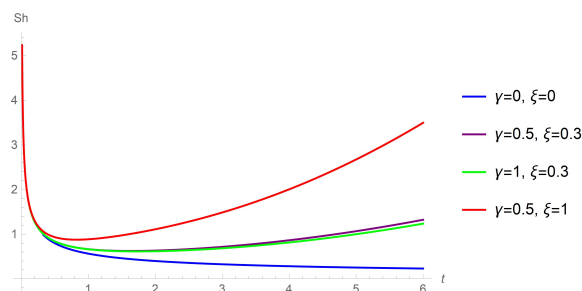**Figure 25.** Effects of γ & ξ on Nusselt Number

Figure 26. Effects of γ & ξ on Sherwood Number

Table 1. The impact of different parameter on Skin Friction, Nusselt Number and Sherwood Number with $t = 2$, $\gamma = 0.5$ and $\xi = 0.3$

M	k_p	Gr	Gc	ϕ	λ	b	τ	Nu	Sh
1	0.5	2	2	$\frac{\pi}{3}$	$\frac{\pi}{3}$	0.2	0.692507	0.641668	0.544578
3	0.5	2	2	$\frac{\pi}{3}$	$\frac{\pi}{3}$	0.2	1.08778	0.604961	0.522554
5	0.5	2	2	$\frac{\pi}{3}$	$\frac{\pi}{3}$	0.2	1.40899	0.580339	0.50778
1	**1.1**	2	2	$\frac{\pi}{3}$	$\frac{\pi}{3}$	0.2	0.323167	0.682832	0.569276
1	**1.7**	2	2	$\frac{\pi}{3}$	$\frac{\pi}{3}$	0.2	0.193087	0.698862	0.578894
1	0.5	**5**	2	$\frac{\pi}{3}$	$\frac{\pi}{3}$	0.2	0.0994802	0.715856	0.58909
1	0.5	**10**	2	$\frac{\pi}{3}$	$\frac{\pi}{3}$	0.2	−0.810403	0.821675	0.652582
1	0.5	2	**5**	$\frac{\pi}{3}$	$\frac{\pi}{3}$	0.2	0.073624	0.720836	0.592079
1	0.5	2	**10**	$\frac{\pi}{3}$	$\frac{\pi}{3}$	0.2	−0.904434	0.840987	0.664169
1	0.5	2	2	$\frac{\pi}{4}$	$\frac{\pi}{3}$	0.2	0.615765	0.649673	0.549381
1	0.5	2	2	$\frac{\pi}{6}$	$\frac{\pi}{3}$	0.2	0.534835	0.658429	0.554635
1	0.5	2	2	$\frac{\pi}{3}$	$\frac{\pi}{4}$	0.2	0.353811	0.684906	0.57052
1	0.5	2	2	$\frac{\pi}{3}$	$\frac{\pi}{6}$	0.2	0.1008	0.716574	0.589521
1	0.5	2	2	$\frac{\pi}{3}$	$\frac{\pi}{3}$	**0.3**	1.47854	0.70505	0.582607
1	0.5	2	2	$\frac{\pi}{3}$	$\frac{\pi}{4}$	**0.4**	2.26457	0.768432	0.620636

Table 2. The influence of γ and ξ on τ, Nu and Sh

	$\gamma = 0$, $\xi = 0$	$\gamma = 0.5$ $\xi = 0.3$	Change in Percentage
τ	−0.733082	−0.488104	33.42% ↑
Nu	0.398942	0.788073	97.54% ↑
Sh	0.398942	0.632421	36.91% ↑

6. CONCLUSION

This article presents an exact analysis of fluid flow across an inclined parabolic plate inside a permeable medium, considering the influence of an inclined magnetic field, as well as heat and mass stratification. Ultimately, the following conclusions are derived.

- Velocity is diminished as a result of diminished buoyancy forces as thermal (γ) and mass (ξ) stratification increases. Temperature is reduced by thermal stratification, while it is elevated by mass stratification. The concentration of

fluid increases as γ increases, while it decreases as ξ decreases. Nusselt number (Nu), Sherwood number (Sh), and Skin Friction are all enhanced by both γ and ξ, which also improves heat and mass transfer.

- The velocity is increased by the stronger buoyancy forces that result from higher Gr and Gc values. Temperature and concentration decrease with increasing Gr and Gc, indicating enhanced convective cooling. Moderate values improve Nu and Sh; very high values may lead to flow reversal near the plate, lowering skin friction.

- Velocity increases with k_p due to improved fluid mobility. Temperature and concentration decrease as permeability increases. Skin friction decreases, while Nu and Sh improve with higher k_p.

- Velocity decreases as M increase due to the resistive Lorentz force. Temperature and concentration increase because of resistive heating and flow confinement. Skin friction increases, while Nu and Sh decrease with increasing M.

- Higher ϕ values decrease velocity by enhancing the Lorentz force. Temperature and concentration rise with increasing ϕ. Also, Heat and mass transfer improve; skin friction decreases slightly.

- Increasing λ reduces velocity due to increased frictional resistance. Temperature and concentration profiles rise with larger plate angles. Also Heat and mass transfer are enhanced; skin friction experiences a minor reduction.

- Velocity increases with b due to stronger propulsive forces. Temperature and concentration decrease due to redistribution of thermal energy. All three quantities—skin friction, Nu, and Sh—increase with b.

- Presence of both stratification leads to:
  - 33.42% increase in skin friction,
  - 97.54% increase in heat transfer rate (Nu),
  - 36.91% increase in mass transfer rate (Sh).

In our study, the values for Pr and Sc must be taken into consideration as unity in order to have a thorough analysis and make the equations tractable, that is, to discover accurate solutions in closed form. To get a thorough grasp of the model, it is advised that future studies use numerical techniques to find solutions for the coupled equations with different values of Pr and Sc. The findings of this study have practical applications in optimizing industrial cooling systems, enhancing heat exchanger efficiency, and improving pollution control strategies. These insights are particularly valuable for engineering and energy systems where precise control of heat and mass transfer is critical.

ORCID

Mukul Medhi, https://orcid.org/0009-0003-2828-0315; **Rudra Kanta Deka**, https://orcid.org/0009-0007-1573-4890

REFERENCES

[1] H. Alfvén, "Existence of Electromagnetic-Hydrodynamic waves," Nature, **150**(3805), 405-406 (1042). https://doi.org/10.1038/150405d0

[2] P. Caldirola, "Shercliff, J. A. - A Textbook Of Magnetohydrodynamics," Scientia, Rivista di Scienza, **60**(101), 364 (1966).

[3] P.H. Roberts, *An introduction to magnetohydrodynamics*, vol. 6, (Longmans, London, 1967).

[4] V.C. Ferraro and C. Plumpton, *Introduction to magneto-fluid mechanics*, (Oxford University, New York, (1966).

[5] K.R. Cramer and S.-I. Pai, *Magnetofluid dynamics for engineers and applied physicists*, (MacGraw-Hill, New York, 1973)

[6] S. Rashidi, J.A. Esfahani and M. Maskaniyan, "Applications of magnetohydrodynamics in biological systems-a review on the numerical studies," Journal of Magnetism and Magnetic Materials, **439**, 358-372 (2017). https://doi.org/10.1016/j.jmmm.2017.05.014

[7] O.M. Al-Habahbeh, M. Al-Saqqa, M. Safi and T Abo Khater, "Review of magnetohydrodynamic pump applications," Alexandria Engineering Journal, **55**(2), 1347-1358, (2016). https://doi.org/10.1016/j.aej.2016.03.001

[8] K. Ramesh, K.K. Asogwa, R.K. Lodhi, M.I. Khan, M. Medani, K.A. Gepreel and D. Abduvalieva, "Numerical investigation of electroosmotic driven transport of MHD Casson fluid over an exponential stretching sheet using quartic B-spline method," Numerical Heat Transfer, Part A: Applications, 1-16, (2024). https://doi.org/10.1080/10407782.2024.2345864

[9] M.V. Krishna, "Analytical study of chemical reaction, Soret, Hall and ion slip effects on MHD flow past an infinite rotating vertical porous plate," Waves in Random and Complex Media, **35**(2), 2475-2501 (2025). https://doi.org/10.1080/17455030.2022.2044094

[10] M. Kazim, S. Hussain, S. Muhammad and M.A. Abbas, "Analysis of MHD viscous fluid flow under the influence of viscous dissipation force over vertically moving plate with innovative constant proportional caputo derivative," Partial Differential Equations in Applied Mathematics, **14**, 101163 (2025). https://doi.org/10.1016/j.padiff.2025.101163

[11] T. Pradhan, S. Jena and S.R. Mishra, "Laplace transformation technique for free convective time-dependent MHD flow over a vertical porous flat plate with heat sink and chemical reaction: An analytical approach," Hybrid Advances, **8**, 100363 (2025). https://doi.org/10.1016/j.hybadv.2024.100363

[12] Sehra, S.U. Haq, S.I.A. Shah, K.S. Nisar, S.U. Jan and I. Khan, "Convection heat mass transfer and MHD flow over a vertical plate with chemical reaction, arbitrary shear stress and exponential heating," Scientific reports, **11**(1), 4265 (2021). https://doi.org/10.1038/s41598-021-81615-8

[13] B.K. Jha, M.M. Altine and A.M. Hussaini, "MHD steady natural convection in a vertical porous channel in the presence of point/line heat source/sink: An exact solution," Heat transfer, **52**(7), 4880-4894 (2023). https://doi.org/10.1002/htj.22903

[14] S. Sarma and N. Ahmed, "Dufour effect on unsteady MHD flow past a vertical plate embedded in porous medium with ramped temperature," Scientific Reports, **12**(1), 13343 (2022). https://doi.org/10.1038/s41598-022-15603-x

[15] S.R. Yedhiri, K.K. Palaparthi, R. Kodi and F. Asmat, "Unsteady MHD rotating mixed convective flow through an infinite vertical plate subject to Joule heating, thermal radiation, Hall current, radiation absorption," "Journal of Thermal Analysis and Calorimetry," **149**(16), 8813-8826 (2024). https://doi.org/10.1007/s10973-024-12954-7

[16] K. Bhaskar, K. Sharma and K. Bhaskar, "MHD squeezed radiative flow of Casson hybrid nanofluid between parallel plates with joule heating," International Journal of Applied and Computational Mathematics, **10**(2), 80 (2024). https://doi.org/10.1007/s40819-024-01720-w

[17] M. Shareef, "MHD flow along a vertical plate with heat and mass transfer under ramped plate temperature," Jordan Journal of Mechanical & Industrial Engineering, **17**(2), 183-193 (2023). https://doi.org/10.59038/jjmie/170203

[18] K. Raghunath, M. Obulesu and K.V. Raju, "Radiation absorption on MHD free conduction flow through porous medium over an unbounded vertical plate with heat source," International journal of ambient energy, **44**(1), 1712-1720 (2023). https://doi.org/10.1080/01430750.2023.2181869

[19] G.I. Taylor, "A model for the boundary condition of a porous material. Part 1," Journal of Fluid Mechanics, **49**(2), 319-326 (1971). https://doi.org/10.1017/S0022112071002088

[20] S. Richardson, "A model for the boundary condition of a porous material. Part 2," Journal of Fluid Mechanics, **49**(2), 327-336 (1971). https://doi.org/10.1017/S002211207100209X

[21] I. Khan, H. Firdous, S. Alshehery, W.A. Khan, S.M. Husnine and A. Khan, "Effect of heat generation and chemical reaction on convective MHD flow of Jeffrey nanofluids in a porous medium," ZAMM - Journal of Applied Mathematics and Mechanics / Zeitschrift Für Angewandte Mathematik Und Mechanik, **105**(1), e202300877 (2025). https://doi.org/10.1002/zamm.202300877

[22] B.P. Jadhav and S.N. Salunkhe, "Chemically and thermally radiated Williamson MHD fluid over porous media with heat source-sink," International Journal of Modelling and Simulation, **45**(2), 544-558 (2025). https://doi.org/10.1080/02286203.2023.2223401

[23] M. Sheikholeslami, H.R. Kataria, A.S. Mittal, "Effect of thermal diffusion and heatgeneration on MHD nanofluid flow past an oscillating vertical plate through porous medium," Journal of Molecular Liquids, **257**, 12-25 (2018). https://doi.org/10.1016/j.molliq.2018.02.079

[24] M.F. Endalew and S. Sarkar, "Capturing the transient features of double diffusive thin film flow of a second grade fluid through a porous medium," International Journal of Applied and Computational Mathematics, **5**(6), 160 (2019). https://doi.org/10.1007/s40819-019-0743-7

[25] M.V. Krishna, "Diffusion-thermo, thermo-diffusion, hall and ion slip effects on mhd flow through porous medium in a rotating channel," Chemical Physics, **593**, 112623 (2025). https://doi.org/10.1016/j.chemphys.2025.112623

[26] K. Sudarmozhi, D. Iranian, I. Khan and S. Al-Otaibi, "Effects of porous medium in MHD flow of Maxwell fluid with Soret/Dufour impacts," Journal of Porous Media, **27**(4), 23-43 (2024). https://doi.org/10.1615/JPorMedia.2023048112

[27] A. Ali, S. Hussain, M. Ashraf, *et al.*, "Theoretical investigation of unsteady MHD flow of Casson hybrid nanofluid in porous medium: Applications of thermal radiations and nanoparticle," Journal of Radiation Research and Applied Sciences, **17**(3), 101029 (2024). https://doi.org/10.1016/j.jrras.2024.101029

[28] H. Nayar and P.A. Phiri, "Investigation of heat and mass transfer of free convective MHD flow along a vertical plate in a porous medium using the new modified differential transform-decomposition method," Results in Engineering, **25**, 104083 (2025). https://doi.org/10.1016/j.rineng.2025.104083

[29] M.F. Endalew, A. Nayak and S. Sarkar, "Flow past an oscillating slanted plate under the effects of inclined magnetic field, radiation, chemical reaction, and time-varying temperature and concentration," International Journal of Fluid Mechanics Research, **47**(3), 247-261 (2020). https://doi.org/10.1615/InterJFluidMechRes.2020026987

[30] M.F. Endalew and A. Nayak, "Thermal radiation and inclined magnetic field effects on MHD flow past a linearly accelerated inclined plate in a porous medium with variable temperature," Heat Transfer - Asian Research, **48**(1), 42-61 (2019). https://doi.org/10.1002/htj.21367

[31] X. Su and Y. Yin, "Effects of an inclined magnetic field on the unsteady squeezing flow between parallel plates with suction/injection," Journal of magnetism and magnetic materials, **484**, 266-271 (2019). https://doi.org/10.1016/j.jmmm.2019.04.041

[32] S. Sadighi, G. Ahmadi, H. Afshar, H.A.D. Ashtiani, and M. Jabbari, "Parametric study of entropy generation in magnetohydro-dynamic Casson fluid flow on a porous stretching sheet under an inclined magnetic field," Journal of Applied and Computational Mechanics, **11**(3), 681-691 (2025). https://doi.org/10.22055/jacm.2024.47739.4778

[33] E.M. Nyariki, M.N. Kinyanjui, and P.R. Kiogora, "Unsteady hydro magnetic couette flow in presence of variable inclined magnetic field," International Journal of Engineering Science and Innovative Technology, **6**(2), 2017. https://www.ijesit.com/Volume%206/Issue%202/IJESIT201702_02.pdf

[34] P.T. Hemamalini and M. Shanthi, "Heat and mass transfer on unsteady MHD flow in two nonconducting infinite vertical parallel plates with inclined magnetic field," International Journal of Mechanical Engineering and Technology, **9**(3), 521-536 (2018).

[35] U.S. Rajput and N.K. Gupta, "Dufour effect on unsteady free convection MHD flow past an exponentially accelerated plate through porous media with variable temperature and constant mass diffusion in an inclined magnetic field," International Research Journal of Engineering and Technology, **3**(8), 2135-2140 (2016). https://www.irjet.net/archives/V3/i8/IRJET-V3I8397.pdf

[36] Md.R. Islam, S. Nasrin and Md.M. Alam, "Unsteady MHD fluid flow over an inclined plate, inclined magnetic field and variable temperature with hall and ion-slip current," Ricerche di Matematica, **73**(5), 2477-2504 (2024). https://doi.org/10.1007/s11587-022-00728-y

[37] A. Selvaraj, S.D. Jose, R. Muthucumaraswamy and S. Karthikeyan, "MHD-parabolic flow past an accelerated isothermal vertical plate with heat and mass diffusion in the presence of rotation," Materials Today: Proceedings, **46**, 3546-3549 (2021). https://doi.org/10.1016/j.matpr.2020.12.499

[38] M. Aruna, A. Selvaraj, S.D. Jose and S. Karthikeyan, "Influence on MHD-parabolic flow across a vertical plate is triggered by a rotating fluid with uniform temperature and variable mass diffusion in the absence of hall and Dufour effects," European Chemical Bulletin, **12**, 1123-1132 (2023).

[39] S.D. Jose, A. Selvaraj, R. Muthucumaraswamy, S. Karthikeyan and E. Jothi, "MHD-parabolic flow past an accelerated isothermal vertical plate with variable temperature and uniform mass diffusion in the presence of rotation," in: *Proceedings of First International Conference on Mathematical Modeling and Computational Science: ICMMCS 2020*, (Springer, 2021), pp. 417-428.

[40] M. Umamaheswar, P.C. Reddy, S.H. Reddy, O. Mopuri, and C.K. Ganteda, "Aspects of parabolic motion of MHD fluid flow past a vertical porous plate with cross-diffusion effects," Heat Transfer, **51**(5), 4451-4465 (2022). https://doi.org/10.1002/htj.22507

[41] M. Muralidharan and R. Muthucumaraswamy, "Parabolic started flow past an infinite vertical plate with uniform heat flux and variable mass diffusion," International Journal of Mathematical Analysis, **8**(26), 1265-1274 (2014). http://dx.doi.org/10.12988/ijma.2014.45143

[42] P.C. Reddy, M. Umamheswar, S.H. Reddy, A.B.M. Raju, and M.C. Raju, "Numerical study on the parabolic flow of MHD fluid past a vertical plate in a porous medium," Heat Transfer, **51**(4), 3418-3430 (2022). https://doi.org/10.1002/htj.22457

[43] M.F. Endalew and S. Sarkar, "Incidences of aligned magnetic field on unsteady MHD flow past a parabolic accelerated inclined plate in a porous medium," Heat Transfer, **50**(6), 5865-5884 (2021). https://doi.org/10.1002/htj.22153

[44] K. Chamuah and N. Ahmed, "MHD flow past an impulsively started inclined plate with parabolic plate velocity in the presence of thermal diffusion and thermal radiation," **14**(3), 1-18 (2024). https://doi.org/10.33263/BRIAC143.060

[45] B.S. Goud, P. Srilatha and M.N.R. Shekar, "Study of hall current and radiation effects on MHD free convective flow past an inclined parabolic accelerated plate with variable temperature in a porous medium," Int. J. Mech. Eng. Technol. **9**(7), 1268-1276 (2018).

[46] D. Jose and A. Selvaraj, "Convective heat and mass transfer effects of rotation on parabolic flow past an accelerated isothermal vertical plate in the presence of chemical reaction of first order," JP Journal of Heat and Mass Transfer, **24**(1), 191-206 (2021). http://dx.doi.org/10.17654/HM024010191

[47] A. Shapiro and E. Fedorovich, "Unsteady convectively driven flow along a vertical plate immersed in a stably stratified fluid," Journal of Fluid Mechanics, **498**, 333-352 (2004). https://doi.org/10.1017/S0022112003006803

[48] E. Magyari, I. Pop and B. Keller, "Unsteady free convection along an infinite vertical flat plate embedded in a stably stratified fluid-saturated porous medium," Transport in porous media, **62**, 233-249 (2006). https://doi.org/10.1007/s11242-005-1292-6

[49] C.-Y. Cheng, "Double-diffusive natural convection along a vertical wavy truncated cone in non-newtonian fluid saturated porous media with thermal and mass stratification," International Communications in Heat and Mass Transfer, **35**(8), 985-990 (2008). https://doi.org/10.1016/j.icheatmasstransfer.2008.04.007

[50] C.-Y. Cheng, "Combined heat and mass transfer in natural convection flow from a vertical wavy surface in a power-law fluid saturated porous medium with thermal and mass stratification," International Communications in Heat and Mass Transfer, **36**(4), 351-356 (2009). https://doi.org/10.1016/j.icheatmasstransfer.2009.01.003

[51] H. Kumar and R.K. Deka, "Thermal and mass stratification effects on unsteady flow past an accelerated infinite vertical plate with variable temperature and exponential mass diffusion in porous medium," East European Journal of Physics, (4), 87-97 (2023). https://doi.org/10.26565/2312-4334-2023-4-09

[52] R.S. Nath and R.K. Deka, "Thermal and mass stratification effects on unsteady parabolic flow past an infinite vertical plate with exponential decaying temperature and variable mass diffusion in porous medium," ZAMM-Journal of Applied Mathematics and Mechanics/Zeitschrift für Angewandte Mathematik und Mechanik, **104**(6), e202300475 (2024). https://doi.org/10.1002/zamm.202300475

[53] D. Sahu and R.K. Deka, "Combined impacts of thermal and mass stratification on unsteady MHD parabolic flow along an infinite vertical plate with periodic temperature variation and variable mass diffusion," Heat Transfer, **54**(2), 1638-1649 (2025). https://doi.org/10.1002/htj.23240

[54] R.S. Nath and R.K. Deka, "Thermal and mass stratification effects on MHD nanofluid past an exponentially accelerated vertical plate through a porous medium with thermal radiation and heat source," International Journal of Modern Physics B, **39**(07), 2550045 (2025). https://doi.org/10.1142/S0217979225500456

[55] N. Ahmed, S. Sengupta and D. Datta, "An exact analysis for MHD free convection mass transfer flow past an oscillating plate embedded in a porous medium with Soret effect," Chemical Engineering Communications, **200**(4), 494-513 (2013). https://doi.org/10.1080/00986445.2012.709474

[56] M. Abramowitz and I.A. Stegun, *Handbook of mathematical functions: with formulas, graphs, and mathematical tables*, vol. 55, (Courier Corporation, 1965).

[57] R.B. Hetnarski, "An algorithm for generating some inverse laplace transforms of exponential form," Zeitschrift für angewandte Mathematik und Physik ZAMP, **26**(2), 249-253 (1975). https://doi.org/10.1007/BF01591514

ТЕПЛО- ТА МАСООБМІН У СТРАТИФІКОВАНІЙ МГД-ТЕЧІЇ ПІД ДІЄЮ ПОХИЛОГО МАГНІТНОГО ПОЛЯ

Мукул Медхі, **Рудра Канта Дека**

[a]Математичний факультет, Університет Гаухаті, Гувахаті-781014, Ассам, Індія

У цій роботі досліджується, як теплова та масова стратифікація впливають на нестаціонарний магнітогідродинамічний потік рідини через проникне середовище над похилою параболічною пластиною за наявності похилого магнітного поля. Метод перетворення Лапласа використовується для знаходження аналітичних контрольних рішень у замкнутій формі для рівнянь, що описують потік. У дослідженні порівнюються результати, отримані за допомогою теплової та масової стратифікації, зі сценаріями, де обидві форми стратифікації відсутні. Нестратифіковані випадки демонструють підвищені швидкості у порівнянні. Також наявність обох стратифікацій збільшує тертя поверхні на $33,42\%$, швидкість теплопередачі на $97,54\%$ та швидкість масопередачі на $36,91\%$. Найбільший вплив на потік рідини виникає, коли магнітне поле ортогональне до напрямку потоку. Висновки цього дослідження є актуальними для оптимізації гідродинаміки в інженерних та екологічних застосуваннях.

Ключові слова: *МГД; пористе середовище; параболічна похила пластина; термічна стратифікація; масова стратифікація; похиле магнітне поле*

EFFECTS OF RADIATION AND ABSORPTION ON THREE DIMENSIONAL MAGNETOHYDRODYNAMIC (MHD) UPPER-CONVECTED MAXWELL NANO-FLUID FLOW

G.P. Gifty[a], S.B. Padhi[a], B.K. Mahatha[b], G.K. Mahato[c]*

aDepartment of Mathematics, Centurion University of Technology and Management, Odisha, India
bRajkiyakrit +2 High School, Latbedhwa, Koderma, Jharkhand, India
cDepartment of Mathematics, Amity Institute of Applied Sciences, Amity University Jharkhand, Ranchi-835303, India
Corresponding Author E-mail: mahatogk@gmail.com
Received May 8, 2025; revised June 20, 2025 accepted July 3, 2025

The present paper deals with the study of the MHD upper-convected Maxwell nano-fluid flow through a bidirectional stretchable surface. The influence of heat absorption and thermal radiation has been studied. Governing non-linear partial differential equations, controlling the mass conservation, momentum conservation, energy conservation, and species concentration, are transformed into ordinary differential equations with the help of an appropriate similarity transformation, which are then solved numerically by using the bvp4c routine of MATLAB. The impact of various physical parameters on the velocity, temperature, and concentration distributions is described briefly with the help of graphs. The skin-friction, rate of heat and mass transfers at the plate are computed numerically and displayed through the table. able. Such a fluid flow problem may find applications in heat transfer mechanisms/devices.

Keywords: *Maxwell Nano-fluid; MHD; Heat absorption; Thermal radiation*
PACS: 47.11.-j, 47.10.ab, 02.30.Jr

List of Symbols (Nomenclature)

a, b:	dimensional constants	Rd:	thermal radiation parameter
B_0:	Magnetic field strength	Re_z:	Reynolds number
C:	Concentration of fluid	Sh_z:	Sherwood number
C:	stretching ratio parameter	T:	temperature of fluid
c_p:	Specific heat at constant pressure	Tw:	wall temperature
C_w:	concentration on wall	T_∞:	ambient temperature
C_∞:	ambient concentration	(u,v,w):	velocity components
D_B:	Brownian diffusion coefficient	α:	Thermal diffusivity
D_T:	Thermophoretic diffusion coefficient	λ:	fluid relaxation time
$f' g'$:	Non-dimensional velocity	v:	Kinetic viscosity coefficient
j_w:	mass flux	θ:	Non-dimensional temperature
K:	Thermal conductivity	σ:	Stefan- Boltzman constant
Le:	Lewis number	τ:	ratio of nanoparticle heat and base
M:	Magnetic parameter	η:	similarity variable
Nb:	Brownian diffusion coefficient (non-dimensional)	ρ:	density of fluid
Nt:	Thermophoretic diffusion coefficient (non-dimensional)	ϕ:	Non-dimensional concentration
Nu_z:	Nusselt number	θ_w:	temperature ratio parameter
Pr:	Prandtl number	Q_0:	Heat absorption coefficient
q_r:	Radiative heat flux	Q:	Heat absorption parameter
q_w:	surface heat flux		

1. INTRODUCTION

Maxwell Nanofluid is used in cooling and heating systems. It enhances the rate of heat transfer by 15%. It is used in chillers, heat pumps, energy recovery systems, pumps, fans and terminal units. In a Maxwell Nanofluid, submicron Aluminum Oxide particles are suspended in the base fluid. Sajid et al. [1] studied the "Darcy-Forchheimer flow of Maxwell Nanofluid flow with nonlinear thermal radiation and activation energy". Increasing the Deborah number leads to decrease in the velocity profile. When the thickness of the wall, Prandtl number and linear thermal radiation is increased then the Nusselt number also increases and decreases when the thermophoresis parameter, magnetic parameter, Lewis number and thermal conductivity is increased. Further it is observed that the Nusselt number increases when the temperature difference parameter, Deborah number, porosity parameter, reaction rate constant and fitted rate constant is increased then the Nusselt number also increases. Due to the presence of the Lorentz force there is a higher rate of collision of the molecules. The velocity profile seems to be going uphill as the magnetic parameter is increased. Bilal et al. [2] studied the "Maxwell Nanofluid flow individualities by way of rotating cone". Kumara et al. [3] studied the "numerical simulation of heat transport in Maxwell nanofluid flow over a stretching sheet considering magnetic dipole effect". In their investigation they kept the Prandtl number constant. For both the type of fluids the radial velocity profile kept decreasing as the ferromagnetic

interaction parameter was increasing while the surface drag force kept increasing. The rate of heat transfer increased as the scalar potential value increased. Thermal distribution is disrupted by increasing the thermal relaxation parameter. The rate of heat transfer is better in the Newtonian liquid compared to the Maxwell liquid when the magnetic value is increased. Biswas et al. [4] studied the "computational treatment of MHD Maxwell Nano fluid flow across a stretching sheet considering higher order chemical reaction and thermal radiation". The velocity of the nanofluid is enhanced by increasing its thermal buoyancy whereas the velocity of the nanofluid falls down due to the resistive force produced by magnetic field and the porosity. The Brownian motion and thermophoresis affect helps the nanoparticles to move about freely due to which the temperature is increased. In the convection mode the rate of heat transfer is enhanced by increasing the Nusselt number. The Lewis number increases as the solutal diffusivity decreases. Shuguang et al. [5] studied the "modelling and analysis of heat transfer in MHD stagnation point flow of Maxwell Nano fluid over a porous rotating disc". The radial velocity and the azimuthal velocity drop down as the Deborah number increased whereas the axial velocity hiked up. When the value of magnetic parameter was increasingly high, increased the viscosity of the fluid which in turn reduced the radial velocity remarkably. The centrifugal force leads to an increased tangential velocity and axial velocity when the thermal biot number value increases the temperature at the boundary layer increases. For higher values of Reynolds number, the concentration profile increased. As the Prandtl number, Brownian motion, thermophoresis effect and the thermal biot number values increased the Nusselt number profile decreased gradually. Adem and Chanie [6] studied the "inclined magnetic field on mixed convection Darcy-Forchheimer Maxwell Nano fluid flow over a permeable stretching sheet with variable thermal conductivity: The numerical approach". In the hot surface the mixed convection parameter increases when the fluid velocity is increased, while it is the opposite in case of the cold surface. There is a negative effect in the magnetic field parameter, inertia coefficient and the angle of inclination when the fluid velocity increases. The Prandtl number is directly proportional to the temperature and concentration profiles. When the activation energy increases the concentration profile also increases. As the radiation parameters steadily increases the temperature spikes up. Faizan et al. [7] studied the "bio convection Maxwell Nano fluid through Darcy-Forehheimer medium due to rotating disc in the presence of MHD". It has been observed the velocity across the radius and tangent increases whereas across the axis it tends to decrease when the magnetic parameter is increased. There is a fall in all the velocity when the Deborah number is increased. When the thermal biot number is increased the polymeric movement is enhanced. The motility of the microorganisms reduces as the bioconvective Lewis number increases. By increasing the Darcy-Forchheimer and Deborah number the skin friction coefficient is increased.

The heat transfer rate of nanofluid is greater due to greater thermal activities as compared to the ordinary base fluids. Rashid et al. [8] studied "the shape effects of nano size particles on magnetohydrodynamic Nano fluid flow and heat transfer over a stretching sheet with Entropy generation". They used Ag-water Nano fluid. Three differently shaped nano particles that is sphere, blade and lamina was used for the study. They used Prandtl number = 6.2 for the experiment. The laminar shaped Nano particles performed better than the other shaped particles in the temperature profile, heat transfer whereas the sphere-shaped Nano particle gave the least performance. Sadiq [9] studied "the heat transfer of a Nano liquid thin film over a stretching sheet with a surface temperature and internal heat generation". He used copper, Alumina and Titanium with water-based fluid. The temperature profile can be increased if the Nano particle volume fraction is increased. When the Nano particle volume parameter and unsteadiness parameter is increased there is a decline in the film thickness parameter. When the Nano particle volume fraction is increased the thermal boundary layer increases. Sarada et al. [10] studied "the effect of magnetohydrodynamics on heat transfer behavior of a non-Newtonian fluid flow over a stretching sheet under a local thermal non-equilibrium condition". They considered their study on Jeffrey and Oldroyd-B fluid. The heat transfer in the liquid and solid phase of both the fluid decreases as the thermophoresis parameter decreases. Qureshi [11] studied "the MHD driven Prandtl-Eyring hybrid nano fluid flow over a stretching sheet with thermal jump condition". He used the Engine oil as his base fluid and the nano particles copper and zirconium dioxide. The heat transfer rate is better when the hybrid nano fluid is used in comparison to the traditional nano fluid. When the size of the nano particles is increased the rate at which the heat is transferred is also increased. The thermal conductivity is better in the Prandtl-Eyring hybrid nano fluid. By increasing the thermal radiative flow, Reynolds number, magnetic field, Brinkman number and Size parameter the entropy of the system increases. Anusha et al. [12] studied "the MHD of nano fluid flow over a porous stretching / shrinking plate with mass transportation and Brinkman ratio". Copper and alumina Nano particles suspended in water as the base fluid was used to carry out the investigation. They found out that when the porosity parameter is increased the transverse velocity will decrease. A similar effect takes place even with the magnetic field. Abbas [13] studied "heat transfer enhancement of copper ethylene glycol based nano particle on radial stretching sheet." Differently shaped nano particle such as cylinder, platelet and sphere shape was used. The maximum flow was recorded when the platelet shaped copper nano particle was used. The minimum heat transfer occurred in the case of sphere-shaped particle. Rao and Deka [14] studied "the analysis of the MHD bi-convection flow of a hybrid nano fluid containing motile micro-organisms over a porous stretching sheet". They used water-based Nano-fluid having motile organisms and copper and alumina nano particles. The nano fluid having the motile micro-organisms showed a better result in heat transfer in comparison to the nano fluid without motile micro-organisms. When the magnetic field is increased there is an increase in the concentration of nano particles and microbes, also the temperature profile while the velocity profile decreases. Same is the effect of porosity parameter the velocity profile increases when the volume fraction of copper and alumina is increased.

When the energy is transferred through a space or medium in the form of waves or particles is called radiation. When the temperature between two sources is different radiation takes place. In the field of medical science radiation is used

for the diagnosis as well as the treatment for many diseases. It is also used in the system of communication etc. Shoaib et al. [15] studied "the numerical investigation for rotating flow of MHD hybrid nanofluid with thermal radiation over a stretching sheet". The velocity profile decreases and the temperature profile increases for higher values of magnetic parameter and rotation parameter. Both the velocity and temperature profiles increase when the Biot number and concentration of nanoparticles are increased. Higher values of magnetic parameter and concentration of the particle decrease the skin friction. Sreedevi et al. [16] studied "the heat and mass transfer analysis of unsteady hybrid nanofluid flow over a stretching sheet with thermal radiation". They have used carbon nanoparticles and silver nanoparticles combinedly and the base fluid considered is water. Fatunmbi et al. [17] studied the "entropy analysis of nonlinear radiative Casson nanofluid transport over an electromagnetic actuator with temperature dependent properties". As and when there is an appreciation in the magnitude of caption fluid perimeter viscosity variation parameter mass section term and nanoparticles concentration flux terms there is a shrinkage in the hydrodynamic boundary layer, thus decelerating the fluid flow. Increasing the Hartmann number and Richardson number accelerates the fluid flow. The temperature field soars high as the wall heating parameter, thermophoresis, thermal conductivity, Brownian movement, viscose dissipation shoots up. Whereas there is an opposite action by mass suction and Prandtl number parameter. Amplification of viscose dissipation and suction leads to hike in entropy generation parameter. It is lowered when the thermophoresis and Richardson numbers steps up. Yaseen et al. [18] studied "the system and opposing flow of MHD hybrid nanofluid flow past a permeable moving surface with heat source/ sink and thermal radiation". They have made their study on hybrid nanofluid (SiO_2 - MoS_2 / water). Hussain and Sheremet [19] studied "the convective analysis of the radioactive Nano fluid flow through porous media over a stretching surface with inclined magnetic field". The thermal profile is intensified as the nanoparticle concentration increases. The fluid velocity and magnitude of drag coefficient diminishes as the Hartmann's number rises. Jagdeesh et al. [20] studied "the convective heat and mass transfer rate on 3D Williams and nanofluid flow via linear stretching sheet with thermal radiation and heat absorption". When there is an upsurge in the magnetic parameter the velocity of the Williamson fluid is higher than that of Nano fluid. The skin friction coefficient is higher in the absence of Williamson parameter. The temperature is high in non-Newtonian fluid. Williamson fluid has higher fluid velocity in comparison to nanofluid motion due to the electrical conductivity.

Absorption is a process in which the substances get absorbed in the solid/liquid/gaseous phase. In the process of absorption, the Nernst distribution law is used. Gopal et al. [21] studied "the impact of thermal stratification and heat generation /absorption on MHD Carreau nanofluid flow over a permeable cylinder". They found out that the curvature parameters led to more friction. Krishna et al. [22] studied "the radiation absorption on MHD convective flow of nanofluids through vertically travelling absorbent plate". They used Al_2O_3-water based and TiO_2-water based nanofluid for their study. The radiation absorption parameter when increased, there is also an increase in the temperature and velocity. The radiation parameter works like a catalyst for the velocity profile. Nemati et al. [23] studied "the MHD natural convection in a cavity with different geometrics filled with a nanofluid in the presence of heat generation/absorption using lattice Boltzmann method". They used Cu-water based nanofluid for their study in a which the particles are shaped as diagonal, smooth and curve. Dahab et al. [24] studied "the double diffusive peristaltic MHD Sisko nanofluid flow through a porous medium in presence of non-linear thermal radiation, heat generation/ absorption and Joule heating". The velocity about the axis first increased and then gradually decreased when the magnetic parameter, heat Grashof number, Darcy number, Nano particle Grashof number, rotation and solutal Grashof number increased. The solutal Grashof number, heat Grashof number nano particle Grashof number, all these parameters, when increased led the pressure gradient distribution to rise then fall after a while. When the non-linear thermal radiation and the temperature ratio parameters are increased, the distribution of the temperature declines gradually. Asghar et al. [25] studied "the magnetized mixed convection hybrid nanofluid with effect of heat generation/ absorption and velocity slip condition". They found out that when the volume fraction of the solute was high, the rate of heat transfer increased also helping in the separation of the boundary layer. Mahmood et al. [26] studied "the numerical analysis of MHD tri- hybrid nanofluid over a non-linear stretching/ shrinking sheet with heat generation /absorption and slip conditions". In their investigation they found that the tri -hybrid nanofluid showed up the best result and the conventional nanofluid showed the least result when compared for the profiles, Nusselt number, velocity, skin friction and temperature. When the volume fraction was increased all the three types of fluid showed an increasing graph for the velocity profile as well as the temperature profile. The rate of heat transfer soar high as the suction parameter was increased. The velocity increased and the temperature decreased for all the three types of fluid when the stretching parameter was increased. Muzammal et al. [27] studied "the transportation of melting heat in stratified Jeffrey fluid flow with heat generation and magnetic field". In their findings they got to know that for higher values of Deborah number, velocity profile and the temperature profile increased. As the stratified parameter increased the temperature profile showed a downhill curve. Also, the temperature of the fluid kept falling when the melting parameter rose high. But higher Eckert number helped to increase the temperature of the fluid. Many researchers [28-32] have contributed in this area of research.

Going through the above cited articles, authors are motivated to investigate the effects of nonlinear thermal radiation and heat absorption on three dimensional MHD upper-convected Maxwell nano-fluid flow past a bidirectional stretching surface. Governing equations are solved, numerically, by using bvp4c routine of MATLAB. The influence of key physical parameters on velocity, temperature, and concentration profiles is analyzed and illustrated through graphical results. Additionally, numerical values for the Nusselt number, and Sherwood number are computed and presented in tabular

form. This investigation is relevant to various engineering applications involving heat and mass transfer processes in complex fluids.

2. MATHEMATICAL MODEL

A steady state, viscous, incompressible, upper-convected Maxwell nano-fluid flow through a bilinear stretchable surface parallel to $xy-$ plane is considered for the study. A uniform magnetic field of strength B_0 is applied normal to the surface i.e. parallel to z-direction. Furthermore, nonlinear thermal radiation and heat absorption are incorporated into the formulation of the energy equation. The stretching surface velocities in the x and y - directions are defined as $U_w(x) = ax$ and $V_w(Y) = by$, respectively, as illustrated in Fig. 1.
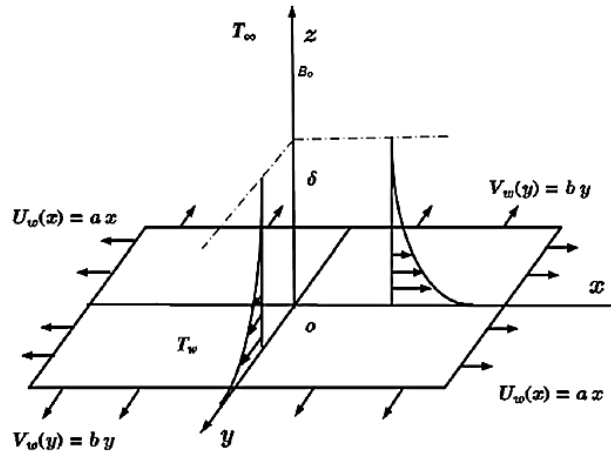
Figure 1. Schematic diagram of the physical configuration

The governing equations for velocity, temperature, and nanoparticle concentration in the described problem are given as follows [33–36]:

Based on the assumptions aforementioned, equations governing to the present problem are:

$$\frac{\partial u}{\partial x} + \frac{\partial v}{\partial y} + \frac{\partial w}{\partial z} = 0 \tag{1}$$

$$u\frac{\partial u}{\partial x} + v\frac{\partial u}{\partial y} + w\frac{\partial u}{\partial z} + \lambda\left(u^2\frac{\partial u^2}{\partial x^2} + v^2\frac{\partial u^2}{\partial y^2} + w^2\frac{\partial u^2}{\partial z^2} + 2uv\frac{\partial^2 u}{\partial x\partial y} + 2uw\frac{\partial^2 u}{\partial x\partial z} + 2vw\frac{\partial^2 u}{\partial y\partial z}\right)$$
$$= \upsilon\frac{\partial^2 u}{\partial z^2} - \frac{\sigma B_0^{\,2}}{\rho}\left(u + \lambda w\frac{\partial u}{\partial z}\right) \tag{2}$$

$$u\frac{\partial v}{\partial x} + v\frac{\partial v}{\partial y} + w\frac{\partial v}{\partial z} + \lambda\left(u^2\frac{\partial v^2}{\partial x^2} + v^2\frac{\partial v^2}{\partial y^2} + w^2\frac{\partial v^2}{\partial z^2} + 2uv\frac{\partial^2 v}{\partial x\partial y} + 2uw\frac{\partial^2 v}{\partial x\partial z} + 2vw\frac{\partial^2 v}{\partial y\partial z}\right)$$
$$= \upsilon\frac{\partial^2 v}{\partial z^2} - \frac{\sigma B_0^{\,2}}{\rho}\left(v + \lambda w\frac{\partial v}{\partial z}\right) \tag{3}$$

$$u\frac{\partial T}{\partial x} + v\frac{\partial T}{\partial y} + w\frac{\partial T}{\partial z} = \alpha\frac{\partial^2 T}{\partial z^2} - \frac{1}{\rho c_p}\frac{\partial q_r}{\partial z} + \tau\left(D_B\frac{\partial C}{\partial z}\frac{\partial T}{\partial z} + \frac{D_T}{T_\infty}\left(\frac{\partial T}{\partial z}\right)^2\right) + \frac{Q_0}{\rho c_p}\left(T - T_\infty\right) \tag{4}$$

$$u\frac{\partial C}{\partial x} + v\frac{\partial C}{\partial y} + w\frac{\partial C}{\partial z} = D_B\frac{\partial^2 C}{\partial z^2} + \frac{D_T}{T_\infty}\frac{\partial^2 T}{\partial z^2} \tag{5}$$

The following boundary conditions regulate the current circumstance:

$$\left.\begin{array}{l} u = U_w = ax,\ v = V_w = by,\ w = 0,\ T = T_\infty,\ C = C_w, \quad \text{at } z = 0 \\ u, v \to 0,\ T \to T_\infty,\ C \to C_\infty, \qquad \text{as } z \to \infty \end{array}\right\} \tag{6}$$

where symbols have their usual meaning (see "List of Symbols").

Introducing similarity and dimensionless variables as follows:

$$q_r = -\frac{4\sigma^*}{3k^*}\frac{\partial T^4}{\partial z}, \quad u = axf'(\eta), \quad v = ayg'(\eta), \quad w = -\sqrt{a\upsilon}\left(f(\eta)+g(\eta)\right)$$

$$\theta(\eta) = \frac{T-T_\infty}{T_w-T_\infty}, \quad \phi(\eta) = \frac{C-C_\infty}{C_w-C_\infty}, \quad \eta = \sqrt{\frac{a}{\upsilon}}z, \quad T = T_\infty\left((\theta_w-1)\theta+1\right)$$

$$q_r = -\frac{16\sigma^*}{3k^*}T_\infty^{\ 3}\left((\theta_w-1)\theta+1\right)^3\frac{\partial T}{\partial z} \tag{7}$$

Using equation (7), the mass conservation (1) is satisfied. Also, together with the B.Cs. (6), governing equations (2), (3), (4) and (5) assume the form:

$$f''' - f'^2 + \left(M^2K+1\right)(f+g)f'' + K\left(2f'(f+g)f'' - (f+g)^2 f'''\right) - M^2 f' = 0 \tag{8}$$

$$g''' - g'^2 + \left(M^2K+1\right)(f+g)g'' + K\left(2g'(f+g)g'' - (f+g)^2 g'''\right) - M^2 g' = 0 \tag{9}$$

$$\theta'' + \left(\tfrac{4}{3}\right)Rd\left[\left(1+(\theta_w-1)\theta\right)^3\theta'' + 3(\theta_w-1)\left(1+(\theta_w-1)\theta\right)^2\theta'^2\right] + \Pr(f+g)\theta' + \Pr Nt\theta'^2 + Q\Pr\theta + \Pr Nb\theta'\phi' = 0 \tag{10}$$

$$\phi'' + \frac{Nt}{Nb}\theta'' + \Pr Le(f+g)\phi' = 0 \tag{11}$$

$$f(0) = 0, \quad f'(0) = 1, \quad g(0) = 0, \quad g'(0) = c, \quad \theta(0) = 1, \quad \phi(0) = 1,$$

$$f'(\infty) = 0, \quad g'(\infty) = 0, \quad \theta(\infty) = 0, \quad \phi(\infty) = 0 \tag{12}$$

Non-dimension parameters are defined as

$$\left.\begin{array}{l} K = \lambda a, \; M^2 = \dfrac{\sigma B_0^{\ 2}}{\rho a}, \; \Pr = \dfrac{\upsilon}{\alpha} = \dfrac{\rho c_p\upsilon}{k}, \; Rd = \dfrac{4\sigma^* T_\infty^{\ 3}}{kk^*}, \; \theta_w = \dfrac{T_w}{T_\infty}, \; Q = \dfrac{Q_0}{a\rho c_p} \\[3mm] Nb = \dfrac{\tau D_B}{\upsilon}\left(C_w-C_\infty\right), \; Nt = \dfrac{D_T}{T_\infty}\dfrac{\tau}{\upsilon}\left(T_w-T_\infty\right), \; Le = \dfrac{\alpha}{D_B}, \; c = \dfrac{b}{a}, \; k = \alpha\rho c_p \end{array}\right\} \tag{13}$$

The most important physical quantities for the problem in engineering point of view are the local Nusselt and Sherwood numbers, which are defined by the following relations:

$$Nu_z = \frac{xq_w}{k\left(T_w-T_\infty\right)}, \qquad Sh_z = \frac{xj_w}{D_B\left(C_w-C_\infty\right)} \tag{14}$$

where, heat and mass fluxes are defined by

$$q_w = -\left(\frac{\partial T}{\partial z}\right)_{z=0}, \qquad j_w = -D_B\left(\frac{\partial C}{\partial z}\right)_{z=0} \tag{15}$$

Thus the non-dimensional Local Nusselt and Sherwood numbers are as follows:

$$\mathrm{Re}_z^{-\frac{1}{2}} Nu_z = -\left[1+\tfrac{4}{3}Rd\theta_w^3\right]\theta'(0), \; \mathrm{Re}_z^{-\frac{1}{2}} Sh_z = -\phi'(0) \tag{16}$$

In equations (8) - (16), symbols have their usual meaning (see "List of Symbols").

3. RESULTS AND DISCUSSION

Non-linear ordinary differential equations are found from the controlling non-linear partial differential equations (1) - (5) with the help of suitable similarity transformation. These equations (8) - (11) together with boundary conditions (12) are solved, numerically, through MATLAB's bvp4c routine.

To gain some physical insight into the flow pattern, the effects of different physical parameters on the velocity ($f'(\eta)$), temperature ($\theta(\eta)$) and nanoparticle concentration ($\phi(\eta)$) profiles have been plotted in the form of graphs (Figures 2 - 28). Figures 2-8 display the effects of various physical parameters on the fluid velocity. It is observed from the Figs. 2-8 that the profiles of fluid velocity are getting increased on increasing thermophoresis parameter, thermal radiation parameter and Lewis number. These concludes that the thermal radiation parameter, thermophoretic diffusion and Lewis number have the tendency to enhance the fluid velocity at the vicinity of the plate. It is also observed that fluid velocity is getting decreased on increasing the Deborah number, magnetic parameter, stretching ratio parameter and Prandtl number. As we know, increase in Deborah number increases viscosity of the fluid and hence the velocity decreases

as shown in Fig. 2. This indicates that the fluid relaxation time, magnetic field, stretching ratio have the tendency to retard the fluid velocity. Since we know that Prandtl number represents the strength of thermal diffusion, on increasing Prandtl number the strength of thermal diffusion is getting reduced and vice-versa. Hence, we can conclude that the thermal diffusion has the tendency to enhance the fluid velocity.

Figures 9 to 18 explain the temperature profiles of the nano-fluid and the influence of flow parameters. It is clearly seen from Figs. 9-18 that with the increase in K, M, Rd, θ_w, Nt, Nb and Q the fluid temperature is getting increased while the fluid temperature is getting decreased on increasing C, Pr and Le. This shows that the Deborah number, magnetic field, thermal radiation, temperature ratio, thermophoretic diffusion, Brownian diffusion, thermal diffusion and heat absorption are the cause for rise in fluid temperature whereas stretching ratio and Lewis number are the cause for fall in fluid temperature. By increasing the magnetic parameter M, a drag force known as Lorentz force also increases which resultantly reduces the velocity of fluid (Fig. 3) and hence rate of heat transfer is reduced (Table - 1) and this leads to an increment in temperature (Fig. 10).

Figures 19 to 28 illustrate the impact of various flow parameters on species concentration. It is evident from Figs. 19-28 that with the increase in K, M, Rd, θ_w and Q there is an increment in the concentration profile, where there is a decrement in the concentration profile with the increase in C, Nt, Nb, Pr and Le. This signifies that the Deborah number, magnetic field, Radiation temperature ratio, heat absorption and thermal diffusion have the tendency to accelerate the concentration of the fluid while stretching ratio, thermophoretic diffusion and Lewis number have opposite effect on this.
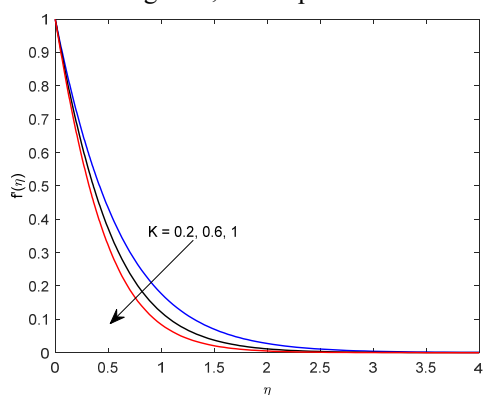
Figure 2. Velocity profiles for K
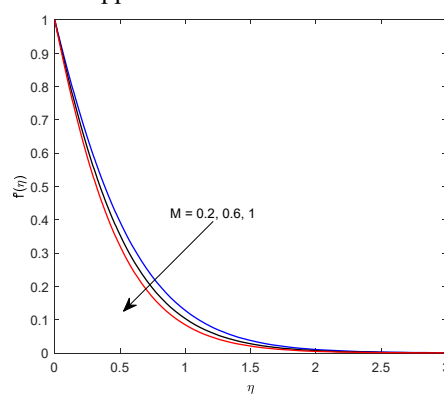
Figure 3. Velocity profiles for M
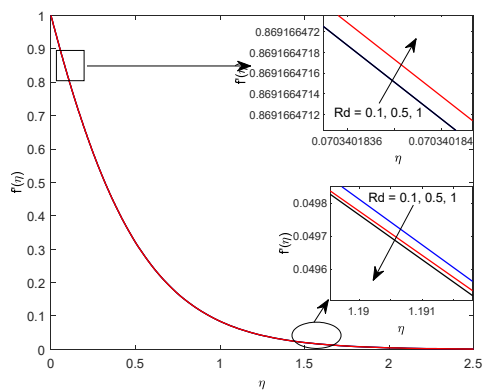
Figure 4. Velocity profiles for Rd
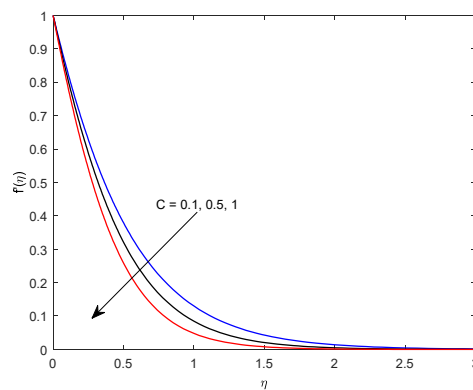
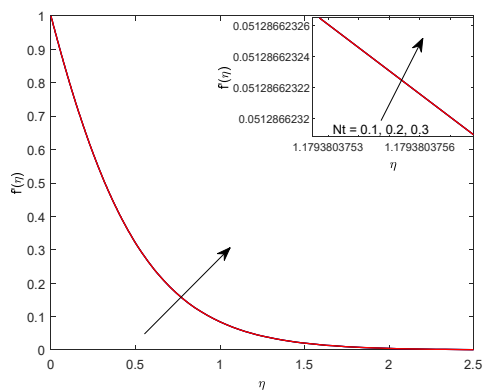**Figure 5.** Velocity profiles for c

Figure 6. Velocity profiles for Nt
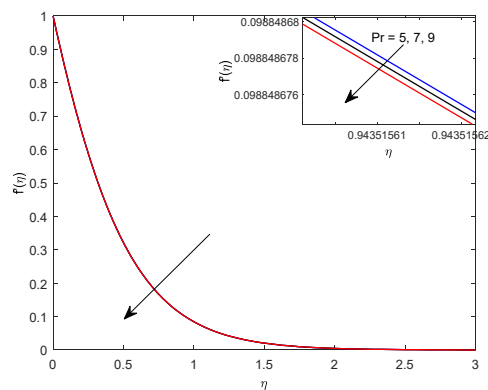

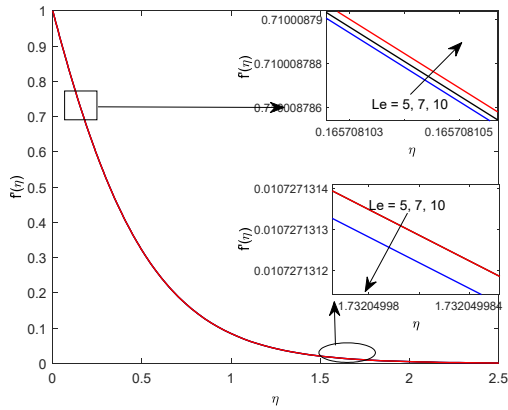**Figure 7.** Velocity profiles for Pr

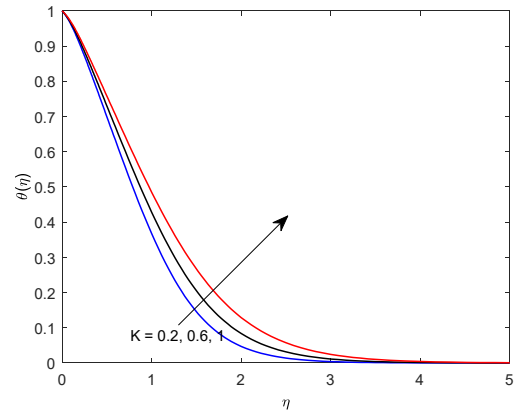**Figure 8.** Velocity profiles for *Le*

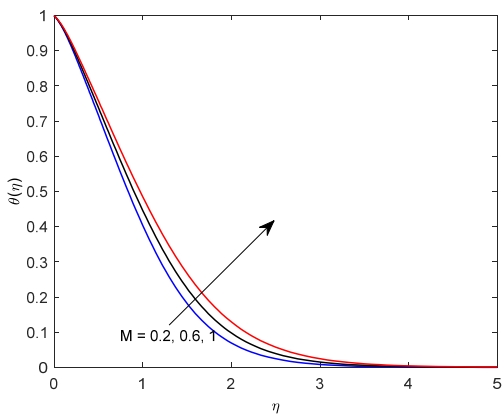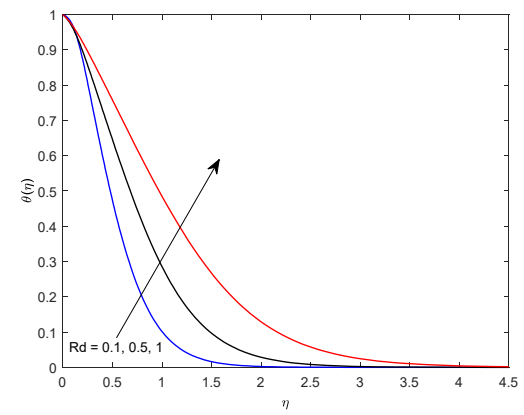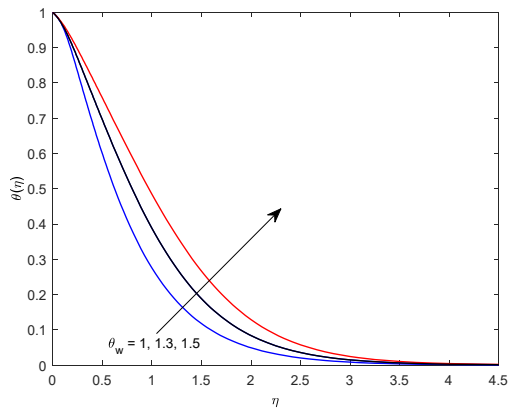**Figure 9.** Temperature profiles for K

Figure 10. Temperature profiles for M

Figure 11. Temperature profiles for Rd

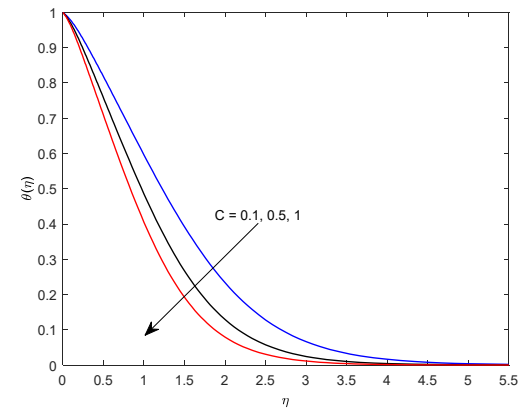**Figure 12.** Temperature profiles for θ_w

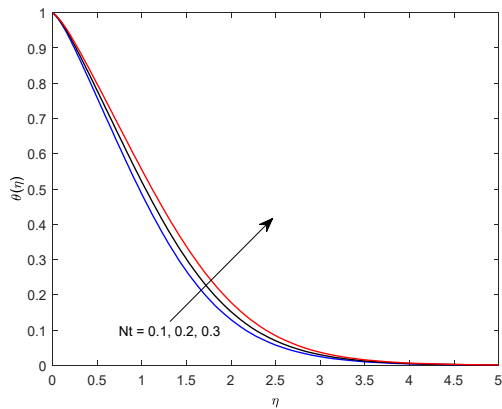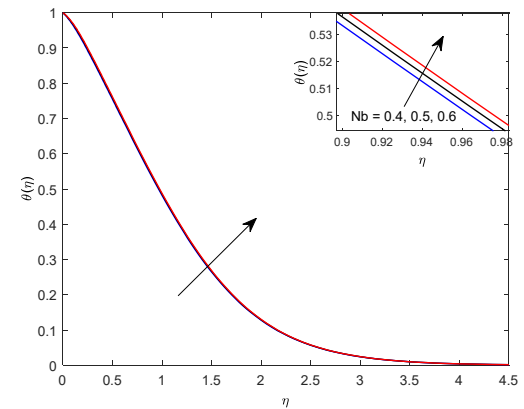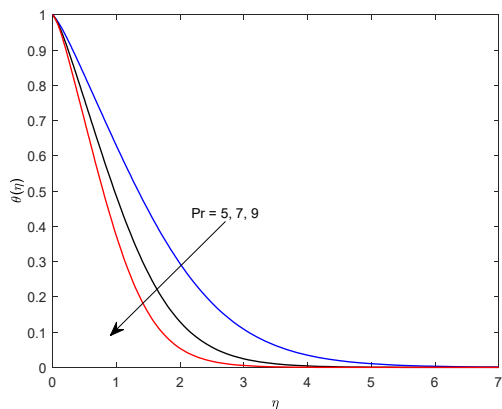**Figure 13.** Temperature profiles for C

Figure 14. Temperature profiles for Nt

Figure 15. Temperature profiles for Nb

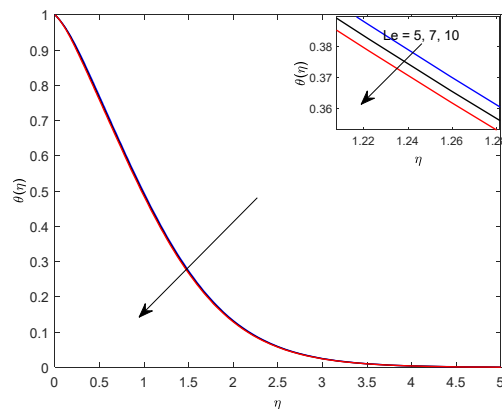**Figure 16.** Temperature profiles for Pr

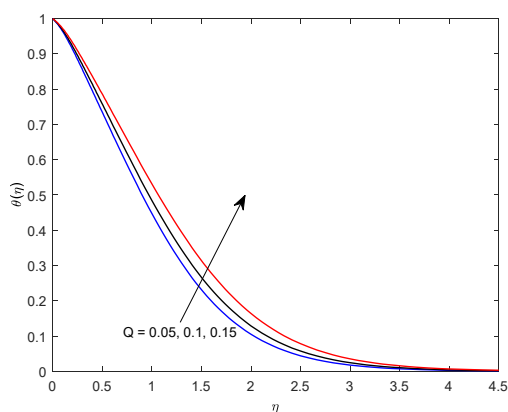**Figure 17.** Temperature profiles for Le

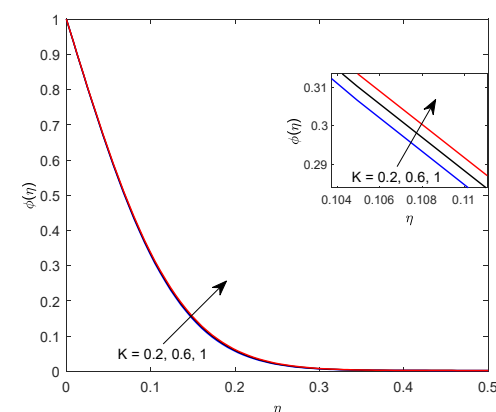**Figure 18.** Temperature profiles for Q

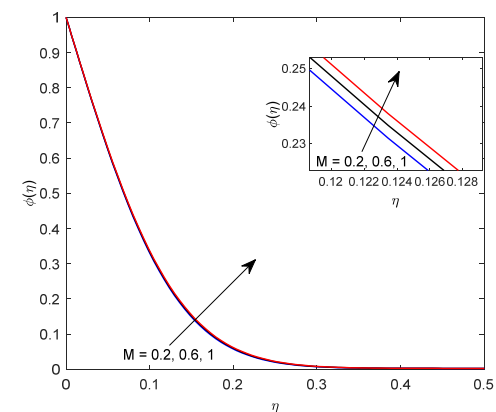**Figure 19.** Concentration profiles for K

Figure 20. Concentration profiles for M

Figure 21. Concentration profiles for Rd

Figure 22. Concentration profiles for θ_w
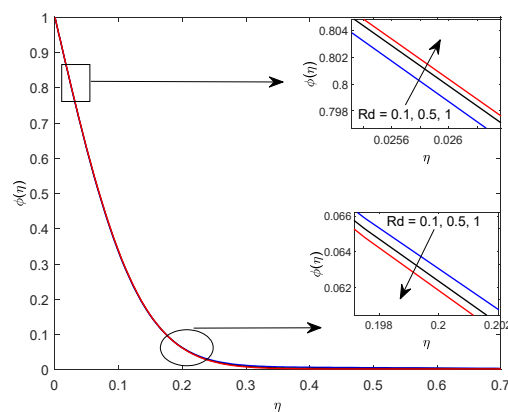
Figure 23. Concentration profiles for C

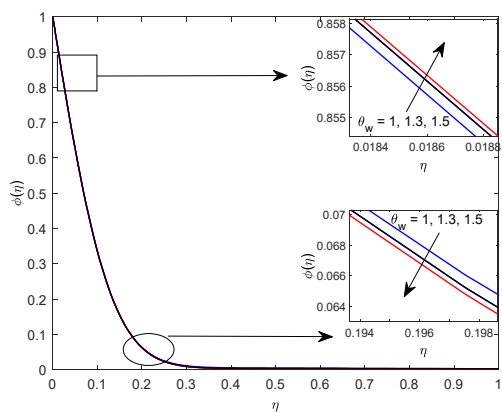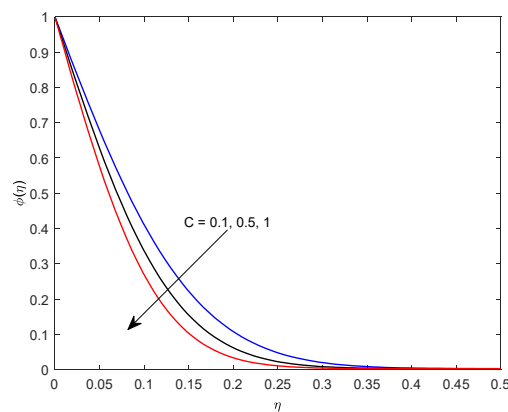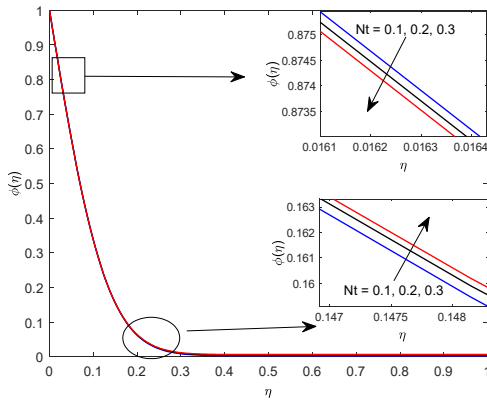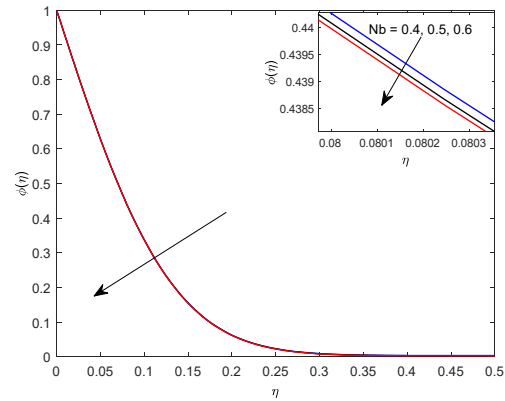**Figure 24.** Concentration profiles for *Nt*

Figure 25. Concentration profiles for Nb
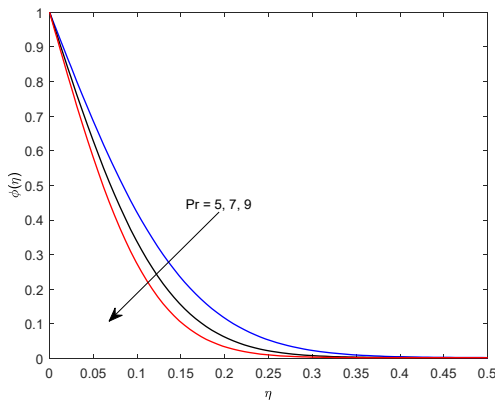

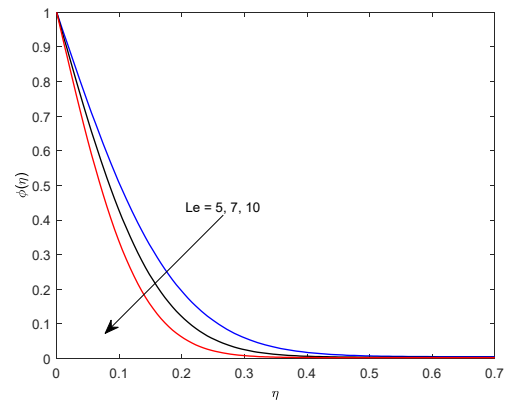**Figure 26.** Concentration profiles for Pr
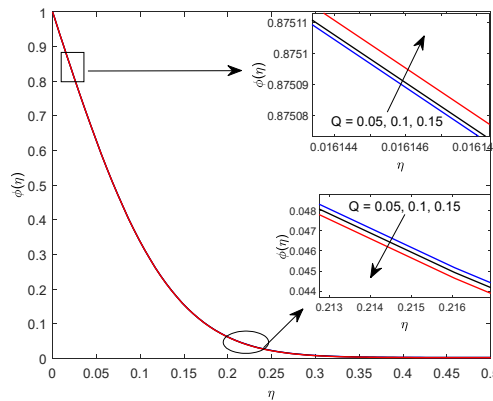

Figure 27. Concentration profiles for *Le*

Figure 28. Concentration profiles for *Q*

To visualize the effects of various physical entities on the rate of heat transfer and rate of mass transfer, a numerical result has been displayed in a tabular form in Table 1. It is noticed from Table 1 that the rate of heat transfer at the surface is getting enhanced by thermal radiation parameter, temperature ratio, stretching ratio and Lewis number, while it is getting reduced by the fluid relaxation time, magnetic field, thermophoretic diffusion, Brownian diffusion, thermal diffusion and heat absorption. It is also visualized from the table 1 that stretching ratio, thermophoretic diffusion, Brownian diffusion and Lewis number are the inducive agent for the rate of mass transfer at the surface while fluid relaxation time, magnetic field, thermal radiation, temperature ratio, thermal diffusion and heat absorption serve as a reducing agent for the rate of mass transfer at the surface.

Table 1. Numerical values of the Nusselt number and Sherwood number against different values of flow parameters

K	M	Rd	θ_w	c	Nt	Nb	Pr	Le	Q	$\mathrm{Re}_z^{-1/2} Nu_z$	$\mathrm{Re}_z^{-1/2} Sh_z$
0.2										1.66974664	7.86824129
0.6										1.50948141	7.81943062
1										1.35790927	7.77406945
	0.2									1.57854902	7.86103299

K	M	Rd	θ_w	c	Nt	Nb	Pr	Le	Q	$\mathrm{Re}_z^{-1/2} Nu_z$	$\mathrm{Re}_z^{-1/2} Sh_z$
	0.6									1.46355607	7.81540597
	1									1.35790927	7.77406945
		0.1								0.14818961	7.84184626
		0.5								0.77939	7.79639224
		1								1.35790927	7.77406945
			1							0.49470041	7.81019105
			1.3							1.00056998	7.78539034
			1.5							1.35790927	7.77406945
				0.1						1.01893114	6.63511542
				0.5						1.35790927	7.77406945
				1						1.63307299	8.97380238
					0.1					1.35790927	7.77406945
					0.2					1.22993982	7.78864098
					0.3					1.11422449	7.8013766
						0.4				1.54494505	7.77329499
						0.5				1.35790927	7.77406945
						0.6				1.19313544	7.77410782
							5			1.17361175	6.49367177
							7			1.35790927	7.77406945
							9			1.38784655	8.88283191
								5		1.35594007	5.36581493
								7		1.35686267	6.43219245
								10		1.35790927	7.77406945
									0.05	1.53680377	7.77435377
									0.1	1.35790927	7.77406945
									0.15	1.14720189	7.7735382

4. CONCLUSIONS

A detailed study has been carried out on steady state, viscous, incompressible, upper-convected Maxwell nano-fluid flow through a bilinear stretchable surface considering the effects of nonlinear thermal radiation and heat absorption. The significant results are summarized as follows:

- "Non-linear thermal radiation, thermophoretic diffusion, thermal diffusion and Lewis number are acting as an inducive agent for fluid velocity near the plate while fluid relaxation time, magnetic field, stretching ratio are acting as a reducing agent for the same".

- "Deborah number, magnetic field, thermal radiation, temperature ratio, thermophoretic diffusion, Brownian diffusion, thermal diffusion and heat absorption are the cause for rise in fluid temperature whereas stretching ratio and Lewis number are the cause for fall in fluid temperature".

- "The Deborah number, magnetic field, radiation, temperature ratio, heat absorption and thermal diffusion have the tendency to accelerate the concentration of the fluid while stretching ratio, thermophoretic diffusion and Lewis number have opposite effect on this".

- "Rate of heat transfer at the surface is getting enhanced by thermal radiation parameter, temperature ratio, stretching ratio and Lewis number, while it is getting reduced by the fluid relaxation time, magnetic field, thermophoretic diffusion, Brownian diffusion, thermal diffusion and heat absorption."

- "Stretching ratio, thermophoretic diffusion, Brownian diffusion and Lewis number are the inducive agent for the rate of mass transfer at the surface while fluid relaxation time, magnetic field, thermal radiation, temperature ratio, thermal diffusion and heat absorption serve as a reducing agent for the rate of mass transfer at the surface".

ORCID

G.P. Gifty, https://orcid.org/0009-0006-6803-9560; **S.B. Padhi,** https://orcid.org/0000-0001-9610-918X
B.K. Mahatha, https://orcid.org/0000-0001-9110-1445; **G.K. Mahato,** https://orcid.org/0000-0003-4549-0042

REFERENCES
[1] T. Sajid, M. Sagheer, S. Hussain and M. Bilal, "Darcy-Forchheimer flow of Maxwell nanofluid flow with nonlinear thermal radiation and activation energy," AIP Advances 8, 035102 (2018). https://doi.org/10.1063/1.5019218
[2] S. Bilal, K. Ur Rehman, Z. Mustafa and M.Y. Malik, "Maxwell Nanofluid Flow Individualities by Way of Rotating Cone," Journal of Nanofluids, **8**, 596–603 (2019). https://doi:10.1166/jon.2019.1607
[3] B.C. Prasannakumara, "Numerical simulation of heat transport in Maxwell nanofluid flow over a stretching sheet considering magnetic dipole effect," Partial Differential Equations in Applied Mathematics, **4**, 100064 (2021). https://doi.org/10.1016/j.padiff.2021.100064
[4] R. Biswasa, Md.S. Hossain, R. Islam, S.F. Ahmmed, S.R. Mishra and M. Afikuzzaman, "Computational treatment of MHD Maxwell nanofluid flow across a stretching sheet considering higher-order chemical reaction and thermal radiation," Journal of Computational Mathematics and Data Science, **4**, 2772-4158 (2022). https://doi.org/10.1016/j.jcmds.2022.100048

[5] S. Li, M. Faizan, F. Ali, G. Ramasekhar, T. Muhammad, H. Abd El-Wahed Khalifa and Z. Ahmad, "Modelling and analysis of heat transfer in MHD stagnation point flow of Maxwell nanofluid over a porous rotating disk," Alexandria Engineering Journal, **91**, 237-248 (2024). https://doi.org/10.1016/j.aej.2024.02.002

[6] G.A. Adem and A.G. Chanie, "Inclined Magnetic Field on Mixed Convection Darcy Forchheimer Maxwell Nanofluid Flow Over a Permeable Stretching Sheet With Variable Thermal Conductivity: The Numerical Approach," Journal of Applied Mathematics, (2024). https://doi.org/10.1155/2024/6750201

[7] M. Faizan, *et al.*, "Bio-convection Maxwell nanofluid through Darcy Forchheimer medium due to rotating disc in the presence of MHD," Ain Shams Engineering Journal, **15**(10), 102959 (2024). https://doi.org/10.1016/j.asej.2024.102959

[8] Rashid, Umair., Dumitru Baleanu, Azhar Iqbal and Muhammd Abbas, "Shape Effect of Nano-size Particles on Magnetohydrodynamic Nanofluid Flow and Heat Transfer over a Stretching Sheet with Entropy Generation," Entropy, **22**(10), 1171 (2020). https://doi.org/10.3390/e22101171

[9] M.A. Sadiq, "Heat transfer of a nano-liquid thin film over a stretching sheet with surface temperature and internal heat generation," J. Therm. Anal. Calorim. **143**, 2075–2083 (2021). https://doi.org/10.1007/s10973-020-09614-x

[10] K. Sarada, R.J.P. Gowda, I.E. Sarris, R.N. Kumar and B.C. Prasannakumara, "Effect of Magnetohydrodynamics on Heat Transfer Behaviour of a Non-Newtonian Fluid Flow over a Stretching Sheet under Local Thermal Non-Equilibrium Condition," Fluids, **6**(8), 264 (2021). https://doi.org/10.3390/fluids6080264

[11] M.A. Qureshi, "A case study of MHD driven Prandtl-Eyring hybrid nanofluid flow over a stretching sheet with thermal jump conditions," Case Studies in Thermal Engineering, **28**, 101581 (2021). https://doi.org/10.1016/j.csite.2021.101581

[12] T. Anusha, U.S. Mahabaleshwar and Y. Sheikhnejad, "An MHD of Nano-fluid Flow Over a Porous Stretching/ Shrinking Plate with Mass Transpiration and Brinkman Ratio," Transp. Porous. Med. **142**, 333–352 (2022). https://doi.org/10.1007/s11242-021-01695-y

[13] A. Iqbal, and T. Abbas, "A study on heat transfer enhancement of Copper (Cu)-Ethylene glycol based nanoparticle on radial stretching sheet," Alexandria Engineering Journal, **71**, 13-20 (2023). https://doi.org/10.1016/j.aej.2023.03.025

[14] S. Rao, and P.N. Deka, "Analysis of MHD Bioconvection Flow of a Hybrid Nanofuid Containing Motile Microorganisms over a Porous Stretching Sheet," BioNanoScience, **13**, 2134–2150 (2023). https://doi.org/10.1007/s12668-023-01180-4

[15] M. Shoaib, M.A.Z. Raja, M.T. Sabir, S. Islam, Z. Shah, P. Kumam and H. Alrabaiah, "Numerical investigation for rotating flow of MHD hybrid nanofluid with thermal radiation over a stretching sheet," Sci. Rep. **10**, 18533 (2020). https://doi.org/10.1038/s41598-020-75254-8

[16] P. Sreedevi, P.S. Reddy and A. Chamkha, "Heat and mass transfer analysis of unsteady hybrid nanofluid flow over a stretching sheet with thermal radiation," SN Appl. Sci. **2**, 1222, (2020). https://doi.org/10.1007/s42452-020-3011-x

[17] E.O. Fatunmbi, A.T. Adeosun and S.O. Salawu, "Entropy analysis of nonlinear radiative Casson nanofluid transport over an electromagnetic actuator with temperature-dependent properties," Partial Differential Equations in Applied Mathematics, **4**, 100152 (2021). https://doi.org/10.1016/j.padiff.2021.100152

[18] M. Yaseen, M. Kumar and S.K. Rawat, "Assisting and opposing flow of a MHD hybrid nano fluid flow past a permeable moving surface with heat source/sink and thermal radiation," Partial Differential Equations in Applied Mathematics, **4**, 100168 (2021). https://doi.org/10.1016/j.padiff.2021.100168

[19] M. Hussain and M. Sheremet, "Convection analysis of the radiative nanofluid flow through porous media over a stretching surface with inclined magnetic field," International Communications in Heat and Mass Transfer, **140**, 106559 (2023). https://doi.org/10.1016/j.icheatmasstransfer.2022.106559

[20] S. Jagadeesh, M.C.K. Reddy, N. Tarakaramu, H.Ahmad, S. Askar and S.S. Abdullaev, "Convective heat and mass transfer rate on 3D Williamson nanofluid f low via linear stretching sheet with thermal radiation and heat absorption," Sci. Rep. **13**, 9889 (2023). https://doi.org/10.1038/s41598-023-36836-4

[21] D. Gopal, S.H.S. Naik, N. Kishan and C.S.K. Raju, "The impact of thermal stratification and heat generation/absorption on MHD Carreau nano fluid flow over a permeable cylinder," SN Appl. Sci. **2**, 639 (2020). https://doi.org/10.1007/s42452-020-2445-5

[22] M.V. Krishna, N.A. Ahamadb and A.J. Chamkha, "Radiation absorption on MHD convective flow of nanofluids through vertically travelling absorbent plate, Ain Shams Engineering Journal, **12**(3), 3043-3056 (2021). https://doi.org/10.1016/j.asej.2020.10.028

[23] M. Nemati, H.M. Sani, R. Jahangiri and A.J. Chamkha, "MHD natural convection in a cavity with different geometries filled with a nanofluid in the presence of heat generation/absorption using lattice Boltzmann method," J. Therm. Anal. Calorim. **147**, 9067-9081 (2022). https://doi.org/10.1007/s10973-022-11204-y

[24] S.M. Abo-Dahab, R.A. Mohamed, A.M.A. Alla and M.S. Soliman, "Double diffusive peristaltic MHD Sisko nanofluid flow through a porous medium in presence of non linear thermal radiation, heat generation/ absorption, and Joule heating," Sci. Rep. **13**, 1432 (2023). https://doi.org/10.1038/s41598-023-27818-7

[25] A. Asghar, A.F. Chandio, Z. Shah, N.a Vrinceanu, W. Deebani, M. Shutaywi and L.A. Lund, "Magnetized mixed convection hybrid nanofluid with effect of heat generation/absorption and velocity slip condition," Heliyon, **9**, 2e13189 (2023). https://doi.org/10.1016/j.heliyon.2023.e13189

[26] M. Zafar, S.M. Eldin, K. Rafique and U. Khana, "Numerical analysis of MHD tri-hybrid nanofluid over a non-linear stretching/shrinking sheet with heat generation/absorption and slip conditions," Alexandria Engineering Journal, **76**, 799-819 (2023). https://doi.org/10.1016/j.aej.2023.06.081

[27] M. Muzammal, M. Farooq, Hashim and H. Alotaibim "Transportation of melting heat in stratified Jeffrey fluid flow with heat generation and magnetic field," Case Studies in Thermal Engineering, **58**, 104465 (2022). https://doi.org/10.1016/j.csite.2024.104465

[28] B.K. Mahatha, R. Nandkeolyar, G.K. Mahato and P. Sibanda, "Dissipative Effects in Hydromagnetic Boundary Layer Nanofluid Flow Past A Stretching Sheet with Newtonian Heating," Journal of Applied Fluid Mechanics, **9**(4), 1977-1989 (2016). https://doi.org/10.18869/acadpub.jafm.68.235.24451

[29] R. Nandkeolyar, B.K. Mahatha, G.K. Mahato and P. Sibanda, "Effect of Chemical Reaction and Heat Absorption on MHD Nanoliquid Flow Past a Stretching Sheet in the Presence of a Transverse Magnetic Field." Magnetochemistry, **4**(1), 1-14 (2018). https://doi.org/10.3390/magnetochemistry4010018

[30] G.K. Mahato, B.K. Mahatha, R. Nandkeolyar and B. Patra, "The Effects of Chemical Reaction on Magnetohydrodynamic Flow and Heat transfer of a Nanofluid past a Stretchable Surface with Melting," AIP Conference Proceedings, **2253**, 020011 (2020). https://doi.org/10.1063/5.0019205

[31] G.K. Mahato, B.K. Mahatha, S. Ram, and S.B. Padhi, "Radiative and Convective Heat Transfer on MHD Stagnation point Nanofluid Flow past a Stretchable Surface with Melting," AIP Conference Proceedings, **2435**, 020037 (2022). https://doi.org/10.1063/5.0083936

[32] B.K. Mahatha, S.B. Padhi, G.K. Mahato and S. Ram, "Radiation, Chemical Reaction and Dissipative Effects on MHD Stagnation Point Nano-Fluid Flow Past a Stretchable Melting Surface," AIP Conference Proceedings, **2435**, 020040 (2022). https://doi.org/10.1063/5.0083933

[33] I.C. Liu and H.I. Andersson, "Heat transfer over a bidirectional stretching sheet with variable thermal conditions," Int. J. Heat Mass Transf. **51**, 4018–4024 (2008). https://doi.org/10.1016/j.ijheatmasstransfer.2007.10.041

[34] M. Awais, T. Hayat, A. Alsaedi and S. Asghar, "Time-dependent three-dimensional boundary layer flow of a Maxwell fluid," Comput. Fluids, **91**, 21–27 (2014). https://doi.org/10.1016/j.compfluid.2013.12.002

[35] K. Jafar, R. Nazar, A. Ishak and I. Pop, "MHD stagnation point flow towards a shrinking sheet with suction in an upperconvected Maxwell (UCM) fluid," Int. J. Math. Compt. Phys. Elect. Comput. Eng. **8**(5), 1–9 (2014).

[36] T. Hayat, M. Awais, M. Qasim and A.A. Hendi, "Effects of mass transfer on the stagnation point flow of an upper-convected Maxwell (UCM) fluid," Int. J. Heat. Mass Trans. **54**, 3777–3782 (2011). https://doi.org/10.1016/j.ijheatmasstransfer.2011.03.003

ВПЛИВ ВИПРОМІНЮВАННЯ ТА ПОГЛИНАННЯ НА ТРИВИМІРНИЙ МАГНІТОГІДРОДИНАМІЧНИЙ (МГД) ПОТІК НАНОРІДИНИ МАКСВЕЛЛА З ВЕРХНЬОЮ КОНВЕКЦІЄЮ

Г.П. Гіфті[a], С.Б. Падхі[a], Б.К. Махатха[b], Г.К. Махато[c]

[a]*Кафедра математики, Технологічний та менеджментний університет Центуріон, Одіша, Індія*
[b]*Середня школа Раджкіякрит +2, Латбедхва, Кодерма, Джаркханд, Індія*
[c]*Кафедра математики, Інститут прикладних наук Аміті, Університет Аміті, Джаркханд, Ранчі-835303, Індія*

У цій статті досліджується МГД-потік нанорідини Максвелла з верхньою конвекцією через двоспрямовану розтяжну поверхню. Було досліджено вплив поглинання тепла та теплового випромінювання. Нелінійні диференціальні рівняння з частинними похідними, що контролюють закони збереження маси, збереження імпульсу, збереження енергії та концентрацію частинок, перетворюються на звичайні диференціальні рівняння за допомогою відповідного перетворення подібності, які потім розв'язуються чисельно за допомогою процедури bvp4c у MATLAB. Вплив різних фізичних параметрів на розподіл швидкості, температури та концентрації коротко описується за допомогою графіків. Тертя поверхні, швидкість тепло- та масоперенесення на пластині обчислюються чисельно та відображаються у таблиці. Така задача потоку рідини може знайти застосування в механізмах/пристроях теплопередачі.

Ключові слова: *нанорідина Максвелла; МГД; поглинання тепла; теплове випромінювання*